VT-Forschungsbericht 2021-04

Uncertainty Quantification in the Simulation of Turbulent Spray Combustion

Benedict Enderle, M.Sc.

Deutsches Zentrum für Luft- und Raumfahrt
Institut für Verbrennungstechnik
Stuttgart

Deutsches Zentrum
DLR   für Luft- und Raumfahrt

DLR

Uncertainty Quantification in the Simulation of Turbulent Spray Combustion

A thesis accepted by the Faculty of Aerospace Engineering and Geodesy
of the University of Stuttgart
in partial fulfillment of the requirements for the degree of
Doctor of Engineering Sciences (Dr.-Ing.)

by

Benedict Enderle, M. Sc.

born in Berlin

Main referee:	Prof. Dr.-Ing. Manfred Aigner
Co-referee:	Prof. Dr.-Ing. Andreas Kempf
Date of defense:	10 December 2021

Institute of Combustion Technology for Aerospace Engineering
University of Stuttgart

2021

Danksagung

Contents

List of Figures

List of Tables

Nomenclature

(U)RANS	(U)nsteady Reynolds Averaged Navier Stokes
ACARE	Advisory Council for Aviation Research and Innovation in Europe
AIAA	American Institute of Aeronautics and Astronautics
ASME	American Society of Mechanical Engineers
BC	Boundary Condition
CAB	Cascade Atomization and Breakup model
CARS	Coherent Anti-Stokes Raman Scattering
CDF	Cumulative Distribution Function
CDS	Central Differencing Scheme
CFD	Computational Fluid Dynamics
CFL	Courant-Friedrichs-Lewy
CRPS	Continuous Ranked Probability Score
CRZ	Central Recirculation Zone
CTM	Continuous Thermodynamics
DDES	Delayed Detached-Eddy Simulation
DES	Detached-Eddy Simulation
DNG	Dutch Natural Gas
DNS	Direct Numerical Simulation
DSHC	Delft Spray in Hot Coflow Flame
EDM	Eddy Dissipation Model
FGM	Flamelet Generated Manifold
FRC	Finite Rate Chemistry
GPR	Gaussian Process Regression
IRZ	Inner Recirculation Zone
LDA	Laser Doppler Anemometry
LES	Large Eddy Simulation

LHS	Latin Hypercube Sampling
LISA	Linearized Instability Sheet Atomization
LOS	Line of sight
MARS	Multivariate Adaptive Regression Spline
MC	Monte Carlo
MILD	Moderate or Intense Low-oxygen Dilution
MMD	Mass Mean Diameter
MOAT	Morris One At a Time
NASA	National Aeronautics and Space Administration
ODE	Ordinary Differential Equation
ORZ	Outer Recirculation Zone
PAMELA	Primary Atomization Model for prEfilming airbLAst injector
PBA	Probability Bounds Analysis
PC	Polynomial Chaos
PCE	Polynomial Chaos Expansion
PDA	Phase Doppler Anemometry
PDF	Probability Density Function
PIV	Particle Image Velocimetry
QoI	Quantity of Interest
RMS	Root Mean Square
RQL	Rich-Quench-Lean
RR	Rosin-Rammler
SAS	Scale Adaptive Simulation
SIMPLE	Semi-Implicit Method for Pressure Linked Equations
SMD	Sauter Mean Diameter
SRIA	Strategic Research and Innovation Agenda
SSB	Standard Spray Burner
SST	Shear Stress Transport
TCI	Turbulence Chemistry Interaction
THETA	Turbulent Heat Release Extension of the TAU code
TPB	Three Point Backward
UQ	Uncertainty Quantification

V&V	Verification and Validation	
VLES	Very Large Eddy Simulation	
VOF	Volume of Fluid	
WALE	Wall-Adapting Local Eddy-viscosity	

Non-dimensional numbers

Nu	Nusselt number	[-]
Re	Reynolds number	[-]
Sh	Sherwood number	[-]
St	Stokes number	[-]
Sw	Geometric swirl number	[-]
We	Weber number	[-]

Calligraphic symbols

$\mathcal{D}_A$	Application domain	[-]
$\mathcal{D}_V$	Validation domain	[-]
$\mathcal{L}$	Integral length scale	[m]
$\mathcal{L}_t$	Turbulent length scale	[m]
$\mathcal{L}_{vK}$	von Karman length scale	[m]
$\mathcal{M}$	Simulation model	[-]
$\mathcal{M}_S$	Sub model	[-]
$\mathcal{N}$	Normal distribution	[-]
$\mathcal{O}$	Order of magnitude	[-]
$\mathcal{R}$	Specific gas constant	$[\text{J kg}^{-1}\,\text{K}^{-1}]$
$\mathcal{S}_M$	Sample set with M samples	[-]
$\mathcal{S}_P$	Physical system	[-]
$\mathcal{S}_{ij}^d$	Traceless symmetric part of the square of the velocity gradient tensor	$[\text{s}^{-2}]$
$\mathcal{U}$	Uniform distribution	[-]
$\mathcal{V}$	Cell volume fraction	[-]

Greek letters

α	Species counter	[-]
α_k	Coefficients of the PCE	[-]
Γ_p	Wiener polynomial chaos	[-]
Δh_{vap}	Specific enthalpy of vaporization	$[\text{J kg}^{-1}]$

Δt	Time step	[s]
$\Delta x, \Delta y, \Delta z$	Grid spacing	[m]
Δ	Filter width	[m]
δ	Dirac function	[-]
Δ_M	Variation step size in MOAT	[-]
δ_{ij}	Kronecker delta	[-]
ϵ	Turbulent dissipation rate	$[\mathrm{m^2\,s^{-3}}]$
ε_{num}	Numerical error	[-]
ζ_α	Ratio between species and total vapor massflux	[-]
$\boldsymbol{\theta} = \{\theta_1, \theta_2,..\}$	Vector of model parameters θ_i	[-]
θ_{ff}	Mean distribution parameter in the CTM	[-]
ϑ_t	Velocity scale	$[\mathrm{m\,s^{-1}}]$
$\kappa(\mathbf{x}_i, \mathbf{x}_j)$	Covariance function in GPR	[-]
λ	Thermal conductivity	$[\mathrm{J\,m^{-1}\,s^{-1}\,K^{-1}}]$
μ	Dynamic viscosity	$[\mathrm{kg\,m^{-1}\,s^{-1}}]$
$\mu*$	Modified mean in MOAT	[-]
ν	Kinematic viscosity	$[\mathrm{m^2\,s^{-1}}]$
$\nu'_{\alpha,r}$	Stochiometric coefficient of the reactant α in reaction r	[-]
$\nu''_{\alpha,r}$	Stochiometric coefficient of the product α in reaction r	[-]
$\boldsymbol{\xi} = \{\xi_1, \xi_2,..\}$	Vector of independent random variables ξ_i	[-]
ρ	Density	$[\mathrm{kg\,m^{-3}}]$
σ	Surface tension	$[\mathrm{kg\,s^{-2}}]$
σ_f	Signal variance function in GPR	[-]
σ_T	Temperature variance in the TCI model	[K]
σ_Y	Species variance in the TCI model	[K]
τ_F	Local time scale of the flow	[s]
τ_v	Velocity time scale	[s]
τ_{ij}	Stress tensor	$[\mathrm{N\,m^{-2}}]$
$\bar{\varphi}$	Mean trajectory angle / Mean spray cone angle	[°]
ϕ	Global equivalence ratio	[-]
φ'	Dispersion angle	[°]
φ_D	Axial angle of a droplet wrt. local coordinate system	[°]

$\boldsymbol{\Psi}(\boldsymbol{\xi})$	Basis of orthogonal polynomials	[-]
ψ_D	Swirl angle of a droplet wrt. local coordinate system	[°]
ψ_{ff}	Second moment distribution parameter in the CTM	[-]
Ω	Parameter space of uncertain inputs / support of a random variable	[-]
ω	Specific dissipation rate	[s^{-1}]

Latin letters

$\vec{a}_d$	Acceleration vector due to drag	[m s^{-2}]
A	Surface area	[m^2]
A_r	Pre-exponential factor in the Arrhenius equation	[-]
B_M	Spalding mass transfer number α	[-]
b_r	Temperature exponent in the Arrhenius equation	[-]
B_T	Spalding heat transfer number α	[-]
c_d	Drag coefficient	[-]
c_p	Specific isobaric heat capacity	[J kg^{-1} K^{-1}]
C_S	Smagorinsky constant	[-]
d	Diameter	[m]
D_α	Diffusion coefficient of species α	[m^2 s^{-1}]
d_i	Elementary effect in MOAT	[-]
D_{32}	Sauter mean diameter	[m]
D_{50}	Mass mean diameter	[m]
E	Energy	[J]
$E_{\alpha,r}$	Activation energy in the reaction r	[J]
F_1,F_2	Blending functions in the k-ω SST model	[-]
f_1,f_2,f_3	Grid levels	[-]
F_s	Safety factor	[-]
G	Filter kernel	[-]
G_k	Production source term of k	[kg m^{-1} s^{-1}]
$\mathbb{H}$	Heaviside function	[-]
h	Measure of grid spacing	[-]
h	Specific enthalpy	[J kg^{-1}]
h_a	Height of the atomizing edge	[m]
k	Turbulent kinetic energy	[m^2 s^{-2}]

k_b	Backward reaction rate	[-]
k_f	Forward reaction rate	[-]
k_w	Wavenumber	[-]
l	Length	[m]
l_c	Correlation length scale in GPR	[m]
L_f	Liquid film length	[m]
$\dot{m}$	Mass flow rate	[kg s^{-1}]
M	Number of samples	[-]
m	Mass	[kg]
M_α	Molar mass of species α	[kg mol^{-1}]
N_s	Number of species	[-]
P	Cardinality of the PCE	[-]
p	Pressure	[Pa]
p_c	Observed order of converge	[-]
P_{th}	Thermal input	[W]
$\boldsymbol{Q} = \{Q_1, Q_2, ..\}$	Vector of random variables for the uncertain quantities of interest	[-]
$\boldsymbol{q} = \{q_1, q_2, ..\}$	Vector of deterministic quantities of interest	[-]
$\dot{q}$	Surface heat flux	[J m^{-2} s^{-1}]
Q	Random variable for an uncertain quantity of interest	[-]
q	Heat flux	[J m^{-2} s^{-1}]
$\mathbb{R}$	Set of real numbers	[-]
R	Radial coordinate	[m]
r_k	Ratio of resolved to total turbulent kinetic energy	[-]
r_p	Density ratio	[-]
r_r	Refinement factor	[-]
$\boldsymbol{S}$	Norm of the train rate tensor	[s^{-1}]
$\boldsymbol{S}_i$	Aggregated first-order Sobol index	[-]
$\boldsymbol{S}_{i,T}$	Aggregated total-order Sobol index	[-]
S^{Sp}	General source term due to spray	[-]
S_i	First-order Sobol index	[-]
S_r	Enthalpy source term due to radiation	[J m^{-3} s^{-1}]
$S_{i,T}$	Total-order Sobol index	[-]

S_{ij}	Strain rate tensor	$[\mathrm{s^{-1}}]$
T	Temperature	$[\mathrm{K}]$
t	Time	$[\mathrm{s}]$
$\vec{u}_p$	Particle velocity vector	$[\mathrm{m\,s^{-1}}]$
$\vec{u}_r el$	Relative velocity vector	$[\mathrm{m\,s^{-1}}]$
U	Velocity magnitude	$[\mathrm{m\,s^{-1}}]$
u, v, w	Velocity components wrt. cartesian coordinates	$[\mathrm{m\,s^{-1}}]$
u_{ax}, u_{rad}, u_{tan}	Velocity components wrt. local polar coordinates	$[\mathrm{m\,s^{-1}}]$
Unc	Uncertainty	$[-]$
$\dot{V}$	Volume flow rate	$[\mathrm{m^3\,s^{-1}}]$
W_1	Wasserstein-1 metric	$[-]$
$\boldsymbol{X} = \{X_1, X_2, ..\}$	Vector of random variables for the uncertain inputs	$[-]$
$\boldsymbol{x} = \{x_1, x_2, ..\}$	Vector of deterministic input variables	$[-]$
$\vec{x}_p$	Particle position vector	$[\mathrm{m}]$
X	Random variable for an uncertain input	$[-]$
x, y, z	Cartesian coordinates	$[\mathrm{m}]$
Y	Mass fraction	$[-]$

Operators

$\bullet'$	Fluctuation wrt. Reynolds averaging
$\bullet''$	Fluctuation wrt. Favre average
$\hat{\Xi}$	Approximation of quantity or model Ξ
$\langle \bullet, \bullet \rangle$	Inner product
$\langle \bullet \rangle$	Expectation from Reynolds averaging
$\mathbb{E}$	Expectation
$\mathbb{V}$	Variance
$\overline{\bullet}$	Filtered value
$\widetilde{\bullet}$	Favre average
$\widetilde{\overline{\bullet}}$	Favre filtered value
Corr	Correlation
Cov	Covariance
Pr	Probability

Common subscripts and superscripts ─────────────────────────

$(..)^\infty$	Quantity at ambient conditions
$(..)^S$	Quantity at the droplet surface
$(..)_\mathrm{E}$	Educt
$(..)_\mathrm{ff}$	Fuel family
$(..)_\mathrm{GP}$	Gaussian process
$(..)_\mathrm{g}$	Gas
$(..)_\mathrm{liq}$	Liquid
$(..)_\mathrm{LO}$	Lift-off
$(..)_\mathrm{PAM}$	Quantities in the PAMELA model
$(..)_\mathrm{P}$	Product
$(..)_\mathrm{p}$	Particle
$(..)_\mathrm{ref}$	Reference value
$(..)_\mathrm{sgs}$	Sub-grid scale quantity
$(..)_D$	Droplet
$\vec{\bullet}$	Vector in cartesian coordinates

Abstract

In order to make risk informed decisions in the simulation-based design and development of aircraft components, uncertainties in the simulation results must be taken into account. This concerns high-consequence decisions regarding financial risks, operational safety and ultimately human lives. A field which combines a variety of possible uncertainties with complex modeling demands and great impact on the system performance and safety is the simulation of combustion in aeroengines. Since the quality of the fuel spray significantly influences the combustion process, the formulation of boundary conditions for the spray after primary atomization introduces a major source of uncertainties in such simulations. Due to the high computing time for their quantification these uncertainties are not explicitly taken into account at the moment.

Although the future need for uncertainty quantification in combustion simulations is recognized in the scientific and engineering community, only a few studies regarding its application can be found in the literature. Therefore, this work aims at applying state of the art methods for uncertainty quantification to simulation problems involving turbulent spray combustion. Special emphasis is placed on the quantification of uncertainties in the simulation results due to incomplete knowledge in the construction of the spray boundary conditions. Possible uncertainties in the input and output quantities are characterized from a probabilistic perspective. The propagation of the uncertainties through the complex simulation problems is analyzed using an efficient, non-intrusive workflow involving surrogate modeling. In this approach, the high fidelity simulation model is replaced by a model of reduced fidelity over a limited parameter range. This drastically reduces the computational burden for complex simulations when facing a large number of uncertain inputs.

The method is applied to two test cases with different complexity. At first, the probabilistic workflow is applied to a well characterized laboratory scale spray flame burning liquid ethanol. The reduced complexity of both the experimental apparatus and the steady-state simulation enables an in-depth analysis of the problem under consideration. Uncertain input parameters are prioritized in a screening study, which allows for a reduction of the parameter space. Two different surrogate modeling methods are compared and analyzed. The computation of the probability bounds reveals extensive uncertainties regarding the gas phase temperature over the reaction zone. In a sensitivity analysis, the majority of this uncertainty is traced back to the uncertainties in the spray cone angle of the atomizer.

In order to assess the methodology for uncertainty quantification in an engineering relevant problem, a semi-technical spray burner reflecting characteristics typically found in modern aeroengine combustors is considered. To overcome the need for costly experimental data

for the spray boundary conditions, an algebraic primary breakup model is incorporated and the resulting reduction in prior knowledge is compensated through probabilistic modeling and uncertainty quantification. Due to their importance in the design process, temperature distribution and flame position are considered as the main quantities of interest. Moderate uncertainties are found in the results for the gas phase temperature as well as the flame position. The predictive capacity of the simulation under the given uncertainties is appraised using accuracy metrics for uncertain observations.

Both test cases successfully demonstrate the potential of uncertainty quantification in the simulation of turbulent spray combustion. From the first test case it is concluded that the identification and adequate characterization of sources of uncertainties should be systematically included in the design of validation experiments. The second test case clearly demonstrates the added value of uncertainty quantification when only limited information regarding the spray boundary conditions is available as this lack of knowledge is reflected as uncertainties in the simulation results. This allows for a quantitative identification of risks when comparing the simulation results with predefined performance targets. With these additional information at hand, simulation-based decision-making in the design and development process can be supported and ultimately extended towards virtual certification for high consequence scenarios.

Kurzfassung

Um risikobehaftete Entscheidungen in der simulationsbasierten Entwicklung von Flugzeugkomponenten treffen zu können, müssen Unsicherheiten in den Simulationsergebnissen systematisch mitberücksichtigt werden. Dies betrifft insbesondere Entscheidungen mit weitreichenden Konsequenzen hinsichtlich finanzieller Risiken, Sicherheit im Betrieb sowie letztlich Menschenleben. Eine Anwendung der simulationsbasierten Entwicklung, der eine Vielzahl an Unsicherheiten mit komplexen Simulationsmodellen und einer großen Auswirkung auf die Systemleistung- und Sicherheit kombiniert, ist die Simulation von Verbrennungsprozessen in Triebwerksbrennkammern. Da die Qualität des Brennstoffsprays den Verbrennungsprozess signifikant beeinflusst, sind Unsicherheiten in den Randbedingungen für das Brennstoffspray eine Hauptquelle für Unsicherheiten in solchen Simulationen. Aufgrund des hohen Rechenzeitaufwands für deren Quantifizierung werden diese Unsicherheiten momentan noch nicht mit in die Simulation einbezogen. Auch wenn die Notwendigkeit der Quantifizierung von Unsicherheiten in Verbrennungssimulationen bereits identifiziert wurde, lassen sich nur wenige Anwendungsbeispiele in der Literatur finden.

Ziel dieser Arbeit ist daher, aktuelle Methoden zur Quantifizierung von Unsicherheiten auf Simulationsprobleme aus dem Bereich der turbulente Sprayverbrennung anzuwenden. Ein besonderes Augenmerk liegt hierbei auf der Quantifizierung von Unsicherheiten in den Simulationsergebnissen aufgrund von unvollständigem Wissen bei der Konstruktion der Sprayrandbedingungen. Mögliche Unsicherheiten in den Eingangs- und Ausgangsgrößen werden mittels Wahrscheinlichkeitstheorie charakterisiert. Die Ausbreitung der Unsicherheiten durch die komplexen Simulationsprobleme werden mit einem effizienten, nichtintrusiven Workflow analysiert, welcher auf Surrogatmodellen aufbaut. Durch den Einsatz von Surrogatmodellen wird das komplexe Simulationsmodell in einem eingeschränkten Parameterbereich mittels eines Modells reduzierter Komplexität approximiert. Dieses Verfahren reduziert den Rechenaufwand drastisch, insbesondere bei einer hohen Anzahl an unsicheren Eingangsgrößen

Die Methodik wird auf zwei Testfälle mit unterschiedlicher Komplexität angewandt. Zuerst wird eine Ethanolsprayflamme im Labormaßstab betrachtet, für die umfangreiche experimentelle Daten vorliegen. Der einfache Aufbau des Experiments sowie die Möglichkeit, diese Flamme mit stationären Simulationen bereits gut abbilden zu können ermöglicht eine detaillierte Analyse des Testfalls sowie der verwendeten Methodik. In einer Screening-Studie werden die unsicheren Parameter der Simulation priorisiert, woraus sich eine Reduktion auf die einflussreichsten Parameter ergibt. Anhand des Testfalls werden zwei unterschiedliche Surrogatmodelle verglichen und analysiert. Durch die Berechnung der Wahrscheinlichkeitsgrenzen für die Temperaturprofile können umfangreiche Unsicherheiten in den Simulationsergebnissen

im Bereich der Reaktionszone identifiziert werden. Mittels einer anschließenden Sensitivitätsanalyse kann der Hauptteil dieser Unsicherheiten auf Unsicherheiten hinsichtlich des Öffnungswinkels der Spraykegels zurückgeführt werden.

Um die Methodik zur Quantifizierung von Unsicherheiten auch in einer technisch relevanten Problemstellung zu bewerten, wird anschließend ein drallstabilisierter Spraybrenner betrachtet, der einige der wesentlichen Eigenschaften moderner Triebwerksbrennkammern aufweist. Um kostspielige Experimente zur Charakterisierung der Sprayrandbedingung zu vermeiden, wird ein algebraisches Primärzerfallsmodell zur Berechnung der Sprayrandbedingung verwendet. Die daraus resultierende Datenlücke wird mittels Wahrscheinlichkeitstheorie als Unsicherheit charakterisiert. Aufgrund ihrer besonderen Bedeutung im Entwurfsprozess von Brennkammern werden die Flammenposition und die Temperaturverteilung als Hauptindikatoren betrachtet. Die systematische Quantifizierung der Unsicherheiten zeigt moderate Unsicherheiten der Simulation hinsichtlich der Flammenposition und Temperaturverteilung. Anhand von Genauigkeitsmetriken wird schließlich die Vorhersagefähigkeit der Simulation unter den gegebenen Unsicherheiten abgeschätzt.

Beide Testfälle zeigen erfolgreich das Potential von Methoden zur Quantifizierung von Unsicherheiten in der Simulation turbulenter Sprayverbrennung. Aus dem ersten Testfall kann gefolgert werden, dass die Identifizierung und umfassende Charakterisierung möglicher Quellen von Unsicherheiten in den Entwurf von Validierungsexperimenten eingeschlossen werden sollten. Der zweite Testfall zeigt deutlich den Mehrwert der systematischen Quantifizierung von Unsicherheiten auf, wenn nur begrenztes Wissen hinsichtlich der Sprayrandbedingungen vorhanden ist. Da diese Wissenslücke klar in den Simulationsergebnissen wiedergespiegelt wird, können aus dem Vergleich mit den geforderten Leistungsparametern Risiken quantitativ identifiziert werden. Mit dieser zusätzlichen Information kann die simulationsbasierte Entscheidungsfindung im Entwicklungsprozess systematisch unterstützt und schließlich ausgeweitet werden, beispielsweise auf die virtuelle Zertifizierung von Flugzeugkomponenten.

1. Introduction

With the ever increasing availability of high performance computing capacities over the past three decades, numerical modeling and simulation of physical processes has emerged as a powerful tool for a variety of problems faced in both research and engineering.

For example, by the end of the 20th century, the design process of an aircraft engine required 90 % of rig tests and 10 % of computational fluid dynamics simulations [164]. By now, these numbers are almost inverted, resulting in a noticeable cost reduction in the development programs due to the lower number of experimental rig tests [144]. Furthermore, modeling and simulation offers the potential of a reduction in turnaround time in the design process as multiple concepts and scenarios can be investigated in parallel given adequate computing capacities. This enables an agile development process which is able to react to changing requirements concerning the final product. Thus, further inclusion and advancement of modeling and simulation in the design cycle might also be a competitive advantage from the economical perspective.

In general, the simulation-based design process aims at demonstrating the compliance of a novel design concept with predefined *performance targets* through modeling and simulations. These targets cover for example load limits for structural safety, increase in system efficiency or regulatory policies regarding pollutant emissions. On the basis of the simulation results, decisions regarding a redesign, advancement to the next design stage or even a market entry are made. Obviously, this concerns decisions with high financial risks and potentially even risks regarding human safety.

An example of such a decision is shown in Fig. 1.1. A quantity of interest is required to lie within a specific interval, depicting the performance target. In the case of an aeroengine, the quantity of interest could be thought of as the concentration of a pollutant at the combustor exit. At first (Fig. 1.1 (a)), simulation results without uncertainties are reported as a point measure. The simulation result is within the performance target and hence complies with the requirement, but uncertainties in the simulation results due to model errors or uncertainties in the simulations inputs are unknown. In the second case (Fig. 1.1 (b)) associated uncertainties were systematically assessed. This reveals possible simulation results outside the performance target which correspond to *risks* regarding the decision making process. Only on the basis of this additional information, a *risk-informed* decision to take the risk of failure or invest further efforts in reducing the uncertainties can be made.

For this purpose, *uncertainty quantification* (UQ) aims at quantitatively characterizing the uncertainties in simulation results. In recent times, probabilistic methods have become increasingly popular for the treatment and quantification of uncertainties [84, 135, 206]. In

(a) No uncertainties considered   (b) Quantification of uncertainties
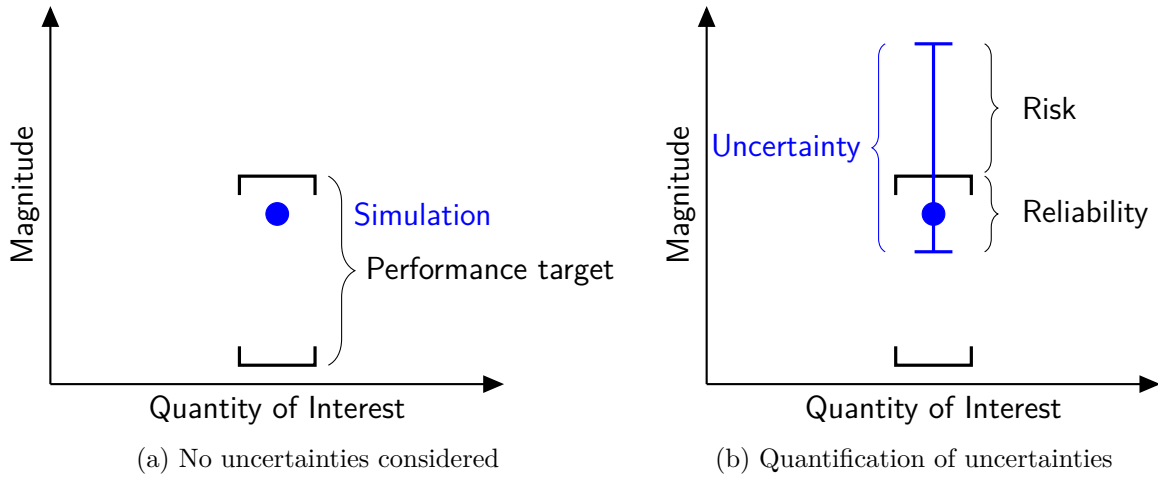
Figure 1.1.: Simulation based decision making.

this approach uncertain quantities are treated as random variables which can be characterized by probability density functions or intervals to portray their probabilistic behavior. As a result, minimum/maximum or confidence intervals can be reported in addition to the simulation results to support the decision makers (see Fig. 1.1 (b)). This finally enables novel approaches towards the design process such as *uncertainty-based design* [283] or *uncertainty-based optimization* [101, 280] in which an optimal design under the given uncertainties is achieved.

The broad term *uncertainties* include, inter alia, approximations in the model formulation, application of the model outside the validation range, and incomplete knowledge about model parameters or boundary conditions [177]. From a practical viewpoint the latter refers to the common issue that inputs to the simulation might be difficult or impossible to measure in accompanying experiments. In the most severe case, some inputs are unknown beforehand - a situation typically found in industrial design processes as the inputs might depend on the final design.

Historically, UQ methods were first established for risk mitigation in the nuclear industry [176]. Due to the impossibility of extensive physical testing, probabilistic simulations were used to identify scenarios for severe accidents of nuclear reactors [8] or to asses the safety and reliability of nuclear warheads [241]. In recent time, these methods have advanced towards other safety critical fields such as the design of aerospace vehicles [225, 283] or medical decision making [13].

Due to their efficiency and their utility for representing and propagating large uncertainties through complex models, surrogate-based UQ methods have drawn increasing attention [172, 254]. For the application to CFD problems most results were reported using Polynomial Chaos Expansion (PCE) [128, 283] and Gaussian Process based sampling [68, 281].

1.1. Uncertainties in the simulation of turbulent spray combustion in aeroengine combustors

Due to the outstanding volumetric and mass energy density, liquid fuels represent the predominant source of energy for aeroengines [197]. Therefore, *spray combustion* is the paramount thermo-chemical process in such combustors, involving the strongly coupled sub-processes of formation of a liquid spray through atomization, vaporization of droplets, mixing of the fuel vapor and finally chemical reaction. Figure 1.2 provides a simplified schematic of the interplay of these mechanisms in a conventional Rich-Quench-Lean (RQL) combustor.

Coming from the compressor stage, air enters the combustor through a diffuser which reduces the air velocity and hence the pressure loss. A portion of the air passes through a succession of swirlers into the primary combustion zone. Here, liquid fuel is injected through carefully designed atomizers, creating a spray of small droplets. A strongly swirling flow allows for an enhanced mixing of the evaporating fuel with fresh air and burned products, and stabilizes the subsequent combustion process. Downstream of the flame, secondary air is injected to quench the rich combustion zone. Towards the combustor exit, the combustion products are further diluted with cold air from the secondary stream, thereby reducing the exit temperature to a level that is acceptable to the turbine [131].

Requirements regarding safe operation of such combustors include reliable relight at high altitude, cold-day ignition and lean blowout limits [54]. In the presence of increasingly strict regulatory policies, reduction of pollutant emissions is of major concern [133]. Clearly, these requirements represent critical performance targets in the design process of a novel combustor. In order to make a simulation-based verdict regarding the compliance with these performance targets, models from the fields of fluid mechanics, droplet dynamics, heat transfer and chemical kinetics are required. Although enormous progress has been made [81, 99, 200], current computer models still struggle with the prediction of these coupled and unsteady
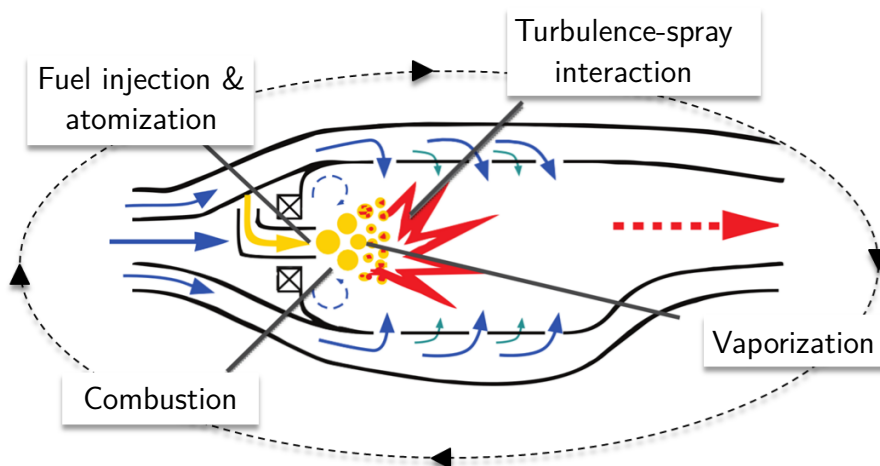
Figure 1.2.: Thermo-chemical processs in an aeroengine combustor (adapted from [202]).

phenomena [50]. The high modeling demand in combination with the complex geometry of aeroengine combustors still requires supercomputing capacities to keep the computing time at a maintainable level [51, 60]. Despite the fact that such models are capturing physical and chemical processes with increasing accuracy, doubts on the reliability of the simulation result remain and hinder the application of numerical simulation to its fullest potential.

The various models involved require input in the form of modeling constants. Typically, these constants are calibrated against results from simplified testcases. Therefore, the application to a full scale combustion system introduces uncertainties regarding the adequacy of the modeling constants. Furthermore, boundary conditions are required to complete the modeling system. This includes for example data for the mass flow, temperature and turbulence degree at the combustor entrance or local heat flux at the combustor walls. While some of these information might be available from measurements, others rely on empirical correlations, simplifications or assumptions.

It is well known [46, 131, 202] that fuel preparation is one of the processes with a major influence on engine safety and operability. Subsequent processes from evaporation up to pollutant formation strongly depend on the quality of the spray [129]. This must be reflected in accurate boundary conditions regarding droplet size, velocity and local volume flux[1]. However, this data is difficult to acquire from experiments [259] or relies on expert opinion and experience in early stages of the design process. The influence of incomplete knowledge regarding the spray boundary condition on simulation results was mentioned for example by Eckel et al. [51], Ruoff et al. [217], or Pei et al. [181] but no systematic assessment in terms of uncertainties in the simulation results was reported. The inclusion of this information would significantly aid in identifying critical scenarios regarding the aforementioned performance targets in the design process of aeroengine combustors. For this reason, comprehensive quantification of uncertainties arising from the specification of spray boundary conditions is identified as the key issue for the work at hand.

1.1.1. Spray boundary conditions

Three methodologies to infer boundary conditions for the spray can be differentiated, namely direct simulation of the primary atomization process, phenomenological modeling of the primary atomization or reconstruction from experimental data.

Although direct simulation methods such as VOF-based interface tracking [238] or level set [152] coupled with DNS or LES offer full insight into the atomization process and thereby detailed information about the resulting dispersed spray, the computational expense associated with the neccessary spatial and temporal resolution currently limit its application to fundamental problems and testcases [86].

As a consequence, phenomenological models with reduced computational requirements have been developed over the past decades [12, 53, 103, 262]. They aim at statistically describing the esssential features of the initial breakup process based on geometric quantities

---

[1]For further details on spray boundary conditions see Sec. 2.4.

of the atomizer, properties of the liquid under consideration or main features of the flow field which are predetermined or extracted during simulation runtime. The assumptions made in the derivation of the model regarding the underlying physical process, and the variety of different breakup mechanisms [86] limit each of these models to a specific range of application, i.e. different types of atomizers. Therefore, models have been proposed inter alia for plain jets [198], pressure-swirl atomizers [231, 234] or prefilming airblast atomizers [26].

In the case of reconstruction from experimental data [56, 195], spray boundary conditions are specified with respect to prior experimental characterization of the dispersed phase. In most cases, this data is only available at further downstream locations, since droplet measurements close to atomizers are difficult to realize due to the presence of non-spherical droplets and liquid ligaments [259]. Consequently, such boundary conditions require further calibration to match downstream experimental data.

For the work at hand, spray boundary conditions from experimental data as well as a phenomenological breakup model are considered.

1.2. Literature review

Although the future need for UQ in combustion simulations is recognized in the scientific community [99, 200], only a few studies regarding its application can be found in the literature: The role of sensitivity and uncertainty analysis in combustion model validation was highlighted in the work of Mueller et al. [169] and Johnson et al. [108]. UQ was utilized in the analysis of sub-phenomena of combustion including acoustics [7], chemical kinetics [194, 237], fuel evaporation [203, 217] and combustion instabilities [11]. A study regarding uncertainties in spray boundary conditions was reported by Van Dam et al. [265] for a non-reacting testcase. The influence of uncertainties in chemical kinetics on a flamelet based Large Eddy Simulation (LES) of a methane jet flame was analyzed through stochastic collocation by Mueller et al. [167]. Pei et al. [181] conducted global sensitivity analysis for a URANS model of the Engine Combustion Network Spray A case to deduce the influence of spray parameters on integral quantities such as ignition delay and flame lift off height. Mueller et al. [168] and Tang et al. [257] combined PCE and LES of single phase flow to quantify the influence of boundary conditions on soot evolution and forced ignition, respectively. PCE based UQ was applied to an LES of a turbulent methane/hydrogen bluff-body flame by Khalil et al. [119] focusing on LES modeling parameters, e.g. Smagorinsky constant C_s. 1D marginal PDFs of mean axial velocity and temperature at a position in the flame were presented, showcasing the computational efficiency of PCE based UQ. Results from PCE based UQ were also reported by Masquelet et al. [148] for an industrial scale aviation gas turbine combustor. For the construction of the PCE, they conducted a series of flamelet based LES, assuming fast evaporation of the fuel and therefore neglecting the multiphase spray regime.

1.3. Objective and structure of the work

The literature review presented in the previous section reveals that comprehensive quantification of uncertainties in the simulation of reacting multiphase flows still remains a major research challenge. Therefore, the work at hand aims at applying state of the art UQ methods to typical problems in the simulation of turbulent spray combustion. Special emphasis is placed on the uncertainties arising from the specification of spray boundary conditions. Two testcases of different complexity are considered. The resulting portrayal of associated uncertainties in the simulation results would aid in advancing towards model based decision making in problems involving spray combustion.

The dissertation is organized as follows. Chapter 2 provides an overview on computational methods for the simulation of turbulent spray combustion.

Chapter 3 summarizes the fundamentals of uncertainty quantification for complex simulations. The focus is put on a comprehensive toolchain for UQ including surrogate modeling.

In Chapter 4, this toolchain is applied to an *academic* testcase consisting of a laboratory scale flame burning liquid ethanol. The testcase can be attribute to a benchmark case in the validation hierarchy[2]. Different methods for surrogate modeling are analyzed and compared.

A further advanced simulation problem is examined in Chapter 5. The *semi-technical* swirl-stabilized spray burner involves essential features of combustion in aeroengines and resides between benchmark and subsystem case. The application of UQ methods to a complex, scale-resolving simulation problem is demonstrated including quantitative measures for the predictive capabilities under the given uncertainties.

Finally, conclusions regarding the two testcases are drawn in Chapter 6 and recommendations for future developments are derived.

---

[2]See Appendix A

2. Computational methods for the simulation of turbulent spray combustion

This chapter provides an overview of the computational methods required for the simulation of turbulent spray combustion. For further details, the reader is referred to the textbooks of Kuo [124] and Poinsot [186] as well as the review paper by Jenny et al. [107]. All methods are selected and discussed with respect to use cases related to gas turbine combustion in aero-engines and stationary power generation. In such systems, liquid fuel is injected, evaporated and mixed in a carrier gas phase - primarily air - prior to combustion. As liquid fuel and gaseous air constitute different thermodynamic *phases*, i.e. different states of matter, the occurring phenomena are characterized as *multi-phase flows*.

2.1. Modeling approaches for multi-phase flows

In general, multi-phase flows can exist in many different forms such as bubbly flows in chemical reactors, slurry flows in gasification, sediment transport in river beds or fluidized beds in coal combustion [123]. However, the thesis at hand focuses at the particular case of *dispersed sprays*, a multi-phase system in which a dynamic collection of microscopic liquid droplets are transported in a gas.

From such a liquid spray, a single droplet moving in an airflow with velocity u_g is considered. Due to momentum exchange between the droplet and the airflow, coupling effects between the two phases occur. The velocity or momentum response time τ_V relates to the timescale at which the droplet responds to a change in u_g. On the other hand, τ_F is a local characteristic timescale of the gas flow field. The ratio between the two timescales then defines the non-dimensional *Stokes number* of the droplet:

$$\mathrm{St} \equiv \frac{\tau_V}{\tau_F} \tag{2.1}$$

The Stokes number allows for a classification of the interaction between droplet and airflow. For $\mathrm{St} << 1$ the droplet follows the streamlines of u_g closely, whereas in case of $\mathrm{St} > 1$ the trajectory of the droplet will not be affected by changes in u_g.

Furthermore, based on the Stokes number a qualitative estimate of the whole spray can be made by considering the average time between droplet-droplet collisions τ_C in the spray as τ_F

(a) Euler - Euler

(b) Euler - Lagrange
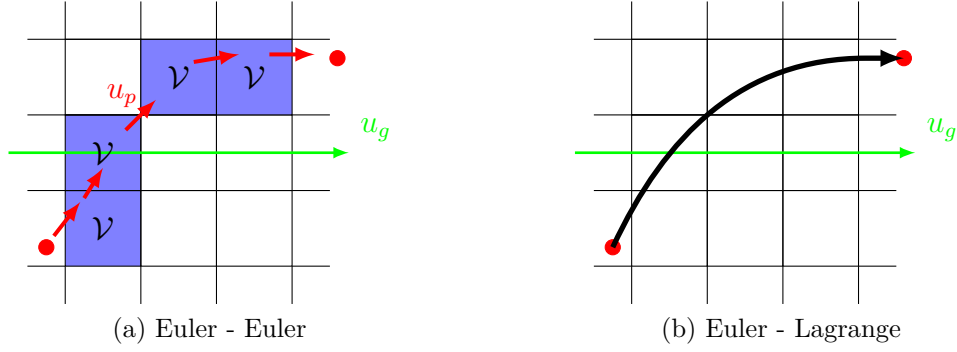
Figure 2.1.: Trajectory of a droplet in a gas crossflow from different numerical approaches.

in Eq. (2.1). The spray is interpreted as *dilute* if $St_C < 1$ and *dense* if $St_C > 1$. In a dilute dispersed phase flow, the droplet motion is controlled by the fluid forces, i.e. drag and lift, while in a dense flow, the droplet motion is controlled by inter-droplet collisions. In the case of a spray evolving from a typical gas turbine atomizer, the atomization process of the fuel takes place in the dense regime, whereas the transport, evaporation and mixing is typically associated with the dilute spray regime [61]. Note that simulation methods for dense sprays are out of scope of this thesis and are only discussed in brief.

While the continuous gas phase in dispersed spray simulations is typically modeled using well known conservation equations for continuum fluid mechanics in an Eulerian reference frame, different modeling frameworks are available for the simulation of the dispersed liquid phase. A comparison of the two most common approaches is shown in Fig. 2.1 for the aforementioned example of a single droplet in a gas flow.

The Euler - Euler approach describes both phases using conservation equations in an Eulerian reference frame, i.e. by observations in fixed co-ordinates of a computational mesh. Both phases are seen as a continuous medium, each inter-penetrating the other. Therefore, a conservation equation for the cell volume fraction $\mathcal{V}$ of the liquid phase is required. In Fig. 2.1 (a) blue regions depict grid cells with $\mathcal{V} \neq 0$, indicating that the droplet is moving trough these cells. The trajectory of the droplet is then derived from all cells with $\mathcal{V} \neq 0$. Since both phases are described in the same reference frame, a single numerical solver can be used for the full multi-phase system by adding the additional conservation equations for the liquid phase. In principle, the Euler-Euler approach is applicable to the entire range of multi-phase flows, including the dense, intermediate and dilute regime. However, this generality comes at the difficulty in prescribing suitable inter-phase models for the flow regime under consideration [233] and the necessity of a high spatial resolution when dealing with dilute flows in order to accurately capture droplet trajectories. Therefore, this approach is more attributed to dense multi-phase flows.

On the other hand, in the Euler - Lagrange approach as shown in Fig. 2.1 (b), individual droplets from the dispersed phase are tracked through the flow domain by solving the droplet's equation of motion in a Lagrangian reference frame, i.e. a reference frame following the trajectory. The Lagrangian equation of motion relates the rate of change of the droplet's velocity to the sum of forces acting upon it. This allows for a precise tracking of the trajectory
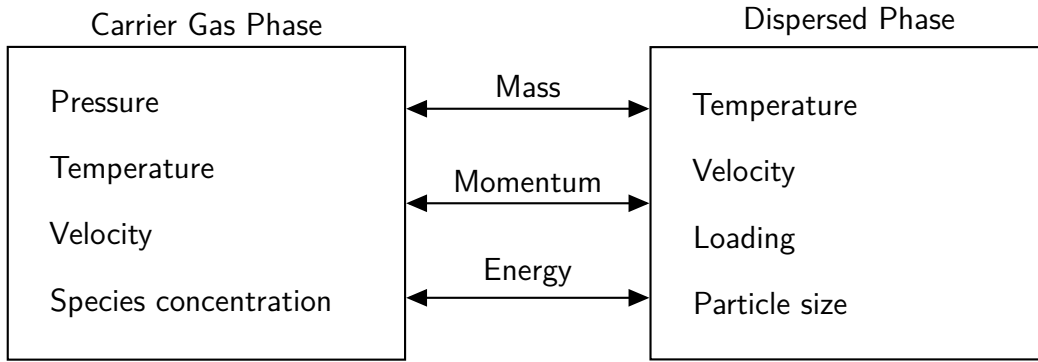
Figure 2.2.: Coupling effects in a dispersed multiphase flow system [233].

and the evolution of the droplet's time history due to evaporation, condensation, collision or wall interaction. Since an individual equation of motion is solved for each droplet, it is relatively easy to account for a distribution of droplet sizes as typically found in sprays. However, as sprays in technical applications can consist of millions of droplets [129] it may become computationally expensive to allow the trajectory of every particle to be calculated. Commonly, droplets with identical properties are therefore summed up to computational parcels replacing the original droplets in the solution procedure. Thus, a representative sample of parcel trajectories is calculated to yield sufficient statistics. Limitations of the Euler - Lagrange approach are found in problems with high droplet densities (dense flows) and small grid cells, since the volume fraction of the dispersed phase is commonly neglected in the continuous phase [50]. As this thesis is focused on applications in the reacting dilute dispersed spray regime, the Euler - Lagrange approach is adopted in the following.

Typical applications in gas turbine relevant spray combustion are considered *two-way coupled*, meaning that there is a mutual effect between the flows of both phases. Coupling applies to all quantities in the carrier gas phase and dispersed phase and is driven by the mutual exchange of mass, momentum and energy. For example, during evaporation, liquid fuel is transferred to the gas phase and converts to fuel vapor while the evaporation process results in a loss in enthalpy in the dispersed phase. Fig. 2.2 displays a schematic of the constitutive quantities in both phases and generalized coupling effects in dispersed multi-phase flow. In the following sections, modeling of each phase and their implementation in the simulation platform used in this work will be detailed.

2.2. Gas phase governing equations and turbulence modeling

In principle, the following set of conservation equations for mass (Eq. (2.2)), species (Eq. (2.3)), momentum (Eq. (2.4)), and energy (Eq. (2.5)) fully describes a compressible, turbulent reacting gas flow involving N_s species in conservative form. Detailed derivations of the governing equations are given in the work of Versteeg [267] or Gerlinger [79]. Indices i,j indicate spatial coordinates whereas $\alpha = 1..(N_s - 1)$ is a counter for the number of species. ρ_g and h denote

the density and enthalpy of the gas, respectively. τ, $j_{\alpha i}$ and q_i are the stress tensor, diffusive mass flux and heat flux. Source terms on the right hand side comprise volume forces f_i and radiative sources S_r. In the presence of an evaporating or condensating spray, S^{Sp} denotes sources from the spray in the respective quantities.

$$\frac{\partial \rho_g}{\partial t} + \frac{\partial}{\partial x_i}\left(\rho_g u_i\right) = S_\rho^{Sp} \tag{2.2}$$

$$\frac{\partial}{\partial t}\left(\rho_g Y_\alpha\right) + \frac{\partial}{\partial x_i}\left(\rho_g u_i Y_\alpha\right) + \frac{\partial j_{\alpha i}}{\partial x_i} = S_\alpha + S_\alpha^{Sp} \tag{2.3}$$

$$\frac{\partial}{\partial t}\left(\rho_g u_i\right) + \frac{\partial}{\partial x_j}\left(\rho_g u_i u_j\right) - \frac{\partial \tau_{ij}}{\partial x_j} + \frac{\partial p}{\partial x_i} = \rho_g f_i + S_{\rho u}^{Sp} \tag{2.4}$$

$$\frac{\partial}{\partial t}\left(\rho_g h\right) + \frac{\partial}{\partial x_i}\left(\rho_g u_i h\right) - \frac{\mathrm{D}p}{\mathrm{D}t} - \tau_{ij}\frac{\partial u_i}{\partial x_j} + \frac{\partial q_i}{\partial x_i} = \rho_g u_i f_i + S_r + S_h^{Sp} \tag{2.5}$$

Note that the species conservation equation is given in terms of mass fractions

$$Y_\alpha = \frac{m_\alpha}{m_1 + m_2 + m_3 + ... + m_{N_s}} = \frac{m_\alpha}{m_{total}}. \tag{2.6}$$

For the calculation of the gas density an ideal gas is assumed. Therefore, the ideal gas law of a mixture is defined as

$$\rho_g = \frac{p_g}{\mathcal{R}T_g \sum_\alpha^{N_s}(Y_\alpha/M_\alpha)}, \tag{2.7}$$

with the specific gas constant $\mathcal{R}$ and the molar mass M.

2.2.1. Modeling of turbulent flows

For some simplified cases, analytical solutions of the system Eq. (2.2) - Eq. (2.5) are available [229]. However, in the vast majority of engineering problems, *turbulence* plays a significant role, leading to strong nonlinearities in the system of governing equations which prohibits the derivation of analytical solutions. These problems can only be tackled by means of further modeling and numerical, i.e. approximate, solution methods.

In general, turbulence is described as a chaotic and random state of motion in which velocity and pressure change continuously with time within substantial regions of a flow [192]. Three-dimensionality and rotational structures with a wide range of length and time scales further characterize turbulent flows. The onset of turbulence in a gas flow with *dynamic viscosity* μ_g, is found above a critical Reynolds number Re_{crit} where Re is defined as

$$\mathrm{Re} \equiv \frac{\rho_g u_g l}{\mu_g}. \tag{2.8}$$

In this definition, l is a certain characteristic length scale of the flow, for example the hydrodynamic diameter in the case of pipe flow or wingspan in case of airfoils. The Reynolds number equals the ratio of viscous to inertial forces of the fluid. Thus, above Re_{crit} viscous forces exceed the damping effects of the inertial forces causing turbulent motion.
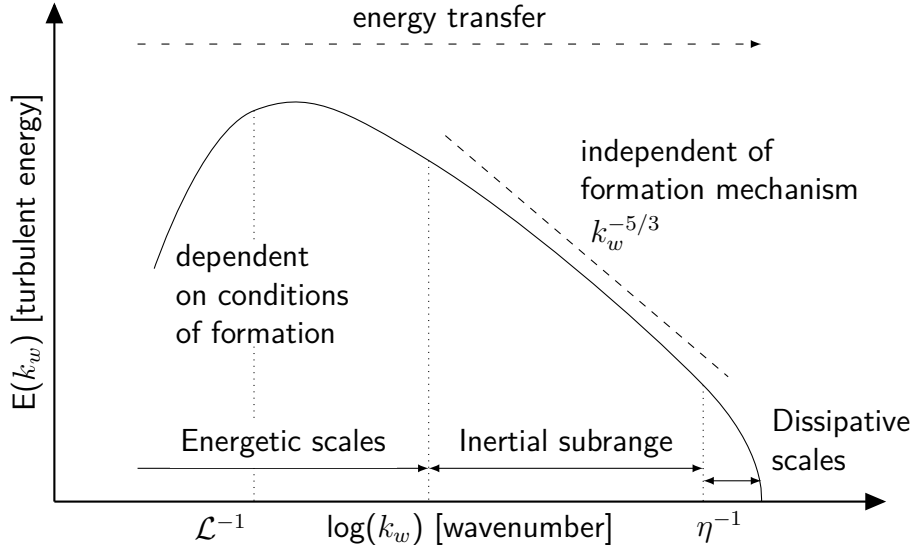
Figure 2.3.: Schematic turbulent kinetic energy spectrum according to Hinze [98].

Despite the irregular and statistical nature of turbulence, a certain spectral distribution of turbulent energy can be observed in turbulent flows. Fig. 2.3 displays an idealized turbulent flow spectrum, dividing the range of turbulent kinetic energy $E(k_w)$ into three distinct regions [98, 122]. In the integral scales $\mathcal{L}$ turbulent energy is extracted from the mean flow establishing the so called *large eddies* which are then transferred to higher wavenumbers and thus smaller scales in the inertial subrange. Finally, in the viscous range turbulent energy is dissipated into internal energy by molecular viscosity and thus vanished. This dissipation mechanism takes place at length scales below the characteristic length scale η of the dissipation range, which is proportional to the molecular viscosity of the gas.

Based on these findings, different modeling strategies for turbulent flows have been established. By resolving the entire spectrum of turbulent motion from Fig. 2.3, Direct Numerical Simulations (DNS) [162] provide the most detailed insight into the mechanism of turbulence. However, due to the very high computational cost of DNS this method is still limited to low Reynolds numbers and simple geometries. Applications to fundamental multi-phase combustion problems are found for example in the work of Borghesi et al. [19] or Domingo et al. [44].

By exploiting the assumption of scale separation, Large Eddy Simulation (LES) [185] aims at resolving the large, energy containing turbulent structures (see Fig. 2.4 (c)) which strongly depend on the problem and geometry under consideration. The dissipation in the fine scales is then provided by an appropriate dissipation model. As a well resolved LES should be able to resolve approximately 80% of the turbulent kinetic energy budget to meet up with the scale separation restrictions [192], computational expenses of such simulations are still high. Nevertheless, LES has emerged as an important research tool in combustion science with applications ranging from lab-scale [51, 62, 209] to realistic combustor geometries [60, 276].

In contrast, Reynolds Averaged Navier-Stokes Simulation (RANS) [186] solves only for the mean values of the fluctuating quantities and incorporates the influence of the turbulence on the mean values by means of a turbulence model (Fig. 2.4 (a)). Consequently, the
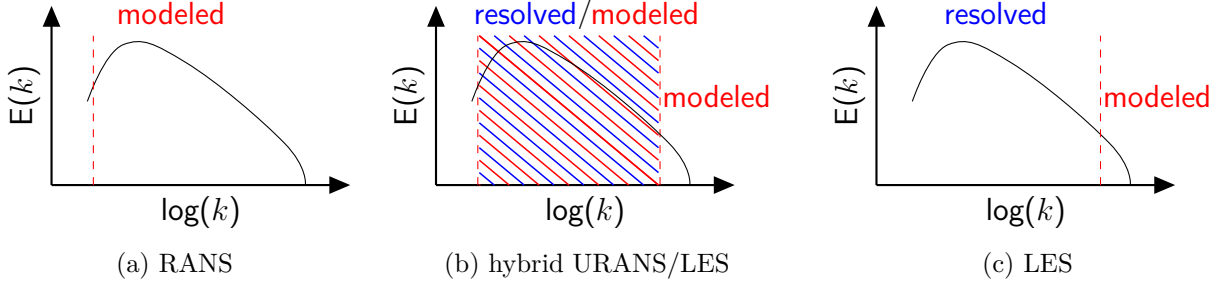
Figure 2.4.: Resolved and modeled part of the energy spectrum from different simulation approaches (adapted from [221]).

computational costs are drastically reduced compared to the aforementioned approaches allowing for short simulation turnaround times. Therefore, RANS has been established as the predominant simulation method in industrial applications [33]. However, since significant aspects of turbulent combustion such as local ignition and extinction, flame turbulence interaction and mixing are inherently unsteady phenomena and strongly coupled to local turbulence, the absence of resolved turbulent structures in RANS gives rise to extensive modeling demand and reduces the precision of such simulations [20].

In an effort to overcome these restrictions especially in industrial turbulence simulations, hybrid URANS/LES methods have been developed in the past decade [186]. In broad terms, hybrid methods set out to selectively use either URANS or LES simulation approaches in the flow domain based on certain criteria. This allows for a reduction in spatial resolution as turbulence is only resolved in regions where necessary, e.g. sheer layers, swirling flow or strongly detached flow (Fig. 2.4 (b)), whereas near wall or low turbulence regions are modeled using cost-effective URANS methods. The variety of available hybrid methods (e.g. DES[1] [246], VLES[2] [249], DDES[3] [247]) stems from the definition of the transition criterion between URANS and LES regions which can be based for example on wall distance, turbulent scales or grid spacing. In this thesis, the Scale Adaptive Simulation (SAS [156]) method is used, details are given in Sec. 2.2.4.

2.2.2. RANS modeling

Conservation equations for RANS simulations are obtained by averaging the instantaneous set of governing equations Eq. (2.2) - Eq. (2.5). This averaging is based on the *Reynolds decomposition* which is given for an arbitrary fluctuating quantity Q as

$$Q = \langle Q \rangle + Q' \text{ with } \langle Q' \rangle = 0, \tag{2.9}$$

where $\langle Q \rangle$ denotes the mean or mathematical expectation of Q and Q' its fluctuation. However, in the case of variable density flows as found in combustion problems, a density-weighted

---

[1]Detached Eddy Simulation
[2]Very Large Eddy Simulation
[3]Delayed Detached Eddy Simulation

formulation known as *Favre averaging* is preferred [186], defined as

$$Q = \widetilde{Q} + Q'' \quad \text{and} \quad \widetilde{Q} = \frac{\langle \rho \, Q \rangle}{\langle \rho \rangle}, \tag{2.10}$$

where $\widetilde{Q}$ is the Favre average of Q and Q'' the fluctuation with respect to the Favre average. Applying these definitions to Eq. (2.2) - Eq. (2.5) yields the system of unsteady Reynolds Averaged Navier Stokes equations for mass (Eq. (2.11)), species (Eq. (2.12)), momentum (Eq. (2.13)) and energy (Eq. (2.14)):

$$\frac{\partial \langle \rho_g \rangle}{\partial t} + \frac{\partial}{\partial x_i} \left(\langle \rho_g \rangle \, \widetilde{u}_i \right) = \\ \left\langle S_\rho^{Sp} \right\rangle \tag{2.11}$$

$$\frac{\partial}{\partial t} \left(\langle \rho_g \rangle \, \widetilde{Y}_\alpha \right) + \frac{\partial}{\partial x_i} \left(\langle \rho_g \rangle \, \widetilde{u}_i \widetilde{Y}_\alpha \right) - \frac{\partial}{\partial x_i} \left(D_\alpha \frac{\partial \widetilde{Y}_\alpha}{\partial x_i} + \langle \rho_g \rangle \, \widetilde{u_i'' Y_\alpha''} \right) = \\ \langle S_\alpha \rangle + \left\langle S_\alpha^{Sp} \right\rangle \tag{2.12}$$

$$\frac{\partial}{\partial t} \left(\langle \rho_g \rangle \, \widetilde{u}_i \right) + \frac{\partial}{\partial x_j} \left(\langle \rho_g \rangle \, \widetilde{u}_i \widetilde{u}_j \right) - \frac{\partial}{\partial x_j} \left(\langle \tau_{ij} \rangle - \langle \rho_g \rangle \, \widetilde{u_i'' u_j''} \right) + \frac{\partial \langle p \rangle}{\partial x_i} = \\ \langle \rho_g f_i \rangle + \left\langle S_{\rho u}^{Sp} \right\rangle \tag{2.13}$$

$$\frac{\partial}{\partial t} \left(\langle \rho_g \rangle \, \widetilde{h} \right) + \frac{\partial}{\partial x_i} \left(\langle \rho_g \rangle \, \widetilde{u}_i \widetilde{h} \right) - \left\langle \frac{\mathrm{D}p}{\mathrm{D}t} \right\rangle - \left\langle \tau_{ij} \frac{\partial u_i}{\partial x_j} \right\rangle - \frac{\partial}{\partial x_i} \left(\frac{\lambda}{c_p} \frac{\partial \widetilde{h}}{\partial x_i} + \langle \rho_g \rangle \, \widetilde{u_i'' h''} \right) = \\ \langle \rho_g \rangle \, \widetilde{u}_i f_i + \langle S_r \rangle + \left\langle S_h^{Sp} \right\rangle. \tag{2.14}$$

In steady state simulations, $\partial/\partial t = 0$. Note that due to the averaging, additional unclosed terms appear in the RANS system:

- Reynolds stresses $\langle \rho_g \rangle \, \widetilde{u_i'' u_j''}$

- Reynolds enthalpy and species fluxes $\widetilde{u_i'' h''}$ and $\widetilde{u_i'' Y_\alpha''}$

- Reynolds averaged species source term $\langle S_\alpha \rangle$

Unclosed enthalpy and species fluxes are treated by using a gradient diffusion model [79, 186]. For the Reynolds stresses and species source terms, a variety of turbulence [274] and combustion models [186] are found in the literature, respectively. RANS models used in this thesis are detailed in the following sections.

Boussinesq hypothesis and eddy viscosity concept

The assumption that the Reynolds stresses $\langle \rho_g \rangle \, \widetilde{u_i'' u_j''}$ are proportional to the mean strain rate tensor S_{ij} gives way for the most common RANS turbulence models [274]. According to the *Boussinesq hypothesis* [192], the proportionality between the two quantities is controlled by a

scalar factor μ_t, the so called *eddy viscosity*:

$$\langle \rho_g \rangle \widetilde{u_i'' u_j''} = -\mu_t \left(\frac{\partial \widetilde{u_i}}{\partial x_j} + \frac{\partial \widetilde{u_j}}{\partial x_i} - \frac{2}{3} \delta_{ij} \sum_{m=1}^{3} \frac{\partial \widetilde{u_m}}{\partial x_m} \right) + \frac{2}{3} \langle \rho_g \rangle k \delta_{ij} \tag{2.15}$$

In this equation, δ_{ij} is the Kronecker Delta and k the turbulent kinetic energy. Thus, the RANS turbulence modeling problem is reduced to appropriately choosing μ_t.

Two-equation turbulence models are utilized in this thesis. From dimensional analysis, they assume that μ_t can be expressed as a product of a turbulent velocity scale ϑ_t and a turbulent length scale $\mathcal{L}_t$ [274].

2.2.2.1. Standard $k - \varepsilon$ turbulence model

In the standard k-ε turbulence model [111], ϑ_t and $\mathcal{L}_t$ are expressed by the turbulent kinetic energy k and the turbulent energy dissipation ε:

$$\vartheta_t = k^{1/2}, \quad \mathcal{L}_t = \frac{k^{3/2}}{\varepsilon}. \tag{2.16}$$

Therefore, two equations must be solved in addition to the RANS set of equations. The transport equation for k can be directly derived from the Navier-Stokes equations and is given as

$$\frac{\partial \rho k}{\partial t} + u_i \frac{\partial \rho k}{\partial x_i} - \frac{\partial}{\partial x_i} \left[\left(\mu + \frac{\mu_t}{\sigma_k} \right) \frac{\partial k}{\partial x_i} \right] = G_k - \rho \epsilon. \tag{2.17}$$

Source terms on the right hand side represent the production (G_k) and dissipation ($\rho \epsilon$) of k. In contrast, the ε transport equation is empirical:

$$\frac{\partial \rho \varepsilon}{\partial t} + u_i \frac{\partial \rho \varepsilon}{\partial x_i} - \frac{\partial}{\partial x_i} \left[\left(\mu + \frac{\mu_t}{\sigma_\varepsilon} \right) \frac{\partial \varepsilon}{\partial x_i} \right] = C_{\varepsilon_1} \frac{\varepsilon}{k} G_k - C_{\varepsilon_2} \rho \frac{\varepsilon^2}{k}. \tag{2.18}$$

The definition of μ_t reads

$$\mu_t = C \rho_g \vartheta_t \mathcal{L}_t = C_\mu \rho_g \frac{k^2}{\varepsilon}. \tag{2.19}$$

Standard modeling constants for Eq. (2.17) - (2.19) are given by Launder and Sharma [125]:

$$C_{\varepsilon_1} = 1.44, \quad C_{\varepsilon_2} = 1.92, \quad C_\mu = 0.09, \quad \sigma_k = 1.0, \quad \sigma_\epsilon = 0.3. \tag{2.20}$$

2.2.3. LES modeling

As mentioned in Sec. 2.2.1, LES relies on the separation of resolved turbulent structures and unresolved sub-grid scales. This separation is formally realized by means of spatial filtering of the governing equations [132]. Thus, a turbulent quantity Q is separated into a filtered part

$\overline{Q}$ and a sub-grid contribution Q':

$$Q = \overline{Q} + Q'. \tag{2.21}$$

Considering only homogeneous spatial filtering the general filtering operation can be written as a convolution integral in the three-dimensional space $\mathbb{R}^3$

$$\overline{Q}(\vec{x}) = \int_{\mathbb{R}^3} G(\vec{x}, \vec{y}, \Delta(\vec{x}) Q(\vec{y})) d\vec{y}, \tag{2.22}$$

$\Delta(\vec{x})$ denoting the filter width and G being the filter kernel. Similar to Reynolds averaging, a density weighted formulation (Favre filtering $\widetilde{(..)}$) is used in varying density flows:

$$\widetilde{Q} = \frac{\overline{\rho_g Q}}{\overline{\rho_g}}. \tag{2.23}$$

Although a broad variety of explicit filter kernels is available in the literature [219, 220], most practical implementations use the grid itself as an implicit filter which resembles a top hat filter [41, 72]. This strategy is also adopted in the used simulation platform (see Sec. 2.6). According to Deardorff [40], the spatial varying filter width Δ then equates

$$\Delta = (\Delta_x \Delta_y \Delta_z)^{\frac{1}{3}}. \tag{2.24}$$

Applying the filtering operation of Eq. (2.22) to the system of equations (2.2) $-$ (2.5) gives the filtered conservation equations for mass (Eq. (2.25)), species (Eq. (2.26)), momentum (Eq. (2.27)) and energy (Eq. (2.28)) for the large structures:

$$\frac{\partial \overline{\rho_g}}{\partial t} + \frac{\partial}{\partial x_i}\left(\overline{\rho_g}\widetilde{u_i}\right) = \\ \overline{S}_\rho^{Sp} \tag{2.25}$$

$$\frac{\partial}{\partial t}\left(\overline{\rho_g}\widetilde{Y}_\alpha\right) + \frac{\partial}{\partial x_i}\left(\overline{\rho_g}\widetilde{u_i}\widetilde{Y}_\alpha\right) - \frac{\partial}{\partial x_i}\left(\overline{\rho_g}\overline{D}_\alpha\frac{\partial \widetilde{Y}_\alpha}{\partial x_i} + \overline{\rho_g}\left(\widetilde{u_i Y_\alpha} - \widetilde{u_i}\widetilde{Y}_\alpha\right)\right) = \\ \overline{S}_\alpha + \overline{S}_\alpha^{Sp} \tag{2.26}$$

$$\frac{\partial}{\partial t}\left(\overline{\rho_g}\widetilde{u_i}\right) + \frac{\partial}{\partial x_j}\left(\overline{\rho_g}\widetilde{u_i}\widetilde{u_j}\right) - \frac{\partial}{\partial x_j}\left(\overline{\tau}_{ij} - \overline{\rho_g}\left(\widetilde{u_i u_j} - \widetilde{u_i}\widetilde{u_j}\right)\right) + \frac{\partial \overline{p}}{\partial x_i} = \\ \overline{\rho_g}f_i + \overline{S}_{\rho u}^{Sp} \tag{2.27}$$

$$\frac{\partial}{\partial t}\left(\overline{\rho_g}\widetilde{h}\right) + \frac{\partial}{\partial x_i}\left(\overline{\rho_g}\widetilde{u_i}\widetilde{h}\right) - \frac{\mathrm{D}p}{\mathrm{D}t} - \overline{\tau}_{ij}\frac{\partial \widetilde{u_i}}{\partial x_j} + \frac{\partial}{\partial x_i}\left(\overline{q}_i - \overline{\rho_g}\left(\widetilde{u_i h} - \widetilde{u_i}\widetilde{h}\right)\right) = \\ \overline{\rho_g}\widetilde{u_i}f_i + \overline{S}_r + \overline{S}_h^{Sp} \tag{2.28}$$

The process of filtering introduces a closure problem for the unresolved Reynolds stresses $\overline{\rho_g}\left(\widetilde{u_i u_j} - \widetilde{u}_i \widetilde{u}_j\right)$ similar to the RANS method since the velocity components u_j are unknown and $\widetilde{u_i u_j} \neq \widetilde{u}_i \widetilde{u}_j$.

WALE sub-grid scale model

Unresolved sub-grid Reynolds stresses are computed by the zero equation WALE (Wall-Adapting Local Eddy-viscosity) model [173]. Similar to to the RANS approach discussed in Sec. 2.2.2 the eddy viscosity concept is adopted to relate the unresolved sub-grid Reynolds stresses to quantities of the resolved flow:

$$\overline{\rho_g}\left(\widetilde{u_i u_j} - \widetilde{u}_i \widetilde{u}_j\right) = -\mu_t \left(\frac{\partial \widetilde{u}_i}{\partial x_j} + \frac{\partial \widetilde{u}_j}{\partial x_i} - \frac{2}{3}\delta_{ij}\sum_{m=1}^{3}\frac{\partial \widetilde{u}_m}{\partial x_m}\right) + \frac{2}{3}\overline{\rho_g}k_{sgs}\delta_{ij}. \tag{2.29}$$

An algebraic relation for μ_t is given by

$$\mu_t = \rho_g \left(C_{\text{sgs}}\Delta\right)^2 \frac{\left(\mathcal{S}_{ij}^d \mathcal{S}_{ij}^d\right)^{\frac{3}{2}}}{\left(\overline{\widetilde{S}}_{ij}\widetilde{S}_{ij}\right)^{\frac{5}{2}} + \left(\mathcal{S}_{ij}^d \mathcal{S}_{ij}^d\right)^{\frac{5}{4}}}, \tag{2.30}$$

where $\mathcal{S}_{ij}^d$ denotes the traceless symmetric part of the square of the velocity gradient tensor. For the presented calculations, a modeling constant $C_{sgs} = 0.5$ is used [105, 173].

2.2.4. Hybrid URANS/LES model: Scale Adaptive Simulation

From the class of hybrid URANS/LES methods the Scale Adaptive Simulation (SAS) approach as introduced by Menter and Egorov [156, 158] is utilized for the thesis at hand. The general SAS concept relies on dynamic transitioning between URANS and LES based on the ratio of turbulent length scale $\mathcal{L}_t$ to the von Karman length scale $\mathcal{L}_{vK}$. The transition is achieved by introducing a source term to the transport equation of the dissipative turbulence scale. Thus, SAS can be applied to a variety of eddy viscosity turbulence models [157].

The SAS formulation in the used simulation platform relies on the k-ω-SST[4] turbulence model [154, 155] in which transport equations for the turbulent kinetic energy k (Eq. (2.31)) and the specific dissipation rate ω (Eq. (2.32)) are solved,

$$\frac{\partial \rho k}{\partial t} + \frac{\partial}{\partial x_i}\rho k u_i - \frac{\partial}{\partial x_i}\left[(\mu + C_{k_1}\mu_t)\frac{\partial k}{\partial x_i}\right] = G - C_{k_2}\rho k\omega, \tag{2.31}$$

$$\frac{\partial \rho \omega}{\partial t} + \frac{\partial}{\partial x_i}\rho\omega u_i - \frac{\partial}{\partial x_i}\left[(\mu + C_{\omega_1}\mu_t)\frac{\partial \omega}{\partial x_i}\right] = \frac{C_{\omega_3}}{\nu_t}G + C_{\omega_2}\rho\omega^2 + 2\rho(1-F_1)\frac{\partial k}{\partial x_i}\frac{\partial \omega}{\partial x_i}. \tag{2.32}$$

The set of equations (2.31) and (2.32) defines an equivalent set of equations for turbulence closure modeling as introduced in Sec. 2.2.2.1, but expressed in terms of turbulent kinetic

---

[4]Shear Stress Transport

energy k and turbulence frequency ω. The eddy viscosity μ_t is calculated by

$$\mu_t = \frac{C_\mu \rho k}{\max\left(C_\mu \omega, \sqrt{2 S_{ij} S_{ij}} F_2\right)}. \tag{2.33}$$

In these equations, G is a production source term, C_i are modeling constants and F_1, F_2 are blending functions to adjust ω depending on wall distance. For a thorough discussion of the k-ω-SST model and its modeling constants in the context of the used simulation platform, the reader is referred to the work of Ivanova [105].

Dynamic adjustment of the k-ω-SST model to an LES like formulation in high turbulence regions is realized by the introduction of an additional source term $F_{SST-SAS}$ to the ω transport equation (Eq. 2.32))

$$F_{SST-SAS} = \max\left[C_{F_1} k \boldsymbol{S}^2 \frac{\mathcal{L}_t}{\mathcal{L}_{vK}} - \frac{2}{C_{F_2}} k \max\left(\frac{1}{\omega^2}\frac{\partial \omega}{\partial x_j}\frac{\partial \omega}{\partial x_j}, \frac{1}{k^2}\frac{\partial k}{\partial x_j}\frac{\partial k}{\partial x_j}\right), 0\right]. \tag{2.34}$$

C_{Fi} are modeling constants, $\mathcal{L}_t = \sqrt{k}/\omega$ is the turbulent length scale, $\mathcal{L}_{vK}$ is the von Karman length scale and $\boldsymbol{S}$ denotes the norm of the strain tensor.

$$\mathcal{L}_{vK} = \max\left(\kappa \frac{\sqrt{2 S_{ij} S_{ij}}}{\sqrt{\frac{\partial^2 u_i}{\partial x_k^2}\frac{\partial^2 u_i}{\partial x_j^2}}}, C_s \sqrt{\frac{\kappa \hat{\zeta}}{\beta_{\omega_2/\beta_k} - \gamma_2}} \Delta\right). \tag{2.35}$$

This formulation allows for $\mathcal{L}_{vK}$ to adjust to the already resolved scales in a simulation and provides a length-scale, which is proportional to the size of the resolved eddies [156] with consideration of the local grid spacing. In unsteady flows, the source term $F_{SST-SAS}$ therefore increases and μ_t is damped by ω, as evident from Eq. (2.33). Ultimately, the dissipating effect of the turbulent viscosity on the resolved fluctuations is reduced.

Appropriate spatial resolution in high turbulence regions of the simulation domain is required to ensure the transition into the LES mode in Scale Adaptive Simulations. Different criteria have been proposed [38, 192] to verify suitable grid resolution. In this work, the ratio

$$\mu_r = \frac{\mu_t}{\mu} \tag{2.36}$$

defined by the turbulent viscosity μ_t and the molecular viscosity μ is considered. In the LES region of an SAS, μ_r should be in the order of $\mathcal{O}(10^1)$ [105].

2.3. Lagrangian modeling of dispersed sprays

Transport and vaporization of liquid droplets in the Lagrangian reference frame are computed by solving ordinary differential equations (ODEs) for the location, velocity, diameter and temperature along the droplets' trajectory. Detailed derivations of the ODEs are given for example in the textbook of Schwarzkopf et al. [233] or Clift et al. [31].

2.3.1. Governing ODEs of a particle

Particle motion   According to Newton's second law, the rate of change in particle velocity $\vec{u}_p$ is equivalent to the sum of accelerations $\vec{a}_p$ acting on the particle:

$$\frac{\mathrm{d}\vec{u}_p}{\mathrm{d}t} = \vec{a}_p = \underbrace{\frac{3}{4}\frac{c_d}{d_p}\frac{\rho_g}{\rho_l}|\vec{u}_g - \vec{u}_p| \cdot \overbrace{(\vec{u}_g - \vec{u}_p)}^{\vec{u}_{rel}}}_{\vec{a}_d} + \left(1 - \frac{\rho_g}{\rho_l}\right)\vec{g}. \tag{2.37}$$

In this equation, drag force $\vec{a}_d$ due to the relative velocity $\vec{u}_{rel}$ between particle and gas flow as well as gravitational force $\vec{g}$ are considered. A spherical drag law based on the drag coefficient c_d of the particle is assumed. The particle position $\vec{x}_p$ is then directly related to the particle velocity

$$\frac{\mathrm{d}\vec{x}_p}{\mathrm{d}t} = \vec{u}_p. \tag{2.38}$$

Particle diameter and temperature   Mass conservation for the particle taking into account changes in liquid density $\mathrm{d}\rho_l/\mathrm{d}t$ and mass flow $\dot{m}_{vap}$ leaving the particle due to vaporization gives the ODE for the rate of change in particle diameter d_p:

$$\frac{\mathrm{d}(d_p)}{\mathrm{d}t} = -\frac{d_p}{3\rho_l}\frac{d\rho_l}{dt} - \frac{2}{\rho_l}\frac{\dot{m}_{vap}}{\pi d_p^2}. \tag{2.39}$$

Similarly, an ODE for the rate of change in particle temperature T_p can be obtained from an energy balance including surface heat flux $\dot{q} = \dot{Q}/A$ and vaporization heat flux $\dot{q}_{vap}$.

$$\frac{\mathrm{d}T_p}{\mathrm{d}t} = -\frac{6}{d_p^3}\frac{\overbrace{j_{m,vap}\Delta h_{vap}}^{\dot{q}_{vap}} + \dot{q}}{\rho_l c_{p,l}} \tag{2.40}$$

The vaporization heat flux is calculated from the massflux $j_{m,vap} = \dot{m}_{vap}/A$ and the specific enthalpy of vaporization Δh_{vap}, where A denotes the particles' surface.

In case of a multi-component liquid (e.g. kerosene), the rate of change in particle composition $Y_{\alpha,l}$ must be considered by applying a relation for the species balance:

$$\frac{\mathrm{d}Y_{\alpha,l}}{\mathrm{d}t} = \frac{6}{\rho_l \pi d_p^3}\dot{m}_{vap}\left(Y_{\alpha,l} - \zeta_\alpha\right). \tag{2.41}$$

In this equation, $\zeta_\alpha = \dot{m}_{\alpha,vap}/\dot{m}_{vap}$ describes the ratio between the species and total vapor mass flux.

2.3.2. Vaporization models

Various vaporization models of different fidelity were proposed in the literature [28, 161, 228], providing analytical expressions for the vapor mass flow $\dot{m}_{vap}$ and heat flux $\dot{q}$ in Eqs. (2.39)-
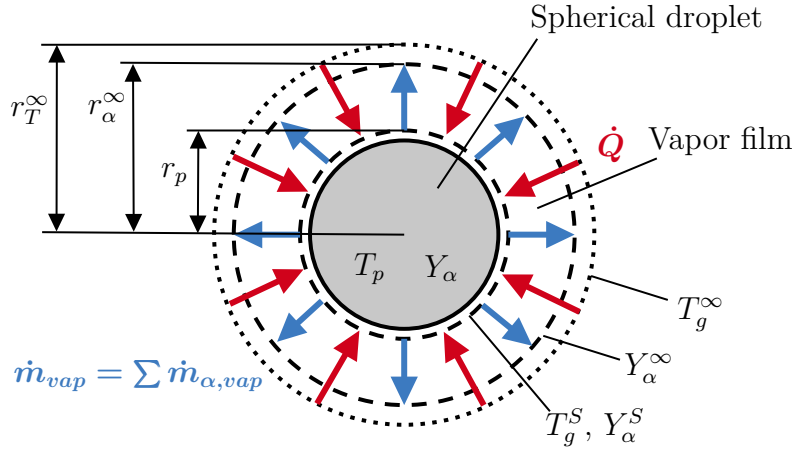
Figure 2.5.: Spherical symmetric solution of evaporation in quiescent ambience (adapted from Eckel [50]).

(2.41). As the main purpose of the used simulation platform is the analysis of technical combustors burning complex aviation fuels, computational efficiency and the ability to account for a multitude of components in the liquid fuel are the main requirements in the selection of suitable vaporization models [50, 202]. Two modeling strategies for vaporization are used in the present study: A discrete component model, in which each component in the liquid is treated individually and mapped to a corresponding species in the gas phase; and the continuous thermodynamics model (CTM) which approximates properties of similar classes of components by probability density functions.

Both models are based on the *film theory* suggested by Abramzon and Sirignano [2, 239]. In this concept, isolated spherical droplets in quiescent ambience are considered. As shown in Fig. 2.5, it is assumed that each droplet with radius r_p is surrounded by a quasi steady-state air-vapor film with radius r^∞. Through this film, heat and mass transfer takes place by heat conduction and molecular diffusion of the fuel vapor. For computational efficiency, a time dependent but spatially uniform temperature of the droplets' interior is presumed (*rapid mixing model*). Therefore, the derivation of governing equations for droplet evaporation reduces to the analysis of heat and mass transfer in the air-vapor film and the solution becomes spherical symmetric over the droplet [2]. Effects of convection from relative velocity between droplet and gas are taken into account by correlations [31] for the enhanced heat and mass transfer.

A comprehensive derivation, discussion and analysis of the two vaporization models is given in the work of Rauch [202]. In the following, essential equations for the calculation of $\dot{Q}$ and $\dot{m}_{vap}$ are outlined.

Discrete component vaporization

Under the aforementioned assumptions, the conservation equations for mass, species mass, and heat flow in the film described in radial coordinates ($f = f(r)$) can be simplified to:

$$\frac{1}{r^2}\frac{\partial}{\partial r}(\rho u_r r^2) = 0 \tag{2.42}$$

$$\frac{1}{r^2}\frac{\partial}{\partial r}(\rho u_r Y_\alpha r^2 + j_{\alpha r}r^2) = 0 \tag{2.43}$$

$$\frac{1}{r^2}\frac{\partial}{\partial r}(\rho u_r h r^2 + q_r r^2) = 0 \tag{2.44}$$

In the following, superscripts $(..)^S$ and $(..)^\infty$ denote quantities at the droplet surface and ambient, respectively (see Fig. 2.5). By integrating Eqs. (2.42) and (2.43) over the film thickness and introducing a modified Sherwood number Sh_α [2, 239] for the non-dimensional species mass transfer rate, the equation for the vapor mass flow rate can be deduced:

$$\dot{m}_{vap} = 2\pi r_p \text{Sh}_\alpha \rho_g D_\alpha \ln(1 + B_M). \tag{2.45}$$

D_α is the diffusion coefficient of species α and B_M the Spalding mass transfer number defined by

$$B_M = \frac{Y_\alpha^S - Y_\alpha^\infty}{\zeta_\alpha - Y_\alpha^S}, \tag{2.46}$$

with the ratio ζ_α between the species and total vapor mass flux. Likewise, the heat flow $\dot{Q}$ results from integrating the conservation equation (2.44) and defining a Spalding heat transfer number B_T:

$$\dot{Q} = \dot{m}_{vap}\frac{\sum \zeta_\alpha c_{p,\alpha}(T_g^\infty - T_g^S)}{B_T}. \tag{2.47}$$

Rearranging this equation and equating with Eq. (2.45) provides a relation between B_T and B_M involving the Nusselt number Nu for the non-dimensional heat transfer rate:

$$B_T = (1 + B_M)^\phi - 1 \quad \text{with} \quad \phi = \frac{\text{Sh}_\alpha}{\text{Nu}}\frac{\rho_g D_\alpha}{\lambda_g}\sum \zeta_\alpha c_{p,\alpha}. \tag{2.48}$$

For the calculation of physical properties of the gas film (e.g. $c_{p,\alpha} = c_{p,\alpha}(T,Y_\alpha)$), reference conditions following the *1/3 rule* [102, 282] are considered to account for varying temperature and mass fraction over the gas film. Therefore, reference conditions are defined as

$$T_{ref} = T_g^S + \frac{1}{3}(T_g^\infty - T_g^S), \tag{2.49}$$

$$Y_{\alpha,ref} = Y_\alpha^S + \frac{1}{3}(Y_\alpha^\infty - Y_\alpha^S). \tag{2.50}$$

The discrete component vaporization model is especially suitable for binary liquids (e.g. ethanol) or mixtures with a moderate number of components since detailed physical properties
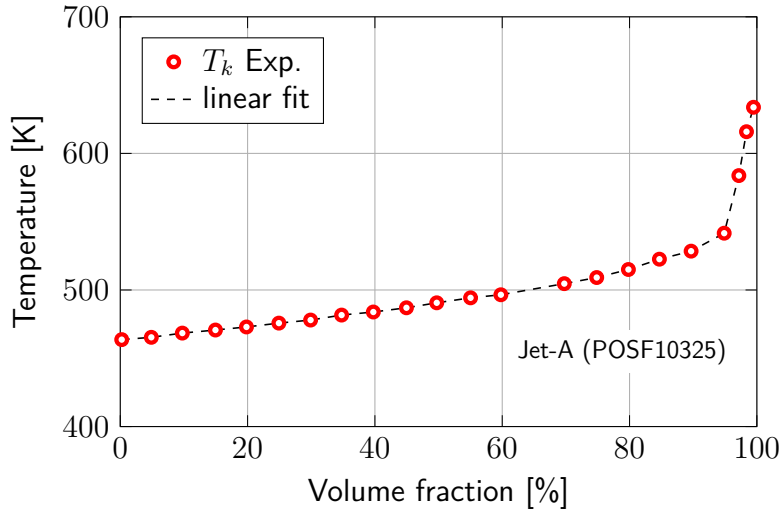
Figure 2.6.: Measured distillation curve for Jet-A (POSF10325). Data extracted from Saggese et al. [222].

of each component within the mixture must be specified and the computational burden increases with each component. However, the determination of all components and their respective properties in a complex technical fuel (e.g. jet fuels, Diesel) might be unfeasible due to the vast number of components and the varying composition within the specification range [202]. A strategy to overcome this limitation is the definition of a single component surrogate, expressing mean properties of the multi-component mixture as succesfully demonstrated for Jet A-1 by Rachner et al. [196]. The major drawback of this method is the inability of a single component surrogate to represent the temperature dependent distillation curve as shown in Fig. 2.6 for Jet A-1. Through this mechanism, components of different volatility evaporate at different temperatures which massively influences subordinated physical and chemical processes, e.g. sooting propensity, as discussed by Saggese et al. [222].

Continuous thermodynamics model

Especially in the case of complex fuels with a large number of mixture components, an alternative modeling strategy is achieved by transforming the discussed discrete description of the fuel composition into a continuous formulation through the Continuous Thermodynamics Model [94, 256]. In the CTM framework, mixture components with similar chemical structure (e.g. n-alkanes, aromatics) are grouped into *fuel families*[5] and family properties are described by a probability density function over a characteristic distribution parameter I. Depending on the availability and quality of experimental data, molar mass, normal boiling point or carbon atom number are possible distribution parameters [202]. With this approach, spectral properties of a multi-components mixture (e.g. latent heat of vaporization, vapor pressure, density) are reflected in the vaporization model. For all physical properties of the liquid, a continuous formulation is required in the CTM model. In addition to the governing equations of a particle as introduced in Sec. 2.3.1, only two additional ODEs for the distributions'

---

[5]In the following, fuel families are given the subscript $(..)_{ff}$
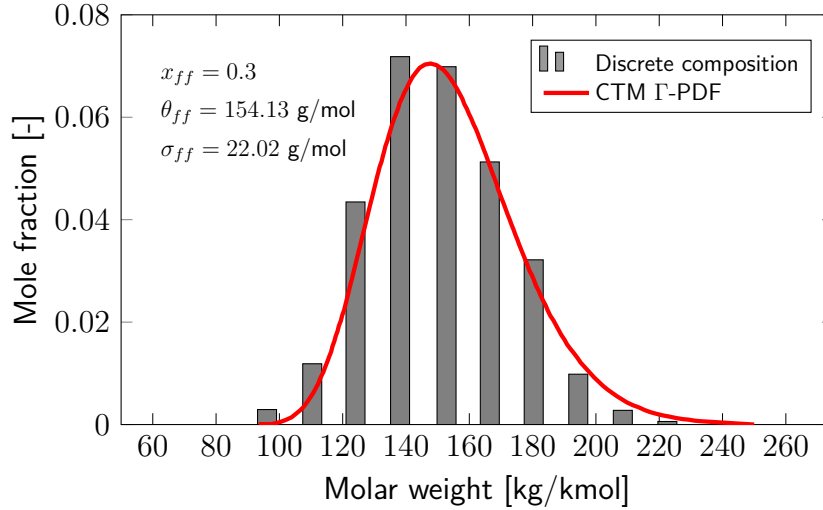
Figure 2.7.: CTM description of the discrete n-alkane fuel family by a Γ-PDF (adapted from Rauch [202]).

parameters θ_{ff} and ψ_{ff} (see following) must be solved. This reduces the computational burden drastically in comparison to the discrete component model, in which each additional component requires additional ODEs. Coupling of the CTM vaporization model to the gas field species is realized by assigning one equivalent gaseous species for each fuel family.

Following the findings of Whitson et al. [272] and Cotterman et al. [35], distribution functions $f_{ff}(I)$ based on the Gamma function Γ are used in the implementation of the CTM model at hand [45]:

$$f_{ff}(I) = \frac{(I - \gamma_{ff})^{\alpha_{ff}-1}}{\beta_{ff}^{\alpha_{ff}}\Gamma(\alpha_{ff})} e^{\frac{I-\gamma_{ff}}{\beta_{ff}}}. \tag{2.51}$$

The Gamma function $\Gamma(\alpha_j)$ is defined as:

$$\Gamma(\alpha_j) = \int_0^\infty t^{\alpha_{ff}-1} e^{-t} \mathrm{d}t. \tag{2.52}$$

From the normalization condition over f_{ff} relations between θ_{ff}, σ_{ff} and ψ_{ff} of a family and the distributions' parameters α_{ff}, β_{ff} and γ_{ff} are obtained, where θ_{ff}, σ_{ff}, ψ_{ff} denote first moment, second moment and variance, respectively.

$$\begin{aligned} \theta_{ff} &= \alpha_{ff}\beta_{ff} + \gamma_{ff} \\ \sigma_{ff}^2 &= \alpha_{ff}\beta_{ff}^2 \\ \psi_{ff} &= \theta_{ff}^2 + \sigma_{ff}^2 \end{aligned} \tag{2.53}$$

Consequently, the distributions' parameters θ_{ff}, σ_{ff} and ψ_{ff} of each family must be fitted against experimental data. An example for the n-alkane fuel family in a jet fuel is shown in Fig. 2.7. The molar weight is chosen as the distribution parameter I in Eq. (2.51).

The vaporization equations in the CTM model resemble the discrete component model with fuel families replacing the discrete species in Eqs. (2.45) − (2.48). Details and full derivations of the CTM equations are given in Rachner et al. [199].

2.4. Specification of boundary conditions for the dispersed Phase

For practical spray combustion simulations, the particle ODEs from Eqs. (2.37) - (2.41) require initial and boundary conditions for the particles diameter, velocity and position. These boundary conditions describe the state of the dispersed phase after primary atomization of the liquid fuel. Three methodologies to infer this data can be differentiated, namely direct simulation of the primary atomization process, phenomenological modeling of the primary atomization or reconstruction from experimental data. For the work at hand, spray boundary conditions from experimental data as well as a phenomenological breakup model are considered. Both approaches are detailed in the following, including a brief overview on primary atomization and the characterization of dispersed sprays.

2.4.1. Remarks on liquid atomization and disperse sprays

The process of a liquid continuum disintegrating into small droplets is commonly referred to as *atomization* [129]. After atomization, the collection of fine droplets forms a dispersed *spray*. Although there are a multitude of mechanisms involved into the atomization process, the classic atomization theory subdivides them into sheet or jet instabilities, ligament formation and droplet formation [31].

An example involving these three categories is depicted in Fig. 2.8 for the case of spray formation from a pressure-swirl atomizer. In this type of atomizer, internal swirl vanes (not shown) produce rotational motion of the liquid inside the atomizer. This causes the
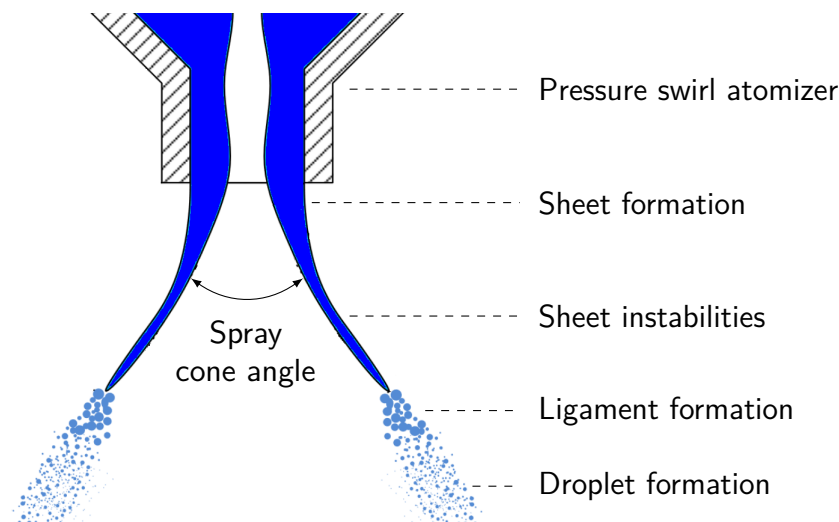
Figure 2.8.: Schematic of the atomization process (adapted from Kang et al. [113]).

formation of a liquid film along the inside walls of the injector as the liquid is forced against the walls. After ejection from the atomizer orifice, rotational forces transform the film into a conical sheet which decreases in thickness due to mass conservation as it progresses from the atomizer. Then, the relative velocity between liquid sheet and surrounding gas enhances aerodynamic instabilities such as Kelvin-Helmholtz waves on the sheet and eventually breaks the liquid into ligaments [231]. Finally, ligaments shatter into droplets according to the Rayleigh mechanism [129]. Once the liquid forms droplets, the spray behavior is mainly determined by drag, collision, coalescence and secondary breakup [231]. This is in accordance with the assumptions for Lagrangian modeling of droplets (see Sec. 2.3) and determines the location at which spray boundary conditions for the dispersed phase should be placed.

Due to the heterogeneous nature of the atomization process, the ligaments formed by the various mechanisms of sheet disintegration vary widely in diameter and length [129]. Consequently, the final droplets after atomization also vary in size and the resulting spray must be seen as a *polydisperse* collection of droplets with a characteristic size distribution about some arbitrarily defined mean value. For combustion and heat transfer problems, a common mean diameter is given by the *Sauter Mean Diameter* (SMD) which relates the total volume of all droplets D_i in the spray to the respective total surface of all droplets:

$$\text{SMD} = D_{32} = \frac{\sum_i N_i D_i^3}{\sum_i N_i D_i^2}. \tag{2.54}$$

A number of size distributions for the description of sprays have been proposed in the literature [129], mostly based on empirical considerations and fitting with experimental data. Since no single distribution can represent all drop size data, it is usually necessary to test several functions to achieve an optimal fit. As an example, the most popular distribution function for technical sprays is the *Rosin-Rammler* function [215] for which the volume PDF is defined as

$$f_{3,RR}(D) = C_{RR} D^{q-1} \exp\left[-\left(\frac{D}{m}\right)^q\right]. \tag{2.55}$$

In this equation, m is the mean value of the distribution and q characterizes its spread, while C_{RR} is a normalizing constant to ensure $\int_0^\infty f_3(D)\, \mathrm{d}D = 1$. Commonly, Rosin-Rammler distributions are expressed through the volume CDF

$$F_{3,RR}(D) = 1 - \exp\left[-\left(\frac{D}{m}\right)^q\right], \tag{2.56}$$

where $F_{3,RR}$ denotes the fraction of total volume contained in droplets of diameter less than D. The influence of q and m on the Rosin-Rammler PDF and CDF is shown in Fig. 2.9 (a) and (b), respectively.

In addition to the polydisperse nature of droplet size, the atomization process also induces a velocity distribution on the droplets. For example, in sprays from pressure-swirl atomizers (see Fig. 2.8) it is observed [56, 245] that large droplets maintain the high velocity of the

(a) Volume PDF f_3

(b) Volume CDF F_3
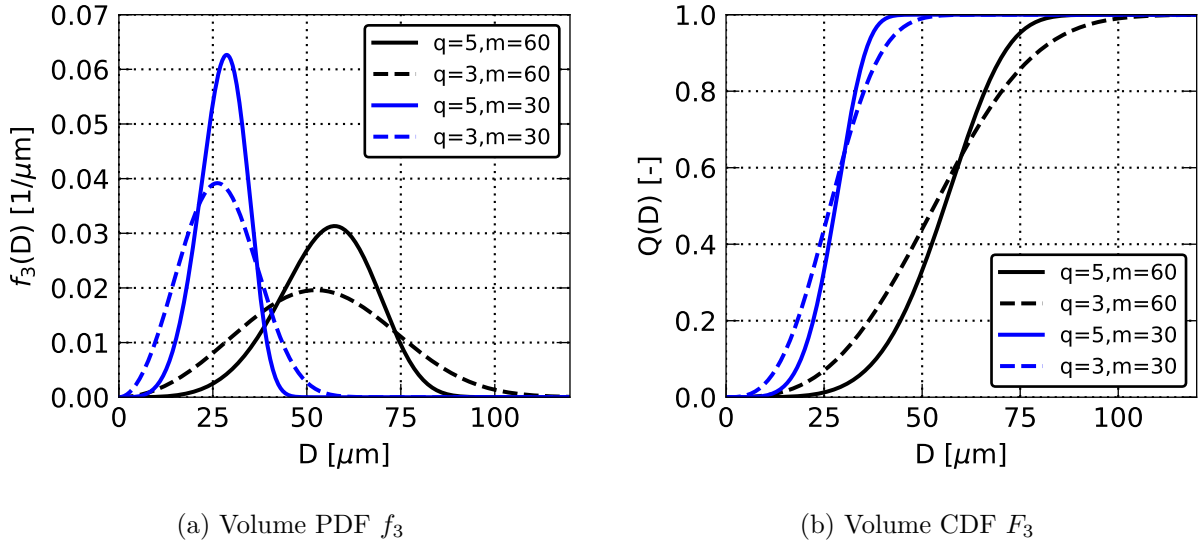
Figure 2.9.: Rosin-Rammler droplet distribution functions for different q and m parameters.

liquid sheet after atomization while small droplets tend to couple to the slower local induced airflow as a result of their lower Stokes number.

2.4.2. Reconstruction from experimental data

Figure 2.10 illustrates the general methodology for the reconstruction of a spray boundary condition from experimental data. While this experimental data is available at an axial distance X_{PDA} from the atomizer, the boundary condition should be placed at a further upstream location X_{BC}. As mentioned before, it is assumed that the disintegration and breakup of the liquid sheet issuing from the atomizer is completed at X_{BC}. Especially in the case of pressure-swirl atomizer, the spray cone can be expected to be axially symmetric [56]. Therefore, the boundary condition is prescribed as a radial profile which is rotated around the symmetry axis to form a starting plane.

Typically, experimental data from Phase Doppler Anemometry (PDA) is given in terms of radial measurement positions at which droplet distribution Q_{PDA} and velocity U_{PDA} is characterized, respectively. In the boundary condition plane, particles start from radial
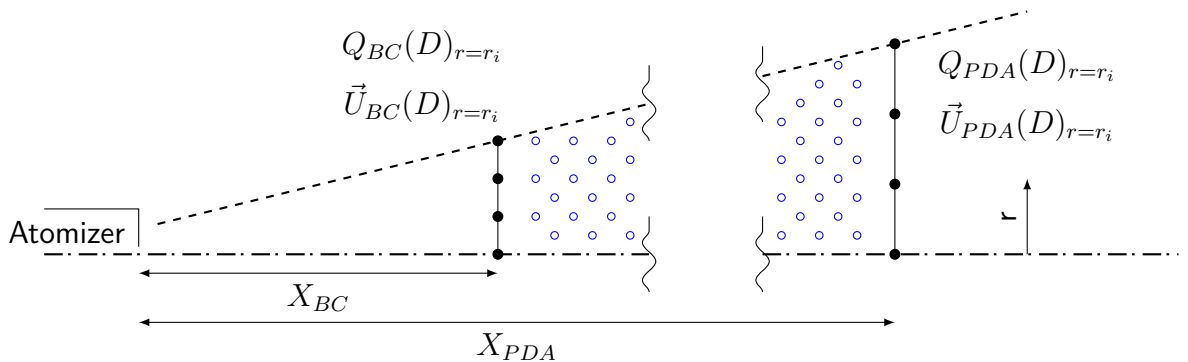
Figure 2.10.: Schematic of the methodology for the reconstruction of a spray boundary condition from experimental data. Blue dots depict droplets.

(a) Prefilming airblast atomizer   (b) Detail at the atomizing edge
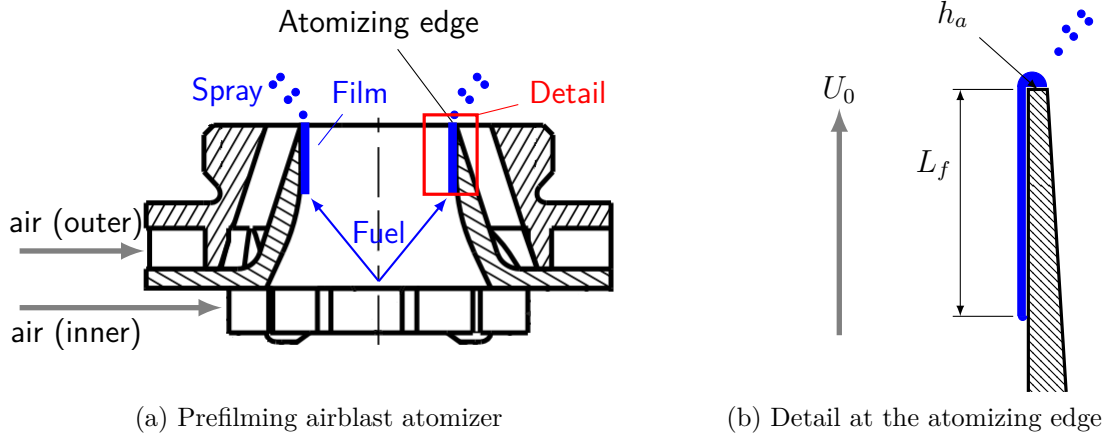
Figure 2.11.: Typical airblast atomizer as considered in the PAMELA model.

starting locations which are projections of the PDA measurement locations according to the intercept theorem. For each starting location, the drop size distribution must be specified as an optimal fit for the experimental data. In order to compensate the deceleration of droplets in the gas field after injection, a weighting factor k_U is introduced as

$$U_{\mathrm{BC}} = k_U U_{\mathrm{PDA}}. \tag{2.57}$$

In addition, radial shifting of the droplet size distribution due to dispersion and partial evaporation between X_{PDA} and X_{BC} is accounted for by a weighting factor k_{SMD} for the droplet distribution function:

$$Q_{\mathrm{BC}} = k_{\mathrm{SMD}} Q_{\mathrm{PDA}}. \tag{2.58}$$

Both k_U and k_{SMD} need to be calibrated against the experimental data.

2.4.3. Prefilming airblast atomization: The PAMELA model

In state of the art aeroengine combustors, liquid fuel is mainly fed and atomized by means of pre-filming airblast atomizers [131] due to their ability to ensure a fine spray of droplets over a wide operating range and hence stable performance of the combustor [130]. A sketch of a pre-filming airblast atomizer and the associated atomization concept is shown in Fig. 2.11 (a). The liquid fuel is spread out as a thin concentric film along the atomizer wall (the *pre-filmer*). Here, the film is sheared by a high-speed airflow which is introduced through an inner swirler system. Finally, the film disintegrates into droplets at the tip of pre-filmer, which is referred to as the *atomizing edge*.

The PAMELA (Primary Atomization Model for prEfilming airbLAst injector) model [26, 27] provides a droplet size distribution characteristic for the spray from such atomizers. In this phenomenological model, the distribution is calculated from a few parameters of the atomizer, namely the thickness h_a of the atomizing edge, the film length L_f and the mean air velocity U_G alongside the film. Fig. 2.11 (b) illustrates these parameters as a detail of the

pre-filming airblast atomizer. For the work at hand, the *global* formulation of the PAMELA model is utilized, i.e. calculations based on steady-state mean values.

Constitutive equations for the PAMELA model were derived from the analysis of an academic experiment of liquid film breakup at an atomizing edge [77, 170] consisting of a planar wing-shaped pre-filmer over which a liquid film was atomized. Simultaneous measurements of the film length, air velocity and resulting spray established a database for a wide range of operating conditions and two different fuels.

In this database, a strong linear correlation between D_{32}/h_a and We_{h_a} is observed:

$$\frac{D_{32}}{h_a} = \frac{C_1}{\sqrt{\mathrm{We}_{h_a}}}. \tag{2.59}$$

We_{h_a} denotes the Weber number with respect to the atomizing edge h_a

$$\mathrm{We}_{h_a} = \frac{\rho_g h_a (r_\rho U_G)^2}{\sigma} \tag{2.60}$$

and r_ρ is the ratio of liquid and gas densities:

$$r_\rho = \frac{\sqrt{\rho_l}}{\sqrt{\rho_l} + \sqrt{\rho_g}}. \tag{2.61}$$

It is assumed that the spray after the atomizing edge follows a Rosin-Rammler distribution with parameters q_{PAM} and m_{PAM}. In this case, a relation between D_{32} and the distribution parameters is given by

$$D_{32}^{RR} = m \frac{\Gamma(3/q + 1)}{\Gamma(2/q + 1)} \tag{2.62}$$

(see Lefebvre [131]). Combining Eqs. (2.62) and (2.59) yields:

$$m_{\mathrm{PAM}} = C_1 \frac{h_a}{\sqrt{\mathrm{We}_{h_a}}} \frac{\Gamma(2/q + 1)}{\Gamma(3/q + 1)} \tag{2.63}$$

in which C_1 is a calibration constant. As mentioned before, q describes the dispersion of the drop size in the spray. Therefore, this parameter cannot be formally linked to a single measurement value [27]. A correlation function for q is obtained from fitting of the Rosin-Rammler distribution to the sprays from the database and comparison with the aerodynamic Weber number We_δ based on the boundary layer thickness δ at the atomizing edge:

$$\mathrm{We}_\delta = \frac{\rho_g \delta U_G^2}{\sigma} \tag{2.64}$$

The thickness δ is defined according to the work of Gepperth et al. [77] as

$$\delta = 0.16 \frac{L_f}{\mathrm{Re}_{L_f}^{\frac{1}{7}}} \quad \text{with} \quad \mathrm{Re}_{L_f} = \frac{U_G L_f}{\nu_g}. \tag{2.65}$$

Table 2.1.: Fitting constants in the PAMELA model.

C_1 [-]	C_2 [-]	C_3 [mm]	C_4 [-]
2.01	9.74	5.99	$1.77 \cdot 10^{-2}$

The correlation for q_{PAM} finally reads

$$q_{\mathrm{PAM}} = \frac{C_2}{\sqrt{\mathrm{We}_\delta}} + \left(\frac{h_a}{C_3} \right)^2 + C_4. \tag{2.66}$$

Again, C_2,C_3,C_4 are calibration constants. Constants for the PAMELA model from fitting against the experimental database are summarized in Tab. 2.1.

2.5. Combustion modeling

Turbulent combustion as found in most technical systems [183] is an intrinsically complex process involving a large range of chemical time and length scales [186]. The specification of the source term $S_\alpha \neq 0$ in the species transport equation (2.3) is therefore only attainable through additional modeling effort. This is further amplified by the assumptions made for the derivation of averaged or filtered governing equations in the (U)RANS and LES context, respectively.

From a chemical perspective, a combustion process can be described by a *reaction mechanism* consisting of a finite set of kinetic forward an backward reactions

$$\sum_\alpha^{N_{sp}} \nu'_{\alpha,r} C_\alpha \overset{k_b}{\underset{k_f}{\rightleftharpoons}} \sum_\alpha^{N_{sp}} \nu''_{\alpha,r} C_\alpha \tag{2.67}$$

for N_{sp} species C_α, with $\nu'_{\alpha,r}, \nu''_{\alpha,r}$ denoting the stochiometric coefficient of the reactant and product in reaction r, respectively. k_f and k_b are the forward and backward rate coefficients. However, this might incorporate thousands of reactions and species [269], especially in case of complex hydrocarbon fuels [37]. Since the computing time increases significantly with each additional species and reaction [78], *reduced* or *skeletal mechanisms* incorporating only the most important reactions and species for the use case under consideration are mostly utilized in 3D combustion simulations [186]. The reduction comes at the cost of a loss in generality or even failure to accurately predict specific phenomena, e.g. ignition [37] which is strongly driven by the formation of chemical radicals [266]. Therefore, reduced mechanisms have to be selected with respect to the conditions (e.g. stochiometric range, temperature, pressure) of the reacting system. In the simplest case of a *global reaction mechanism* only the net reaction of the fuel and oxidizer to stable products[6] is considered [10, 271].

Within this thesis, two combustion models are used: The Eddy Dissipation Model [143], which is based on global chemistry for reduced simulation complexity, and the Finite rate

---

[6]e.g. CO_2 and H_2O in case of hydrocarbons

chemistry model [79] for non-equilibrium effects and detailed chemistry. Both models are discussed in the RANS context, remarks on LES are made at the end of this section.

2.5.1. Global chemistry: Eddy dissipation model

On the basis of the Eddy breakup model first proposed by Spalding [248], the Eddy Dissipation Model (EDM) assumes that in most technical applications, the chemical reaction rates are fast compared to the mixing [123]. Hence, the reaction rate is controlled by the rate of intermixing of fuel- and oxygen containing eddies and the reaction zone is seen as a collection of fresh and burnt gaseous pockets transported by turbulent eddies. With this assumption, chemical equilibrium prevails. The reaction rate - and therefore the chemical source term - is assumed to be inversely proportional to the turbulent time scale τ_t [143]:

$$\langle S_\alpha \rangle \propto \frac{1}{\langle \tau_t \rangle}. \tag{2.68}$$

Incorporating an ω based RANS turbulence model[7] for the calculation of τ_t, the averaged EDM source term reads

$$\langle S_\alpha \rangle^{\text{EDM}} = M_\alpha \sum_{r}^{N_r} \left(\nu''_{\alpha,r} - \nu'_{\alpha,r} \right) \langle \rho \rangle C_1 \underbrace{\frac{1}{\beta_k \widetilde{\omega}}}_{\langle \tau_t \rangle} \min \left(\frac{\widetilde{Y}_E}{\nu'_{E,r} M_E}, C_2 \frac{\sum \widetilde{Y}_P}{\sum \nu''_{P,r} M_P} \right). \tag{2.69}$$

$C_1 = 4$ and $C_2 = 0.5$ are modeling constants and Y_E and Y_P denote mass fractions of educts and products. To account for increased $\widetilde{\omega}$ values close to walls leading to unphysical behavior, $1/\langle \tau_t \rangle$ is limited to $1/2500$ s in the used implementation of the EDM [207].

Important limitations of the EDM are the restriction to a few global and irreversible reactions of the fuel, and the inability to account for non-equilibrium effects. The latter may produce erroneous results in case chemical kinetics limit the reaction rate [207].

2.5.2. Finite rate chemistry

In contrast to the EDM, the Finite Rate Chemistry (FRC) modeling approach is based on the key idea that mixing processes of gas mixtures are much faster than kinetically controlled mechanisms [112]. Therefore, fuel and oxizider can exist together in the reaction zone [186] and the model is able to account for non-equilibrium effects and detailed chemistry. This addresses the shortcomings of the previously introduced EDM. However, the FRC model requires the computational expensive evaluation of kinetic reaction rates k_r and the solution of $N_{sp} - 1$ additional transport equations for each species C_β but the last one, which is calculated from the sum of species.

---

[7]See Eqs. (2.31) − (2.33) in Sec. 2.2.4.

The FRC model computes the averaged source term $\langle S_\alpha \rangle^{\text{FRC}}$ by summing over all forward and backward reactions of the considered reactions mechanism (see Eq. (2.67)):

$$\langle S_\alpha \rangle^{\text{FRC}} = M_\alpha \sum_{r=1}^{N_r} \left(\nu''_{\alpha,r} - \nu'_{\alpha,r} \right) \left[\langle k_{f,r} \rangle \prod_{\beta=1}^{N_{sp}} [C_\beta]^{\nu'_{\beta,r}} - \langle k_{b,r} \rangle \prod_{\beta=1}^{N_{sp}} [C_\beta]^{\nu''_{\beta,r}} \right]. \tag{2.70}$$

The concentration $[C_\beta]$ of the species C_β is defined as

$$[C_\beta] = \frac{\langle \rho_g \rangle \widetilde{Y}_\alpha}{M_\alpha}. \tag{2.71}$$

The reaction rates k_f and k_b are calculated using the Arrhenius function [269]

$$\langle k_r \rangle = A_r \langle T \rangle^{b_r} \exp \left(-\frac{E_{a,r}}{\mathcal{R} \langle T \rangle} \right), \tag{2.72}$$

with the pre-exponential factor A_r, the temperature exponent b_r and the activation energy $E_{\alpha,r}$.

Note that, since chemical timescales in a detailed reaction mechanism can vary by orders of magnitude, the system of equations resulting from Eq. (2.70) is prone to *numerical stiffness* [79]. This term denotes the fact that numerical methods for solving the system are unstable, unless an extremely small integration step size is chosen. The present implementation of the FRC model therefore utilizes additional source term splitting and preconditioning [79, 92] to overcome this limitation.

2.5.3. Turbulence-Chemistry interaction

Owing to the fact that the FRC source term in Eq. (2.70) is calculated based on averaged properties of the flow, the influence of turbulent fluctuations - specifically in temperature and species - are not taken into account. Therefore, this modeling approach is also referred to as *laminar chemistry*. However, in turbulent flames, turbulence-chemistry interaction (TCI) can lead to significant deviations from the assumption of laminar chemistry [151] due to strong non-linearities in the source term S_α. The general modeling problem of turbulence-chemistry interaction in RANS simulations can be summarized as

$$\langle S_\alpha \left(\phi \right) \rangle \neq S_\alpha \left(\langle \phi \rangle \right) \quad \text{with} \quad \phi = (T, Y_1, Y_2, .., Y_{N_{sp}}). \tag{2.73}$$

For the thesis at hand, a probability density function (PDF) method [79] is included to account for turbulence-chemistry interactions in the FRC model. Under the assumption that the turbulent fluctuations of ϕ are stochastic, the averaged source term $\langle S_\alpha \rangle$ for *turbulent chemistry* is inferred from integrating the source term S_α over all possible states of ϕ, weighted by their respective probability which is expressed through a joint-PDF $\mathcal{P}(\phi)$:

$$\langle S_\alpha \rangle = \int_{-\infty}^{\infty} S_\alpha(\hat{\phi}) \mathcal{P}(\hat{\phi}) \mathrm{d}\hat{\phi}. \tag{2.74}$$

Although methods exist for the direct calculation of $\mathcal{P}(\phi)$ at each position of the reaction zone (*transported PDF* [189, 190]), the associated computational burden still limits their application to academic test cases [65]. As an alternative, the used TCI model assumes the shape of $\mathcal{P}(\phi)$ a-priori (*assumed PDF*/aPDF [79]). Thus, only a few low order moments of $\mathcal{P}(\phi)$ have to be transported and calculated over the reaction zone.

For the temperature[8], a Gauss distribution is assumed:

$$\mathcal{P}_{mod,T}(\hat{T}) = \frac{1}{\sqrt{2\pi}\sigma_{T_0}} \exp\left(-\frac{(\hat{T} - \langle T_0\rangle)^2}{2\sigma_{T_0}}\right) + C_{min}\delta(\hat{T} - T_{min}) + C_{max}\delta(\hat{T} - T_{max}). \quad (2.75)$$

The Dirac functions δ limit the temperature to $[T_{min}; T_{max}]$ to avoid unphysical temperatures caused by the general definition of $\mathcal{P}_{Gauss}$ in $]-\infty; \infty[$. The scaling factors C_{min} and C_{max} are given by the normalization condition over $\mathcal{P}_{mod,T}$.

To reflect the intermittency in turbulent fluctuations of species [79], a β-PDF is assumed for $\mathcal{P}_Y$:

$$\mathcal{P}_{mod,Y}(\hat{Y}) = \frac{\Gamma(\sum_{\alpha=1}^{N_{sp}} \beta_\alpha)}{\prod_{\alpha=1}^{N_{sp}} \Gamma(\beta_\alpha)}\delta\left(1 - \sum_{\alpha=1}^{N_{sp}} \hat{Y}_\alpha\right)\prod_{\alpha=1}^{N_{sp}} Y_\alpha^{\beta_\alpha - 1}, \quad (2.76)$$

with

$$\Gamma(\beta_\alpha) = \int_{t=0}^{t=\infty} t^{\beta_\alpha - 1} \exp^{-t} dt \quad (2.77)$$

and

$$\beta_\alpha = Y_\alpha\left(\frac{\sum_{\beta=1}^{N_{sp}} Y_\beta(1 - Y_\beta)}{\sigma_Y} - 1\right). \quad (2.78)$$

In order to define the shape of both distribution functions (2.75) and (2.76), the variances

$$\sigma_T = \left\langle T'^2\right\rangle \quad \text{and} \quad \sigma_Y = \sum_{\alpha=1}^{N_{sp}} \left\langle Y_\alpha'^2\right\rangle \quad (2.79)$$

have to be known over the reaction zone. Therefore, two additional transport equations for convection, production and dissipation of σ_T and σ_Y need to be solved within the TCI model. Further details on the additional transport equations and the implementation of the aPDF-TCI model in the simulation platform are given in the work of Di Domenico [42] and Blacha [16].

In this section, combustion models have been described in a RANS context, i.e. based on averaged quantities. The use of the FRC model in LES requires a filtered formulation $\overline{S}_\alpha$ of the chemical source term in Eq. (2.70). Furthermore, since LES is able to resolve parts of the turbulence-chemistry interaction, the aforementioned TCI model is only used for the unresolved sub-grid scale interaction. Filtered equations for the FRC model and a discussion of the TCI model for sub-grid scale interaction are detailed in the work of Eckel [50].

---

[8]Quantities with turbulence-chemistry interaction are indicated by $(\hat{..})$.

2.6. Simulation platform

The simulations for the work at hand are performed using the DLR in-house simulation platform THETA/SPRAYSIM [50–52] which implements the discussed models. The simulation platform consists of the two codes THETA and SPRAYSIM for the gaseous and dispersed phase, respectively. By analogy with the generalized coupling effects in a dispersed multiphase flow as shown in Fig. 2.2, Fig. 2.12 provides a summary of the simulation platform and its sub-modules.

THETA (Turbulent Heat Release Extension of the TAU Code) [42, 43] is a 3D finite volume solver for structured and unstructured dual grids that has been optimized for combustion problems typical for gas turbine combustion [16, 48, 136, 207]. Since gas velocities and Mach numbers[9] in gas turbine applications are moderate [131], THETA is based on an incompressible formulation of the governing equations from Sec. 2.2. Due to this assumption, the following simplifications hold:

- Viscous dissipation $\tau_{ij}\frac{\partial u_i}{\partial x_j}$ is neglected in the energy equation (2.5)

- The substantial pressure derivative is approximated as $\frac{\mathrm{D}p}{\mathrm{D}t} \approx \frac{\mathrm{d}p}{\mathrm{d}t}$

- Density is calculated w.r.t the reference pressure as $\rho(p,T) \approx \rho(p_{ref},T)$

Incompressible modeling results in a weak coupling of pressure and velocity. For steady-state simulations, the SIMPLE algorithm for pressure-velocity coupling is used, whereas in transient cases, a projection based method is applied. A variety of second order accurate spatial and temporal discretization schemes are available.

The ODEs for Lagrangian particle tracking are solved in SPRAYSIM [53, 126, 196] via a predictor-corrector scheme with automatic adaption of order and step size. In addition to the models discussed in Sec. 2.3, droplet secondary atomization is included by Tanner's Cascade Atomization and Breakup (CAB) model [258] in combination with the droplet deformation law of Schmehl [230]. Furthermore, unresolved turbulent dispersion of droplets is accounted for using a variant of the Gosman-Ioannides model [87] for RANS simulations and the SGS dispersion model of Bini and Jones [15] in LES cases. For a discussion of both

THETA		SPRAYSIM
Gas field	S_ρ, S_α	Particle transport
Turbulence	$S_{\rho u}$	Particle dispersion
Species transport		Secondary breakup
Chemical reaction	S_h	Evaporation
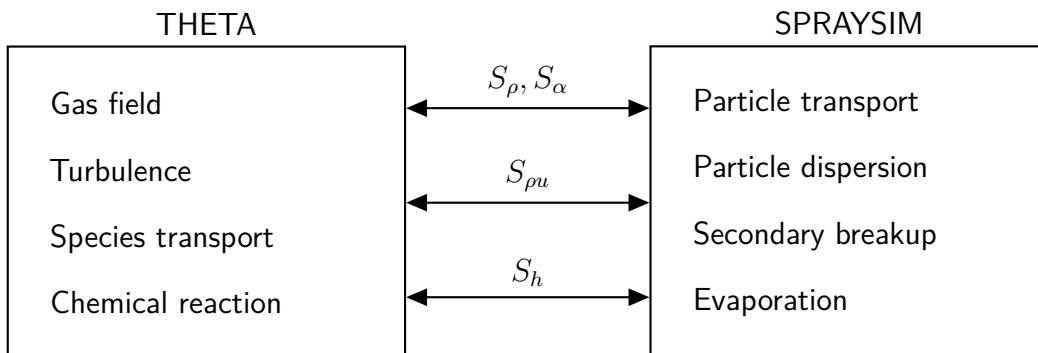
Figure 2.12.: Schematic of the simulation platform for turbulent spray combustion.

---

[9]Mach number relates the local gas velocity to the local speed of sound

models, the reader is referred to Eckel et al. [49]. In the particle tracking approach realized in SPRAYSIM, particles or droplets with equal properties are replaced by *numerical parcels* and given a representative liquid loading to speed up computation. The phase coupling relies on a point source approximation. In this simplification parcels are assumed to be discrete points providing point sources and point forces to the gas field [107]. Source terms are exchanged between the two codes online at each iteration or timestep via iterative two-way coupling [50]. Derivations of the spray source terms $S_\rho, S_\alpha, S_{\rho u}, S_h$ are given in the work of Eckel [50].

3. Fundamentals of Uncertainty Quantification and Probabilistic Modeling for complex Simulations

This chapter outlines the fundamentals of uncertainty quantification in complex simulations and the associated probabilistic modeling approaches. For the sake of brevity, only the most essential elements of probability theory are discussed. Fundamental definitions are summarized in Appendix B. A comprehensive introduction to this topic is given in the compedium of Durrett [47].

The general uncertainty quantification approach for the dissertation at hand follows the framework proposed by Roy and Oberkampf [216], additional information is available in their textbook [177]. For an in-depth review of probabilistic modeling with an emphasis on spectral methods, the reader is referred to the work of Le Maître and Knio [128] or Sudret [253].

3.1. Types and sources of uncertainties

From a theoretical point of view, sources of uncertainties of a given simulation model can be subdivided into three major categories, namely model form uncertainties, numerical uncertainties and input uncertainties [177].

As pointed out by Oberkampf [177] the term *model* can have a wide variety of meanings depending on the field and context. Therefore, in the following discussion, the term *simulation model* $\mathcal{M}$ refers to a rather abstract definition of a mathematical model with arbitrary complexity, which aims at approximating the behavior of a physical system $\mathcal{S}_P$ through a mathematical description. The output of $\mathcal{M}$ is driven by a finite vector of input variables $\boldsymbol{x} = \{x_1, x_2, x_3, .., x_{n_x}\}$ with n_x components:

$$\mathcal{M}(\boldsymbol{x}) \approx \mathcal{S}_P \quad \text{for} \quad \boldsymbol{x} \in \mathcal{D}_V. \tag{3.1}$$

The assumptions made in the derivation of $\mathcal{M}$ limit $\boldsymbol{x}$ to a *validation domain $\mathcal{D}_V$*, although extrapolation to a wider *application domain $\mathcal{D}_A$* is commonly accepted [260]. Model form uncertainties then stem from the process of abstraction and formulation of the mathematical models while approximating the physical system $\mathcal{S}_P$ by the simulation model $\mathcal{M}$. These uncertainties are commonly estimated using model validation [216], i.e. by means of a comparison of the simulation results with experimental measurements over the validation

domain $\mathcal{D}_V$. Associated uncertainties are further amplified when applying the model to conditions for which validation data is not available (application domain $\mathcal{D}_A$). Model form uncertainties of the used vaporization models have been studied by Rauch [202].

The fact that most simulation models consist of a set of non-linear differential equations requires numerical - i.e. approximate - solution methods in the computation of model outputs, thereby causing numerical uncertainties. They include discretization errors from both temporal and spatial discretization of the continuous model formulation, insufficient iterative convergence of the numerical solver and round-off errors in the computing system [210]. Therefore, numerical uncertainties are inherently present in the simulation of turbulent spray combustion. The latter two sources of uncertainties, namely convergence and round-off errors, are assumed to be negligible in the simulation platform under consideration due to previous and ongoing verification and validation efforts. Discretization errors can be assessed using the grid convergence method proposed by Roache [211].

Input uncertainties comprise uncertainties in all data required to fully specify the model, i.e. constitutive parameters and modeling constants of the model as well as inputs for the model defined by the environment in which the model is evaluated. Model inputs are subdivided into initial conditions, boundary conditions and geometry representation. In many situations, this data cannot be exactly specified due to a lack of experimental data or measurement uncertainties. Furthermore, in early design stages parameters may not be known beforehand as the exact definition of geometrical dimensions and resulting boundary conditions will be subject to the design process. For the identification of input uncertainties, it is therefore advisable to consider an input as uncertain unless there is strong evidence that the uncertainty in the input will result in minimal uncertainty in the quantities of interest (QoIs) [216].

As identified in the introduction (see Sec. 1.1), uncertainties arising from the specification of spray boundary conditions are the key topic for the work at hand. Such uncertainties can be assigned to the category of input uncertainties. Therefore, in the following, special emphasis will be placed on the treatment of input uncertainties.

3.2. Probabilistic model definition

By virtue of the simulation model from Eq. (3.1), a vector $\boldsymbol{q} = \{q_1, q_2, q_3, .., q_{n_q}\}$ consisting of n_q *quantities of interest*[1] q is observed, which results in the mapping

$$\boldsymbol{x} :\mapsto \boldsymbol{q} = \mathcal{M}(\boldsymbol{x}). \tag{3.2}$$

Due to this general definition, $\mathcal{M}$ can also consist of several sub-models $\mathcal{M}_{s,i} \subset \mathcal{M}$, which contribute to the mapping in Eq. (3.2). Note that, due to the complexity of $\mathcal{M}$ in typical simulation applications, this mapping is only known through pointwise evaluations

$$\boldsymbol{q}^{(i)} = \mathcal{M}(\boldsymbol{x}^{(i)}) \tag{3.3}$$

---

[1]In the following abbreviated as QoI
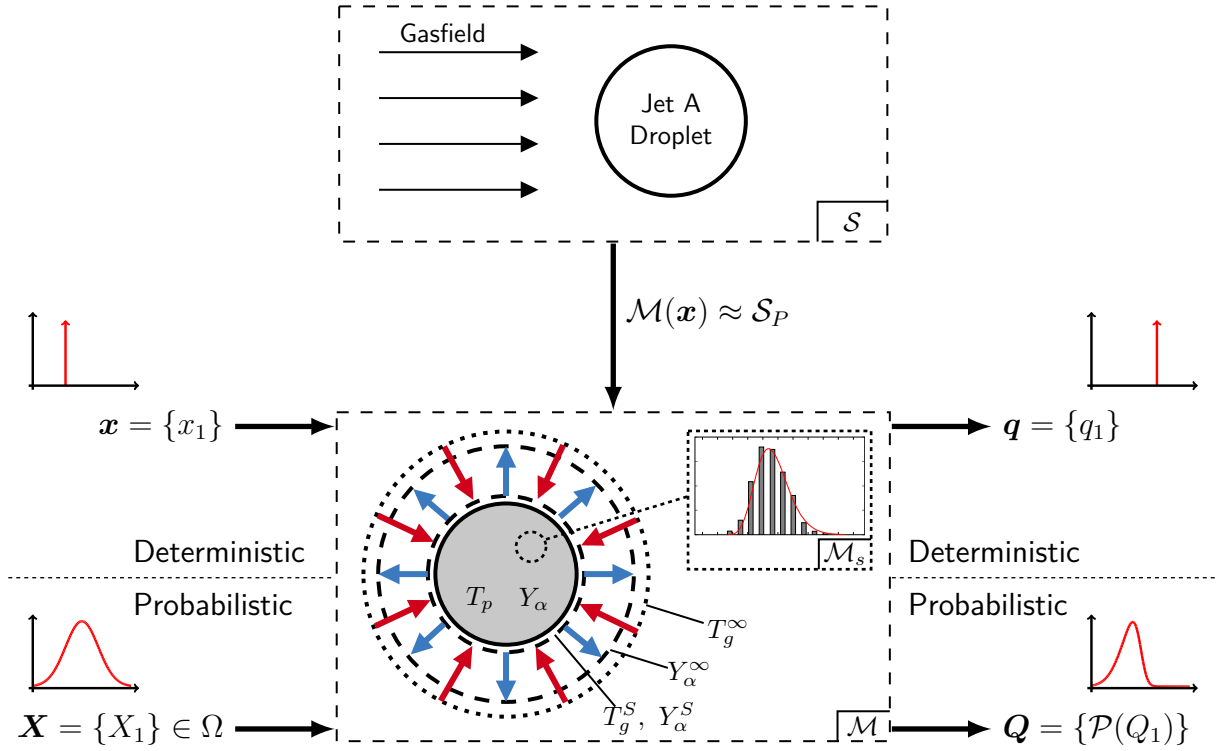
Figure 3.1.: Modeling of the physical system *evaporating droplet* ($\mathcal{S}_P$) by the simulation model *quasi-steady state droplet evaporation* ($\mathcal{M}$).

for which the simulation is run [253]. In the following, the mapping from Eq. (3.2) and the set $(\boldsymbol{x}^{(i)}, \boldsymbol{q}^{(i)})$ are referred to as a *deterministic* model and a *deterministic* simulation, respectively. This is motivated by the fact that the values for the dependent variable $\boldsymbol{q}$ are completely determined by the choice of $\boldsymbol{x}$ [208]. In other words, each evaluation of $\mathcal{M}$ with identical input $\boldsymbol{x}$ will result in the identical output $\boldsymbol{q}$.

To further clarify these definitions, Fig. 3.1 illustrates a modeling example for droplet evaporation. The physical system $\mathcal{S}_P$ consists of a single, isolated Jet A fuel droplet in a flow field of hot gas. In the presence of the hot gas field, the droplet with diameter D_0 fully evaporates within a time scale $\tau_{ev.}$. The physical system is approximated by the quasi-steady state droplet evaporation model $\mathcal{M}$ (see Sec. 2.3.2), thereby causing a model form uncertainty. The simulation model maps $\boldsymbol{x} = \{D_0\}$ to the respective time scale $\boldsymbol{q} = \{\tau_{ev.}\}$. Jet A properties are accounted for by inclusion of the Continuous Thermodynamics Model (CTM, see Sec. 2.3.2) as a sub model $\mathcal{M}_s \subset \mathcal{M}$.

However, the deterministic modeling approach is unable to reflect cases in which uncertainties in $\boldsymbol{x}$ must be included, i.e. simulations with input uncertainties which arise for example from incomplete or unavailable data. From the mapping in Eq. (3.2) it is obvious that in such situations, uncertainties in the input $\boldsymbol{x}$ introduce uncertainties in the output which must be associated with $\boldsymbol{q}$. In order to account for such uncertainties, it is therefore useful to define a *probabilistic model* of the simulation model by introducing a probabilistic description of $\boldsymbol{x}$ via a random vector $\boldsymbol{X} = \{X_1, X_2, X_3, .., X_{n_x}\} \in \Omega$, which describes the variability in $\boldsymbol{x}$ over a

parameter space Ω of uncertain inputs:

$$\boldsymbol{X} :\mapsto \boldsymbol{Q} = \mathcal{M}(\boldsymbol{X}) \tag{3.4}$$

As a consequence, $\boldsymbol{q}$ also becomes a probabilistic quantity $\boldsymbol{Q}$ from which statistical measures about the output variability - i.e. the output uncertainty due to the input uncertainties - can be derived. It is important to note that, although the mapping in Eq. (3.4) defines a probabilistic model, the underlying mathematical description $\mathcal{M}$ is still deterministic.

The example from Fig. 3.1 depicts both the deterministic and probabilistic evaluation of $\mathcal{M}$. For the deterministic case, the discrete evaluation results in a discrete output, characterized by a Dirac delta [47]. In contrast, in the probabilistic approach, the output $\boldsymbol{Q}$ is given in terms of a probability density function $\mathcal{P}(Q_1) = \mathcal{P}(\tau_{ev.})$ for the random vector of droplet diameters $\boldsymbol{X} = \{D_0\} \in \Omega_{D_0}$. It should be pointed out that due to the non-linear character of the simulation model, distributions of input and output quantities follow different distribution functions.

Due to the aforementioned complexity in most simulation models, the efficient exploration of the mapping from Eq. (3.4) becomes the key challenge in an uncertainty quantification. Keeping in mind the variety of complex submodels involved (see Cp. 2), the simulation of turbulent spray combustion still poses major challenges in the quantification of associated uncertainties. Strategies and methods facilitating this task are discussed in the following sections.

3.3. Workflow for uncertainty quantification

Uncertainty quantification (UQ) of complex simulation models covers a variety of tasks from the fields of system analysis, probabilistic modeling or large scale simulation processing. It is therefore useful to subdivide a generalized UQ analysis into distinct steps, which structure a workflow for uncertainty quantification. Based on the recommendations of Oberkampf [177, 178, 216], the workflow for the present thesis is given in Fig. 3.2. Three major steps are identified:

- **Step A: Specification** consists of the thorough identification of all relevant sources of uncertainties for the simulation model under the given scenario. The input uncertainties are then classified either as aleatoric or epistemic and characterized by a mathematical description, resulting in the vector of uncertain inputs $\boldsymbol{X}$.

- **Step B: Propagation** comprises the forward propagation of the uncertain input through the simulation model, i.e. the evaluation of the probabilistic mapping from Eq. (3.4).

- **Step C: Analysis** studies the probabilistic content of the uncertain output $\boldsymbol{Q}$. Depending on the methodology chosen for Step A, different statistical measures (mean,
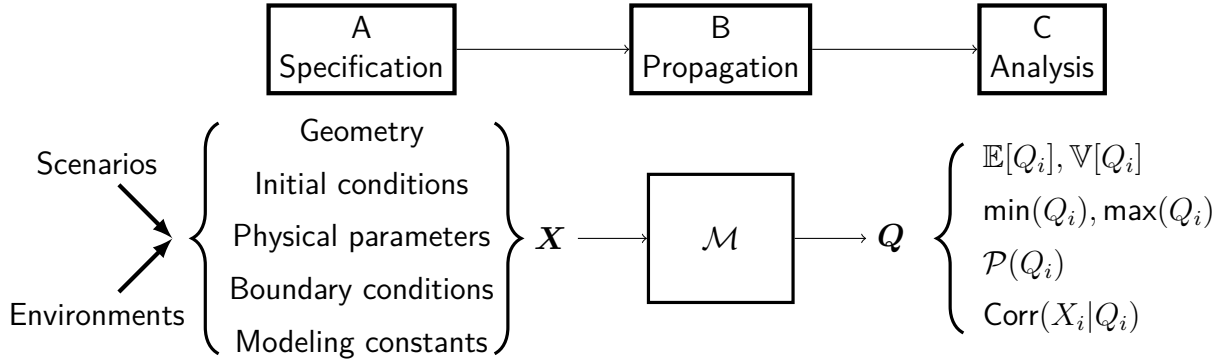
Figure 3.2.: Workflow for uncertainty quantification, adapted from Oberkampf [177].

variance, bounds) are derived. Furthermore, sensitivity analysis provides information on the respective impact of the input parameters onto the response randomness.

3.3.1. Step A: Specification of the UQ problem

Within this step, sources of uncertainties for the modeling problem under consideration are identified with respect to the aforementioned three categories.

It is important to note that the relevance of an uncertainty must always be assessed with respect to the given *scenario*. In the example from Fig. 3.1, this could mean that the effect of uncertainties in droplet diameter on the evaporation time scale might differ between a scenario with a hot gas field (e.g. full load operation of the combustor) and a scenario with a cold gas field and slow evaporation (e.g. cold start ignition of the combustor).

Once all sources of uncertainties are identified, specifically in the case of input uncertainties a mathematical representation for the vector X of uncertain inputs in the mapping from Eq. (3.4) must be stated. Here, it is important to distinguish between the different nature of uncertainties, namely *aleatoric* and *epistemic* uncertainties. While the first describes an inherent and irreducible variation or randomness in a quantity that could be characterized by a PDF, the latter refers to uncertainties due to a lack of knowledge which can be reduced by incorporating additional data [63, 177]. Based on this categorization, several methods for the mathematical representation of input uncertainties have been proposed in the literature: In the traditional framework of *probability theory* [188], each aleatoric and epistemic uncertain input is characterized by a PDF over a respective probability space. Additional information concerning the belief and plausibility of assumptions is incorporated in the *evidence theory*[2]-based representation of uncertainties [93, 236]. In contrast, *interval analysis* [117, 165] is based on the specification of intervals of possible values for mainly epistemic variables. Further approaches include *possibility theory* [264] and the application of *fuzzy logic* [25]. A comparative discussion of methods for uncertainty representation based on simple test problems has been reported by Helton et al. [96].

For the work at hand, probability theory is adopted for the representation of X. Therefore, uncertain inputs are characterized by PDFs if adequate data is available or by minimum

---

[2]Also referred to as *Dempster-Shafer* theory.

(a) aleatoric - PDF   (b) epistemic - interval
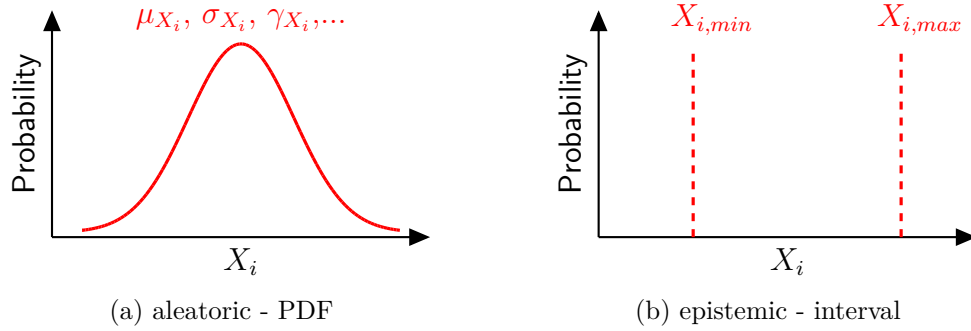
Figure 3.3.: Representation of uncertainty in input X_i within a probabilistic approach.

and maximum bound intervals, with the latter of which treated as *imprecise probability distributions* [6, 177]. Figure 3.3 demonstrates this method for an aleatoric (Fig. 3.3 (a)) and an epistemic (Fig. 3.3 (b)) probabilistic input X_i. In contrast to the aleatoric case, where the *probability* over X_i is given by a PDF and its respective moments, in the epistemic case, all values within the interval $[X_{i,min}, X_{i,max}]$ are treated as *possible* realizations with a probability of unity. Note that this is less definitive than claiming that all values within the interval are *equally* possible, i.e. a uniform PDF over the interval [177].

Screening: Morris One At a Time

Due to the high modeling demand in the simulation of turbulent spray combustion, the dimension n_x of the vector of uncertain inputs $\boldsymbol{X}$ from modeling parameters as well as boundary conditions might become large. It is therefore advisable to conduct an *a priori* screening study to identify the most relevant elements of $\boldsymbol{X}$, i.e. the parameters which cause high variation in the simulation outcome [270]. Based on the screening results, parameters of minor influence might be fixed to mean values to reduce the input parameter space for the following forward uncertainty propagation.

For the work at hand, the Morris One At a Time (MOAT) [166] screening method is selected, as it provides a robust qualitative measure for parameter importance based on a relatively small number of model evaluations [224]. In a MOAT analysis, input parameters X_i from $\boldsymbol{X}$ are varied one at a time with a substantial variation step size Δ_M, while the afore changed parameter remains at the changed value. An *elementary effect d_i* associated to this variation is computed through the forward difference

$$d_i = \frac{Q\left(\boldsymbol{X} + \Delta_M e_i\right) - Q(\boldsymbol{X})}{\Delta_M},\tag{3.5}$$

where e_i is the coordinate vector of the changed parameter in the respective variable subspace. For practical computations, *trajectories* in the input space are constructed from a series of successive variation steps. An example trajectory for a two-dimensional input space $[X_1 \times X_2]$ is displayed in Fig. 3.4 (a). Details on optimal trajectory placement for MOAT are given in Saltelli et al. [224].

(a) Trajectory

(b) (μ^*,σ) plane
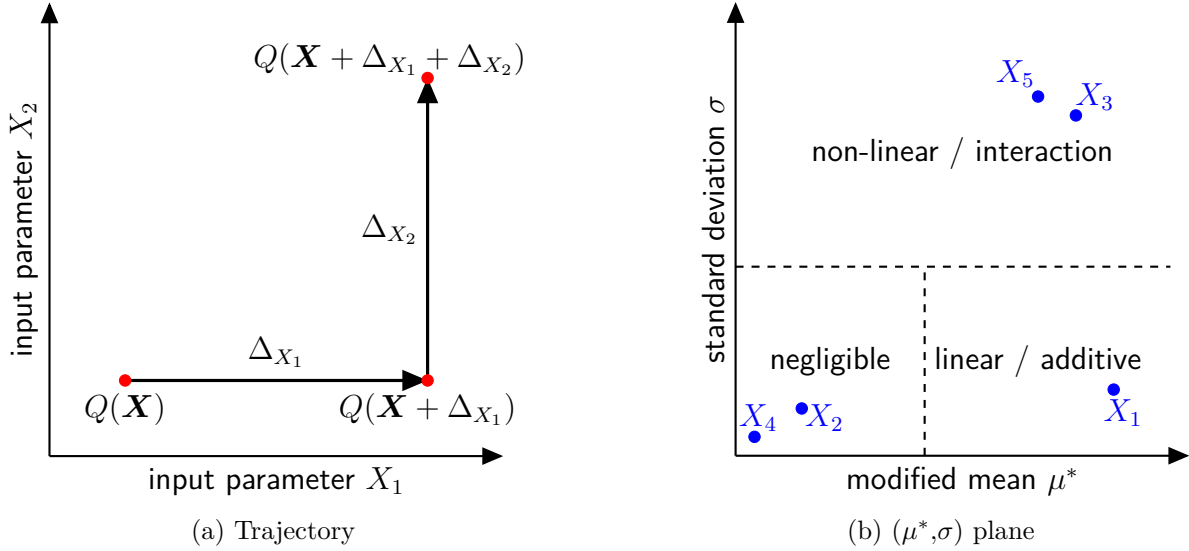
Figure 3.4.: Example trajectory in a two-dimensional input space and display of MOAT results in the (μ^*,σ) plane. Function evaluations (•) and MOAT results (•) for a quantity of interest Q.

After generating r elementary effects, mean μ_i and standard deviation σ_i are approximated by

$$\mu_i = \frac{1}{r}\sum_{j=1}^{r} d_i^{(j)} \tag{3.6}$$

and

$$\sigma_i = \sqrt{\frac{1}{r}\sum_{j=1}^{r}\left(d_i^{(j)} - \mu_i\right)^2}. \tag{3.7}$$

While μ_i estimates the overall effect of the input X_i on the output, σ_i ranks the ensemble of the second- and higher-order effects in which X_i is involved [166]. As an improvement to the original MOAT method, Campolongo et al. [21] recommended a modified mean μ_i^* instead of μ_i to overcome the effect of alternating signs in d_i. μ_i^* is defined by

$$\mu_i^* = \frac{1}{r}\sum_{j=1}^{r} |d_i^{(j)}|. \tag{3.8}$$

For interpreting results via the two sensitivity measures, the estimated modified mean and standard deviation of each input parameter are displayed in the (μ^*,σ) plane. The plotted values can then be examined relative to each other to see which parameters appear to be the most important ones.

This is illustrated in Fig. 3.4 (b) for five arbitrary input parameters, alongside a rough division of the (μ^*,σ) plane into characteristic regions. From this division, it can be concluded that parameters X_2 and X_4 have a negligible influence on the output while X_1 demonstrates a strong linear effect. The fact that X_3 and X_5 both reside in the upper-right portion of the

(μ^*,σ) plane leads to the assumption that these parameters interact in their effect on the output.

3.3.2. Step B: Forward propagation of uncertainties

Techniques enabling the forward propagation of uncertainties through a simulation model are commonly subdivided into two categories, namley *intrusive* and *non-intrusive* methods [128, 177, 253].

Intrusive propagation methods require the reformulation of the models' governing equations to incorporate stochastic behavior in the computation of output quantities, e.g. through stochastic Galerkin methods [127]. Clearly, this demands extensive adjustments in the case of an existing deterministic simulation code and even specific numerical solvers [128]. Since the reformulated intrusive model $\mathcal{M}_I$ directly results the probabilistic output $\boldsymbol{Q}$, intrusive methods are highly effective and can provide a connection between the probabilistic nature of the output and the underlying physics [104]. Although the use of intrusive methods has been succesfully demonstrated for test case problems in multi-phase flows [263], intrusive models remain challenging to implement and difficult to verify for complex simulation problems [104].

In contrast, non-intrusive methods rely on space-filling sampling of the simulation model over the parameter space Ω of uncertain inputs, which essentially divides the solution of the probabilistic mapping from Eq. (3.4) into multiple deterministic model evaluations $(\boldsymbol{x}^{(i)},\boldsymbol{q}^{(i)})$. Thus, $\mathcal{M}$ is treated as a *black box* and no further adjustments to the model or implementation are required. Statistical moments of $\boldsymbol{Q}$ are then estimated from the set $\mathcal{S}$ of M sample outputs $\mathcal{S} = \{\boldsymbol{q}^{(i)}, i = 1,..,M\}$. For example, the expectation $\mathbb{E}$ of the probabilistic output $\boldsymbol{Q}$ can be approximated by

$$\mathbb{E}[\boldsymbol{Q}] \approx \frac{1}{M}\sum_{i=1}^{M}\boldsymbol{q}^{(i)}. \tag{3.9}$$

The fact that $\boldsymbol{X}$ is propagated through discrete model evaluations results in a discrete distribution of probabilities for $\boldsymbol{Q}$, i.e. a histogram of model responses $\boldsymbol{q}^{(i)}$. By considering a large set of model evaluations, an approximated probability density function $\hat{\mathcal{P}}(\boldsymbol{Q})$ may be obtained using kernel smoothing techniques [268]. Major drawbacks of sampling-based uncertainty propagation are the relatively low convergence rate of higher moments [127] and the *curse of dimensionality* [14] when facing high dimensional inputs. This requires a large set of samples which may be impossible for computationally expensive models. Methods to overcome this limitation are discussed in Sec. 3.4.

Non-intrusive methods are utilized for the work at hand, since the existing simulation platform (see Sec. 2.6) can be used without further adjustments within this approach.

Sampling methods for non-intrusive uncertainty propagation

To obtain the sampling set S, samples have to be drawn from Ω, taking into account the probabilistic structure of $\boldsymbol{X}$. The most classical approach is *Monte Carlo sampling* (MC) [66],
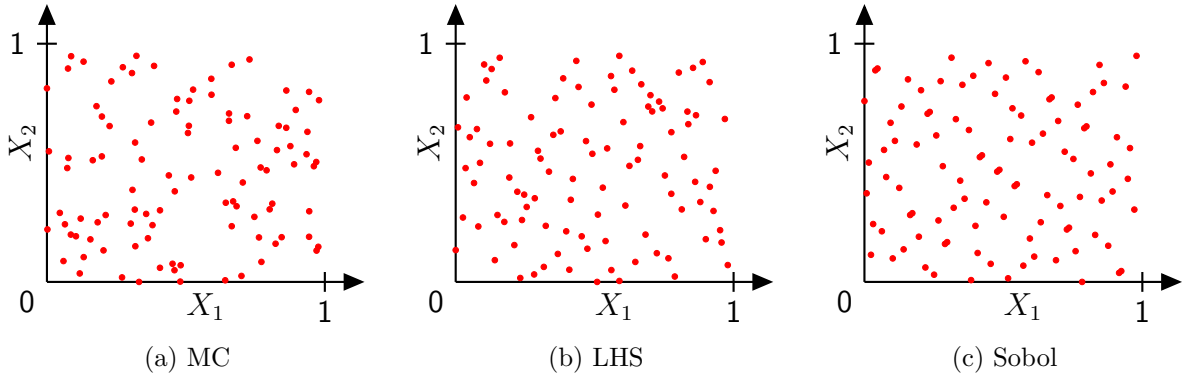
Figure 3.5.: Sample sets from a two-dimensional unit square $U = \mathcal{U}(0,1) \times \mathcal{U}(0,1)$.

in which independent samples are drawn at pseudo-random. The addition *pseudo* refers to the fact that samples in all computational sampling procedures are generated from deterministic algorithms, which thereby only provide approximations for sequences of random numbers. In fact, they are fully determined by their initial value, the so-called *seed* [174]. Although simple to implement, crude MC sampling suffers from clustering tendencies due to the independence of individual samples and a comparably low asymptotic convergence rate in $\mathcal{O}(1/\sqrt{M})$ for the statistical moments [66].

In order to avoid clustering tendencies of crude MC methods, stratified sampling techniques such as *Latin Hypercube Sampling* (LHS) [150] divide the input space into segments of equal probability before drawing the samples. Thus, the range of each input variable is divided into m equally probable intervals. $M = m$ sampling points are then placed to satisfy the Latin Hypercube requirements [226], forcing the number of divisions to be equal for each variable. In practice, MC and LHS lead to the same asymptotic convergence rate in $\mathcal{O}(1/\sqrt{M})$ [128].

As a third option, *quasi Monte Carlo*[3] (qMC) methods seek to minimize the spatial discrepancy of the sampling, i.e. how the spread of the sampling points deviate from a uniform spread over the input space. Different qMC methods have been proposed, e.g. by Sobol [244], Halton [187] or Hammersley [95]. Since these methods are based on a sequential calculation of samples, they hold the favorable property that the sequence for $M - 1$ is a subset of the sequence for M, making them easy to extend by adding points to an existing sequence [68]. This is in contrast to LHS, where the entire sampling must be recomputed if an LHS containing more samples is required. For inputs with high dimension n_x, the convergence rate improves compared to MC and LHS, e.g. in the case of a Sobol sequence to $\mathcal{O}((\ln M)^{n_x}/M)$.

Sample sets from the three sampling methods for a two dimensional unit square $U = \mathcal{U}(0,1) \times \mathcal{U}(0,1)$ are compared in Fig. 3.5. The qMC samples are clearly more uniformly distributed while the MC sample set exhibits clusters of points.

Fig. 3.6 illustrates results from non-intrusive propagation of uncertainty for the example of single droplet vaporization (see Sec. 3.2). As a test case, the initial droplet diameter D_0 is treated as an uncertain input, following a normal distribution with mean $\mu = 50$ µm

---

[3]Also called *low discrepancy sequences generators*.

(a) $M = 100$ (b) $M = 1000$
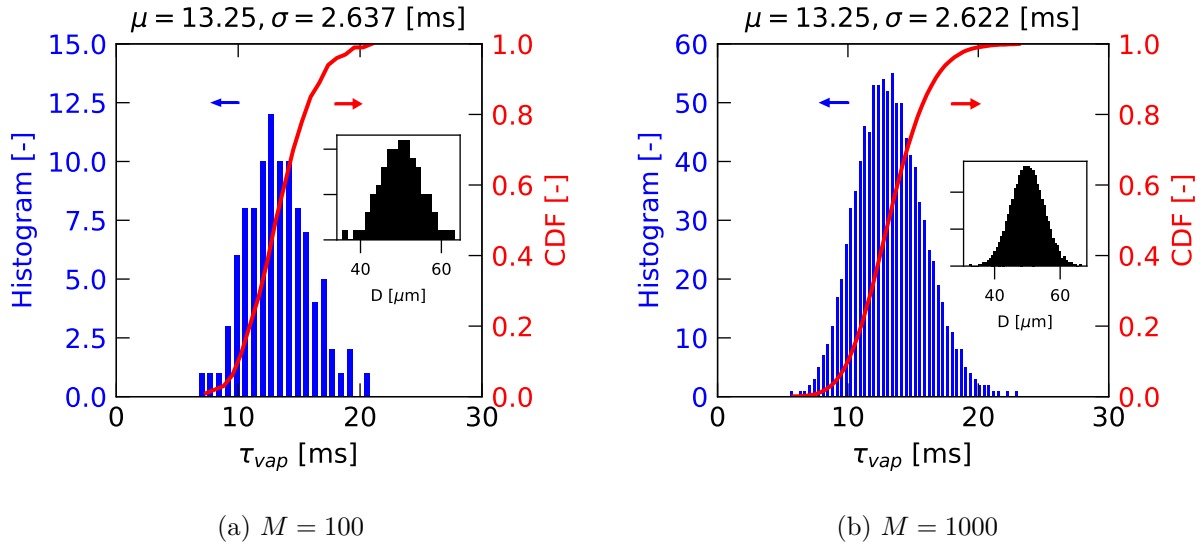
Figure 3.6.: Non-intrusive sampling of the simulation model for quasi-steady state droplet evaporation. Histogram for $q^{(i)}$ (—), histogram for $x^{(i)}$ (—), empirical CDF for Q (—).

and standard deviation $\sigma = 5\mu m$. Thus, the random input variable reads $X = \mathcal{N}(50,5)$ µm over $\Omega = [20,70]$ µm. To avoid unphysical results, the normal distribution is truncated by setting it to minimum and maximum bounds. 100 and 1000 LHS samples are drawn from X. Results are given in Fig. 3.6 (a) and Fig. 3.6 (b), respectively. The blue histograms depict model responses $q^{(i)}$, i.e. vaporization time scale τ_{vap} from each model evaluation. Corresponding inputs $x^{(i)}$ are given as black histograms. Furthermore, the approximated or *empirical* cumulative distribution function (CDF) $\hat{\mathcal{C}}(Q)$ is plotted as a red line. Although the mean and variance of the output are almost identical for $M = 100$ and $M = 1000$, the empirical CDF becomes smoother for the large sample set and the output histograms clearly resembles a normal distribution. Due to the fact that the input is also sampled from a normal distribution, it can be assumed that the mapping $D_0 \mapsto \tau_{vap} = \mathcal{M}(D_0)$ is nearly linear over the considered input space.

3.3.3. Step C: Analysis of the probabilistic output

By analyzing the probabilistic output of the preceding uncertainty propagation, this step clearly depicts the implications of uncertainties on the simulation outcome. Therefore, acceptance criteria for simulation predictions may be established, i.e. quantitative information about the predictive capabilities of the simulation model under the given uncertainties.

Helton et al. [96] pointed out that results of uncertainty propagation must always be interpreted in the context of the theory from which the uncertainty representation was derived (see Sec. 3.3.2). A consistent analysis framework when using probability theory for uncertainty representation is given by *Probability Bounds Analysis* (PBA) [63, 64, 261]. Concepts of PBA are outlined in this section.
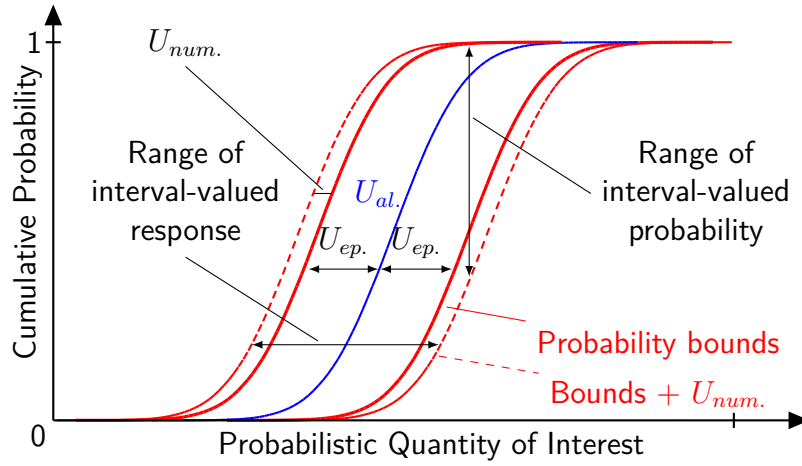
Figure 3.7.: p-box of a QoI in the presence of aleatoric and epistemic uncertainties, according to Oberkampf [177].

Finally, the contribution of each uncertain model input X_i on the uncertain output Q can be assessed and ranked through *a posterior* sensitivity analysis. Based on the resulting ranking of importance, strategies for curtailing the predictive uncertainties of $\mathcal{M}$ by reducing the dominating input uncertainties may be deduced. A wide variety of methods for sensitivity analysis is available in the literature. For the work at hand, variance-based global sensitivity analysis using Sobol indices [243] is selected. For a broad perspective of sensitivity analysis, the reader is referred to the work of Saltelli [223, 224].

Probability Bounds Analysis

Probability Bounds Analysis is based on a strict separation between aleatory and epistemic uncertainties. While model form and numerical uncertainties are generally interpreted as epistemic, input uncertainties must be characterized mathematically as either aleatory or epistemic using a probabilistic approach (see Fig. 3.3). In the presence of mixed input uncertainties, two-dimensional sampling incorporates the interaction of aleatory and epistemic uncertainties [177]. This results in an ensemble of CDFs for the Quantity of Interest under consideration. The widest extent of such an ensemble is interpreted as the *probability bounds* of the QoI and probabilistic measures are inferred from the resulting *probability box* or *p-box* [63]. Thereby, a p-box expresses that a QoI cannot be displayed as a precise probability under the given uncertainties, but it is now an interval valued probability [216]. The use of a p-box for the representation of uncertainties in a QoI caused by input uncertainties also facilitates the clear portrayal of total output uncertainties for the QoI within a PBA. Since additional numerical and model form uncertainties are treated as epistemic, they are simply added to the probability bounds of the p-box [30, 177].

A conceptual example for a p-box as a result from PBA is given in Fig. 3.7. The blue line represents a CDF for the QoI Q from a single propagation of aleatoric uncertainties through the model. Further CDFs are obtained by stepwise inclusion of epistemic uncertainties (not shown for brevity). The red lines indicate the resulting probability bounds from the ensemble of CDFs. In addition, numerical uncertainties are added to probability bounds, thereby
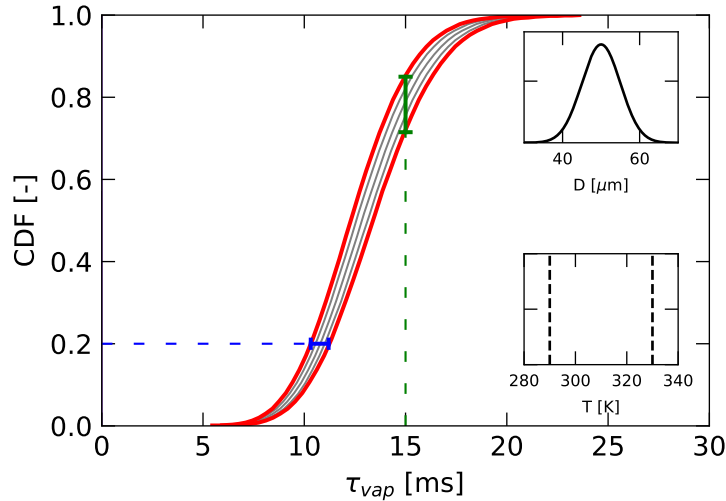
Figure 3.8.: p-box from the PBA of the simulation model for quasi-steady state droplet evaporation. Example CDF (—), Probability bounds (—). Subplots show input distributions.

widening the p-box. From the resulting p-box representation, a range of interval-valued response or a range of interval-valued probability can be derived for a given probability or response level, respectively. Stated differently, a fixed value of Q will be observed within an interval-valued probability $[\mathrm{Pr}_{min}; \mathrm{Pr}_{max}]$. Likewise, a given probability level yields a corresponding interval of response $[Q_{min}; Q_{max}]$.

For further clarification, the concept of PBA and p-box representation is applied to the UQ example of single droplet evaporation as introduced previously. In addition to the aleatoric uncertain input for droplet diameter[4], the droplet temperature T_D is considered as an epistemic input with interval value $T_D \in [290; 330]$ K. For each computation of a single CDF, 200 samples are drawn from the input space of aleatoric uncertainties which is repeated over 40 steps in the epistemic input space. Results from two-dimensional sampling of the mixed aleatoric/epistemic input are displayed in Fig. 3.8. Three examples from the ensemble of CDFs and the resulting probability bounds are shown. The p-box now provides information concerning response and probability levels of the simulation model. For instance, the probability of an evaporation time less than 15 ms lies in the interval $[0.65; 0.82]$ (green line). Similarly, it can be deduced that for a probability level of 0.2, evaporation times within $[10; 11]$ ms are expected (blue line).

Note that in case of purely epistemic input uncertainties, the p-box from PBA simplifies to an interval of possible values [177]. Numerical and model form uncertainties are then appended to both sides of the interval.

Precise probability theory

A simplification of the strict PBA approach can be achieved when interpreting uncertainties with minimum/maximum bounds as uniformly distributed. Thus, these uncertainties are

---

[4]$D = \mathcal{N}(50,5)$ μm, test case conditions as previously.

associated with a *precise* probability distribution function instead of the *imprecise* characterization through intervals in PBA. This enables the calculation of probability levels for the uncertain simulation results in cases of purely epistemic input uncertainties. However, it should be pointed out that these probability levels purely rely on the assumption of uniform input uncertainties.

Accuracy metrics for uncertain predictions

The quantitative comparison of observations and uncertain predictions, i.e. experimental data and uncertain simulation results, demands for validation metrics which take into account the probabilistic structure of the uncertain predictions. Two validation metrics are utilized in the thesis at hand to evaluate the quality of uncertain predictions:

Deterministic observations In the case of deterministic observations, for example experimental data without measurement uncertainties, the *Continous Rankend Probabibilty Score* (CRPS) [83] evaluates the difference between the CDF of the uncertain prediction and the idealized perfect observation. The CRPS is defined as

$$\text{CRPS} = \int_{-\infty}^{\infty} \left(\mathcal{C}_Q(\chi) - \mathbb{H}(\chi - q_{obs}) \right)^2 \mathrm{d}\chi, \tag{3.10}$$

where $\mathcal{C}_Q$ is the CDF of the uncertain prediction of a QoI q, q_{obs} is the certain observation of q and $\mathbb{H}$ denotes the Heaviside function. Therefore, the CRPS yields a generalized mean absolute error in case of uncertain predictions.

Uncertain observations In contrast, the *Wasserstein-1* metric W_1 is utilized to compare the probability structure of an uncertain prediction Q with an uncertain observation Q_{obs}. A typical example for an uncertain observation could be experimental data with measurement errors. In the Euclidian space, the quantity $W_1(Q, Q_{obs})$ can be interpreted as the minimum amount of work that is required to turn the respective distribution $\mathcal{C}_Q$ into $\mathcal{C}_{Q_{obs}}$ [108]. In case of one-dimensional distributions on the real line, W_1 can be written in explicit form as

$$W_1 = \int_0^1 |\mathcal{C}_Q^{-1}(\chi) - \mathcal{C}_{Q_{obs}}^{-1}(\chi)| \mathrm{d}\chi. \tag{3.11}$$

In this equation $\mathcal{C}_Q^{-1}$ and $\mathcal{C}_{Q_{obs}}^{-1}$ are the corresponding inversions of $\mathcal{C}_Q$ and $\mathcal{C}_{Q_{obs}}$. For further derivations, the reader is referred to the work of Bobkov and Ledoux [17].

Sensitivity analysis: Sobol indices

The construction of Sobol indices relies on the decomposition of the variance in the model output Q^5 into contributions from each input X_i. As proposed by Sacks et al. [218], the probabilistic quantity Q is described by a general function f which is driven by the input

---

[5]Q is a single QoI from the vector of probabilistic outputs $\boldsymbol{Q}$

quantities $\boldsymbol{X}$:

$$Q = f\left(\boldsymbol{X}\right) = f\left(X_1, X_2, ..., X_{n_x}\right), \quad X_i \in [0,1]^{n_x}. \tag{3.12}$$

For ease of computation, X_i are normalized to the interval $[0,1]$. Sobol demonstrated [243] that f can be expanded into terms of increasing dimensions

$$f = f_0 + \sum_i f_i + \sum_i \sum_{j<i} f_{ij} + ... + f_{12...n_x}, \tag{3.13}$$

where f_0 is a constant and all terms f must be orthogonal in pairs [223]. Note that this decomposition is not a series decomposition, as it has a finite number of 2^{n_x} terms. Due to the orthogonality constraint, the terms f can be calculated using the conditional expectation $\mathbb{E}[\,\cdot\,|\,\cdot\,]$ of the model output:

$$f_0 = \mathbb{E}[Q] \tag{3.14}$$

$$f_i = \mathbb{E}[Q|X_i] - \mathbb{E}[Q] \tag{3.15}$$

$$f_{ij} = \mathbb{E}[Q|X_i, X_j] - f_i - f_j - \mathbb{E}[Q] \tag{3.16}$$

It can be demonstrated [252] that the variances $\mathbb{V}[f]$ of the terms f are measures of importance for the input $\boldsymbol{X}$. In particular, through expressing $\mathbb{V}[f_i(X_i)]$ by $\mathbb{V}[\mathbb{E}[Q|X_i]]$ in Eq. (3.15) and diving by the total output variance, the *first-order* sensitivity index S_i is obtained:

$$S_i = \frac{\mathbb{V}[\mathbb{E}[Q|X_i]]}{\mathbb{V}[Q]}. \tag{3.17}$$

S_i describes the direct contribution of X_i to the variance of Q. In principle, higher order indices $S_{ij}, ..., S_{ij..n_x}$ can be derived from the expansion (3.13) taking into account interactions between two or multiple inputs. However, for a large input dimension this might become unfeasible. Homma and Saltelli [100] therefore proposed a *total-effect* index $S_{i,T}$

$$S_{i,T} = \frac{\mathbb{V}[\mathbb{E}[Q|X_{\sim i}]]}{\mathbb{V}[Q]}, \tag{3.18}$$

which includes direct effects of X_i and all interaction effects of X_i with $X_{j\neq i}$. As a result, it follows that $S_{i,T} \geq S_i$.

For practical computations, Sobol indices are estimated based on Monte Carlo sampling of the simulation model $\mathcal{M}$ (see Sec. 3.3.2). However, this requires a large sample set to ensure convergence of the variances. Variance-based sensitivity analysis is therefore often used in combination with surrogate models, which are discussed in the next section.

3.4. Surrogate modeling

As pointed out in Sec. 3.3.2, non-intrusive uncertainty quantification requires space filling sampling of the input space Ω in order to assess the probabilistic mapping from Eq. (3.4). However, this direct approach is prohibitive for large scale models such as the simulation of turbulent spray combustion, where each model evaluation requires computing time in $\mathcal{O}(10^4 - 10^6)$ CPU hours. A common strategy to overcome this limitation is to replace the high fidelity simulation model $\mathcal{M}$ by a suitable *surrogate model*[6] $\hat{\mathcal{M}}$, i.e. a model of reduced fidelity which mimics the behavior of the high fidelity model over Ω. Since surrogate models rely on a generalized mathematical description of the input-output mapping rather than physical modeling, computing time reduces drastically. Consequently, a surrogate model yields a cheap-to-evaluate approximation $\hat{q}$ for the QoI q under consideration, taking into account an approximation error $\hat{\epsilon}$:

$$q = \mathcal{M}(\boldsymbol{x}) = \hat{\mathcal{M}}(\boldsymbol{x}) + \hat{\epsilon} = \hat{q} + \hat{\epsilon}, \quad \forall \ \boldsymbol{x} \in \Omega. \tag{3.19}$$

A vast number of surrogate modeling strategies have been proposed and demonstrated in the literature. Overviews, comparisons and recommendations for model selection are given for example in the work of Forrester et al. [67, 68], Booker et al. [18] or Yondo et al. [281]. For the work at hand, surrogate models for the use in uncertainty quantification are categorized into *data-fit* surrogate models and *stochastic spectral expansions*.

Data-fit surrogate models presuppose a model of the form $q = \hat{\mathcal{M}}(\boldsymbol{x}, \boldsymbol{\theta})$ in which $\boldsymbol{\theta}$ is a vector of model parameters that have to be adjusted to accurately fit the output of the high fidelity model. For this purpose, a set of *n observation* or *training points* $\{(\boldsymbol{x}^{(1)}, \boldsymbol{q}^{(1)}), (\boldsymbol{x}^{(2)}, \boldsymbol{q}^{(2)}), ..., (\boldsymbol{x}^{(n)}, \boldsymbol{q}^{(n)})\}$ must be computed from the high fidelity model within Ω. Model parameters $\boldsymbol{\theta}$ are then optimized with respect to the training points. From a mathematical perspective, this is referred to as a *regression problem*.
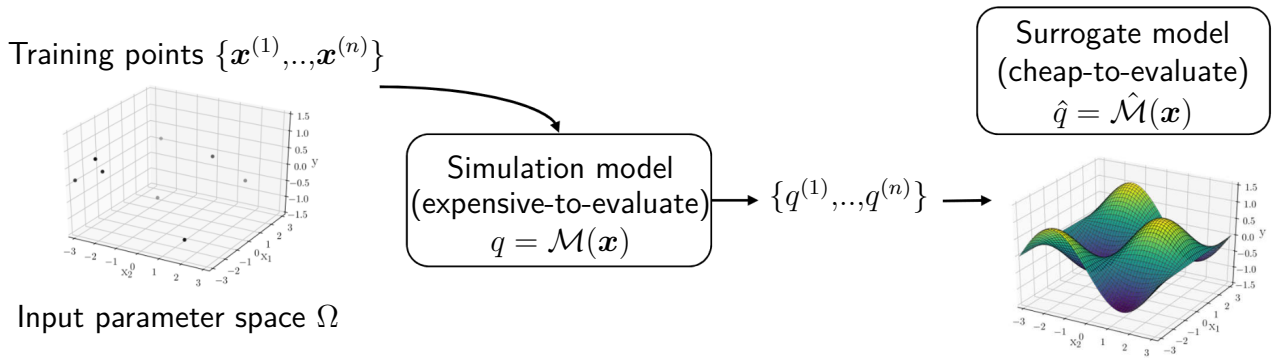
Figure 3.9.: General framework for data-fit surrogate modeling.

---

[6]Also known as *metamodel*, *proxy model* or *emulator* [281].

The number of training points highly depends on the dimension of Ω (i.e. the number of inputs), the number of model parameters, the required accuracy of the surrogate model as well as the nature of the underlying physical problem, and is therefore always case dependent. As a rule of thumb, Jones et al. [109] suggested a minimum number of $n = 10d$ training points for a surrogate model with d inputs. In a further analysis, Loeppky et al. [134] confirmed this recommendation while pointing out that the sensitivity of training data size on the surrogate model quality must always be examined.

Further attention must be paid for the optimal distribution of the training points over the input parameter space in order to extract optimal information about the input-output mapping of the high fidelity model. These distribution rules are referred to as *sampling plans*. Although sampling plans from the well established design of experiments theory [163] can be used, it has been demonstrated [59, 281] that sampling plans with a low spatial discrepancy should be preferred for surrogate construction. They are generally based on sparse quasi-random sampling of Ω through LHS or low discrepancy sequences (e.g. Sobol series, see Sec. 3.3.2).A schematic of the methodology for the construction of data-fit surrogate models is given in Fig. 3.9.

One of the most common and simplest data-fit surrogate models is the class of polynomial regression models [171] which approximate the true data trend over Ω by a global polynomial function. As an extension to polynomial models, Friedman et al. [69] suggested the use of piecewise polynomial splines which adapt to local trends in Ω, making the resulting *Multivariate Adaptive Regression Spline* (MARS) model more flexible than global polynomials. In recent time, methods from the emerging field of *machine learning*[7] have drawn increasing attention for the use in surrogate modeling [85, 120]. They include, amongst others, *support vector machines* [36], *gradient boosting* [70] or *artificial neural networks* [97]. From this category, *Gaussian process regression* [201] is reviewed in depth in the present work.

In contrast to the data-driven approach, stochastic spectral expansions aim at directly reconstructing the functional dependence of the output quantity on the stochastic input [253], which makes them popular for the use in uncertainty quantification and stochastic modeling [172, 204, 205]. For a generalized stochastic expansion, the probabilistic output quantity Q is expressed in terms of a series expansion

$$Q(\boldsymbol{\xi}) = \sum_{k=0}^{\infty} \boldsymbol{s}_k \Psi_k(\boldsymbol{\xi}). \tag{3.20}$$

In this expansion, Ψ_k denotes suitably selected functionals of the random variables $\boldsymbol{\xi}$ (the input quantities) and $\boldsymbol{s}_k$ are deterministic coefficients which need to be calculated. Thus, a spectral, i.e. continuous mathematical representation of Q in terms of $\boldsymbol{\xi}$ is achieved from which statistics about Q can be directly inferred [128].

---

[7]Although there is a large overlap in the theoretical foundation of surrogate modeling and machine learning, the latter specifically relates to purely data-driven modeling of input-output maps, i.e. without connection to a physical model.

The main tasks in the construction of a stochastic spectral expansion are the specification of functionals $\Psi_k(\boldsymbol{\xi})$ depending on the stochastic input $\boldsymbol{\xi}$ and the computation of series coefficients $\boldsymbol{s}_k$ from pointwise evaluations of $\mathcal{M}$. In the present work, spectral expansions based on generalized *polynomial chaos* (PCE) [128, 172] are utilized, in which $\Psi_k(\boldsymbol{\xi})$ consists of a basis of orthogonal polynomials. In the PCE approach, the computation of $\boldsymbol{s}_k$ can be traced back to a multidimensional integration problem, which provides a relation between the expansion accuracy and the required number of high-fidelity model evaluations. Details on PCE construction are given in Sec. 3.4.2.

3.4.1. Gaussian process regression

Gaussian process regression (GPR) describes a popular class of methods for surrogate modeling. Due to the broad definition of the underlying stochastic methodology (i.e. the Gaussian process), GPR can be adjusted to a wide range of statistical modeling problems with arbitrary input dimension. Applications and theoretical foundations trace back to exploration problems in geostatistics where it is also known as *Kriging* [149].

Remark on Bayesian statistical modeling

Gaussian Process Regression is based on a *Bayesian* approach towards statistical modeling [76]. The term *Bayesian* describes the basic assumption that a statistical model is constructed from *prior* knowledge (e.g. the mathematical shape of the model, estimate about model parameters) that is updated by the training data to form a *posterior* model, i.e. a model after having seen the training data. This concept is illustrated in Fig. 3.10 for the example of a model parameter θ. The prior distribution $\mathcal{P}(\theta)$ in Fig. 3.10 (a) represents the initial knowledge or guess about θ, in this case an arbitrary normal distribution. Training data θ_y is observed in Fig. 3.10 (b). Finally, the prior distribution is updated by the training data to form the posterior distribution $\mathcal{P}(\theta|\theta_y)$ using the *Bayes theorem* [47]

$$\mathcal{P}(\theta|\theta_y) = \frac{\mathcal{P}(\theta_y|\theta) \cdot \mathcal{P}(\theta)}{\mathcal{P}(\theta_y)}, \tag{3.21}$$

(a) prior distribution   (b) observation   (c) posterior distribution
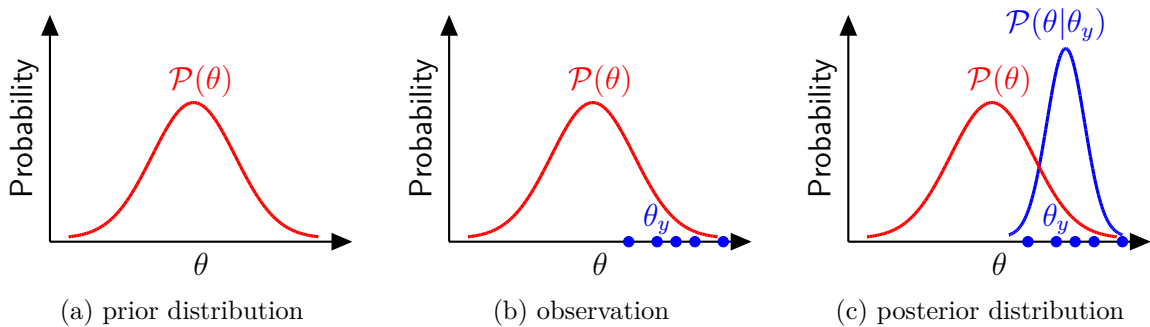
Figure 3.10.: Bayesian inference of a model parameter θ.

where $\mathcal{P}(\theta_y|\theta)$ is the *likelihood* of observing θ_y given θ. It is important to note that although data has been observed, θ is still a stochastic quantity in the Bayesian modeling approach. This is in contrast to the *frequentist* approach to statistical modeling, in which data observation results in a deterministic value for θ that is inferred for example through maximum likelihood estimation of θ_y [23].

Therefore, GPR provides not only a point estimate $\hat{\boldsymbol{q}}$ for an input $\boldsymbol{x}$, but the full distribution function $\mathcal{P}(\hat{\boldsymbol{q}}|\boldsymbol{x})$ from which quantitative information about the local regression quality can be deduced.

Gaussian process

In GPR, the posterior distribution is inferred from a prior consisting of a distribution over functions - the so called *Gaussian process*. A Gaussian process $\mathcal{GP}$ is completely specified by its mean function $m(\mathbf{x})$ and the covariance function $\kappa(\mathbf{x}_i,\mathbf{x}_j)$ which models the dependence between two function values at different input points $\mathbf{x}_i$ and $\mathbf{x}_j$:

$$f(\mathbf{x}) \sim \mathcal{GP}(m(\mathbf{x}),\kappa(\mathbf{x}_i,\mathbf{x}_j)). \tag{3.22}$$

By definition [275], a Gaussian process is a stochastic process[8] in which any point $\mathbf{x} \in \mathbb{R}^d$ is assigned a random variable $f(\mathbf{x})$ and where the joint distribution of a finite number N of these variables $\mathcal{P}(f(\mathbf{x}_1),..,f(\mathbf{x}_N))$ is itself Gaussian. The prior distribution of the Gaussian process therefore reads

$$\mathcal{P}(\mathbf{f}|\mathbf{X}) = \mathcal{N}(\mathbf{f}|\boldsymbol{\mu},\mathbf{K}). \tag{3.23}$$

The vector of prior means $\boldsymbol{\mu}$ is commonly set to zero in order to reduce computational costs [232] in the calculation of posteriors. Thus, the prior distribution is completely determined by the covariance matrix $\mathbf{K}$ which reflects the correlation between all points $\mathbf{X}$ in the Gaussian process computed from the covariance function $\kappa(\mathbf{X},\mathbf{X})$. A key element in the definition of a Gaussian process is therefore the specification of a suitable covariance function or *kernel*. The choice of the kernel is based on assumptions such as smoothness and likely patterns to be expected in the data [232]. From the variety of possible kernels found in the literature, the *squared exponential* covariance function[9] [275] is selected for the present work,

$$\kappa(\mathbf{x}_i,\mathbf{x}_j) = \sigma_f^2 \exp\left(-\frac{1}{2l_c^2}(\mathbf{x}_i - \mathbf{x}_j)^T(\mathbf{x}_i - \mathbf{x}_j)\right). \tag{3.24}$$

It expresses the favorable property that the correlation between two points decays with increasing distance between the points. The two hyper-parameters σ_f (signal variance) and l_c (correlation length-scale) can be varied to adjust the correlation in the prior distribution.

---

[8]Roughly speaking a stochastic process is a generalization of a probability distribution to functions [275].
[9]Also called *radial basis function* kernel.

Regression

After having observed training data $\mathbf{y}$, the prior distribution of the Gaussian process $\mathcal{P}(\mathbf{f}|\mathbf{X})$ can be converted into the posterior distribution $\mathcal{P}(\mathbf{f}|\mathbf{X},\mathbf{y})$. New output $\mathbf{f}_*$ for given new input $\mathbf{X}_*$ is predicted using the *posterior predictive distribution*

$$\mathcal{P}(\mathbf{f}_*|\mathbf{X}_*,\mathbf{X},\mathbf{y}) = \mathcal{N}(\mathbf{f}_*|\boldsymbol{\mu}_*,\boldsymbol{\Sigma}_*) \tag{3.25}$$

which is also Gaussian with mean $\boldsymbol{\mu}_*$ and variance $\boldsymbol{\Sigma}_*$. By definition of the Gaussian process from Eq. (3.23), the joint distribution of observed data $\mathbf{y}$ and predictions $\mathbf{f}_*$ is

$$\begin{pmatrix} \mathbf{y} \\ \mathbf{f}_* \end{pmatrix} \sim \mathcal{N} \left(\mathbf{0}, \begin{pmatrix} \mathbf{K} & \mathbf{K}_* \\ \mathbf{K}_*^{\mathrm{T}} & \mathbf{K}_{**} \end{pmatrix} \right). \tag{3.26}$$

Consequently, $\boldsymbol{\mu}_*$ and $\boldsymbol{\Sigma}_*$ in case of noise free data are given by

$$\boldsymbol{\mu}_* = \mathbf{K}_*^{\mathrm{T}}\mathbf{K}^{-1}\mathbf{y}, \tag{3.27}$$

$$\boldsymbol{\Sigma}_* = \mathbf{K}_{**} - \mathbf{K}_*^{T}\mathbf{K}^{-1}\mathbf{K}_* \tag{3.28}$$

with the covariance matrices calculated using the kernel as

$$\mathbf{K} = \kappa(\mathbf{X},\mathbf{X}), \quad N \times N, \tag{3.29}$$

$$\mathbf{K}_* = \kappa(\mathbf{X},\mathbf{X}_*), \quad N \times N_*, \tag{3.30}$$

$$\mathbf{K}_{**} = \kappa(\mathbf{X}_*,\mathbf{X}_*), \quad N_* \times N_*. \tag{3.31}$$

For further details on derivation and implementation of Eqs. (3.27) − (3.31), the reader is referred to the textbook of Williams and Rasmussen [275]. In addition to Eq. (3.25), hyper-parameters of the kernel (here: σ_f and l_c) have to be adjusted with respect to the training data $\mathbf{y}$. Although this could also be achieved through Bayesian inference, most practical implementations use global optimization to find the set of correlation parameters that maximizes the likelihood of the model given the training data $\mathbf{y}$ [68, 82].

In the context of surrogate modeling, the mean $\boldsymbol{\mu}_*$ represent the approximation $\hat{\boldsymbol{q}}$ at $\boldsymbol{x}$ for which the GP is evaluated. In addition, a confidence interval for $\hat{\boldsymbol{q}}$ can be computed from the trace of $\boldsymbol{\Sigma}_*$.

Illustrative example

An example of Gaussian process regression for noise-free training data with one input dimension is given in Fig. 3.11.

The left column shows samples from the prior distribution (dashed black lines) in combination with the mean (blue line) and 95% confidence interval (gray shade) from the Gaussian process. As mentioned before, $\boldsymbol{\mu}$ is set to zero in the prior. For normal distributions, the 95%

confidence interval is computed as $\boldsymbol{\mu} \pm 1.96\boldsymbol{\sigma}$. Correlation length scale l_c increases from the first to the third row. Clearly, this resembles a decay in frequency of the Gaussian process. Note that this does not affect the overall properties (mean, variance) of the prior.
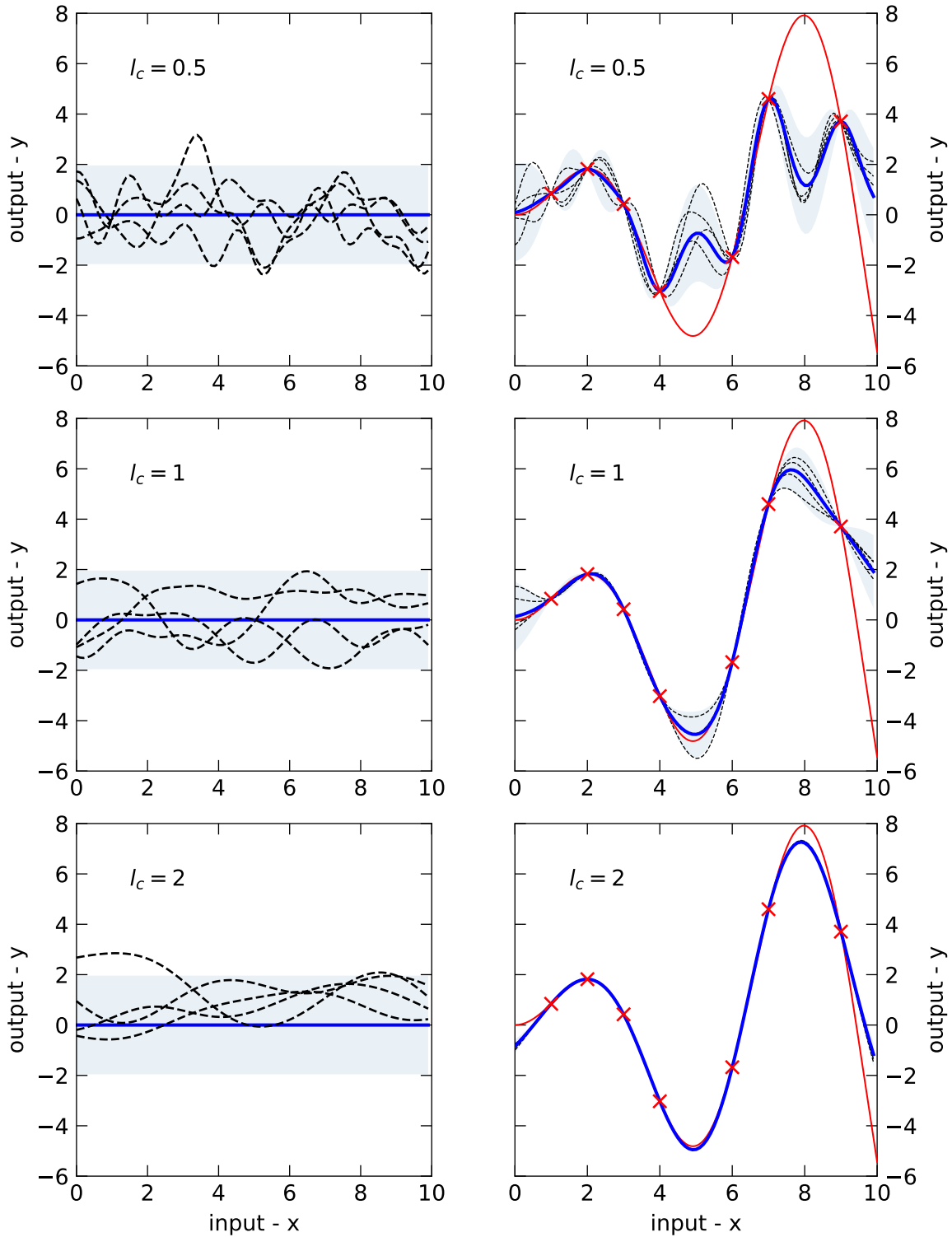
(a) Prior distribution

(b) Predictive posterior distribution

Figure 3.11.: One-dimensional Gaussian process regression with different correlation length scales l_c. GP samples (- - -), GP mean (—), GP 95% CI (—), training data (×), true function (—)

In the right column, training data (red crosses) is observed by the corresponding prior and the mean and confidence interval from the resulting predictive posterior distribution is shown. Since the training data is noise-free, the Gaussian process is fixed at these points and the variance vanishes. For the lowest correlation length scale (first row), the posterior distribution demonstrates a strong tendency towards the prior mean and variance between the training data points, e.g. at $x = 5$ and $x = 8$. As a consequence, the confidence interval increases and the mean notably deviates from the the underlying true function (red line). With increasing correlation length scales (row two and three), the true function is met with increasing precision and the confidence intervals become more narrow between training points. Evidently, the correlation length scale amplifies the fundamental assumption of the covariance function that if points $\mathbf{x}_i$ and $\mathbf{x}_j$ are similar by the kernel, the function values $f(\mathbf{x}_i)$ and $f(\mathbf{x}_j)$ at these points can be expected to be similar, too.

3.4.2. Polynomial chaos expansion

This section focuses on the non-intrusive application of Polynomial Chaos Expansion, consisting of the selection of a suitable *polynomial chaos* basis, the computation of series coefficients from high-fidelity model evaluations and the post-processing of the PCE to obtain statistical measures.

Polynomial chaos

The original polynomial chaos (PC) traces back to the work of Wiener [273] who demonstrated that any random variable Q with finite variance can be represented as a series expansion

$$Q = a_0 \Gamma_0 + \sum_{i_1=1}^{\infty} a_{i_1} \Gamma_1(\xi_{i_1}) + \sum_{i_1=1}^{\infty} \sum_{i_2=1}^{i_1} a_{i_1 i_2} \Gamma_2(\xi_{i_1}, \xi_{i_2}) \tag{3.32}$$
$$+ \sum_{i_1=1}^{\infty} \sum_{i_2=1}^{i_1} \sum_{i_3=1}^{i_2} a_{i_1 i_2 i_3} \Gamma_3(\xi_{i_1}, \xi_{i_2}, \xi_{i_3}) + ...,$$

where $\{\xi_i\}_{i=1}^{\infty}$ is a set of independent standard Gaussian random variables on a support Ω. Γ_p then represents the *Wiener PC* of order p, and $a_{()}$ are real-valued coefficients. Eq. (3.32) may be rewritten more compactly in terms of multivariate polynomials $\mathbf{\Psi}_k$ and corresponding coefficients α_k,

$$Q = \sum_{k=0}^{\infty} \alpha_k \mathbf{\Psi}_k \left(\xi_1, \xi_2, ... \right). \tag{3.33}$$

Due to the orthogonality constraint on $\mathbf{\Psi}_k$ (or Γ_p) and the fact that each $\xi_{()}$ is Gaussian, it follows [273] that $\mathbf{\Psi}_k$ must be a basis of multivariate Hermite polynomials [74].

The concept of the Wiener PC was further generalized by Xiu et al. [279] to account for a broad range of possible distributions ξ. They derived corresponding orthogonal polynomials $\mathbf{\Psi}_k$ for standard probability distributions ξ using the family of hypergeometric orthogonal polynomials known as the *Askey scheme* [5]. Table (3.1) summarizes the most common

Table 3.1.: Standard continuous probability distributions ξ and corresponding Askey scheme
of continuous orthogonal polynomials $\Psi_k(\xi)$.

Distribution ξ	Density $p_\xi(x)$	Polynomial $\Psi_k(\xi)$	Support range
Normal	$e^{-x^2/2}$	Hermite $He_k(\xi)$	$]-\infty;\infty[$
Uniform	$\frac{1}{2}$	Legendre $P_k(\xi)$	$[-1;1]$
Exponential	e^{-x}	Laguerre $L_n(\xi)$	$[0;\infty[$
Beta	$\frac{(1-x)^\alpha(1+x)^\beta}{2^{\alpha+\beta+1}B(\alpha+1,\beta+1)}$	Jacobi $P_n^{(\alpha,\beta)}(\xi)$	$[0;\infty[$

distributions and their polynomials in the Askey scheme. The resulting *generalized PC* (gPC) enables the use of PCE in UQ problems, where ξ is interpreted as a random variable for the input and Ψ_k is selected according to the probability distribution of the uncertain input (see Sec. 3.3.1).

In practical computations, the infinite series from Eq. (3.33) is truncated in both order p and dimension n to represent the expansion of an uncertain output $f(\boldsymbol{\xi})$:

$$Q = f(\boldsymbol{\xi}) = \sum_{k=0}^{P} \alpha_k \boldsymbol{\Psi}_k\left(\xi_1,\xi_2,...,\xi_n\right) = \sum_{k=0}^{P} \alpha_k \boldsymbol{\Psi}_k\left(\boldsymbol{\xi}\right). \tag{3.34}$$

While the dimension n relates to the number of input variables, the *cardinality P* of the PCE, i.e. the number of terms in the resulting finite PCE, corresponds to

$$P + 1 = \frac{(n+p)!}{n!p!}. \tag{3.35}$$

Computation of the expansion coefficients

For the computation of the expansion coefficients α_k in Eq. (3.34), two different approaches have been proposed in the literature, namely *projection* methods [80] and *regression* methods [29]. The former one involves multi-dimensional numerical integration whereas the latter utilizes linear regression. In the present dissertation, only projection methods are applied and discussed, for a synopsis on regression in PCE, the reader is referred to the work of Sudret [253].

Due to the orthogonality of the PC expansion, each coefficient α_k is simply the projection of the response Q onto the k-th dimension of $\boldsymbol{\Psi}_k$ [253]. The spectral projection method exploits this property to extract each coefficient. Taking the inner product with respect to $\boldsymbol{\Psi}_k$ of both sides in Eq. (3.34) yields

$$\alpha_k = \frac{\langle f(\boldsymbol{\xi}), \boldsymbol{\Psi}_k \rangle}{\langle \boldsymbol{\Psi}_k, \boldsymbol{\Psi}_k \rangle}, \tag{3.36}$$

in which $\langle \bullet, \bullet \rangle$ is the inner product defined by

$$\langle u, v \rangle = \int_{\boldsymbol{\Omega}} u(\boldsymbol{\xi}) v(\boldsymbol{\xi}) \mathcal{P}(\boldsymbol{\xi}) \, \mathrm{d}\boldsymbol{\xi}, \tag{3.37}$$

where $\boldsymbol{\Omega}$ denotes the support spanned by $\boldsymbol{\xi}$. For polynomial bases from the Askey scheme, $\langle \boldsymbol{\Psi}_k, \boldsymbol{\Psi}_k \rangle$ is known analytically, such that only the numerator from Eq. (3.36) requires further analysis.

By applying definition (3.37), Eq. (3.36) can be rewritten as

$$\alpha_k = \frac{1}{\langle \boldsymbol{\Psi}_k, \boldsymbol{\Psi}_k \rangle} \int_{\boldsymbol{\Omega}} f(\boldsymbol{\xi}) \boldsymbol{\Psi}_k(\boldsymbol{\xi}) \mathcal{P}(\boldsymbol{\xi}) \, \mathrm{d}\boldsymbol{\xi}. \tag{3.38}$$

Therefore, the primary computational effort resides in evaluating the multidimensional integral from Eq. (3.38) which is achieved using efficient numerical integration methods. The order of accuracy of the numerical integration directly provides a measure for the accuracy of the PCE. Obviously, an increased order of accuracy requires an increased number of function evaluation $f(\boldsymbol{\xi})$, i.e. evaluations of the original model $\mathcal{M}$.

In general, multidimensional quadrature rules are derived through a tensor product of one-dimensional quadrature rules, e.g. Gaussian quadrature, Clenshaw-Curtis or Genz-Keister [39]. However, it is observed that quadrature rules from full tensorization are non-optimal in the sense that their degree of exactness could actually be achieved using a lower number of integration nodes [128], which resembles fewer evaluations of the high-fidelity simulation model. This allows for a reduction of the fully tensorized quadrature rule to a so called *sparse grid* while preserving the desired level of accuracy. Accordingly, sparse grid tensorization as proposed by Smolyak [242] has become popular for the use in PCE [118, 128] and is also used for the work at hand.

For a further enhancement of computational efficiency, *nested* quadrature rules are advisable for the construction of multi-dimensional quadrature methods. In this context, nested refers to the favorable property that integration points for a rule with order $\mathcal{O}(n)$ are a subset of the integration points for order $\mathcal{O}(n+1)$ which enables efficient adaptation of PCE accuracy.

Fig. 3.12 illustrates the resulting integration points in two and three dimensions when combining Smolyak sparse grid tensorization with a nested Fejer rule [39]. Two consecutive grid levels $L = 2$ and $L = 3$ are displayed in Fig. 3.12 (a) and (b), respectively. The grid levels corresponds to different orders of accuracy for the multi-dimensional integration. Clearly, the $L = 2$ points are a subset of the $L = 3$ points due to the nested nature of the integration rule. In contrast, Fig. 3.12 (c) displays the fully tensorized Fejer rule for the $L = 3$ case, highlighting the drastic reduction in integration points by using a sparse grid.

Post-processing of the PCE

After computation of the PCE coefficients, first and second moment of Q can be calculated directly without further sampling. Due to the orthogonality of the PC expansion, analytical expressions for the expectation and variance of Q are given by

$$\mathbb{E}[Q] = \sum_{k=0}^{P} \alpha_k \langle \boldsymbol{\Psi}_0, \boldsymbol{\Psi}_k \rangle = \alpha_0, \tag{3.39}$$

(a) Sparse grid L=2   (b) Sparse grid L=3   (c) Fully tensorized L=3
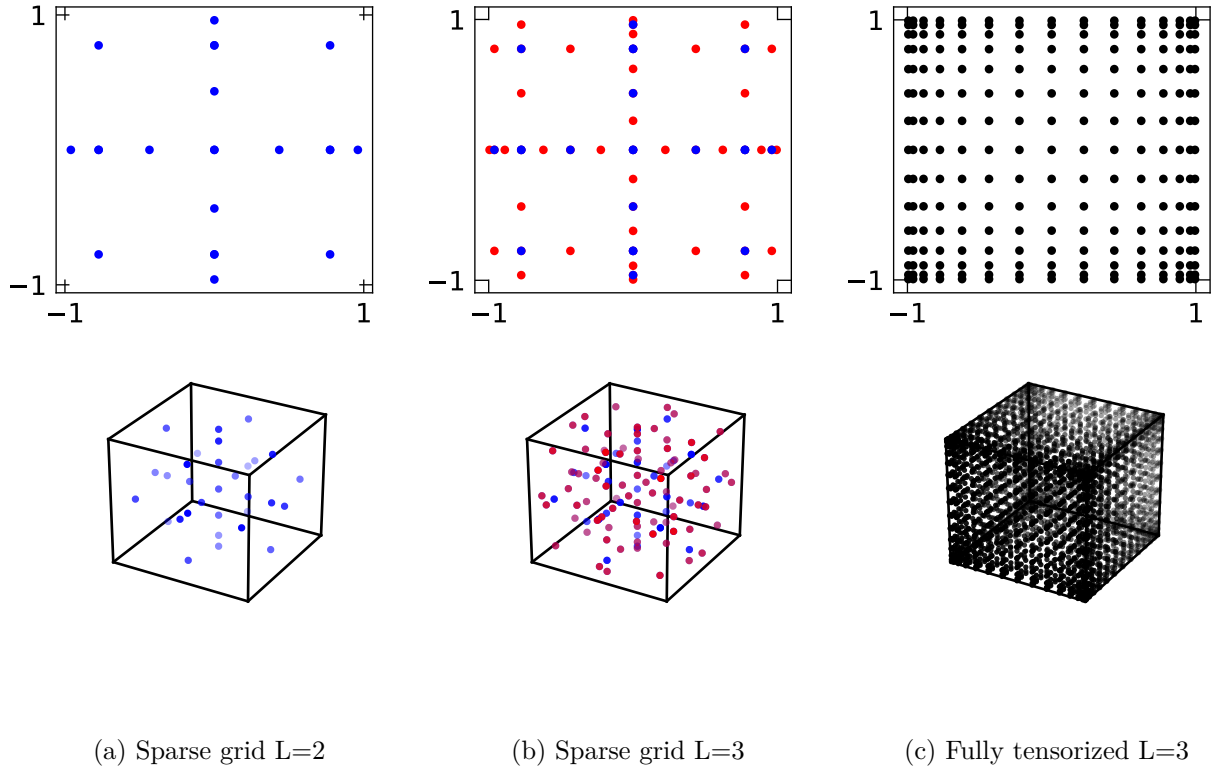
Figure 3.12.: Two and Three-dimensional quadrature points of a Smolyak sparse grid using a nested Fejer rule. Level 2 points (•), additional Level 3 points (•), Fully tensorized points (•).

$$\mathbb{V}[Q] = \mathbb{E}[(Q - \mathbb{E}[Q])^2] = \sum_{k=1}^{P} \alpha_k^2 \langle \boldsymbol{\Psi}_k, \boldsymbol{\Psi}_k \rangle. \tag{3.40}$$

Although similar expressions can be derived for higher moment of Q, full distributions or probabilities are usually estimated by means of sampling strategies (see Sec. 3.3.2) [128], i.e. by sampling of $\boldsymbol{\xi}$ with respect to its density $\mathcal{P}(\boldsymbol{\xi})$ followed by the evaluation of the PC series from Eq. (3.34) at the respective sample point.

Note that Eqs. (3.39) and (3.40) also enable the direct computation of the Sobol indices as introduced in Eqs. (3.17) and (3.18) as a post-processing step of the PCE coefficients without further sampling [252].

4. Delft Spray in Hot Coflow Flame

The aim of this chapter[1] is to apply the previously introduced methods for probabilistic modeling and uncertainty quantification to a simple, well defined test case for spray combustion involving a single component liquid fuel with well-documented physical properties. This allows for a detailed analysis and comparison of the methods for sensitivity analysis and surrogate modeling while keeping the modeling demands and associated uncertainties at a moderate level.

First, a deterministic reference LES is conducted to validate the selected models. Based on these results, the numerical setup is simplified to RANS modeling in order to reduce computing time and enable detailed testing of different surrogate modeling methods for uncertainty propagation. Key uncertainties in the input parameters of the simulation model as well as numerical uncertainties are identified followed by a sensitivity analysis to reduce the parameter space of uncertain inputs. For the propagation of uncertainties, Gaussian Process based surrogate modeling and Polynomial Chaos Expansion are applied and reviewed in-depth.

4.1. Test case description

The *Delft Spray in Hot Coflow* Flame (DSHC) [213] is selected as a test case for the following investigations. Originally designed as a generic laboratory scale burner to study fundamental aspects of liquid fuel combustion under MILD conditions, it provides an extensive database of experimental data for both gaseous and dispersed phase over the reaction zone.

Moderate or Intense Low-oxygen Dilution (MILD) [24] combustion has drawn attention in recent years due to its potential for a drastic reduction in NO_x emissions [277]. This combustion concept is characterized by a high temperature and intense dilution of the oxidizer stream with combustion products, resulting in a moderate temperature increase during oxidation. In technical combustors, dilution is typically realized through either staged combustion or recirculation of the combustion productions within the combustion chamber [278].

Figure 4.1 provides a schematic of the DSHC burner. The burner consists of a cylindrical coflow generator with a diameter of 160 mm. The coflow is fed by the lean combustion of Dutch Natural Gas (DNG) to increase the airflow temperature and dilute the air with combustion products prior to the primary combustion zone. Resulting temperature and oxygen concentrations mimic the oxydizer properties found in a combustor operating under MILD conditions. For the primary flame, liquid ethanol is supplied through a commercial

---

[1]Parts of this chapter have been published in [55], [59] and [58]
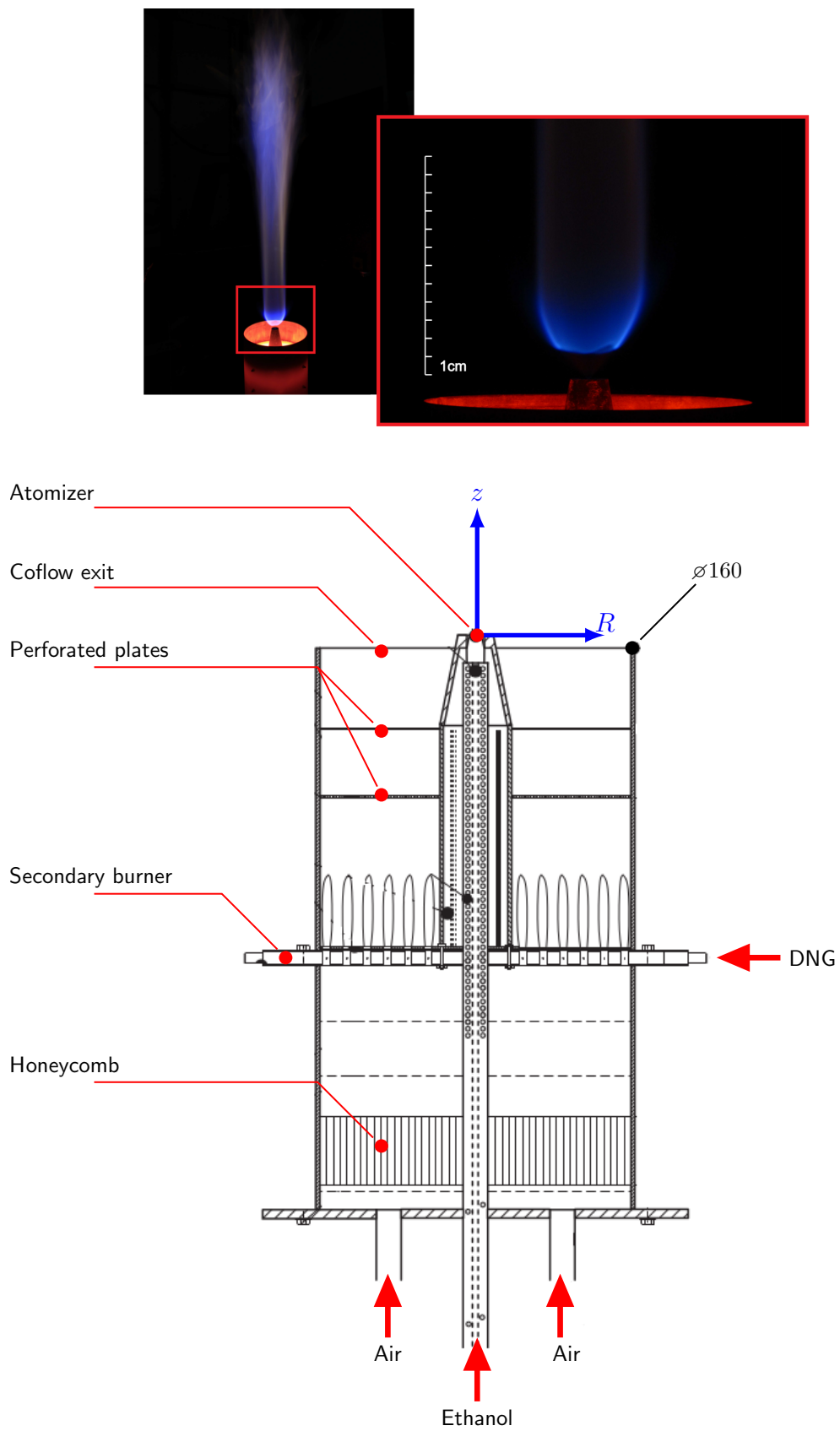
Figure 4.1.: Schematic of the DSHC burner and flame image for the H_{II} case (adapted from Rodrigues et al. [212]).

Table 4.1.: Mean operating conditions of DSHC $\mathbf{H_{II}}$.

Case	T_{cf} [K]	U_{cf} [m s^{-1}]	Y_{O_2} [%]	I_{cf} [%]	$m_{liq.}$ [kg h^{-1}]	p_{inj} [bar]
H-II	1400	2.5	9.9	2.0	1.46	11.5

hollow cone pressure swirl atomizer (Delavan WDA 0.5 GPH) installed in the center of the coflow generator. The atomizer forms a fine spray of ethanol droplets which quickly evaporate in the hot coflow and feed a stable lifted-off flame above the burner. In the literature [139, 213], the atomizer is reported to have a 0.21 mm exit orifice and a nominal spray cone angle of 60°. For further reference, a quasi-cylindrical (z,R) coordinate system is included in Fig. 4.1.

The DSHC flame was characterized over a variety of operating conditions using laser diagnostics [32, 213]. This included Coherent Anti-Stokes Raman Scattering (CARS) for gas phase temperature as well as Laser Doppler Anemometry (LDA) and Phase Doppler Anemometry (PDA) for droplet size and velocities. Measurement data was collected along radial profiles through the reaction zone at different z-positions above the atomizer. In addition, properties of the coflow after primary combustion were reported at $z = 0$ mm.

From the experimental database, the so-called $\mathbf{H_{II}}$ case is selected. Mean operating conditions are summarized in Tab. 4.1. Properties with subscript $()_{cf}$ refer to the coflow after primary combustion. Low coflow velocity and moderate turbulence intensity result in a moderate Reynolds number which enables an efficient use of both LES and RANS methods.

The DSHC $\mathbf{H_{II}}$ case was widely adopted in the simulation community. In a first study, Ma et al. [138] used RANS simulations with a Flamelet Generated Manifold (FGM) combustion model. For a similar setup, Jamali [106] reported results from a variation of spray boundary conditions. Gallot-Lavallée et al. [73] conducted an LES of different DSHC cases with a stochastic fields combustion model. In further LES/FGM studies [140–142], Ma et al. investigated the fundamental flame structure and the stabilization mechanism of the DSHC flame. The LES reported by Enderle et al [55, 57] contribute to the results discussed in Sec. 4.3.

4.2. Numerical setup

For all simulations, the FRC combustion model in combination with a detailed reaction mechanism for ethanol oxidation [214] is used. The mechanism includes 38 species and 228 reactions. The assumed PDF model provides turbulence-chemistry interaction in the RANS simulation, whereas in the LES it is used for the subgrid temperature fluctuations. Vaporization of liquid ethanol (C_2H_5OH) is modeled by the single component vaporization model.
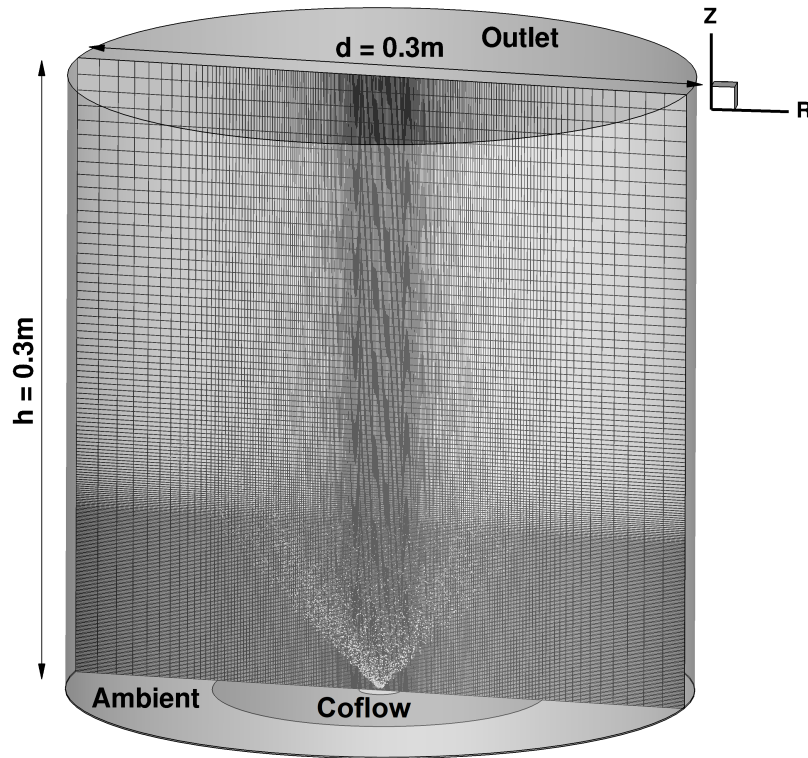
Figure 4.2.: Computational domain for the LES simulation and depiction of the grid in a cut
plane. Dots indicate the spatial extent of the spray.

4.2.1. Computational domain and spatial discretization

In the computational domain, only the region above the atomizer is considered while the
secondary DNG burner is not simulated explicitly. Properties of the coflow after secondary
combustion are prescribed through a boundary condition based on the radial profiles of
temperature and its fluctuations, velocity components, turbulence properties and gas phase
composition from the experimental characterization (see Sec. 4.2.2).

LES

The computational domain for the LES is shown in Fig. 4.2 and consists of a cylinder with
diameter $d = 0.3$ m and height $h = 0.3$ m. The fully structured grid comprises approximately
$1.565 \cdot 10^6$ elements in an O-Grid topology. As evident from the depiction of the grid in
Fig. 4.2, strong clustering of cells is realized in the liquid injection region and alongside the
reaction zone. Cell spacing along the axial (Δz) and radial (ΔR) direction is shown in Fig. 4.4
(a).

RANS

Due to the statistical rotational symmetry of the flame [213], the computational domain for
the RANS simulations is reduced to an axisymmetric 20° wedge. A region of 300 mm axial
and 150 mm radial extent above the atomizer is included (see Fig. 4.3). For examination
of the discretization accuracy, three different grids are considered, all relying on the same
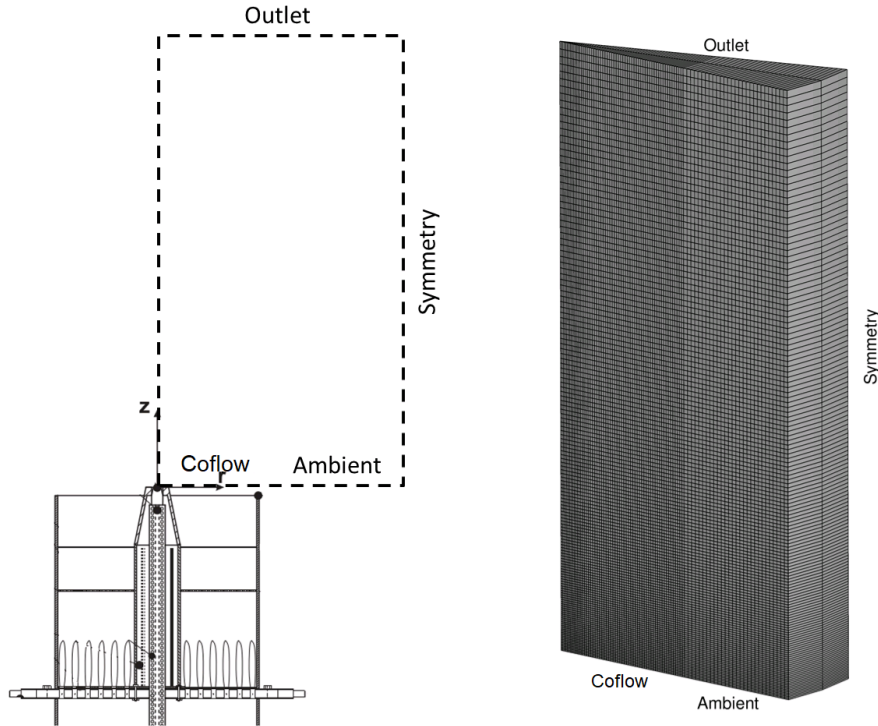
Figure 4.3.: Sketch of the computational domain and grid for the RANS simulations. Periodic symmetry around the z-axis

fully structured, orthogonal grip topology in analogy to the LES grid. The reference grid consists of approximately $80 \cdot 10^3$ elements, while the coarse and the fine grid incorporate half and twice the number of elements, respectively. Grid refinement strategies proposed by Roache [210] were followed in order to keep main characteristics of the grid consistent over the three levels of resolution. Again, cell spacing is shown in Fig. 4.4 (b).

4.2.2. Gas phase boundary conditions

Since both simulations comprise a radial domain larger than the burner, the coflow inlet is surrounded by an ambient inflow with $U = 0.1 \ \mathrm{m\,s^{-1}}$ to enhance numerical stability. The coflow from the secondary burner is modeled as a velocity inlet where inlet quantities such as temperature and species composition are set according to the experimental database. Figure E.1 in Appendix E depicts the radial distribution of these quantities. In the LES, all other cylindrical areas are set as outflow with static pressure set to zero whereas in the RANS simulations, boundary conditions are prescribed as shown in Fig. 4.3.

Modeling of the inlet temperature fluctuations for LES

As evident from the experimental data in Fig. E.1 in the appendix, the secondary DNG burner causes strong fluctuations in temperature at the coflow exit. Since the secondary burner is not included in the computational domain, temporal fluctuations in temperature and velocity at the coflow inlet must be modeled for the use in LES in order to accurately capture the temperature fluctuations within the flame. For this purpose, the inlet is subject to stochastic,

(a) LES   (b) RANS
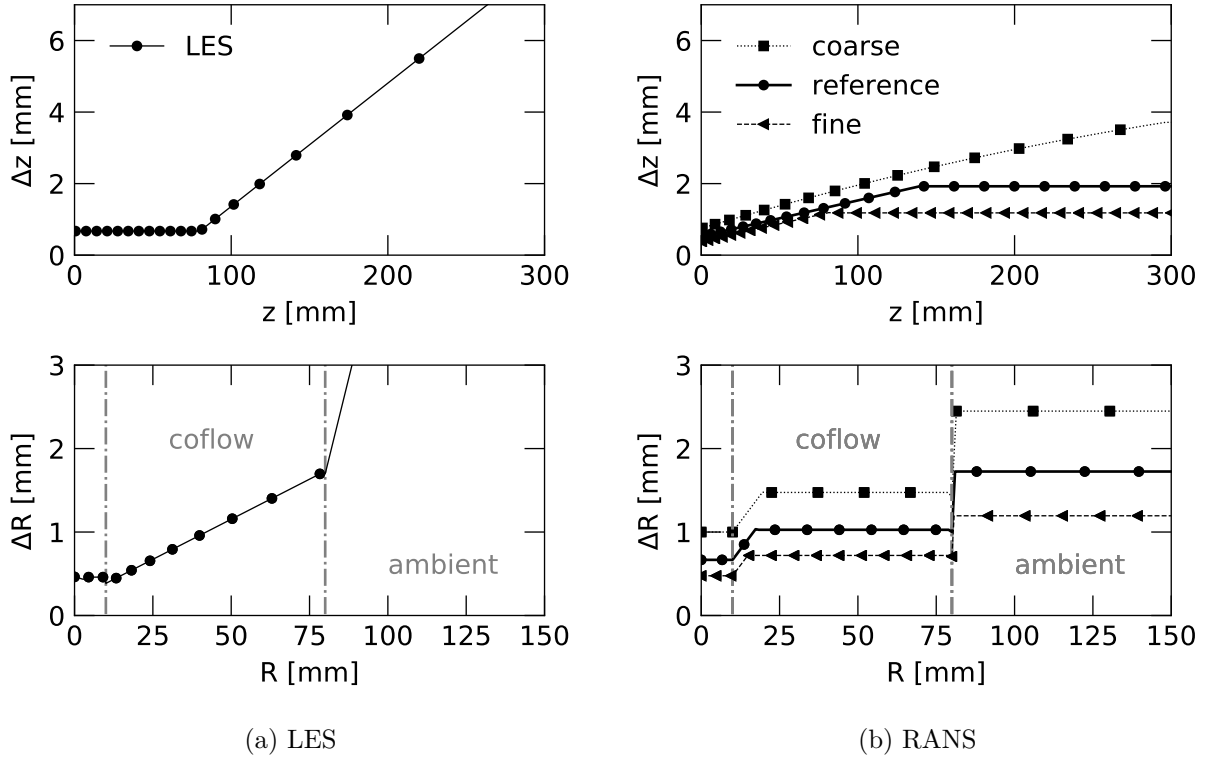
Figure 4.4.: Grid cell spacing along the axial (Δz) and radial direction (ΔR) in the used structured grids.

time-correlated forcing for temperature and velocity. This forcing approach realizes turbulent decay in time. Spatial decorrelation of the turbulent signals due to shear effects is neglected in the forcing due to the very low bulk velocity of $2.5 \, \mathrm{m \, s^{-1}}$. Time-coherent, stochastic forcing is realized with a first order Langevin equation [192] for which integral time-scales are inferred from the experimental characterization of the coflow.

Details of the stochastic forcing approach were reported by Enderle et al. in [57]. A summary is given in Appendix C. Note that in the RANS simulations, experimental data for inlet temperature fluctuations serve as boundary conditions for the assumed PDF turbulence-chemistry interaction model.

4.2.3. Spray boundary conditions

Spray boundary conditions are reconstructed from experimental data as described in Sec. 2.4.2. PDA data at $z = 8$ mm is projected onto an injection disk with diameter $d_{in} = 1$ mm at a distance of $z_{in} = 1$ mm from the actual atomizer orifice which defines the boundary condition for the liquid droplets. The distance z_{in} resembles the mean liquid sheet breakup length of the pressure-swirl atomizer under the given conditions and is derived from preliminary calculations with the LISA primary breakup model [234]. In the RANS simulation, the injection disk reduces to a 20° wedge according to the computational domain.

As reported by Rodrigues et al. [213], the atomization mechanism of the pressure-swirl atomizer is greatly influenced by the hot flue gases of the secondary burner. Due to the high
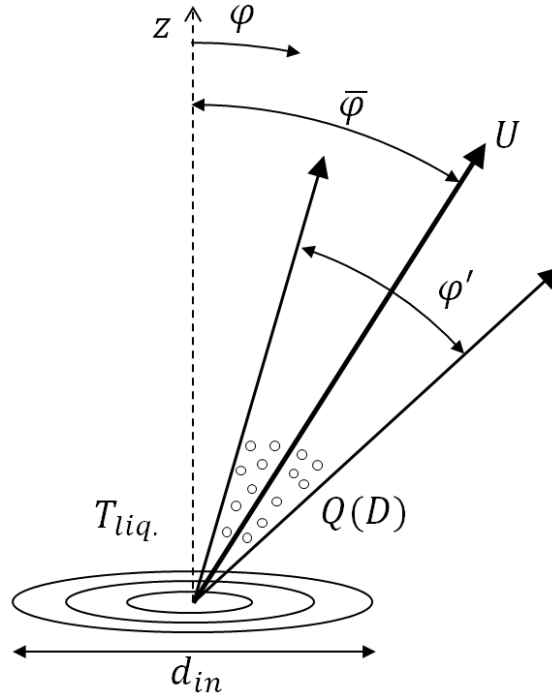
Figure 4.5.: Spray boundary condition and input parameters at the injection plane.

Table 4.2.: Nomenclature and nominal values for parameters of the droplet boundary condition. RR = Rosin-Rammler.

D_0:	Mean droplet diameter in the RR distribution	42.5	[µm]
U_D:	Starting velocity of fuel droplets	35.7	$[\mathrm{m\,s^{-1}}]$
$\bar{\varphi}$:	Mean trajectory angle of droplets	30	[°]
φ':	Trajectory dispersion angle	20	[°]
$\bar{T}_{liq}$:	Starting temperature of fuel droplets	301	[K]
q:	Spread of the RR distribution	3	[−]

coflow temperature, flash boiling atomization phenomena are present causing a shortened liquid breakup length, smaller droplet size and a wider radial distribution, as pointed out by Ma et al. [140]. Therefore, the mean trajectory angle $\bar{\varphi}$ of the droplets is augmented with a dispersion angle φ' which was inferred from calibration against the experimental data. Due to the absence of detailed data, a constant absolute droplet starting velocity U_D and a liquid droplet temperature T_{liq} is set. The droplet size spectrum of the polydisperse spray is modeled by a Rosin-Rammler distribution (see Eq. (2.56)). An illustration of the boundary condition and its quantities at the injection disk is given in Fig. 4.5. Table 4.2 provides a nomenclature for parameters of the spray boundary condition and the nominal values for the deterministic reference simulation.

4.3. Deterministic reference simulation

For the LES, a constant timestep of $\Delta t = 10^{-5}$ s is set resulting in local CFL numbers significantly below unity. The simulation is initialized over 10 characteristic flow through times $\tau_h = h/\bar{U}_{\mathrm{cf}}$ and averaged over additional $20\tau_h$. The same initializing and averaging intervals are applied for the liquid phase in which droplet statistics are recorded by means of registration planes at different heights above the atomizer. In addition to averaging in time, simulation data is averaged circumferentially in post-processing, which results in symmetric profiles for the mean data.

4.3.1. Flame structure

An overview of the temperature field in the gas phase is given in Fig. 4.6 by means of transient and time-averaged contours in the $z - R$ plane. Black scatter dots indicate liquid fuel droplets (magnified). In the transient snapshot (Fig. 4.6 (a)), a dense droplet region is observable close to the atomizer exit plane at $z = 0$ mm. Further upstream, the flame stabilizes in the outer

(a) Transient   (b) Time-averaged
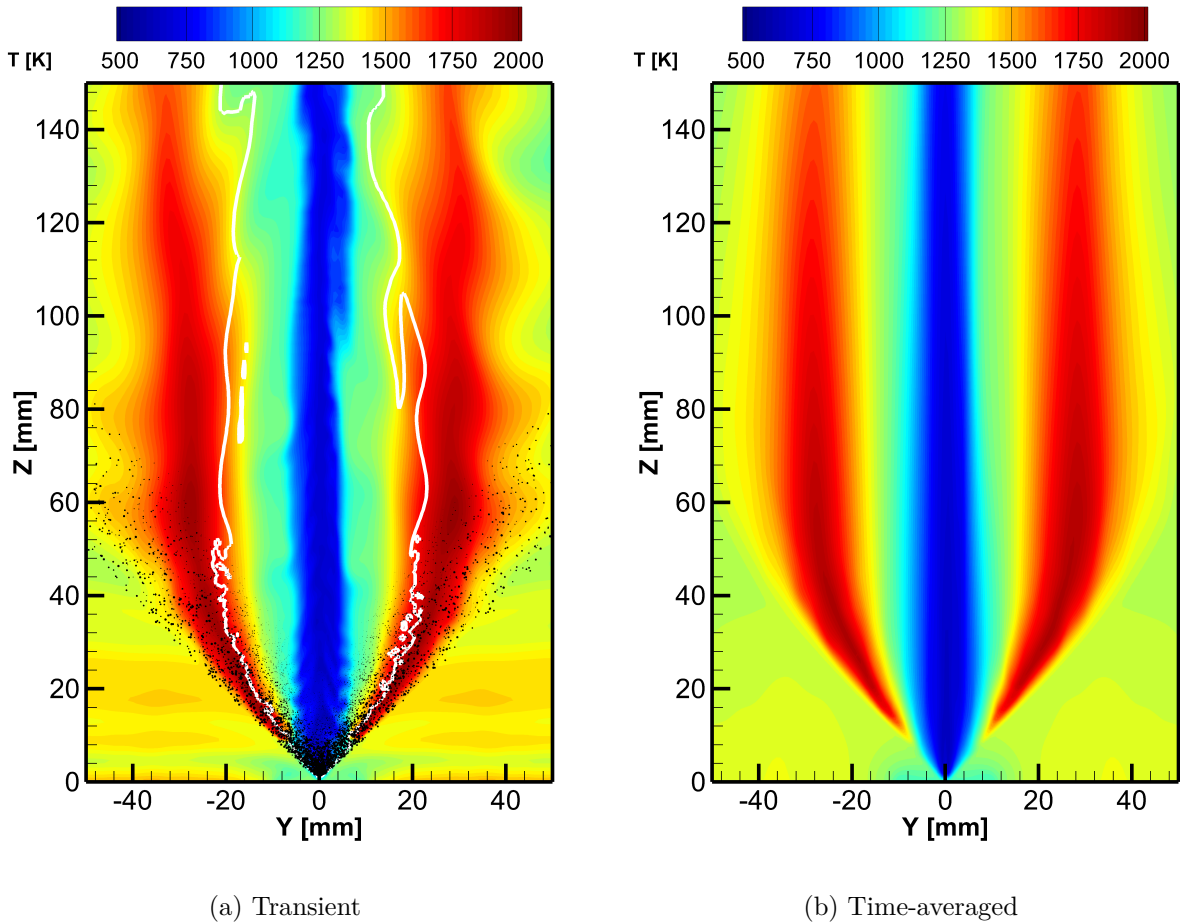
Figure 4.6.: Gas phase temperature of the DSHC H-II flame. Black dots represent liquid droplets. The white iso-line indicates the stochiometric mixture fraction.

flank of the evolved spray cone, causing a clearly lifted flame. The white iso-line represents the stochiometric fuel/oxidizer mixture fraction, separating the flame front from the inner

fuel rich region. Few droplets are able to escape from the flame front above $z = 40$ mm due to their high initial momentum. Along the center line temperature in the gas phase drops significantly below the coflow temperature as a result of strong droplet evaporation.

From the time-averaged temperature field in Fig. 4.6 (b) a mean lift-off height of the flame of $h_{\mathrm{LO}} = 11$ mm is deduced, based on the first axial position where the temperature in the flame exceeds the coflow temperature of $\overline{T}_{cf} = 1400$ K. This is slightly below the experimental value of $h_{\mathrm{LO,exp.}} = 13$ mm. However, in the experiments the lift-off height was derived from a more qualitative criterion based on the average flame luminescence from photographs [212].

4.3.2. Gas phase results

A comparison between profiles of mean temperature from LES and experiment at different heights above the atomizer is given in Fig. 4.7. The general trend of the experimental data is accurately reproduced by the simulation, peak and minimum temperature magnitude and position are in good agreement. At the most downstream positions, the simulation predicts a higher flame spread leading to radial temperature deviations. This tendency was also reported by [73] and [142].

At all axial positions, three characteristic features of the flame are visible [141]:

- Gas phase temperature drops below the coflow temperature along the center line ($R = 0$ mm) due to strong evaporation of fuel droplets and therefore absorption of enthalpy from the gas field

- An inner and outer flame front characterized by strong radial gradients in temperature

- Maximum temperature increase $\Delta T = T_{\max} - \overline{T}_{cf} = 625$ K with respect to the inlet temperature stays below the self-ignition temperature $T_{si} = 706$ K of the mixture

The fact that $\Delta T < T_{si}$ and $T_{in} = \overline{T}_{cf} > T_{si}$ verifies that the flame is operating in the MILD combustion regime as defined by Cavaliere et al. [24].
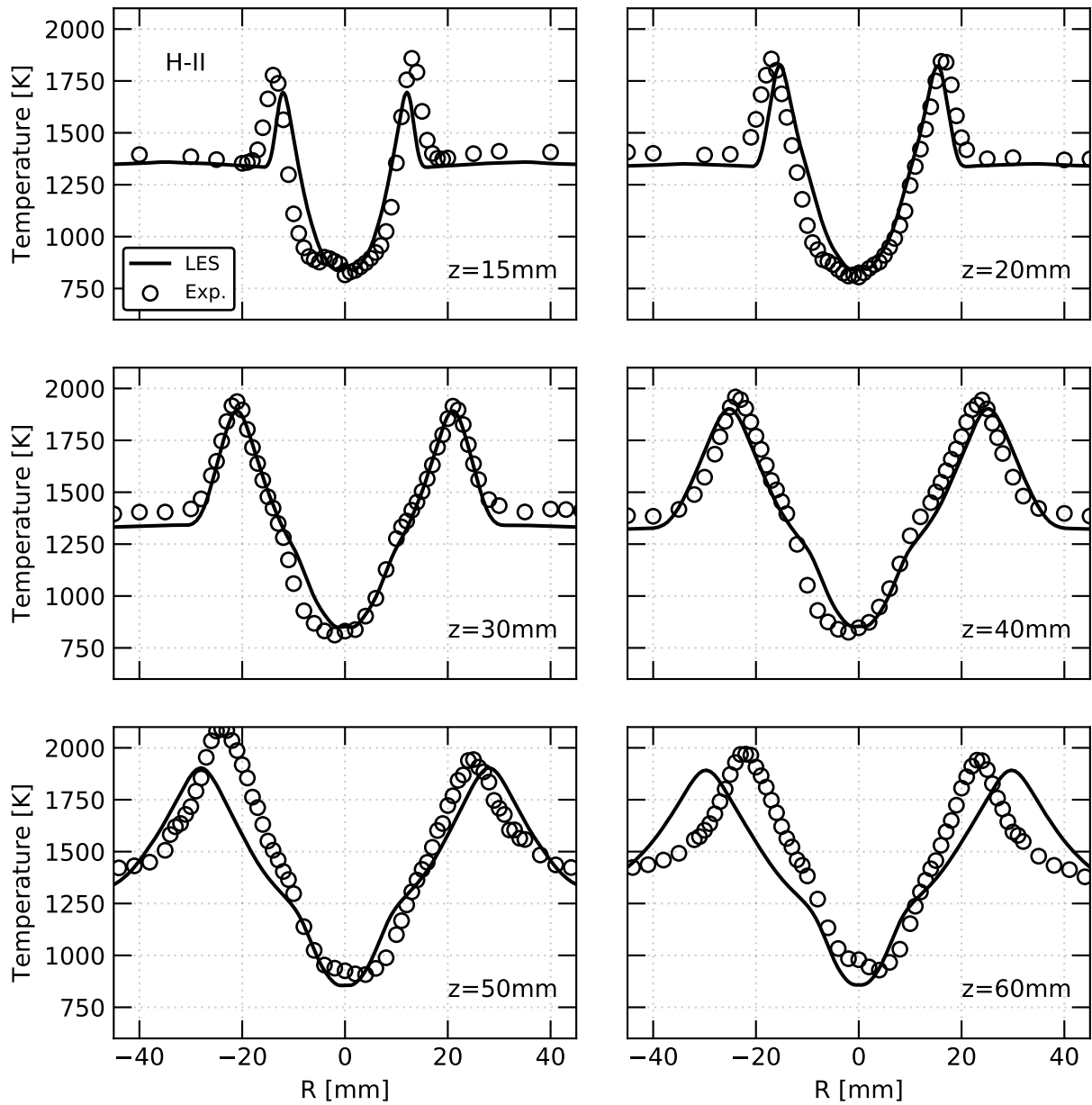
Figure 4.7.: Radial profiles of mean gas temperature at different heights above the atomizer. Atomizer exit at $z = 0$ mm.
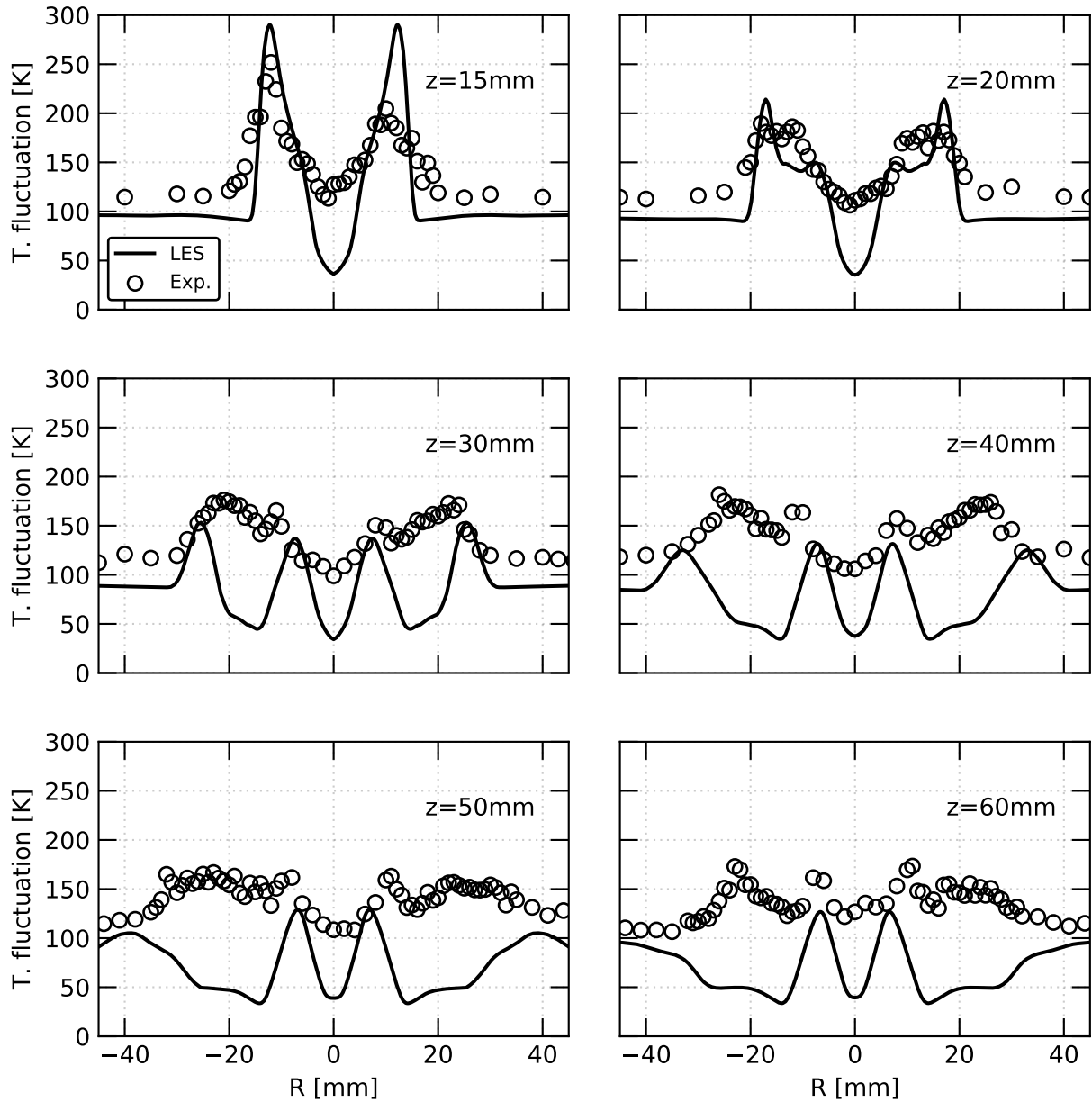
Figure 4.8.: Radial profiles of RMS gas temperature fluctuations at different heights above the atomizer. Atomizer exit at $z = 0$ mm.

Results for Root Mean Square (RMS) temperature fluctuations are displayed in Fig. 4.8. As evident from the plots, the considerable high background level of fluctuations induced by the secondary burner is met by the simulation. This verifies the modeling of the inlet temperature fluctuations through the stochastic Langevin equation. At the first two axial positions the peaks in fluctuation at the flame edge are clearly visible in the simulation results. With increasing axial distance from the atomizer, the LES matches the general trend of fluctuations with two characteristic peaks but underestimates the magnitude in the flame region.
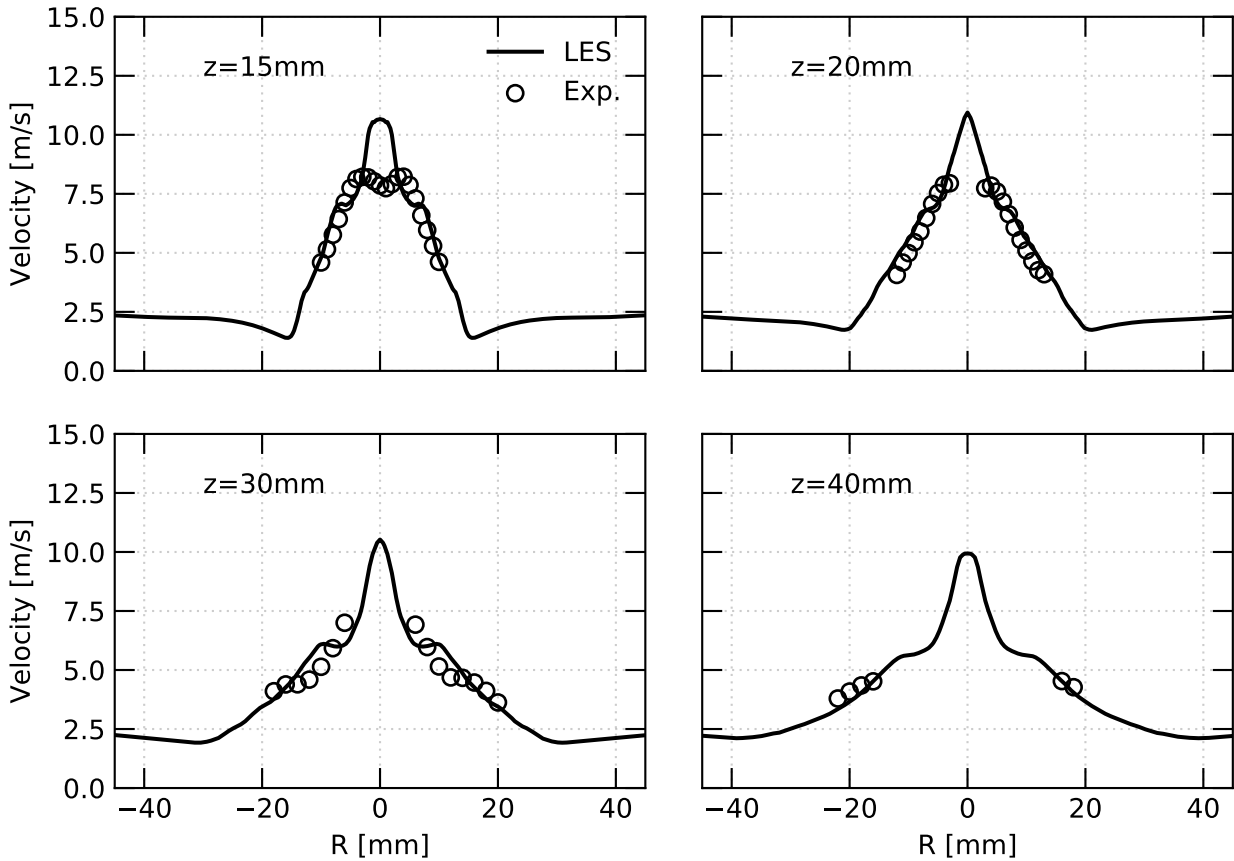
Figure 4.9.: Radial profiles of mean axial velocity of the gas phase.

For a verification of the flow field, radial profiles of mean axial gas velocity are compared with PDA data from the DSHC database. In the experiment, droplets with a diameter $d < 6$ µm were used as tracer particles since their respective Stokes number was well below unity [212]. Consequently, these droplets closely followed the gas field trajectories. Results can be found in Fig. 4.9. Again, the simulation correctly reproduces the experiment with exception of the center line region. Even though measurement data for $R < \pm 2.5$ mm is only available at $z = 15$ mm, experimental data indicates a slight drop in velocity in this region. In contrast, the LES shows a further acceleration of the gas along the center line resulting in a notable overestimation of axial velocity. As shown by Enderle et al. in [55] this could be caused by the liquid phase due to strong momentum source terms imposed by droplets which concentrate along the center line.

4.3.3. Dispersed phase results

A characterization of the dispersed phase from the experiments is given by means of PDA data for droplet size and velocity components. This data is compared to mean statistics of computational particles from the dispersed phase solver.

Profiles for the local Sauter Mean Diameter (SMD) from experiment and simulation are displayed in Fig. 4.10 at different axial positions. The experimental data demonstrates a radial distribution of mean diameter typically found for a pressure-swirl atomizer as the mean diameter increases towards outer radii [56, 227]. This tendency is also visible in the LES which reproduces both maximum SMD and maximum extent of the spray with high accuracy. A large deviation is identified in the inner region of the spray where the SMD in the simulation is distinctly below the experiment. However, it should be kept in mind that results for the dispersed phase are statistical means of a collection of discrete events, i.e. liquid droplets passing through the registration plane. Therefore, the simulation results must be interpreted with respect to the radial distribution of liquid mass flux. This means that the agreement between predicted SMD and experiments should be weighted by the radial distribution of liquid mass flux. For this purpose, simulation results for the normalized liquid mass flux are added to the SMD data at $z = 20$ mm and $z = 40$ mm. Apparently, regions of high mass
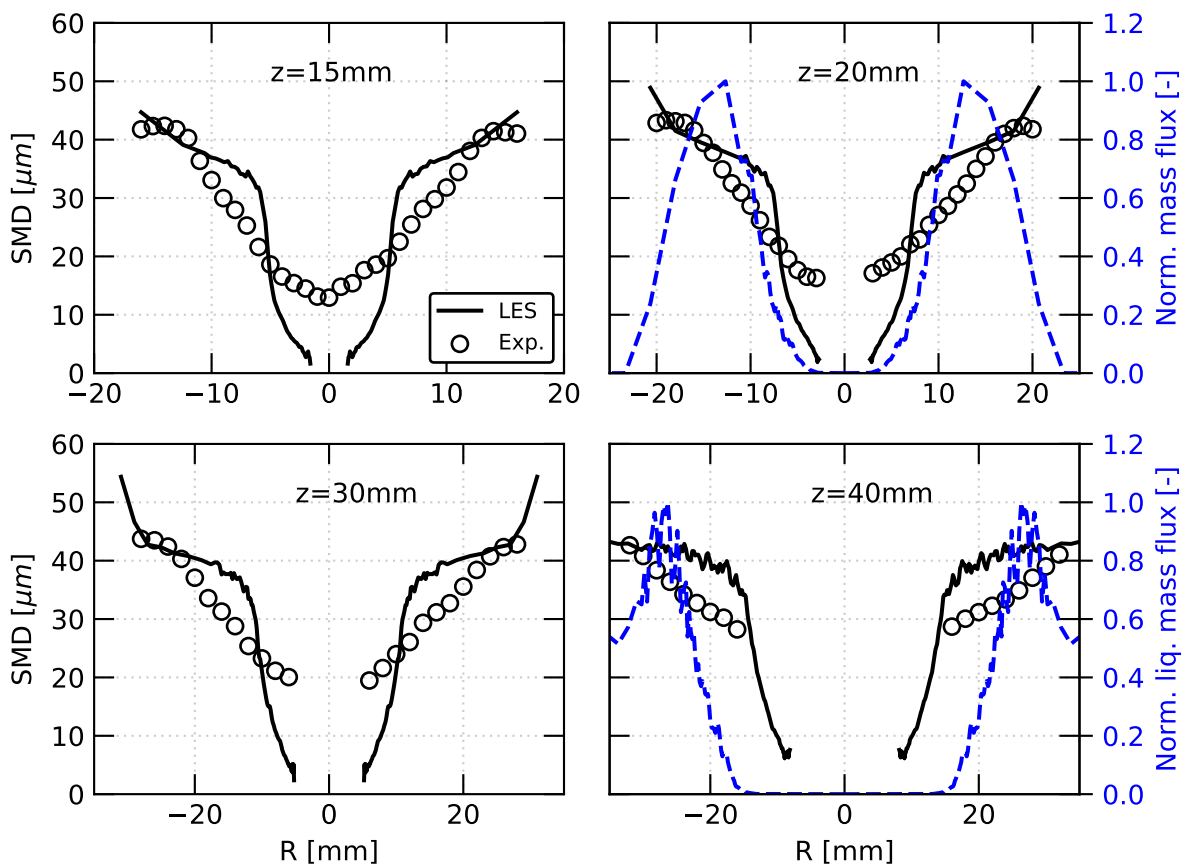
Figure 4.10.: Radial distribution of Sauter Mean Diameter (SMD) from experiment and simulation and liquid mass flux from the simulation at different heights above the atomizer. Atomizer exit at $z = 0$ mm.

flux coincide with regions of low discrepancy between simulation and experiment whereas highest deviation is observed in the presence of almost zero mass flux. Although not added to the plots for the sake of brevity, this tendency is also found at the other axial positions. It is therefore concluded that the simulation is able to reproduce the SMD profiles with good accuracy which also verifies the chosen boundary condition for the liquid phase.

Figure 4.11 summarizes results for the axial and radial velocity components of the liquid fuel droplets. For comparison with the experiment, the droplet size spectrum is divided into representative three size classes for small ($10\,\mu m \leq d \leq 20\,\mu m$), medium ($20\,\mu m < d \leq 30\,\mu m$), and large ($40\,\mu m \leq d \leq 50\,\mu m$) droplets. Although all droplets in the simulation are injected under the simplification of a uniform initial absolute velocity $U_D = 35.7\ \mathrm{m\,s^{-1}}$, a dispersion of axial and radial velocity over the droplet size is clearly visible in the simulation results. Due to their high momentum, large droplets maintain the initial velocity over the first 30 mm. This results in too high velocities for this size class until $z = 40$ mm, indicating a too low deceleration of the large droplets by the gas field. However, as the axial gas velocity agrees well with the experiments (see Fig. 4.9), this behavior reveals that the injection velocity for large droplets should be reduced. In contrast, small droplets in the simulation are in good agreement with the experiment for both axial and radial velocity. As a result of their low Stokes number, these small droplets couple to the local gas velocity and are therefore subject to fast deceleration. The same effect is valid for medium size droplets with exception of the first measurement location where axial and radial velocities are slightly overestimated by the simulation.

Based on the results for the gaseous and dispersed phase, it is concluded that the LES is able to reproduce all relevant effects and properties of the test case under consideration. Furthermore, this verifies the suitability of the chosen spray boundary condition in combination with the present modeling approach. The results from this section will serve as a reference in the following study.

(a) Axial

(b) Radial
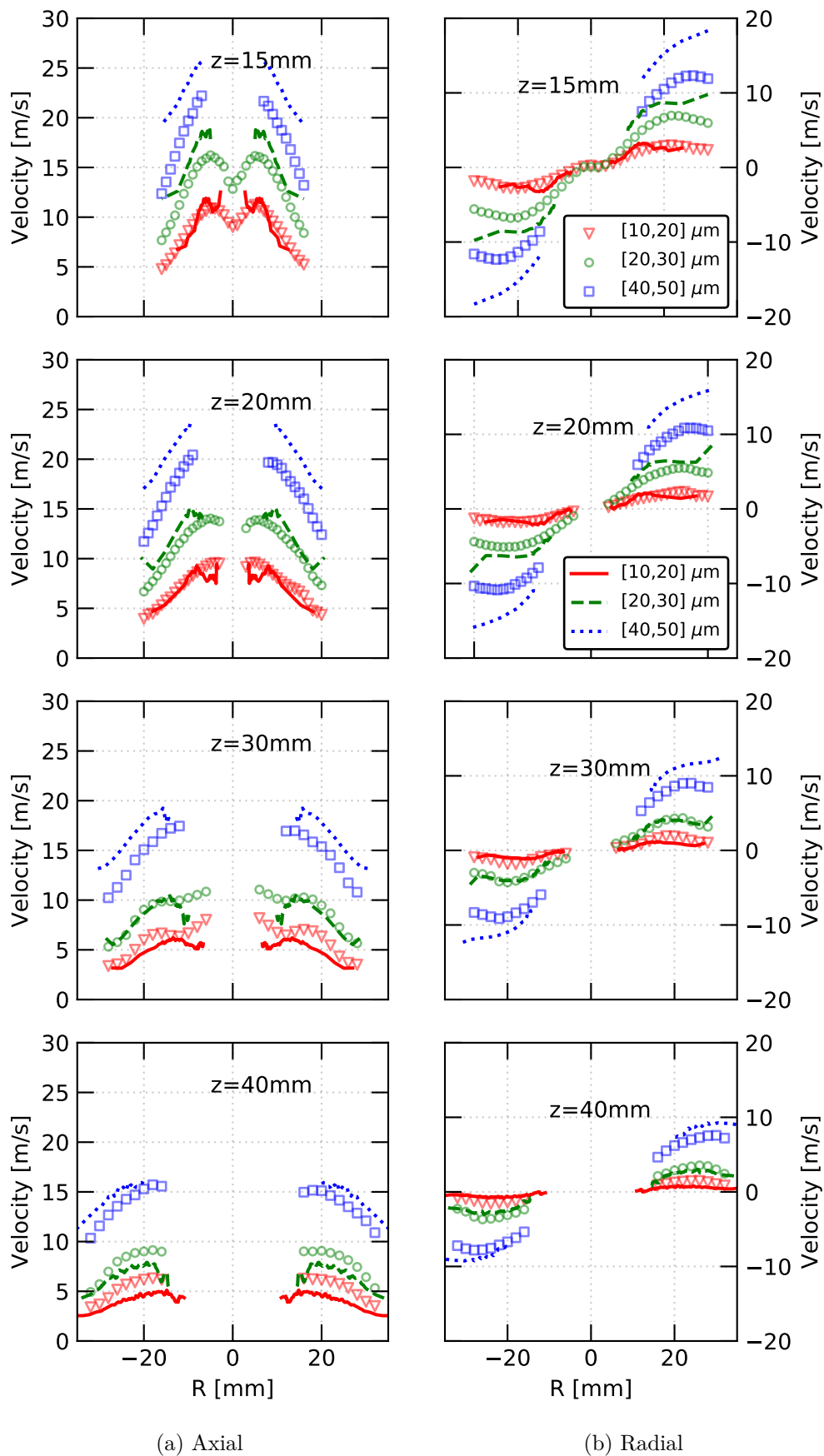
Figure 4.11.: Droplet velocity components for different droplet size classes. Symbols indicate experimental data, lines are simulation results.

4.4. Uncertainty Quantification

In the following, the workflow for uncertainty quantification as detailed in Sec. 3.3 is applied to the DSHC case. Figure 4.12 provides an overview of the methods related to the three main steps of this workflow. First, the simulation setup is reduced to a RANS setup and numerical uncertainties are quantified. Then, uncertainties in the spray boundary condition are identified from a survey of existing studies on the DSHC case. Most important parameters are ranked by means of a MOAT analysis. For the propagation of the uncertainties, Gaussian Process regression and Polynomial Chaos Expansion are tested and analyzed. Finally, probability bounds are inferred and *a posteriori* sensitivity is examined through Sobol indices.

Accurate prediction of gas phase temperature is a key factor for the determination of thermal loads, pollutant emissions and soot distribution in gas turbine applications [131]. Therefore, special emphasis is put on the quantification of uncertainties in the calculation of gas phase temperature. Thus, the radial profiles of mean temperature as shown in Fig. 4.7 will be considered as the main Quantities of Interest in the following study. It should be pointed out that the method demonstrated in this section can be applied to any other quantity of interest from the simulation.
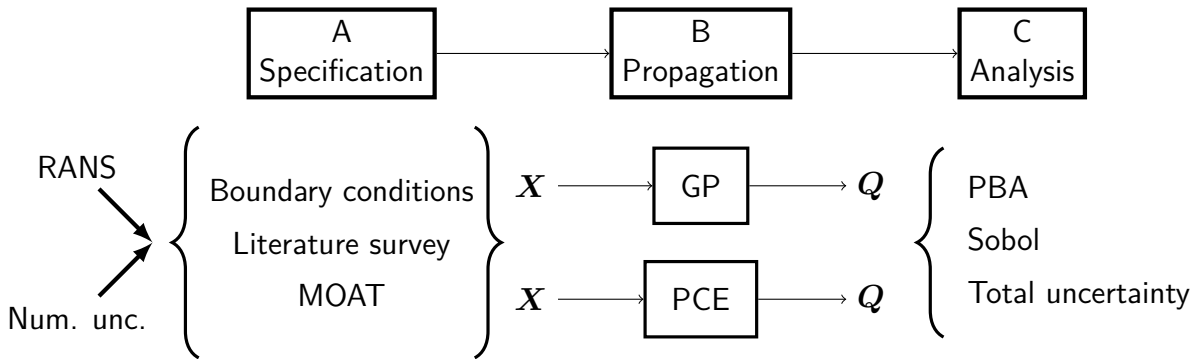
Figure 4.12.: Application of the workflow for uncertainty quantification to the DSHC case.

4.4.1. Reduced simulation model and numerical uncertainties

The reduced RANS simulation model as detailed in Sec. 4.2.1 is used in lieu of the LES to speed up computation and enable the detailed analysis of mechanisms for uncertainty propagation. The RANS model drastically reduces the required CPU hours by a factor of 70 for a single computation compared to the LES. For a qualitative assessment of the RANS model as applied here, a simulation with the same boundary conditions and models as the deterministic reference is conducted and compared to the LES results.

Radial profiles of gas phase temperature from both simulations are displayed in Fig. 4.13. Since the RANS simulation model is based on a 20° wedge, in the following, all results will be given along the positive radial axis (R-axis). Due to the radial bias in the experimental data for gas phase temperature [213], especially in the region of strong gradients, experimental results for both $R < 0$ mm and $R > 0$ mm are included. The RANS is able to reflect all main features of the flame as discussed in Sec. 4.3.2 and accurately reproduces the experimental
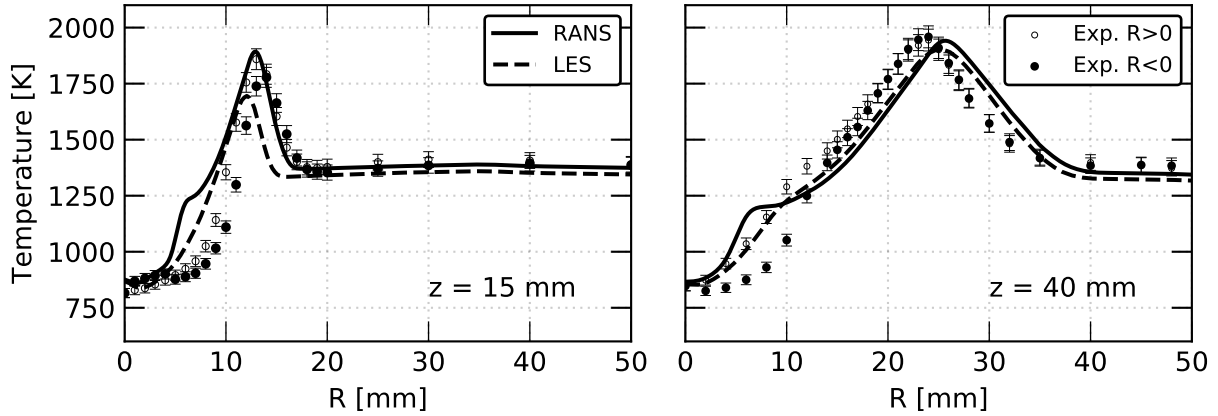
Figure 4.13.: Radial profiles of gas phase temperature at $z = 15$ mm and $z = 40$ mm from LES and RANS.

data. At $z = 40$ mm and further downstream, the RANS demonstrates the same tendency in overpredicting the radial spread of the flame as the LES. Note that this spread is slightly larger in the RANS than in the LES. A major deviation of the RANS from both experiment and LES is found at the beginning of the inner reaction zone ($R \approx 5$ mm). Considering that this deviation is present at all axial positions, it is concluded that this must be a systematic error of the RANS. The absence of resolved unsteady flow structures in the RANS and their influence on particle dispersion, droplet evaporation and local fuel mixing could be a key factor causing these deviations. For example, Abani et al. [1] pointed out that RANS models are prone to errors in the near injector region, where phase-coupling effects play a significant role. Furthermore, one should keep in mind that the spatial grid resolution in this area for the LES is well above the RANS. In the next section, it is shown that this area is subject to considerable numerical uncertainties. Nonetheless, the RANS simulation provides a suitable accuracy for the following uncertainty study.

Numerical uncertainties

In addition to the qualitative assessment of RANS simulation quality, numerical uncertainties are systematically quantified. As discussed in Sec. 3.3.1, these uncertainties arise from discretization error, iterative convergence error, roundoff error and errors due to computer programming mistakes. The latter two are assumed to be negligible due to previous and ongoing verification and validation efforts for the simulation platform. From the inspection of residuals and their convergence, iterative errors are expected to be in the order of machine accuracy. Therefore, special emphasis is put on discretization errors stemming from spatial grid resolution.

To evaluate this error, the grid convergence method proposed by Roache [210] is adopted. It relies on the analysis of multiple solutions from a sequence of grids with decreasing grid spacing h. For the case considered, a coarse (f_3) and fine (f_1) mesh with respect to the reference (f_2) is used, keeping the refinement ratio $r_r = h_{i+1}/h_i$ constant at $r_r = \sqrt{2}$. The influence of grid resolution on the radial temperature profiles is displayed in Fig. 4.14 (a).

(a) Grid convergence   (b) Numerical uncertainties
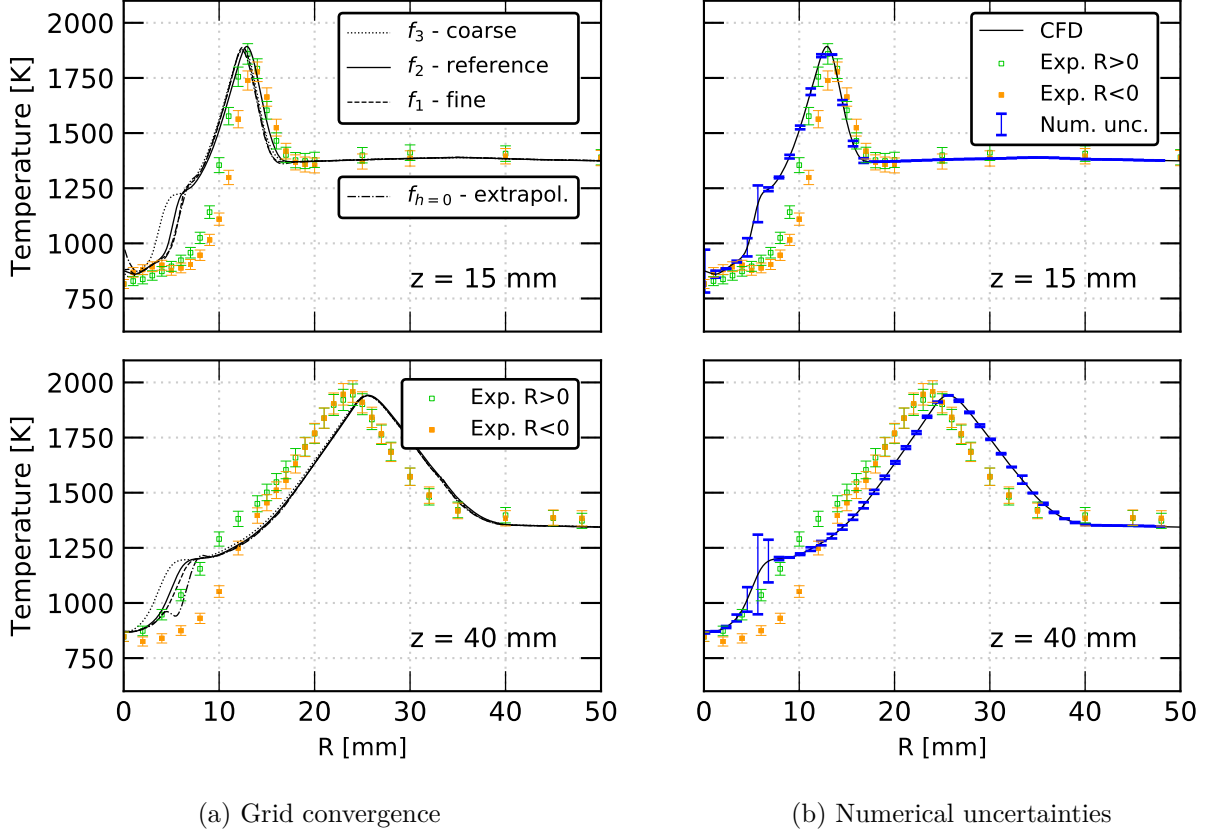
Figure 4.14.: Results from grid convergence study and associated numerical uncertainties of the RANS simulation model.

Highest sensitivity is found at the beginning of the inner averaged reaction zone ($R \approx 5\,\text{mm}$) at both axial positions. Apart from that, the solution is nearly insensitive to grid refinement at $z = 40\,\text{mm}$. In order to get a quantitative assessment of sensitivity to grid resolution, the temperature profiles are extrapolated to a hypothetical infinitely small grid spacing $h = 0$ using Richardson extrapolation [210]. An observed order of convergence p_c is calculated by

$$p_c \equiv \frac{\log\left(\frac{f_2 - f_1}{f_3 - f_2}\right)}{\log r_r}. \tag{4.1}$$

As Stern et al. [251] pointed out, this equation is not robust especially in cases where the datapoints f_i are nearly constant with change in grid size or when $f_2 - f_1 < f_3 - f_2$. We therefore limit p_c to an interval $[p_{c,min}, p_{c,max}]$ with $p_{c,min} = 0.5$ and $p_{c,max} = 3$ as recommended by Phillips and Roy [184]. The extrapolated solution is then determined by

$$f_{h=0} = f_1 + \frac{f_1 - f_2}{r_r^{p_c} - 1}. \tag{4.2}$$

A cubic interpolation is used to transfer the medium and fine grid solution to the coarse mesh locations. Extrapolated profiles are included in Fig. 4.14 (a). The numerical error $\varepsilon_{num} = |f_{h=0} - f_2|$ is low and the reference grid f_2 represents an appropriate spatial resolution of the problem. Based on ε_{num}, numerical uncertainties U_{num} are estimated using the approach

proposed by Roy and Oberkampf [216]:

$$U_{num} = F_s \varepsilon_{num} = F_s |f_{h=0} - f_2|, \tag{4.3}$$

with a safety factor F_s which is recommended to be 1.25 for extrapolations involving three or more grids. Resulting uncertainties are included as error bars in the reference simulation results in Fig. 4.14 (b). Note that the regions of largest numerical uncertainties correspond to the scope of highest deviation between RANS and LES as found in the previous section. Here, uncertainties in the magnitude of 300 K are present.

Following the suggestion of Oberkampf et al. [177], the calculated numerical uncertainties of the simulated temperature profiles are treated as purely epistemic uncertainties and will be added as an interval to the results of the later propagation of input uncertainties. All following results will be computed on the reference grid f_2.

4.4.2. Step A: Characterization of the input uncertainties

Section 4.3 demonstrated that the used simulation platform is able to reproduce the experimental data with high accuracy using an optimized set of boundary conditions for the spray. The focus of this section is therefore on identifying the impact of possible uncertainties on the simulation results.

A detailed characterization of gas phase boundary conditions was conducted in the experiments. Thus, associated uncertainties are deemed to be negligible compared to uncertainties in the dispersed phase and special emphasis is put on the boundary condition for the dispersed phase. In the spray boundary condition as defined in Sec. 4.2.3, six parameters remain to be determined. As the spray characterization in the transition regime from dense to dilute spray is challenging and subject to large measurement errors [259], the first available data is at a distance of $z = 8$ mm from the atomizer orifice.

Furthermore, some reported characteristics of the atomizer are either incomplete (φ'), highly uncertain (T_{liq}) or potentially wrong (U_{liq}). For example, Ma et al. [140] pointed out that using the droplet injection velocity based on the experimental data of the atomizer, the downstream velocity will be significantly overpredicted. This could be traced back to cavitation within the atomization chamber, which decreases the discharge coefficient of the atomizer and hence the exit velocity of the liquid.

Consequently, parameters of the spray boundary condition have to be calibrated against the downstream experimental data resulting in a best fit for the used simulation methods and models. As a result, different values for these parameters are found in the literature on simulations of the DSHC flame. Although in each of the studies a slightly different scheme for the construction of the spray boundary condition was utilized, main parameters as defined previously can be identified and compared:

For a RANS simulation with a Flamelet Generated Manifold (FGM) combustion model, Ma et al. [138] computed the parameters with the LISA primary breakup model [234]. In a similar setup, Jamali [106] considered slightly different inputs for the LISA model. Gallot-Lavallée et

Table 4.3.: Spray boundary conditions for the DSHC $\mathbf{H_{II}}$ case from literature and uncertain input space.

		D_0 [µm]	U_D [m s^{-1}]	$\bar{\varphi}$ [°]	φ' [°]	T_{liq} [K]	q [-]
Ma et al.	[140]	40.0	35-70[1]	35-40[1]	5-15[1]	-	3.0
Ma et al.	[138]	41.0	29.5	35	6	301	3.5
Gallot-Lavallée et al.	[73]	41.0	-[2]	30	10	301	3.0
Jamali	[106]	41.0	29.5	35	5	301	3.0
Enderle et al.	[55]	45.2	35.7	30	20	301	3.0
Experiment	[213]	-	51.7[3]	30[4]	-	301	3.0
Uncertainty input space Ω_{BC}							
Minimum		40	27.3	30	6	300	3.0
Maximum		45	35.7	40	20	310	3.5
Reduced input space $\Omega_{\mathrm{BC,r}}$							
Minimum		40	27.3	30	6	-	-
Maximum		45	35.7	40	20	-	-
Constant		-	-	-	-	301	3.0

[1] Function of droplet diameter
[2] PDF from experimental data
[3] Liquid velocity at the atomizer exit (U_{liq})
[4] Nominal value for Delavan WDA 0.5 GPH atomizer

al. [73] conducted an LES with a stochastic fields combustion model and derived a PDF for the injection angle as a function of the droplet diameter. In a further LES/FGM study, Ma et al. [140] proposed a conditional droplet injection model for the DSHC case. A calibrated spray boundary condition for the THETA/SPRAYSIM framework was presented using LES and FRC by Enderle et al. [55].

Table 4.3 summarizes parameters for the spray boundary condition in the DSHC $\mathbf{H_{II}}$ case from the different authors. As an example for the variation of the input parameters over the mentioned studies, Fig. 4.5 gives a comparison of the cumulative drop size distribution from different simulations of the DSHC $\mathbf{H_{II}}$ case. Although Rosin-Rammler distribution parameters D_0 and q only vary slightly, the corresponding cumulative drop size distributions $Q(D)$ differ clearly among the collected simulations.

For the following uncertainty quantification, the six input parameters of the spray boundary condition from Tab. 4.2 are considered as uncertain. The parameter space of uncertain inputs Ω_{BC} is constructed from the respective minimum and maximum values found in the aforementioned literature as they all demonstrated good agreement with the experimental data of the test case. Since no further information is available, all six input quantities are treated as purely epistemic interval-valued uncertainties, bounded by the respective minimum and maximum which are given in Tab. 4.3.
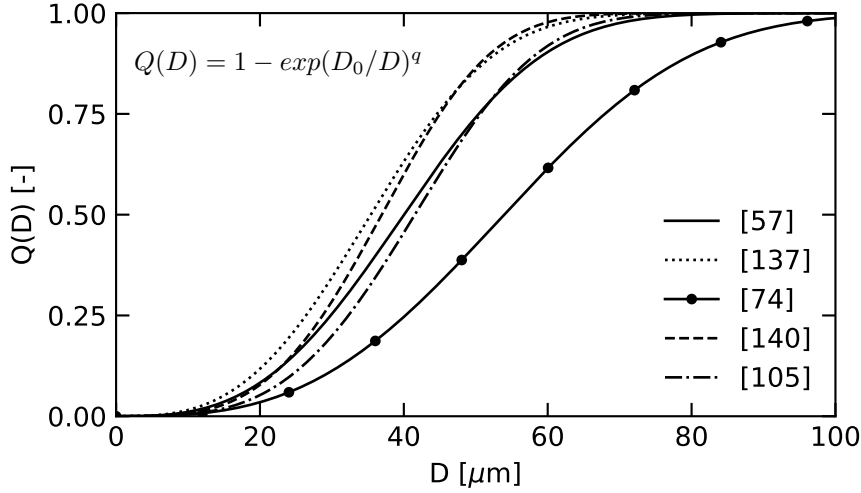
Figure 4.15.: Cumulative drop size distributions from different simulations of DSHC $\mathbf{H_{II}}$.

4.4.3. Step A: MOAT screening

Although six uncertain parameters have been identified, their contribution to the output uncertainty, i.e. the uncertainty in the profiles for gas phase temperature, might differ widely. Thus, the parameter space of uncertain inputs Ω_{BC} could be reduced to the most important parameters prior to the propagation of the input uncertainties in order to decrease computational costs. For this reduction, a screening of the input parameter space from Tab. 4.3 is performed using MOAT sensitivity analysis as described in Sec. 3.3.1. As a result, the influence of the input parameters on the gas phase temperature can be assessed.

For the MOAT screening, a total of 28 RANS simulations are conducted, resulting in $r = 4$ elementary effects for each of the six input parameters. According to Saltelli [224], $r = 4$ is the minimum value to place confidence in the method, while keeping the computational expense at a minimum. For the analysis of the results, the modified mean as recommended by Campolongo et al. [21] is used.

MOAT analysis is performed for the radial profiles of temperature at the six axial positions where experimental data is available ($z = 15, 20, 30, 40, 50, 60$ mm). This allows for a characterization of the sensitivity with proceeding evaporation and reaction over the flame. At each axial position, radial data for $\sigma(r)$ and $\mu^*(r)$ is averaged and weighted by the local variance in temperature from all 28 simulations. Thus, aggregated effects μ_z^* and σ_z are computed by

$$\mu_z^* = \frac{\sum_r \mu^*(r)\mathbb{V}[T(r)]}{\sum_r \mathbb{V}[T(r)]} \quad \text{and} \quad \sigma_z = \frac{\sum_r \sigma(r)\mathbb{V}[T(r)]}{\sum_r \mathbb{V}[T(r)]}. \tag{4.4}$$

For further details on this aggregation approach for sensitivity analysis of spatially distributed quantities, the reader is referred to the work of Marrel et al. [146].

Aggregated MOAT results at different axial positions are shown in the upper plot of Fig. 4.16. Data is plotted in a μ_z^* - σ_z space which enables a fast classification of sensitivities: linear or direct effects increase along the μ_z^* axis while non-linear or interaction effects advance along the σ_z axis. Consequently, high influence parameters are found on the right and upper

Figure 4.16.: Standard deviation σ of elementary effects for temperature plotted against their modified mean μ^* from MOAT analysis. Labels indicate axial positions.
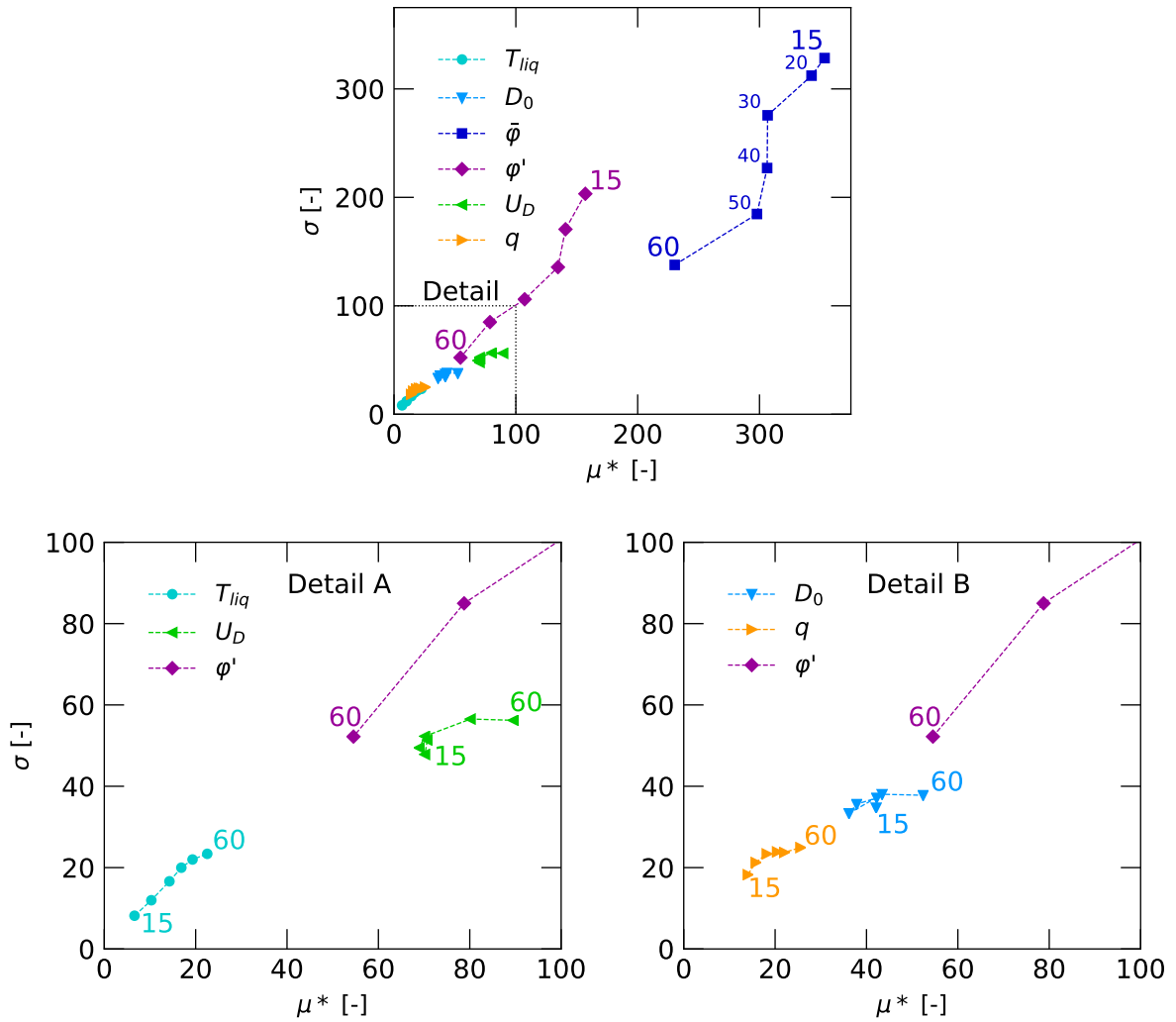
portion of the μ_z^* - σ_z space. Labels at the data points in Fig. 4.16 indicate its axial position in the computational domain.

Largest linear and interaction effects are visible for mean trajectory angle $\bar{\varphi}$ and dispersion angle φ' although both decrease in magnitude with increasing distance from the spray boundary condition. It is assumed that the strong interaction effect arises from the fact that both parameters determine the opening angle of the spray cone. As the effect of the other four parameters is substantially smaller, a detail of the lower left portion of the μ_z^* - σ_z space is included in Fig. 4.16 . In contrast to $\bar{\varphi}$ and φ', the relative influence of liquid droplet temperature T_{liq}, droplet starting velocity U_D, distribution factor q and mean droplet diameter D_0 rises with increasing z - position . However, in particular T_{liq} and q only have minor influence on the temperature when compared to $\bar{\varphi}$ and φ'. It is therefore concluded that these two parameters can be fixed to the reference values from Tab. 4.2 and neglected for the following uncertainty quantification. Thus, the parameter space of uncertain inputs Ω_{BC} is reduced to $\Omega_{BC,r}$ comprising $\bar{\varphi}$, φ', D_0 and U_D with the respective bounds from Tab. 4.3.

4.4.4. Step B: Gaussian process based propagation of uncertainties

In this section, Gaussian process based regression as detailed in Sec. 3.4.1 is used as a surrogate model for the RANS simulation model of the DSHC H-II flame. Thus, uncertainties from $\Omega_{BC,r}$ can be efficiently propagated. As GP based surrogate modeling relies on a data-fit approach, training data is first acquired from the RANS model. Then, GP regression models $\hat{\mathcal{M}}_{GP}$ are constructed based on this training data and model quality is estimated through cross validation and holdout validation. Finally, uncertainty bounds for the profiles of gas phase temperature are inferred from space filling sampling of $\hat{\mathcal{M}}_{GP}$ over $\Omega_{BC,r}$.

Training data and surrogate model construction

Radial profiles of gas phase temperature are predicted by a series of independent GP models at each grid point location. The input vector $\boldsymbol{x}$ comprises the four uncertain parameters which span $\Omega_{BC,r}$. Thus, the GP surrogate model formally reads:

$$T^{r,z} = \hat{\mathcal{M}}_{GP}^{r,z}\left(\boldsymbol{x}\right) = \hat{\mathcal{M}}_{GP}^{r,z}\left(U_D, D_0, \bar{\varphi}, \varphi'\right). \tag{4.5}$$

Following the recommendation of Jones et al. [109], 40 training data points are distributed over $\Omega_{BC,r}$ using a Sobol series (see Sec. 3.3.2). At these points, RANS simulations are run with the respective input parameters for the spray boundary condition, resulting in the set of training data $\mathcal{S}_{40} = \{(\boldsymbol{x}^{(1)}, \boldsymbol{T}^{(1)}), (\boldsymbol{x}^{(2)}, \boldsymbol{T}^{(2)}),...,(\boldsymbol{x}^{(40)}, \boldsymbol{T}^{(40)})\}$. Additionally, the Sobol series for the distribution of training data points is extended by 20 additional points, forming a training set $\mathcal{S}_{60}$ to study the influence of training data size. Projections of the training data points onto two-dimensional subspaces are shown in Fig. 4.17.

Fig. 4.18 illustrates selected profiles of gas phase temperature from the set of training data. In addition, the respective sample point in the $D_0 - \bar{\varphi}$ subspace is indicated by colored dots
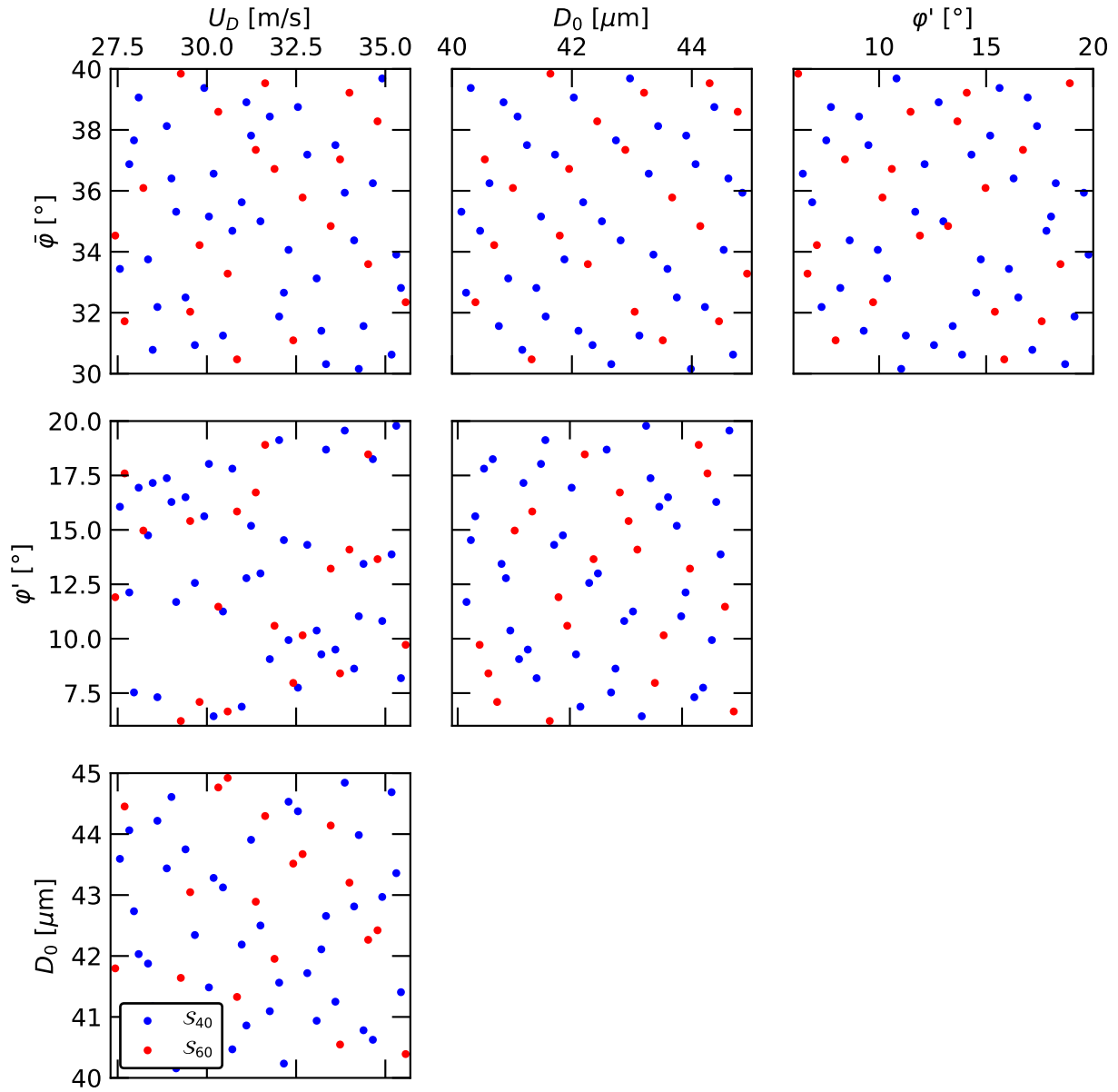
Figure 4.17.: Training data points from a Sobol series over $\Omega_{BC,r}$. $\mathcal{S}_{40}$ points (•), additional $\mathcal{S}_{60}$ points (•).
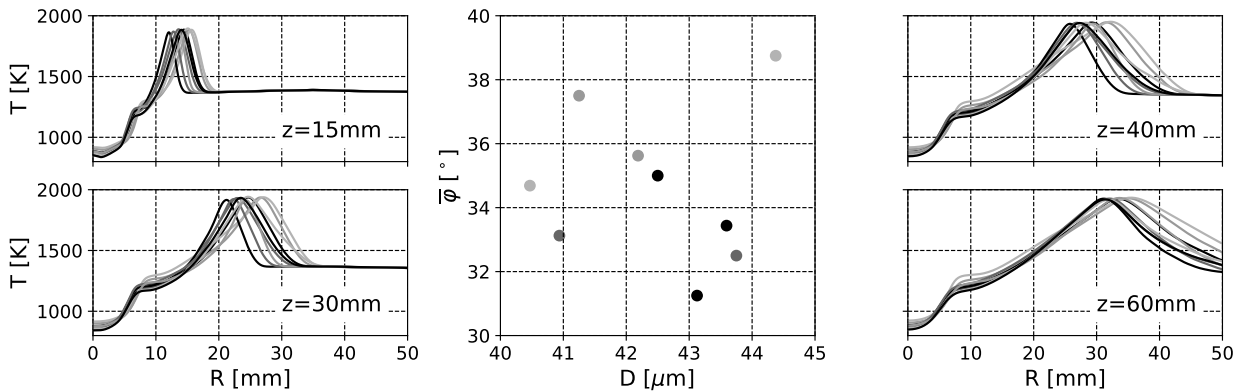

Figure 4.18.: Temperature profiles at different training data points from RANS simulations.

in the central plot of Fig. 4.18. From this data it is already evident that the considered variation in input parameters results in significant variations of the temperature distribution over the computational domain. Especially the radial position of the peak temperature, which is connected to the reaction zone of the flame, varies over a range of $\Delta r = 10$ mm at all axial positions. In contrast, the hot gas temperature from the coflow outside of the reaction zone (e.g. $R > 20$ mm at $z = 15$ mm) is not affected by the variation in droplet starting properties.

Based on the set of training data, Gaussian process regression models are constructed using the Sandia DAKOTA 6.4 software package [3]. DAKOTA optimizes the Hyper-parameters of the GP (see Sec. 3.4.1) through a Maximum Likelihood Optimization with respect to the training data.

As the constructed surrogate models will be used in lieu of the RANS simulation for detailed uncertainty analysis of the DSHC $\mathbf{H_{II}}$ case, surrogate model reliability and quality must be assessed. The fact that a surrogate model will always be an approximation of the true simulation model gives rise to an absolute surrogate model prediction error

$$\hat{\epsilon} = q - \hat{q} = T_{RANS}^{r,z} - T_{GP}^{r,z}, \tag{4.6}$$

which is the difference between the prediction of a quantity of interest from the simulation and the corresponding surrogate model [68]. Two validation and testing techniques, namely cross validation and holdout validation, are used to estimate $\hat{\varepsilon}$.

Surrogate model validation: Cross Validation

For the purpose of GP model validation, cross validation is conducted during the process of surrogate model construction. In cross-validation, the set of training data $\mathcal{S}$ is split into k equal subsets $\mathcal{S}_k$ followed by the construction of the surrogate model on $k - 1$ subsets while keeping the remaining subset for model testing, i.e. computation of the prediction error from Eq. (4.6). This procedure is subsequently repeated for all subsets. Consequently, the mean cross-validation error yields

$$\hat{\epsilon}_{CV} = \frac{1}{k} \sum_{i=1}^{k} \hat{\epsilon}_i. \tag{4.7}$$

In this study, the training data sets are split into $k = 40$ and $k = 60$ subsets, respectively. This corresponds to a leave-one-out cross validation [71].

Radial profiles of mean relative cross validation errors are given in Fig. 4.19. At $z = 15$ mm, two distinct peaks are present at $R = 5$ mm and $R = 15$ mm which might be related to high local variance in the training data. Outside of the reaction zone ($R > 25$ mm) the error drops to zero as the coflow remains unaffected by the variation in spray boundary conditions. A more uniform radial distribution of errors is found at $z = 40$ mm due to the fact that the radial spread of the flame increases with axial distance from the atomizer and the reaction zone widens. It should be pointed out that the increase in training set size from 40 to 60 does not lead to a reduction of cross validation errors.
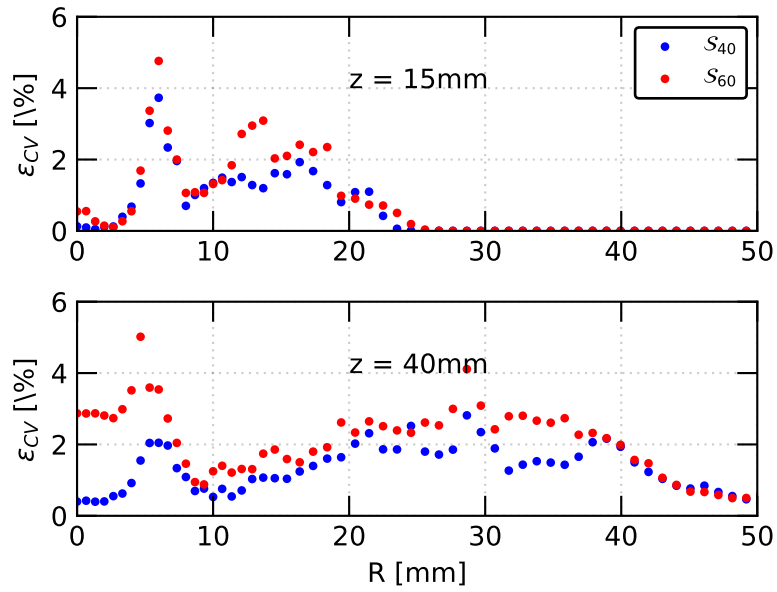
Figure 4.19.: Radial profiles of mean relative cross validation error ϵ_{CV}.
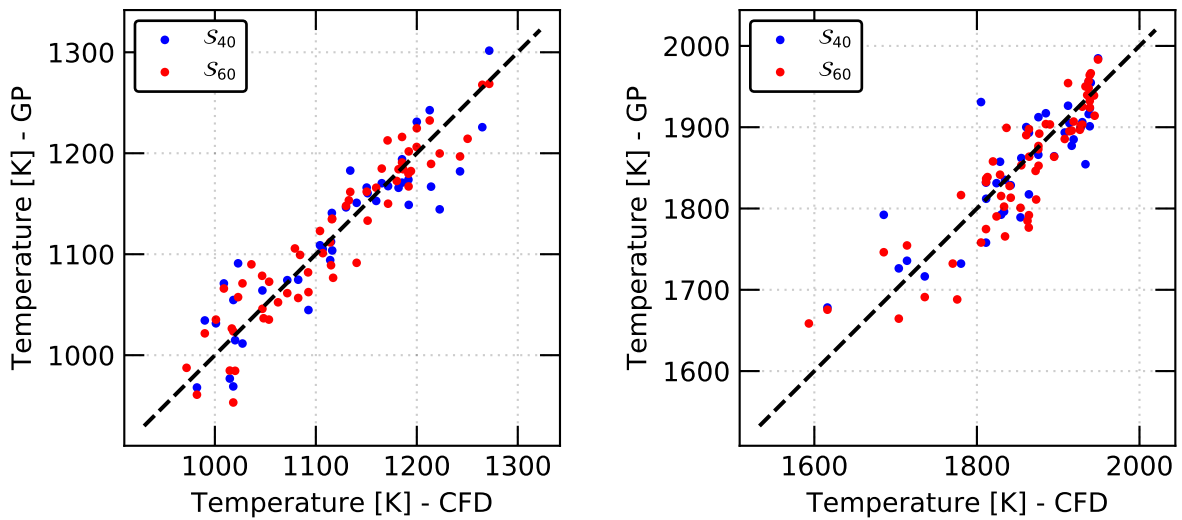
(a) $(z,R) = (15,10)$ mm

(b) $(z,R) = (40,20)$ mm

Figure 4.20.: Local cross validation plots at two positions of the radial profiles.

As an example of local cross validation data, the surrogate models at $(z,R) = (15,10)$ mm and $(z,R) = (40,20)$ mm are selected. Results from the leave-one-out runs are shown in Fig. 4.20 by means of cross validation plots. In the ideal case, all points would line up along the dashed diagonal. Contrarily, the deviation from the diagonal indicates the single run cross validation error. Thus, the mean cross validation error as defined in Eq. (4.7) increases as more points deviate from the diagonal. A minor tendency towards reduced deviation is shown by the surrogate model based on the $\mathcal{S}_{60}$ sampling set at both position.

Although not shown for brevity, relative cross validation error stays below 2 % at all axial positions for both training data set which indicates that the constructed models have the ability to generalize to independent datasets.

Surrogate model testing: Holdout Validation

In addition to the training data sets $\mathcal{S}_{40}$ and $\mathcal{S}_{60}$, a holdout validation dataset $\mathcal{S}_{HO}$ comprising 20 points from LHS sampling of $\Omega_{BC,r}$ is computed by the RANS simulation model and kept aside for model testing. Consequently, the constructed GP surrogate models are tested against new data and the predictive capability can be visualized and quantified.

A qualitative comparison of GP surrogate model prediction and CFD simulation for an exemplary point from S_{HO} at $z = 15$ mm and $z = 40$ mm is given in Fig. 4.21. For both training data sets, the surrogate models are able to predict the simulation data with high accuracy at both axial positions. At the transition from the flame front to the coflow ($(z,R) = (15,15)$ mm), prediction quality improves slightly when considering the larger training data set S_{60}.

In analogy to the mean cross validation error, a quantitative representation of the surrogate model quality is calculated using the normalized root mean squared error

$$\varepsilon_{GP} = \frac{||\mathcal{M}_{GP} - \mathcal{M}||_2}{||\mathcal{M}||_2} = \frac{||T_{GP}^{r,z} - T_{RANS}^{r,z}||_2}{||T_{RANS}^{r,z}||_2} \qquad (4.8)$$
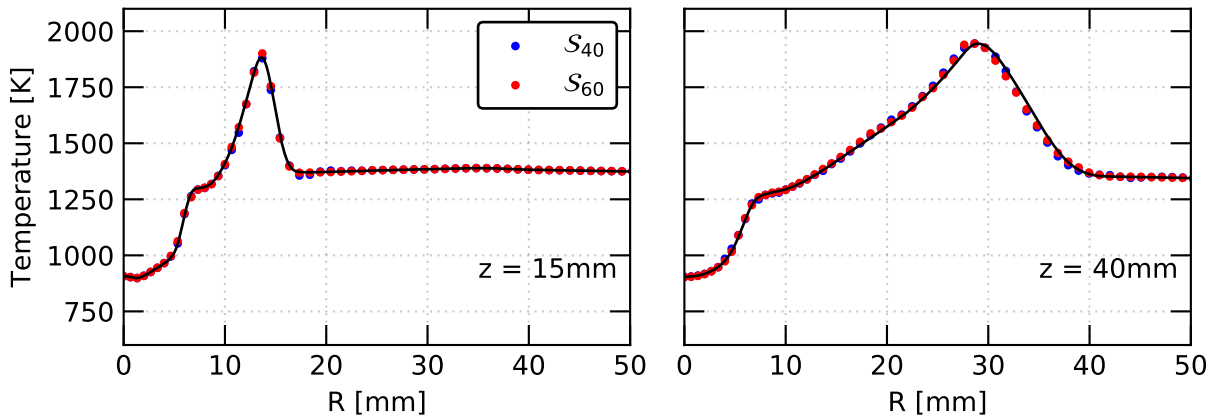
Figure 4.21.: GP surrogate model predictions and RANS simulation results at a holdout validation point from $\mathcal{S}_{HO}$.
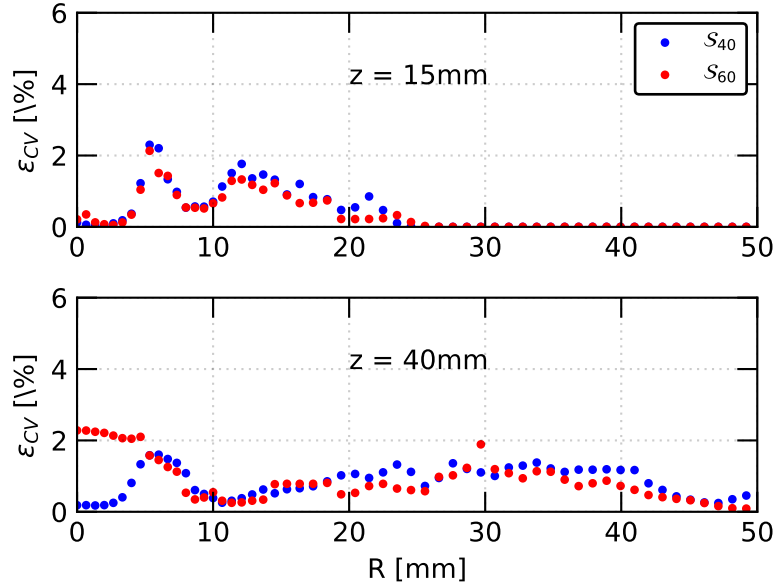
Figure 4.22.: Radial profiles of mean GP prediction error from holdout validation.

which resembles the mean relative deviation between GP surrogate model and RANS data over the 20 holdout data sets. Radial profiles of the error at $z = 15$ mm and $z = 40$ mm are displayed in Fig. 4.22. Mean error stays below 2.1% for both training data sets. As already seen in cross validation analysis, maximum error is identified in the flame-coflow transition region. A marginal enhancement in prediction quality is demonstrated by the $\mathcal{S}_{60}$ training data with exception of the first radial positions at $z = 40$ mm. The fact that these positions are also subject to higher cross validation errors in the $\mathcal{S}_{60}$ data (see Fig. 4.19) implies that the additional 20 training points in the $\mathcal{S}_{60}$ include points with substantially higher variance in the temperature data compared to the $\mathcal{S}_{40}$ data set.

In conclusion, the GP surrogate models constitute an accurate approximation of the RANS simulation model. Keeping in mind that the use of such surrogate models will reduce the computation time for temperature data by several orders of magnitude, the prediction error is seen as sufficient for the following uncertainty propagation.

Probability Bounds Analysis

Based on the previous assessment of surrogate model quality, the Gaussian Process surrogate model $\mathcal{M}_{GP}$ trained by the $\mathcal{S}_{40}$ training data set is used for the forward propagation of input uncertainties from $\Omega_{BC,r}$, replacing the RANS simulation model. Probability Bounds Analysis as described in Sec. 3.3.2 is utilized for the interpretation of the resulting non-deterministic simulation.

Since all input uncertainties were characterized as purely epistemic, minimum and maximum bounds of the temperature profiles are computed rather than precise distribution functions. Bounds are obtained by Latin Hypercube Sampling of $\mathcal{M}_{GP}$ over $\Omega_{BC,r}$. Space filling, uniform sampling over $\Omega_{BC,r}$ is required since each sample from $\Omega_{BC,r}$ is treated as a possible value instead of a value associated with a probability when dealing with interval valued epistemic
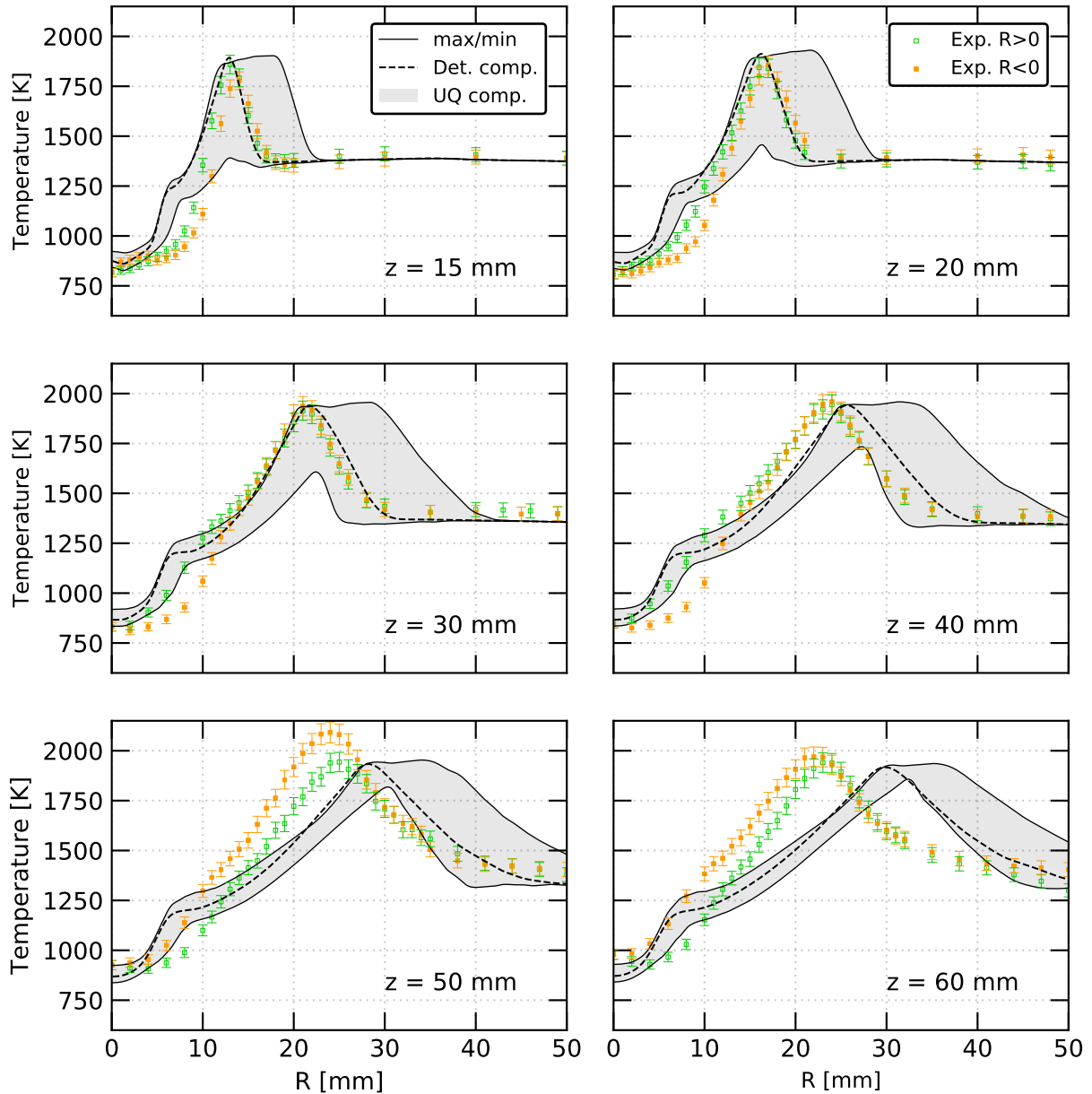
Figure 4.23.: GP based uncertainty regions and probability bounds for the temperature profiles.

uncertainties [177]. 10^4 samples are drawn from the GP surrogate model within a few minutes of computing time. Sampling statistics regarding mean μ, variance σ and skewness γ of the LHS sampling are summarized in Tab. 4.4. All moments are approximated with very high accuracy using 10^4 samples. The sample size is therefore seen as sufficient.

Resulting temperature realizations and corresponding bounds are shown in Fig. 4.23. As a consequence of the PBA framework and the epistemic input, all realizations are assigned an equal probability of unity. Therefore, the gray area represents the uncertainty region in the temperature results given the uncertainties in the input. In addition, the deterministic reference simulation from Sec. 4.3 is indicated by dashed lines. Highest uncertainties exist around the region of peak temperature at all axial positions highlighting that the spray input parameters significantly influence the position of the flame. Over all radial positions in the

Table 4.4.: Sampling statistics over the reduced input space $\Omega_{BC,r}$: LHS / analytical solution.

Input	μ	σ	γ
D_0 [µm]	42.5 / 42.5	2.0835 / 2.0833	$4 \cdot 10^{-6}$ / 0
U_D [m s^{-1}]	35 / 35	0.1455 / 0.1455	$3 \cdot 10^{-4}$ / 0
$\bar{\varphi}$ [°]	13 / 13	0.2851 / 0.2851	$2 \cdot 10^{-5}$ / 0
φ' [°]	31.5 / 31.5	5.8806 / 5.8801	$5 \cdot 10^{-6}$ / 0

reaction zone an uncertainty level between 100 K and 1400 K is revealed.

Further discussion and analysis of the PBA results is detailed in Sec. 4.4.6.

4.4.5. Step B: Polynomial chaos expansion based propagation of uncertainties

In this section, input uncertainties from $\Omega_{BC,r}$ are propagated through the test case by using Polynomial Chaos Expansion. In contrast to the data-driven GP surrogate modeling strategy, data points for the evaluation of the RANS simulation model are given by the quadrature points for the calculation of the expansion coefficients.

Sparse grid and PCE construction

In analogy to the GP based propagation of uncertainties, radial profiles of gas phase temperature are predicted by a series of independent PCEs at each grid point location. The vector of random input distributions $\boldsymbol{\xi}$ is defined by the four uncertain parameters which span $\Omega_{BC,r}$. Thus, the truncated PCE formally reads:

$$T^{r,z} = \sum_{k=0}^{P} \alpha_k \boldsymbol{\Psi}_k \left(\boldsymbol{\xi} \right) = \sum_{k=0}^{P} \alpha_k \boldsymbol{\Psi}_k \left(\xi_{U_D}, \xi_{D_0}, \xi_{\bar{\varphi}}, \xi_{\varphi'} \right). \tag{4.9}$$

In order to apply this formal definition of the chaos expansion to the UQ problem at hand, a structure for the multivariate polynomials $\boldsymbol{\Psi}_k$ in Eq. (4.9) must be specified. Since $\boldsymbol{\Psi}_k = f(\boldsymbol{\xi})$ this choice depends on the structure of the random input vector $\boldsymbol{\xi}$, i.e. the probability distribution of the uncertain inputs over $\Omega_{BC,r}$. For the construction of the PCE, the interval valued epistemic uncertainties from Tab. 4.3 are defined to be uniformly distributed over $\Omega_{BC,r}$. Therefore, a uniform transformation $\xi_i \sim \mathcal{U}(-1,1)$ is applied, corresponding to Legendre polynomials for $\boldsymbol{\Psi}_k$ (see Tab. 3.1).

Multidimensional numerical integration based on the Smolyak sparse grid tensorization method as detailed in Sec. 3.4.2 is employed for the computation of the PCE coefficients α_k. The nested Fejer rule forms the basis for the multidimensional integration.

In the sparse grid computation, different grid levels are considered, corresponding to different orders of accuracy of the resulting PCE. A Level-1 expansion (L1) of the four-dimensional input space $\Omega_{BC,r}$ requires nine quadrature points which increases to 49 points for a Level-2
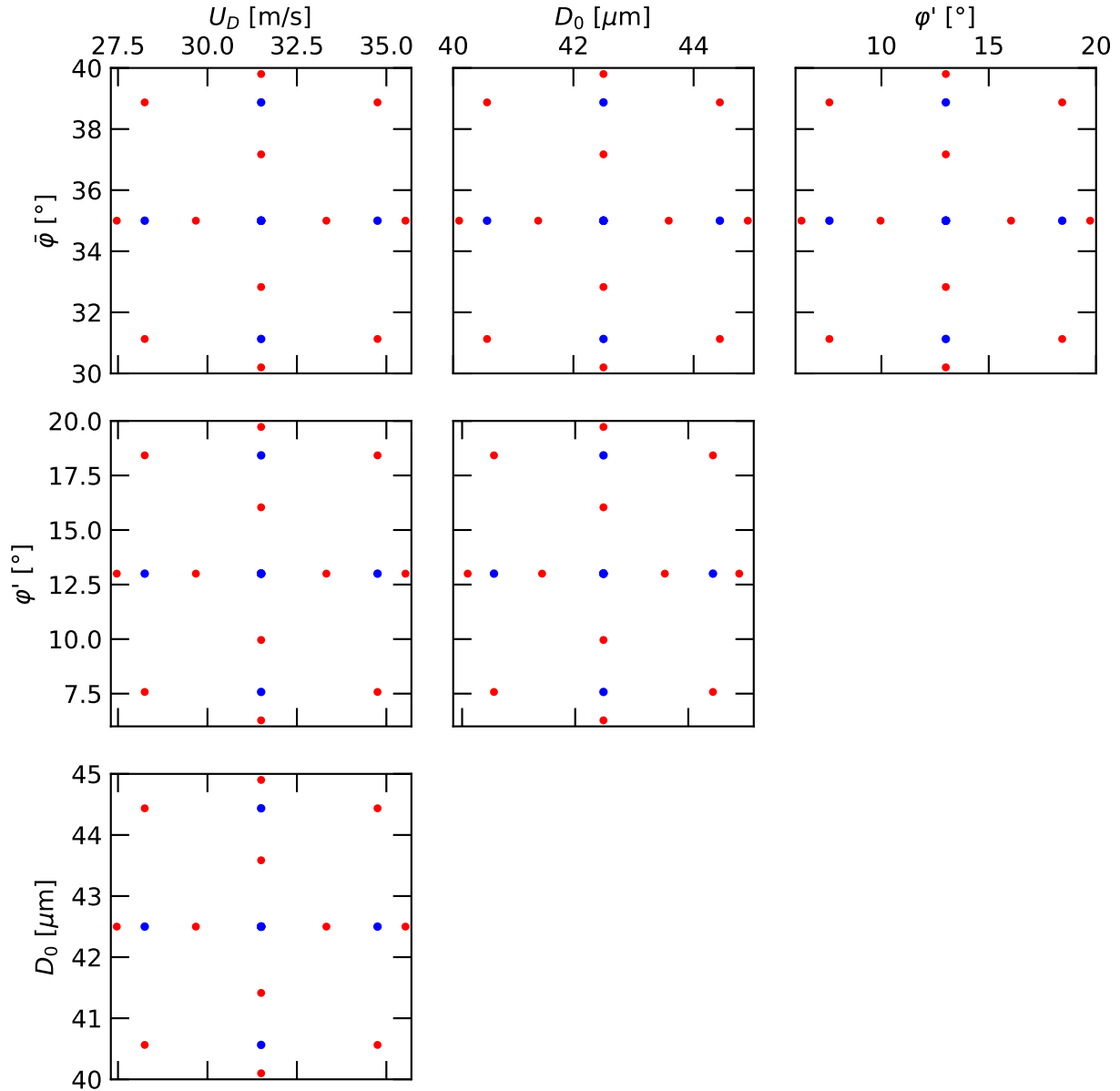
Figure 4.24.: PCE quadrature points of a Smolyak sparse grid using a nested Fejer rule. Level 1 points (•), additional Level 2 points (•).

expansion (L2). Each quadrature point requires an evaluation of the RANS simulation model. Due to the choice of a nested quadrature rule, points of the L1 expansion are a subset of the L2 points. Note that a Level-2 expansion of the six-dimensional input space Ω_{BC} would require 97 points which emphasizes the importance of *a priori* sensitivity analysis and reduction of the stochastic dimension.

Two-dimensional projections of the resulting sparse grids are shown in Fig. 4.24. In contrast to the pseudo-random distribution from the Sobol series in Fig. 4.17, points coincide in the two-dimensional projection. Therefore, less points are visible although the total number of points is similar to the training set $\mathcal{S}_{40}$.

Based on the evaluation of the RANS model at the sparse grid integration points, L1 and L2 Polynomial Chaos Expansions are constructed using DAKOTA 6.4.
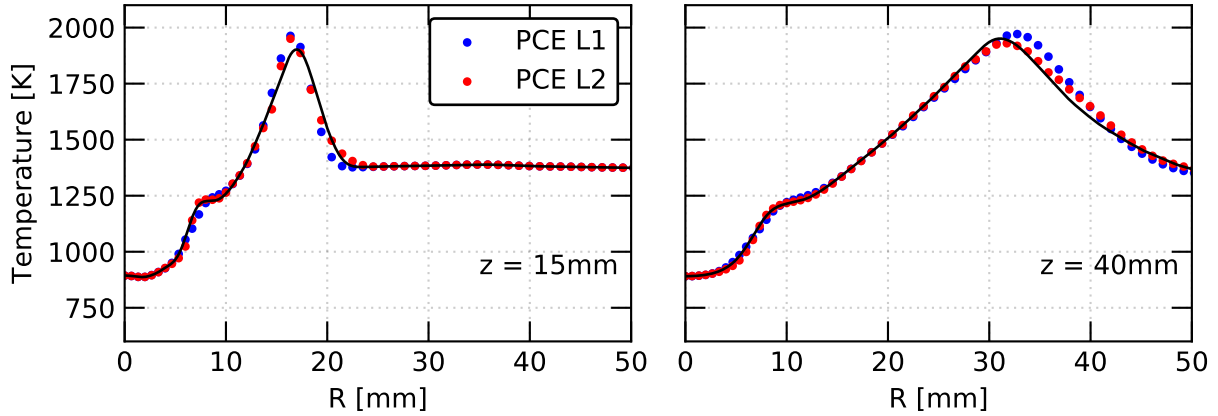
Figure 4.25.: PCE predictions and RANS simulation results at a holdout validation point from $\mathcal{S}_{HO}$.

PCE testing: Holdout validation

PCE accuracy is examined through holdout validation against the additional validation data set $\mathcal{S}_{HO}$ from the previous section. This allows for a direct comparison of GP and PCE errors.

A qualitative comparison of radial temperature profiles from RANS simulation and PCE with different expansion orders at an exemplary holdout test point is illustrated in Fig. 4.25. Note that this is the same test point as for the GP surrogate model in Fig. 4.21. The PCE prediction reproduces the RANS simulation data with high accuracy with exception of the radial position of maximum temperature which is slightly shifted at both axial positions. Prediction quality marginally improves between L1 and L2 expansion. The same tendency is also found at the other holdout validation points, which are not shown for brevity.

Radial profiles of the root mean squared PCE prediction error as defined in Eq. (4.8) are displayed in Fig. 4.26 for the two expansion levels. At $z = 15$ mm mean prediction error stays
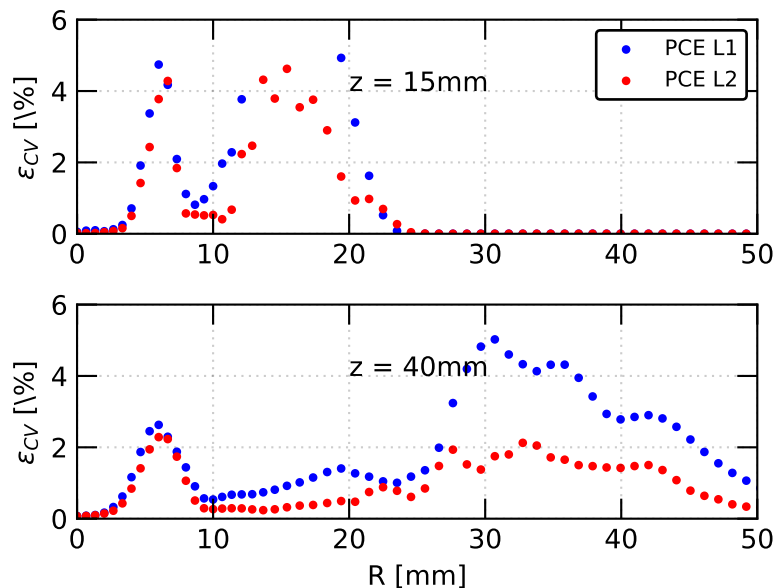
Figure 4.26.: Radial profiles of mean PCE prediction error from holdout validation.

below 10 % for the L1 expansion and reduces to 5 % for the L2 expansion. As for the GP surrogate model, maximum errors are found at the radial positions of maximum temperature gradients. At $z = 40$ mm prediction error stays below 2 % for the L2 expansion.

Based on these findings, the L2 PCE is used for the following forward propagation of input uncertainties.

Probability Bounds Analysis

Probability bounds for the temperature profiles under the given input uncertainties are inferred from space filling sampling of the PCE in lieu of the RANS model as already detailed in the previous section. Again, 10^4 samples are drawn following the same Latin Hypercube sampling as for the GP surrogate model.

Resulting temperature bounds are shown in Fig. 4.27. Similar uncertainty regions as in Fig. 4.23 are identified. A comparison of the two surrogate modeling strategies and detailed discussion and analysis of the output uncertainties will be given in the following section.

4.4.6. Step C: Discussion

In the previous sections, both Gaussian Process and Polynomial Chaos Expansion demonstrated their potential to enable non-intrusive propagation of uncertainties in a complex application case for the simulation of spray combustion. The assessment of surrogate model error using holdout validation verified that this is achieved with minor loss in accuracy compared to the high fidelity RANS simulation model. Both approaches revealed similar probability bounds for the temperature profiles when considering input uncertainties.

Comparing the PBA results from GP (Fig. 4.23) and PCE (Fig. 4.27), oscillating bounds in the PCE results around the peak temperature at $z = 15$ mm and $z = 20$ mm constitute the major difference between the two propagation strategies. These oscillations clearly coincide with high prediction errors as evident from Fig. 4.26 in which the holdout error peaks at the aforementioned radial positions. Hence, they are assumed to be a result of outliners in the uncertainty propagation.

Although prediction errors of the GP surrogate model are slightly lower than in the PCE case, it should be emphasized that GP prediction quality highly depends on the sampling strategy for the underlying training data. For the case at hand, this was demonstrated by the author in [59]. In contrast, PCE construction through sparse grid integration comes along with a fixed scheme for the evaluation of the high fidelity simulation ensuring a predetermined approximation order.

Since both strategies for surrogate modeling resulted similar probability bounds, the following discussion is solely based on the L2 PCE results displayed in Fig. 4.27 and aims at connecting the considerable uncertainties in the temperature profiles to the input uncertainties from Ω_{BC}.

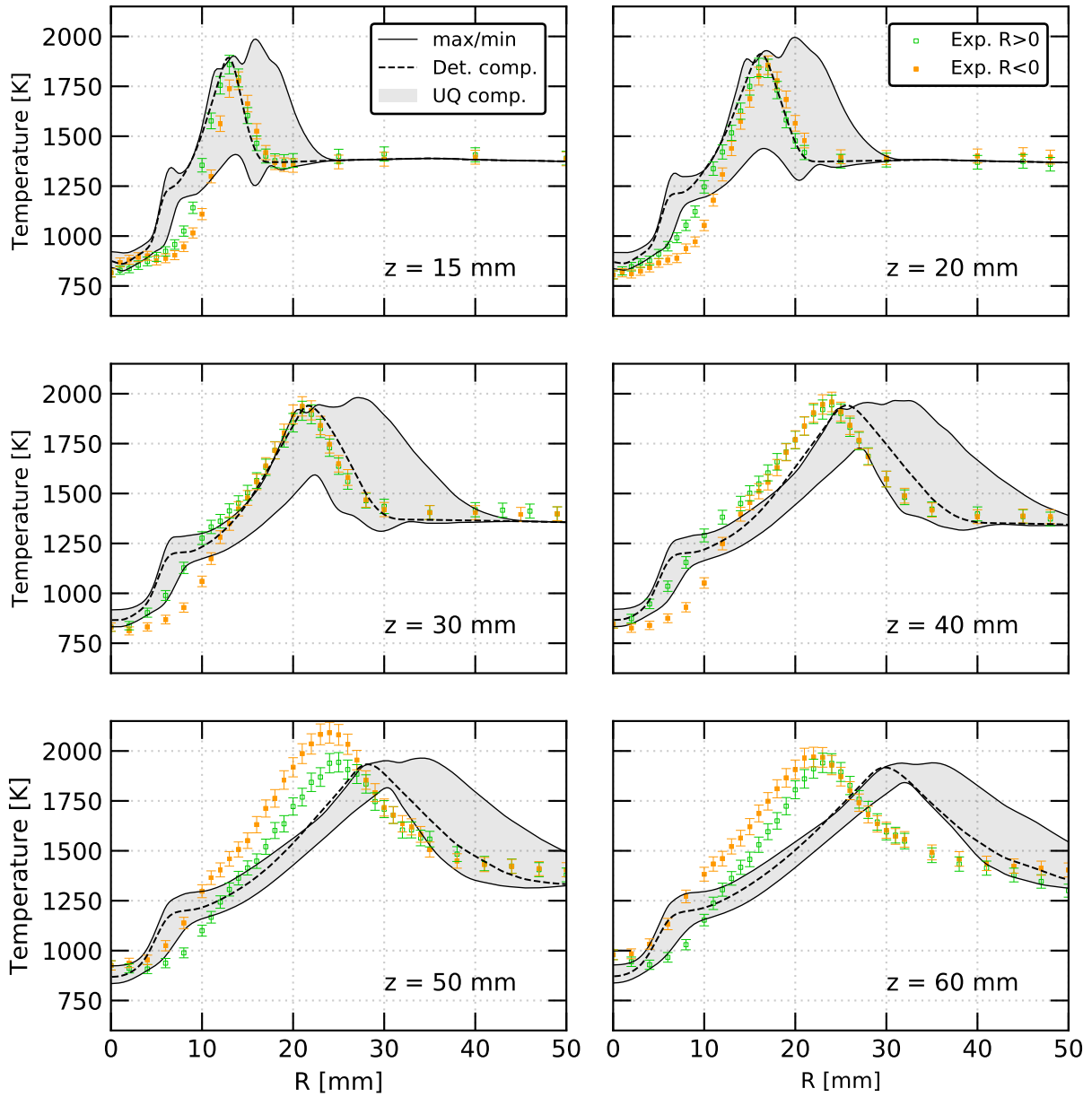Figure 4.27.: PCE based uncertainty regions and probability bounds for the temperature profiles.

Output uncertainties from PBA

In addition to the output uncertainties, regions exist in Fig. 4.27 where the UQ based simulation is unable to bracket the experimental data, especially at $5 < R < 10$ mm for $z = 15$ and 20 mm as well as for large parts of the flame zone at $z = 50$ and 60 mm. Reason for this could be further uncertainties which are not included in the analysis, a general model form error of the used simulation model or uncertainties and measurement errors in the experimental data which could be larger than reported. Since a major deviation between RANS and LES as well as notable numerical uncertainties were found in Sec. 4.2 for the inner flame zone at $z = 15$ and 20 mm, it is most likely that a modeling error in the RANS is propagated through the PCE surrogate model.

The fact that even by inclusion of the input uncertainties, the simulation is not able to capture the spread of the flame at the furthest downstream positions confirms the assumption from Sec. 4.3 that this is a general modeling error in the used simulation platform.

It should be pointed out that the bias in experimental data for $R < 10$ mm at $z = 30$ and 40 mm prohibits a definitive evaluation of simulation credibility at this position as experimental data for $R > 0$ mm is within the uncertainty region but not the portion from $R < 0$ mm.

Effects of parameter reduction

In order to assess the influence of parameter space reduction on the PBA results, an L2 Polynomial Chaos Expansion of the original parameter space Ω_{BC} is calculated and used for forward propagation, too. Resulting bounds are compared to the outcome of the reduced parameter space $\Omega_{BC,r}$ in Fig. 4.28. No significant deviations between the two bounded areas are observable, confirming that the parameter reduction does not affect the results of the PBA in the case considered. As already suspected in the MOAT analysis, the four parameters in $\Omega_{BC,r}$ essentially contribute to the variance in the temperature profiles. However, it should be pointed out that this conclusion only applies to the minimum and maximum bounds of the Quantities of Interest since the inner structures, i.e. the distribution functions of the output uncertainties, are not explored in PBA for strictly epistemic, interval-valued input uncertainties.

Computing time statistics for the different methods in the UQ process are summarized in Tab. 4.5. L2 PCE of Ω_{BC} corresponds to the aforementioned PCE based sampling of the full parameter space. Based on the statistics, it is deduced that the proposed workflow of parameter space reduction (MOAT) and sampling of the reduced parameter space $\Omega_{BC,r}$ already results in a notable reduction in computing time, although the parameter space is only slightly reduced from six to four parameters. Note that this reduction increases in cases with further parameter reduction.

In the following, results from the PBA over Ω_r are again used for further analysis.
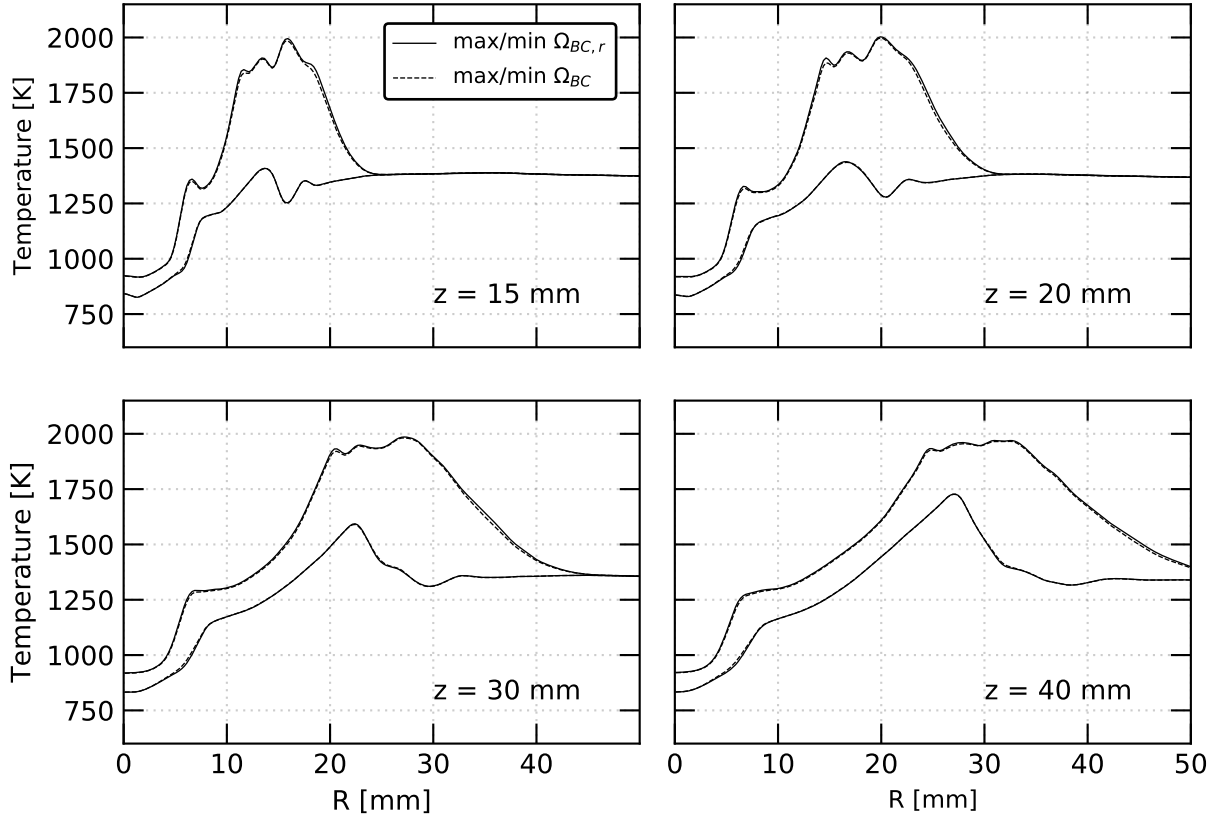
Figure 4.28.: Probability bounds of computed temperature profiles for the full (Ω_{BC}) and reduced ($\Omega_{BC,r}$) input parameter space.

Table 4.5.: Computing time statistics for the used UQ methods.

Case	RANS model evaluations	CPU hours [h]
L2 PCE of Ω_{BC}	97	32600
L2 PCE of $\Omega_{BC,r}$	49	16500
MOAT of Ω_{BC}	28	9500
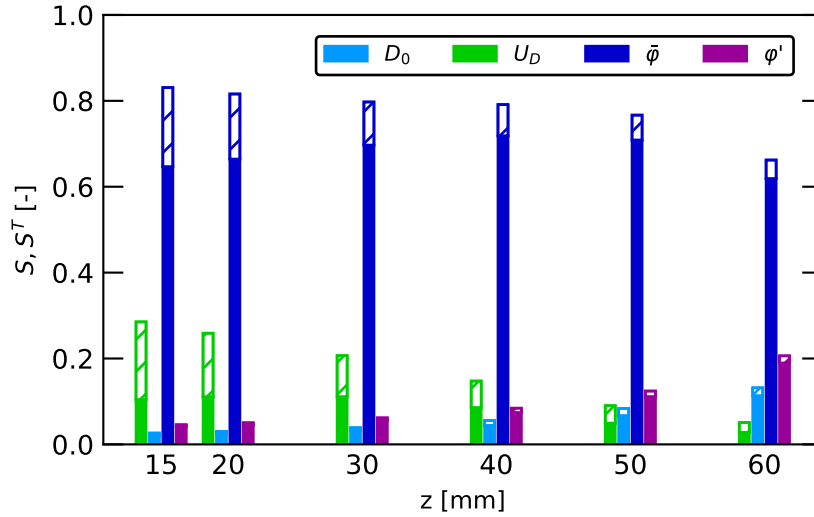
Figure 4.29.: Aggregated Sobol' indices for temperature at different axial positions. Hatched bars indicate total indices.

Posterior sensitivity analysis

To appraise the contribution of the uncertain input parameters to the high variance in the simulation results indicated by the uncertainty region, first order and total order Sobol' indices are derived from the coefficients of the PC expansion. For a simplified interpretation, indices are aggregated over the radial coordinate by weighting the local index $S_i(r)$ with the local variance in PCE temperature predictions [145]:

$$\boldsymbol{S}_i = \frac{\int_R \mathbb{V}\left[\mathcal{M}_{PCE}(r)\right] S_i(r)\mathrm{d}r}{\int_R \mathbb{V}\left[\mathcal{M}_{PCE}(r)\right]\mathrm{d}r} \tag{4.10}$$

Aggregated Sobol' indices $\boldsymbol{S}_i$ for temperature at different axial positions are given in Fig. 4.30. Solid bars illustrate first order indices $\boldsymbol{S}_i$, i.e. the direct contribution of a parameter to the variance, whereas augmented hatched bars indicate total indices $\boldsymbol{S}_{i,T}$ which include interactions with other parameters.

The mean injection angle $\bar{\varphi}$ is identified as the dominant parameter over all axial positions, causing more than 60 % of the variance in temperature. Close to the injector, the starting velocity U_D of the fuel droplets demonstrates some influence, yet with decreasing magnitude. The minor influence of the trajectory dispersion angle φ' rises with increasing z-position. It should be pointed out that differences between $\boldsymbol{S}_i$ and $\boldsymbol{S}_{i,T}$ are only observable for $\bar{\varphi}$ and U_D, which indicates a coupled effect between the two parameters.
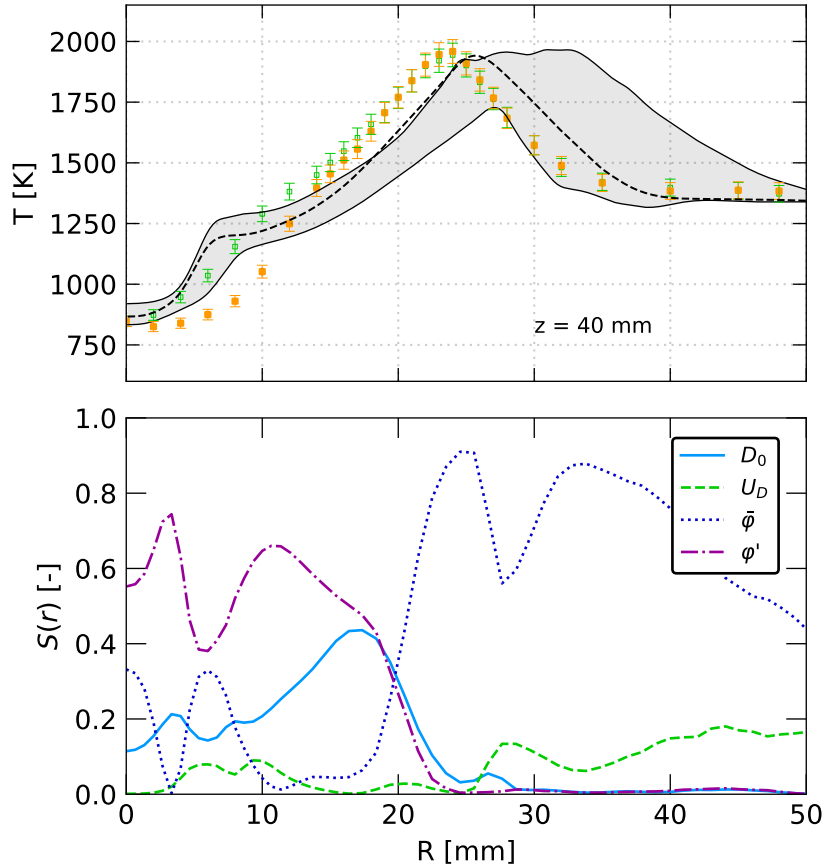
Figure 4.30.: Local Sobol' indices for temperature at $z = 40$ mm.

To clarify the influence of $\bar{\varphi}$, profiles of local Sobol' indices $S_i(r)$ are shown in Fig. 4.30 at an axial position of $z = 40$ mm. Highest first order Sobol' indices for $\bar{\varphi}$ are present at the outer flame region ($R > 25$ mm). Here, influence of other parameters are negligible. As $\bar{\varphi}$ corresponds to the spray cone opening angle, $\bar{\varphi}$ primarily determines the radial position of liquid droplets. In the outer flame region, this is closely connected to the supply of gaseous ethanol to the reaction zone. Consequently, changes in $\bar{\varphi}$ shift and stretch the temperature profile along R and cause high uncertainties in the outer flame region. In contrast, influence of $\bar{\varphi}$ decays in the inner flame region and the mean droplet diameter D_0 becomes more dominant. This reaction zone is formed by the fuel rich premixed reaction of ethanol vapor as a result of strong evaporation of droplets [141]. As D_0 is the only uncertain parameter directly connected to evaporation, it influences the evaporation process in this region and contributes to the variance in temperature. Note that the discussed phenomena are also found at the other axial positions.
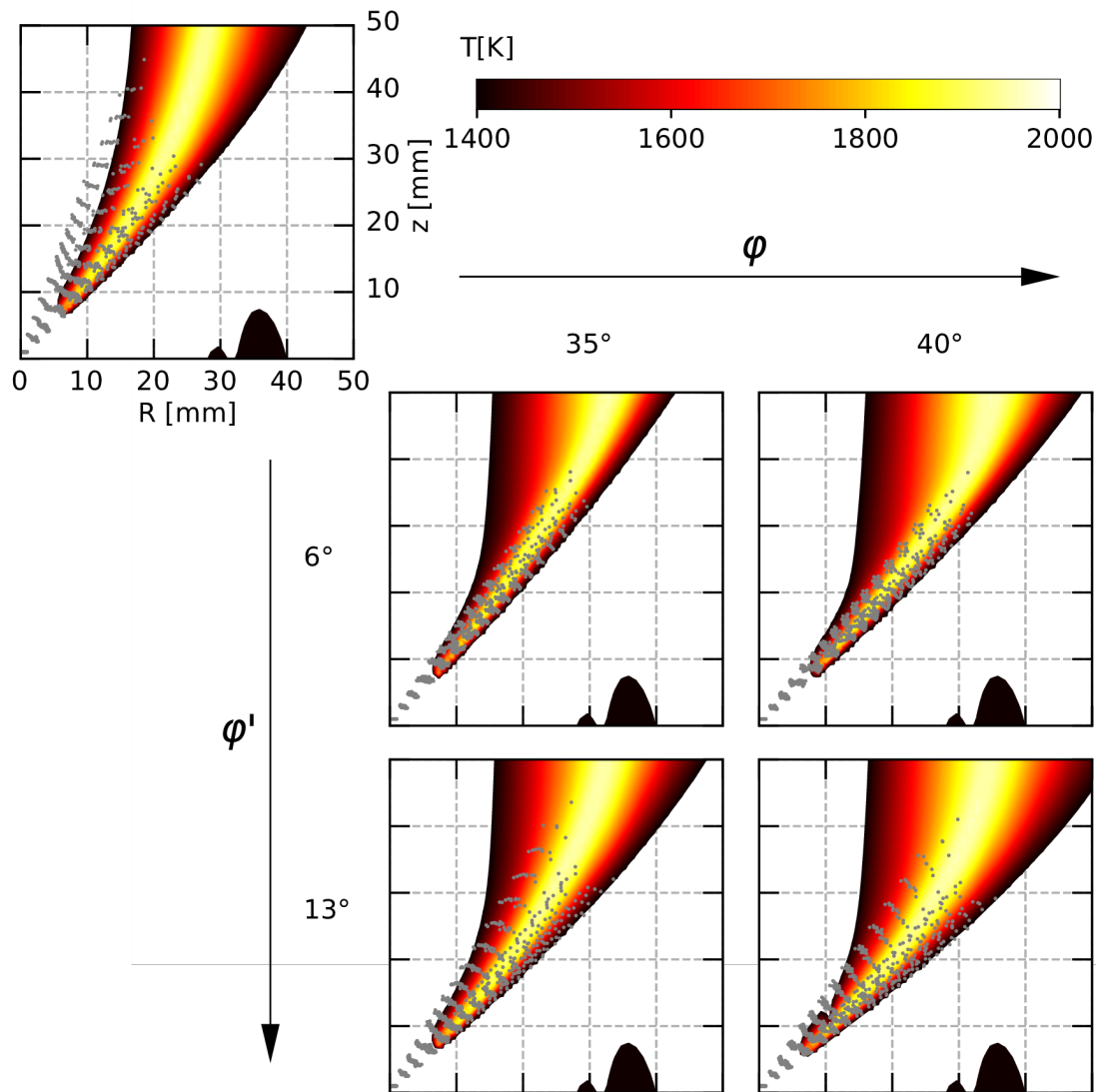
Figure 4.31.: Temperature contours in the flame zone for varying $\bar{\varphi}$ and φ'. Upper left plot shows the corresponding deterministic reference data.

Fig. 4.31 provides a global perspective towards the influence of $\bar{\varphi}$ and φ' on the flame position. Contours of gas phase temperature for varying $\bar{\varphi}$ and φ' are shown, as well as the deterministic reference data (upper left plot). For better visibility, only data exceeding the coflow temperature is shown, i.e. the flame zone. Mean droplet trajectories are indicated by gray dots. Clearly, the flame shifts towards higher radii with increased cone angle $\bar{\varphi}$. Furthermore, with increased dispersion angle φ' the flame thickness widens, especially at the lower axial positions.

Determination of total uncertainty

Finally, total uncertainty in the considered simulation is determined using the method of composite probability boxes (p-boxes) as introduced in Sec. 3.3.3. Due to the functional nature of the output Quantity of Interest, this is only illustrated exemplarily at three distinct points in the simulation domain. Results are presented in Fig. 4.32. A p-box consists of the cumulative distribution function (CDF) of the QoI which was obtained by propagating the input uncertainty with the help of the PCE surrogate model. Furthermore, numerical uncertainties Unc_{num} and PCE prediction errors ε_{PCE} from Sec. 4.4.1 and Sec. 4.4.5 are appended to both sides of the CDF. This is motivated by the epistemic nature of these uncertainties [210]. Again, the CDF from input uncertainties is given as brackets without a probability structure inside the p -box as a result of the interval-valued input. Owing to the deterministic approach, results from the reference simulation (see Sec. 4.4.1) are shown as Dirac pulses (dashed vertical lines).

At all three positions total predictive uncertainty is primarily due to the uncertainties in the simulation inputs. Additional PCE uncertainty is visible at the first two positions, while numerical uncertainties are negligible compared to the magnitude of Unc_{in}. Even when considering all three types of uncertainties, experimental data at $(z,R) = (40,17)$ mm (Fig. 4.32 (c)) cannot be met by the simulation which further affirms the presence of a general model form error. While the deterministic simulation accurately meets the experiment in Fig. 4.32 (b), the uncertainty quantification reveals notable uncertainties of 500 K at this position.

Figure 4.32.: Total uncertainty in temperature predictions characterized by probability boxes: (—) Unc_{in}, (—) $Unc_{in} + Unc_{num}$, (—) $Unc_{in} + Unc_{num} + Unc_{PCE}$, (- -) det. ref. simulation, (●) exp. $R > 0$ mm

5. DLR Standard Spray Burner

In this chapter, uncertainty quantification and probabilistic modeling are utilized to enhance the prediction quality of a simulation model w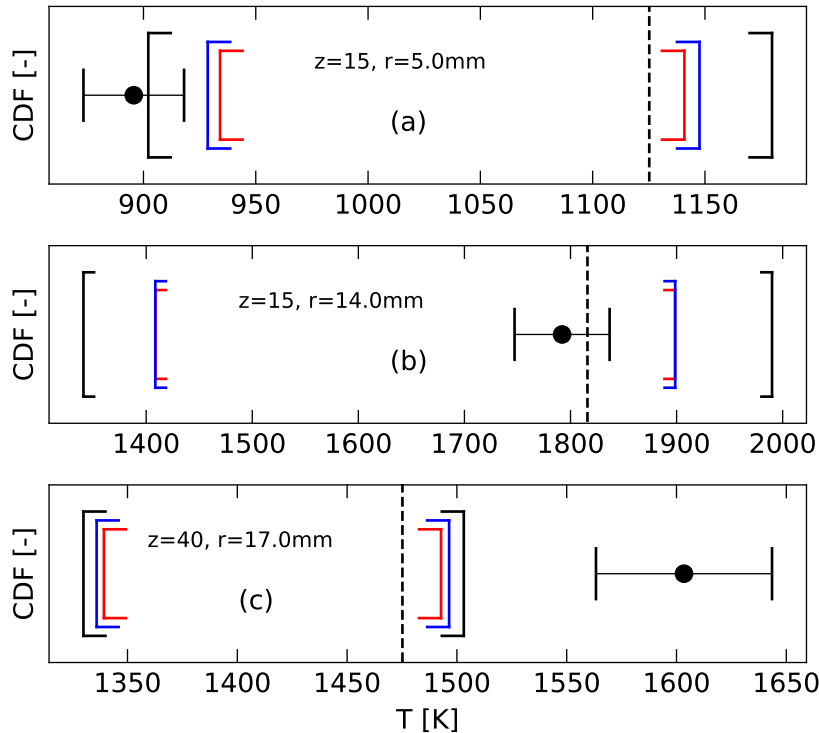hen only limited knowledge regarding the spray boundary condition is available. The testcase under consideration reflects characteristics typically found in aero-egine combustors. This includes, among others, a complex multi-component fuel, pre-filming airblast atomization, flame confinement through combustor walls and a swirl-dominated flow field for the purpose of flame stabilization. Certainly, all of these aspects increase the modeling demand and the simulation complexity compared to the DSHC case from Chapter 4.

In order to validate the simulation setup, a deterministic reference simulation using all available information from the experimental characterization is conducted, in which unknown parameters of the spray boundary condition are calibrated against the experimental data. Then, the calibrated spray boundary condition is replaced by a simple algebraic model for primary atomization. This gives rise to uncertainties in the model inputs which are propagated through the simulation by Polynomial Chaos Expansion. The clear portrayal of the output uncertainties finally allows for an assessment of the prediction quality of the simulation model.

5.1. Test case description

The DLR *Standard Spray Burner* (SSB) serves as a test case for the application of UQ methods to a semi-technical combustor under aero-engine relevant conditions. The SSB has been investigated experimentally by Grohmann [89] for a variety of single component fuels [88] as well as conventional Jet A fuel [22].

Figure 5.1 provides a sketch of the experimental apparatus. The combustor consists of two main parts: an air nozzle equipped with a pre-filming airblast atomizer and a rectangular combustion chamber. In the air nozzle, an inner and outer swirler consisting of quadratic swirl vanes provide air for secondary atomization and the formation of a co-rotating swirling flow inside the combustion chamber. Geometrical swirl numbers of $\mathrm{Sw}_i = 1.17$ and $\mathrm{Sw}_o = 1.22$ were reported for the inner and outer swirler, respectively [91]. In the center of the air nozzle, a primary pressure-swirl injector (Schlick Mod. 121) ejects fuel droplets onto the pre-filmer surface on which a liquid film evolves and finally disintegrates into a fine spray at the atomizing edge. At the exit plane, the inner and outer air nozzles have a diameter of $D_i = 8$ mm and $D_o = 11.6$ mm, respectively. The quadratic combustion chamber with a cross section of 85 mm × 85 mm and a height of 169 mm facilitates optical access to the reaction zone through four quartz glass windows. At the top, the cross section of the combustion

Jet A-1 flame

Swirl-stabilized burner

Pre-filming airblast atomizer
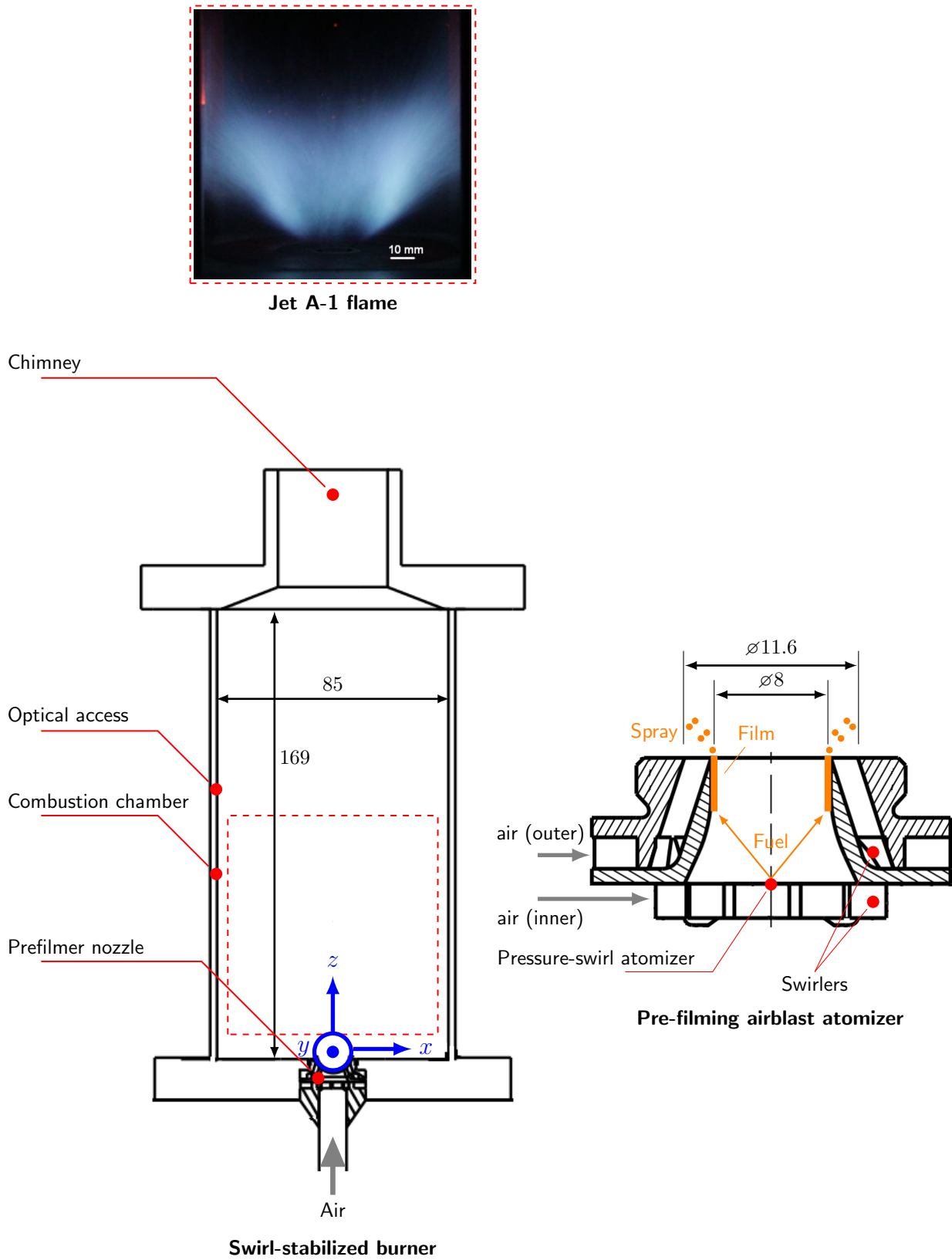
Figure 5.1.: Sketch and details of the swirl-stabilized *Standard Spray Burner* (adapted from Grohmann [89]).

Table 5.1.: Operating conditions of the baseline Jet A-1 case.

Fuel	Jet A-1		
Fuel temperature	T_f	303	[K]
Fuel mass flow rate	$\dot{m}_f$	850	[g/h]
Oxidizer	Air		
Air pressure	p_{air}	1.0	[bar]
Air temperature	T_{air}	323	[K]
Air volume flow rate	$\dot{V}_{air}$	200	[l/min]
Global equivalence ratio	ϕ	0.8	[−]
Thermal input	P_{th}	10.2	[kW]

chamber reduces to a duct (chimney) with 40 mm in diameter to ensure well defined outflow conditions.

The comprehensive experimental database for the SSB includes a characterization of the flow field from PIV, temperature profiles over the reaction zone obtained by CARS and dispersed phase data from PDA. Furthermore, a qualitative portrayal of the reaction zone is available from the line-of-sight integrated signal of CH* chemiluminescence. Due to the challenges for PIV in the presence of additional fine fuel droplets, PIV was only conducted for the non-reacting flow field.

In the work of Grohmann, a variety of operating conditions were investigated, ranging between 200 and 600 l/min air flow rate and air pre-heat temperatures up to 423 K. By variation of the thermal input, global equivalence ratios of $\phi = 0.6$ and $\phi = 0.8$ were realized. All experiments were conducted on an atmospheric test rig. For the work at hand, the *baseline* case for Jet A-1 as summarized in Tab. 5.1 is considered.

5.2. Numerical setup

The strongly swirling flow inside the SSB not only supports the favorable feature of enhanced fuel-oxidizer mixing and stabilization of the flame but also causes a hydrodynamic instability called *precessing vortex core* [90] (PVC). This term describes a highly transient, coherent structure found in the center of a swirling flow [255]. It has been shown [75] that steady-state RANS simulations using linear-eddy-viscosity turbulence models as discussed in Sec. 2.2.2 fail to reproduce such complex three-dimensional, unsteady flow features. It is therefore advisable to use an unsteady, scale resolving simulation approach. Although Eckel et al. [51] reported encouraging results for the SSB baseline case using LES, the associated computational burden restricts its application for UQ studies. As a consequence, a hybrid URANS/LES method based on the Scale Adaptive Simulation (SAS) approach (see Sec. 2.2.4) is utilized for the present study.

The compositional complexity of Jet A-1 [46, 202] is captured by the CTM vaporization model from Sec. 2.3.2. It approximates the wide range of species via distribution functions
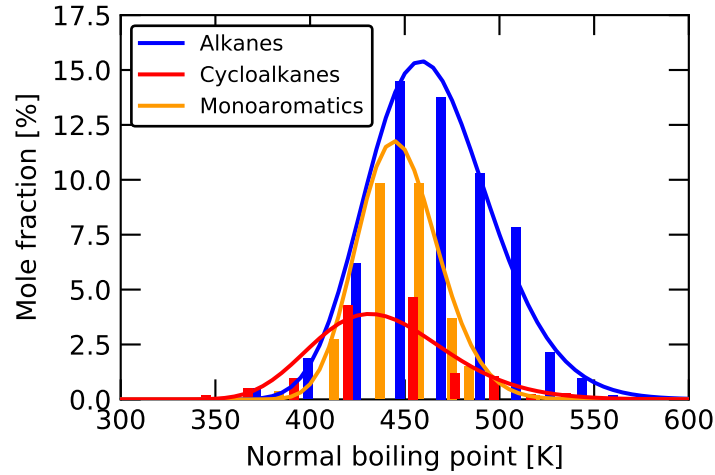
Figure 5.2.: Continuous description of Jet A-1 composition using 3Γ-PDFs. GCxGC data (bars), CTM fuel families (lines).

and representative species families. A Γ-PDF is chosen as distribution function and three species families are considered, namely normal-alkanes, cyclo-alkanes and mono-aromatics. The three PDFs are then calibrated to match the corresponding GCxGC chromatograhpy data [126]. A comparison between experimental data (bars) and CTM approximation (lines) is shown in Fig. 5.2 for the distribution of molar mass fraction over the normal boiling point.

After vaporization, species from the CTM fuel families are mapped to equivalent species in the gas phase. Normal-alkanes, cyclo-alkanes and mono-aromatics are assigned to normal-decane, iso-octane and toluene, respectively. These species form the main fuel species in a detailed reaction mechanism comprising 49 species and 300 reactions. The mechanism is based on the work of Slavinskaya et al. [240] and has been optimized for enhanced stability and computational speed using a linear transformation method [160]. Furthermore, a sub-mechanism for the formation of the OH* radical by Kathrotia et al. [115] is included. Although in the experiment, the reaction zone was qualitatively characterized by the signal of the CH* chemiluminescence, OH* and CH* are known to be closely located over a wide range of equivalence ratios [51, 193]. Chemical reactions and source terms are computed by the Finite Rate Chemistry combustion model in combination with the assumed PDF approach. It serves as a subgrid-scale closure in the LES regions and models the turbulence-chemistry interaction in the URANS regions. For the sensitivity analysis in Sec. 5.4, computational speed is increased by using the Eddy Dissipation Model instead of the detailed FRC combustion model. In this case, only global reactions for the three main fuel species are considered. These reactions are derived from the general scheme for hydrocarbon fuels proposed by Westbrook and Dryer [271].

Convective and diffusive terms are discretized through a second-order accurate central differencing scheme (CDS) while for the temporal discretization a second-order Three Point Backward (TPB) method is employed. A constant time step $\Delta t = 5 \cdot 10^{-6}$ s is set ensuring CFL numbers below unity. For all cases, the simulation is initialized over $\tau_{init} = 0.1$ s before

Figure 5.3.: Distribution of grid spacing in a central plane.

temporal statistics are collected over consecutive $\tau_{avg} = 0.1$ s. This is based on an estimation of the integral time scales inside the combustor and previous test simulations.

5.2.1. Computational domain and spatial discretization

The computational domain comprises the air nozzle, the quadratic combustion chamber and the outlet duct. Furthermore, the air plenum from which the preheated air is distributed to the swirler stages is included to obtain a well defined inlet region.

An unstructured grid consisting of approximately 1.2 million nodes or 5.7 million cells provides a spatial discretization of the computational domain. The grid mainly consists of tetrahedral cells augmented with 4 prismatic layers alongside the walls. In regions with a distinct flow direction (inlet plenum, swirler vanes, outlet duct) hexaedron cells are used. Figure 5.3 displays the relative distribution of grid spacing over the computational domain. Smallest cells are found in the swirler region, where element size ranges between 0.4 and 0.6 mm. Additional refinement is also given in the flame zone where the element size is in the magnitude of 0.75 mm. In the further downstream regions, cell size increases towards 3 mm.

Inlet boundary conditions for the oxidizer stream are summarized in Tab. 5.1. Wall temperatures were experimentally determined by phosphor thermometry. Following the results of Eckel [50], the bottom plate of the combustion chamber is divided into three zones in which the temperature boundary condition is set to constant values of 717 K, 901 K and 831 K, respectively. At the combustor sidewalls, a temperature profile in dependence of the axial direction is imposed. Details on the thermal boundary conditions are given in Appendix F.

5.2.2. Spray boundary conditions

For the deterministic reference simulation, the projection method from Sec. 2.4.2 is used to obtain a boundary condition for the spray of liquid droplets after atomization. An annulus with an inner radius of 3.5 mm and an outer radius of 4.5 mm defines the starting positions of the droplets. To account for the region of primary breakup close to the atomizer edge, the annulus is placed with an axial offset $\Delta z = 1.5$ mm with respect to the atomizer edge. A depiction of the starting annulus is given in Fig. 5.4.
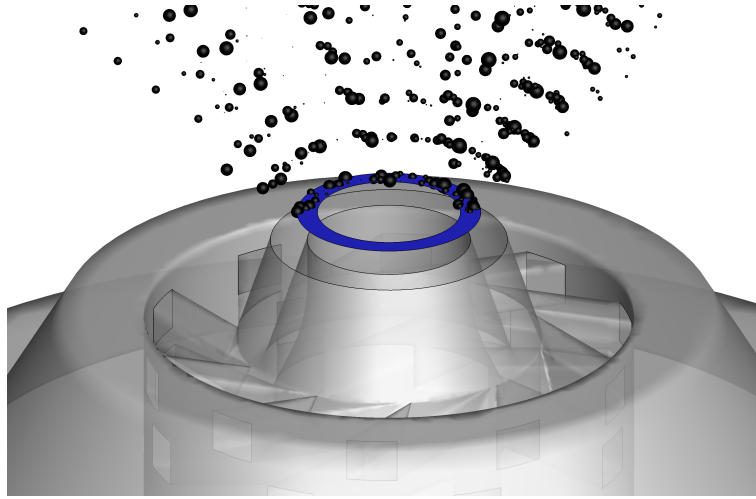
Figure 5.4.: Starting annulus (blue) for the droplets from the spray boundary condition.

Droplet data from PDA measurements at $z = 15$ mm is projected to 12 corresponding circumferential starting positions on the annulus. At all positions, a modified logarithmic Rosin-Rammler distribution function is optimized to fit the experimental data. Furthermore, droplet velocities and relative mass flow distribution are taken from the PDA measurements. During simulation runtime, droplets are sampled from the distribution functions and started at randomly distributed positions on the annulus. In total, $6 \cdot 10^7$ droplets are injected per second.

5.3. Deterministic reference simulation

Based on the described setup, a deterministic reference simulation is conducted. In order to validate the modeling setup, only main features for which experimental data is available are discussed. For a thorough analysis of the SSB baseline case, the reader is referred to the work of Eckel [50] and Grohmann [89].

Since the quality of Scale Adaptive Simulations strongly depends on the ability of the grid to locally resolve turbulent fluctuations and thereby switch into LES mode, the local spatial resolution must be reassessed for each problem under consideration. For this purpose, a first criterion is given by the ratio r_k of resolved to total turbulent kinetic energy. It is defined as

$$ r_k = \frac{\overline{k}_{res.}}{\overline{k}_{res.} + \overline{k}_{mod.}} = \frac{\frac{1}{2}\overline{u_i' u_i'}}{\frac{1}{2}\overline{u_i' u_i'} + \overline{k}_{mod}} \tag{5.1} $$

where $\overline{u_i' u_i'}$ denotes the time-averaged product of velocity fluctuations u_i', while $\overline{k}_{mod}$ is the modeled turbulent kinetic energy from the SST turbulence model. According to Pope [191], in a well-resolved LES this ratio should be at least 0.8, meaning that 80 % of the local turbulent kinetic energy budget is being resolved. Fig. 5.5 (a) shows the distribution of r_k over the computational domain for the reacting flow. The criterion is satisfied for the most parts of the domain, with exception of the inlet plenum and the swirler vanes, where a URANS solution is obtained.

(a) Ratio of turbulent kinetic energy
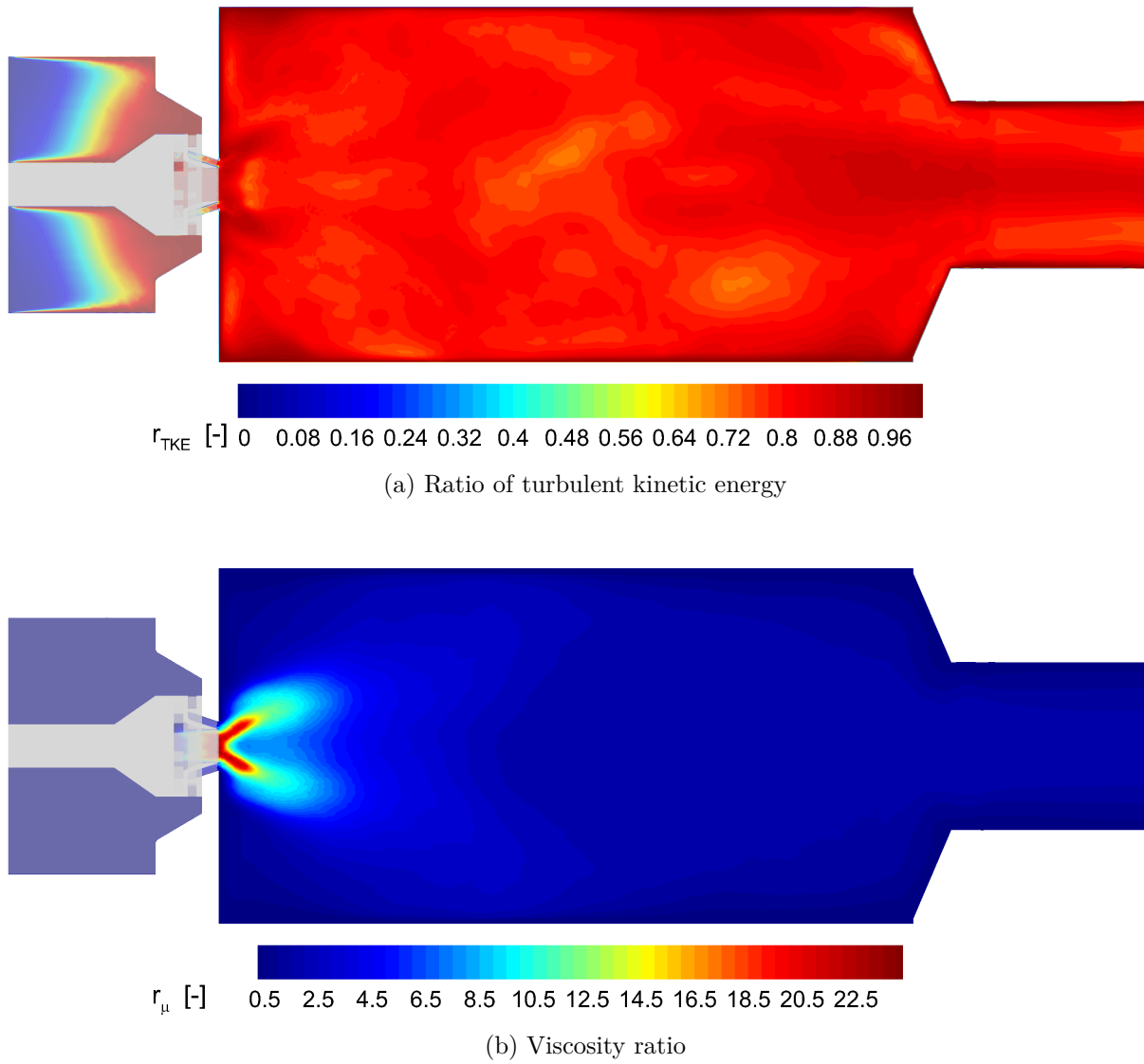
(b) Viscosity ratio

Figure 5.5.: Quality criteria for Scale Adaptive Simulation. Depiction in the $x - z$ plane

As a further criterion, the ratio of turbulent to molecular viscosity $r_\mu = \overline{\mu_t}/\overline{\mu}$ is calculated. In LES regions, this ratio should not exceed $\mathcal{O}(10^1)$ [105, 153]. From Fig. 5.5 it is evident that this is not the case for the core region of the air nozzle, whereas in the combustion chamber, the criterion is met. Since the primary region of interest is the reaction zone downstream of the air nozzle, it is concluded that the spatial resolution is sufficient for a Scale Adaptive Simulation of the SSB.

5.3.1. Non-reacting flow: Velocity field

Since PIV data is only available for the non-reacting flow field without spray injection, this case is considered at first. An overview of the structure of the flow field is given in Fig. 5.6 by means of contours of absolute velocity in the central $y - z$ plane. In the transient snapshot (Fig. 5.6 (a)), highest velocities are found inside the air nozzle, specifically at the nozzle exit where the flow reaches a maximum of $|U|_{\max} \approx 120 \mathrm{~m\,s^{-1}}$. This corresponds to a local Mach number of $\mathrm{Ma} \approx 0.34$ which is close to the limit of the incompressibility assumption [186]. The superimposed streamlines (gray lines) display a strongly turbulent and three-dimensional flow field with vortices shedding from the shear layer caused by the high local velocities at the exit of the air nozzle.

Figure 5.6 (b) displays the flow field averaged over the simulation runtime. Flow patterns typical for confined swirling flows [137] are observable: A small central recirculation zone (CRZ) is formed around $z = 0$ mm reducing the effective outflow area of the inner nozzle. As a consequence, velocity is increased along the prefilmer. Furthermore, a negative pressure gradient along the $z - $ axis causes a backflow and thus a large inner recirculation zone (IRZ) with a stagnation point at $z \approx 110$ mm. Finally, the back-pressure of the walls and the strong shear layer from the air nozzle establish a counter-rotating outer recirculation zone (ORZ).

(a) Transient   (b) Time-averaged
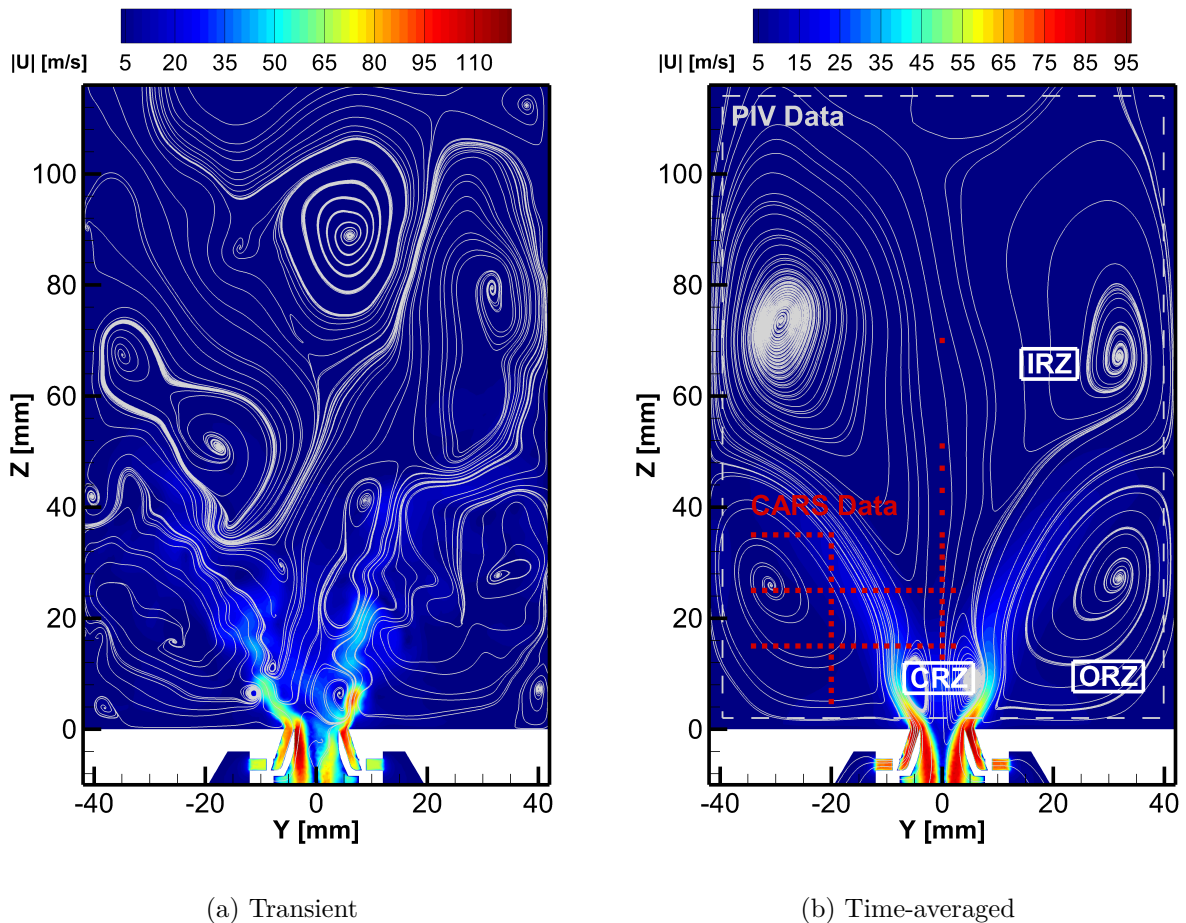
Figure 5.6.: Simulation results for absolute velocity and streamtraces of the non-reacting flow field.
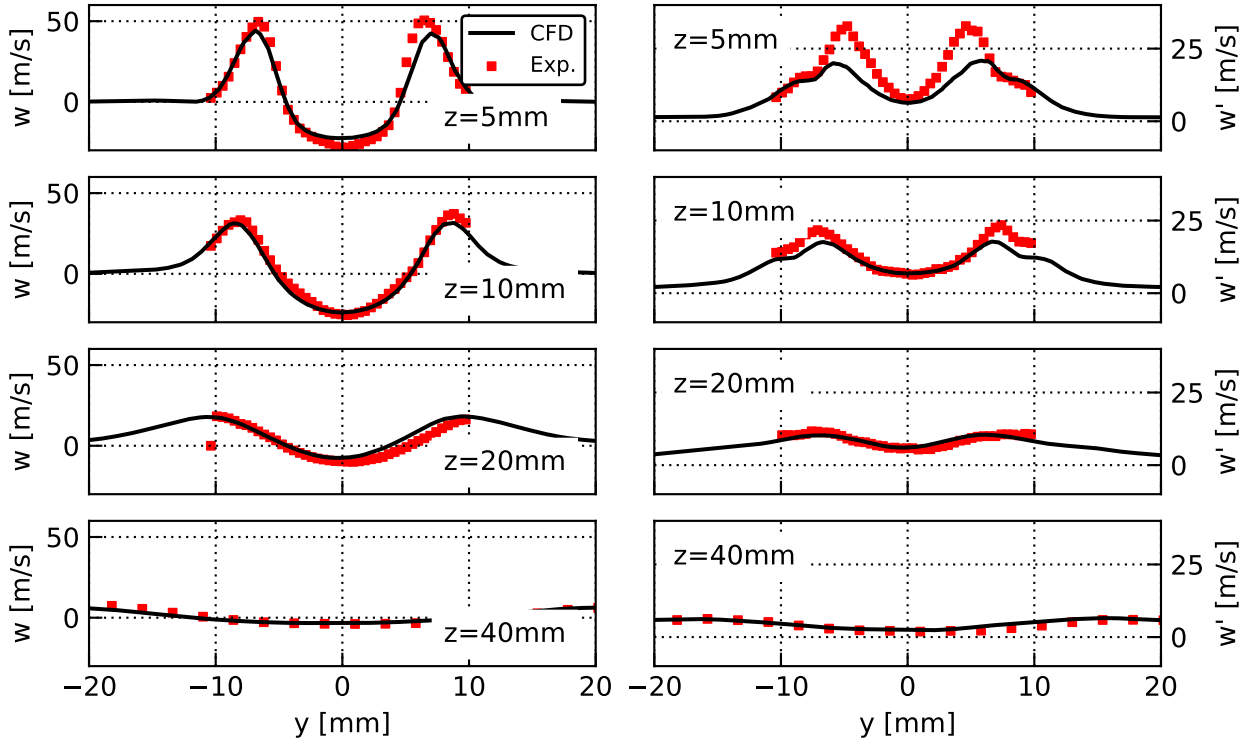
Figure 5.7.: Time-averaged profiles of axial (w) velocity component at different axial positions. Mean (left column) and fluctuations (right column).

Radial profiles of the velocity components from PIV enable a quantitative validation of simulation results. Figure 5.6 (b) indicates the region for which PIV data is available. A comparison of the time-averaged axial velocity and the respective RMS fluctuation is given in Fig. 5.7 by means of profiles along the lateral y-axis. Axial positions between $z = 5$ mm and 40 mm are considered as this region contains the main reaction zone in the following simulation of the reacting flow. For the mean velocity $\overline{w}$, simulation and experiment are in excellent agreement regarding magnitude and radial distribution. As aforementioned, a backflow along the z-axis ($y = 0$ mm) is visible. Regarding fluctuations $\overline{w'}$, the simulation underestimates the fluctuation intensity, specifically at $z = 5$ mm and $z = 10$ mm. Note that for the simulation, the displayed fluctuation is the total budget of resolved and modeled fluctuations:

$$\overline{w'}_{\mathrm{SAS}} = \overline{w'}_{res} + \overline{w'}_{mod} = \overline{w'}_{res} + \sqrt{\frac{2}{3}\overline{k}_{mod}}. \tag{5.2}$$

Thus, the underestimation could be a potential imbalance between resolved and modeled fluctuations as a result of the transition from URANS to LES mode of the SAS model, which was identified in the previous section.

Further comparison between experiment and simulation is shown in Fig. 5.8 and Fig. 5.9 for the v and u velocity components, respectively. Again, mean data is accurately reproduced by the simulation, while fluctuations are slightly too low, especially at the first axial position.
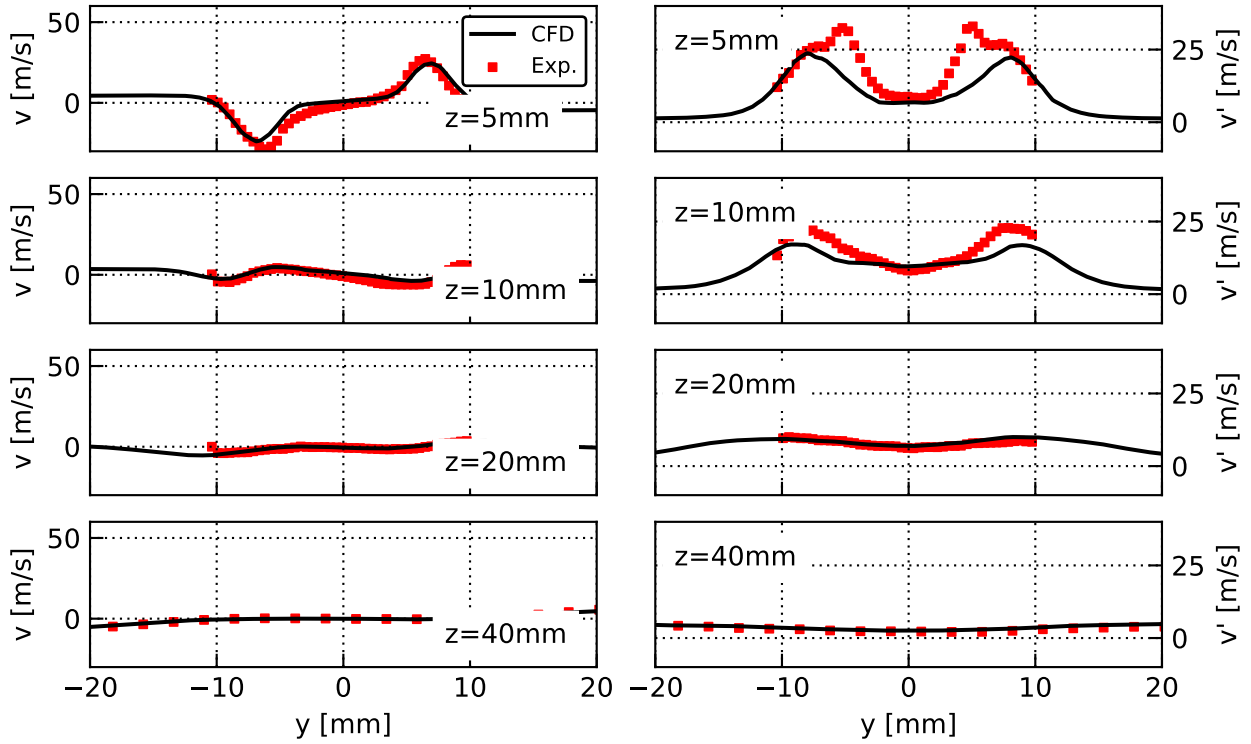
Figure 5.8.: Time-averaged profiles of v velocity component at different axial positions. Mean (left column) and fluctuations (right column).
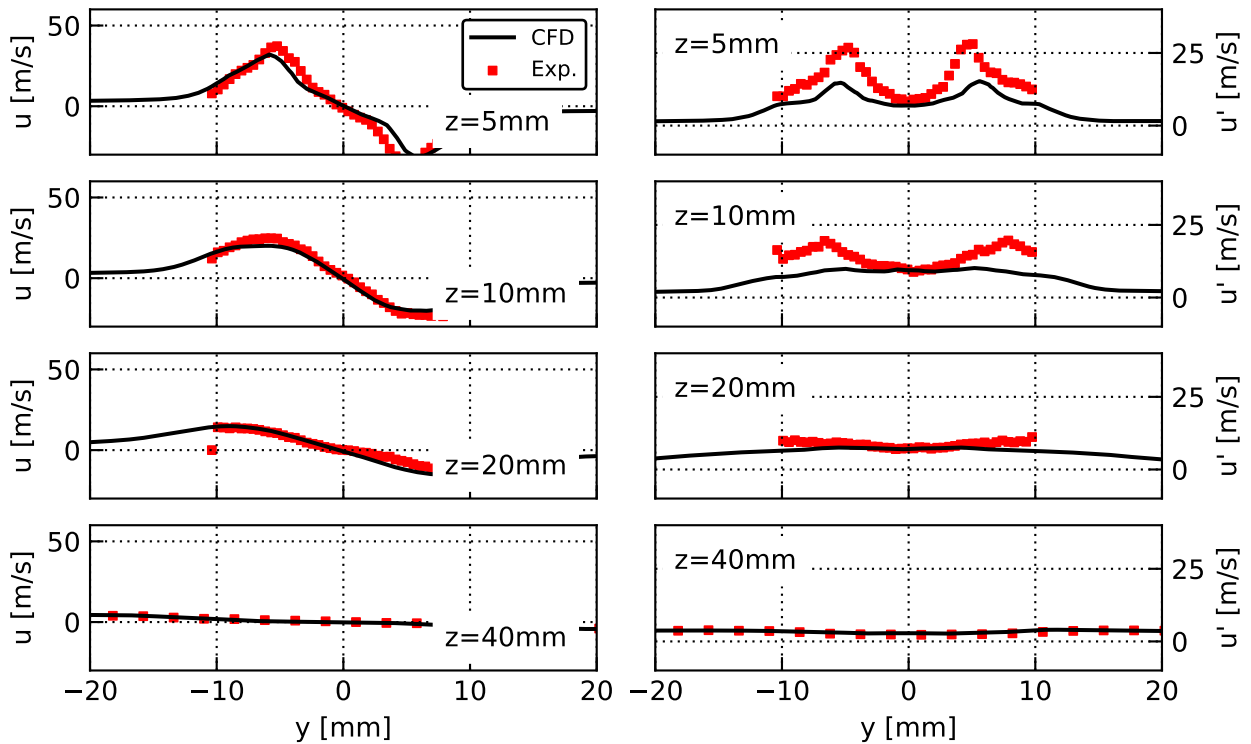
Figure 5.9.: Time-averaged profiles of u velocity component at different axial positions. Mean (left column) and fluctuations (right column).

5.3.2. Reacting flow: Gas phase results

All following results are obtained from the simulation of the reacting flow inside the SSB, including dispersion and evaporation of the spray. An impression of the combustion process is given by means of contours of gas phase temperature in Fig. 5.10. The transient snapshot in Fig. 5.10 (a) shows a wrinkled flame front, indicated by gray contour lines of heat release. In this flame front, fuel that has been transferred to the gas phase is consumed and local temperature increases significantly. Maximum temperature ranges in the order of $T_{max} = 2000$ K which is well below the maximum temperature $T_{max}^{adi} \approx 2250$ K in case of an adiabatic equilibrium. The reaction zone extends from $z = 5$ mm up to $z = 40$ mm. Hot gases from the flame front accumulate in the outer recirculation zone and are partly transported back to the centerline by large eddies from the inner recirculation. Close to the exit of the air nozzle, these hot gases mix with the cold air flow. With increasing axial distance from the reaction zone, the temperature field becomes more homogeneous.

In the time-averaged field of gas phase temperature (Fig. 5.10 (b)), an M-shaped cold inner zone with axially increasing temperature is visible as well as local hot spots in the outer recirculation zone. In the vicinity of the walls, the influence of the isothermal boundary condition is observable.

(a) Transient
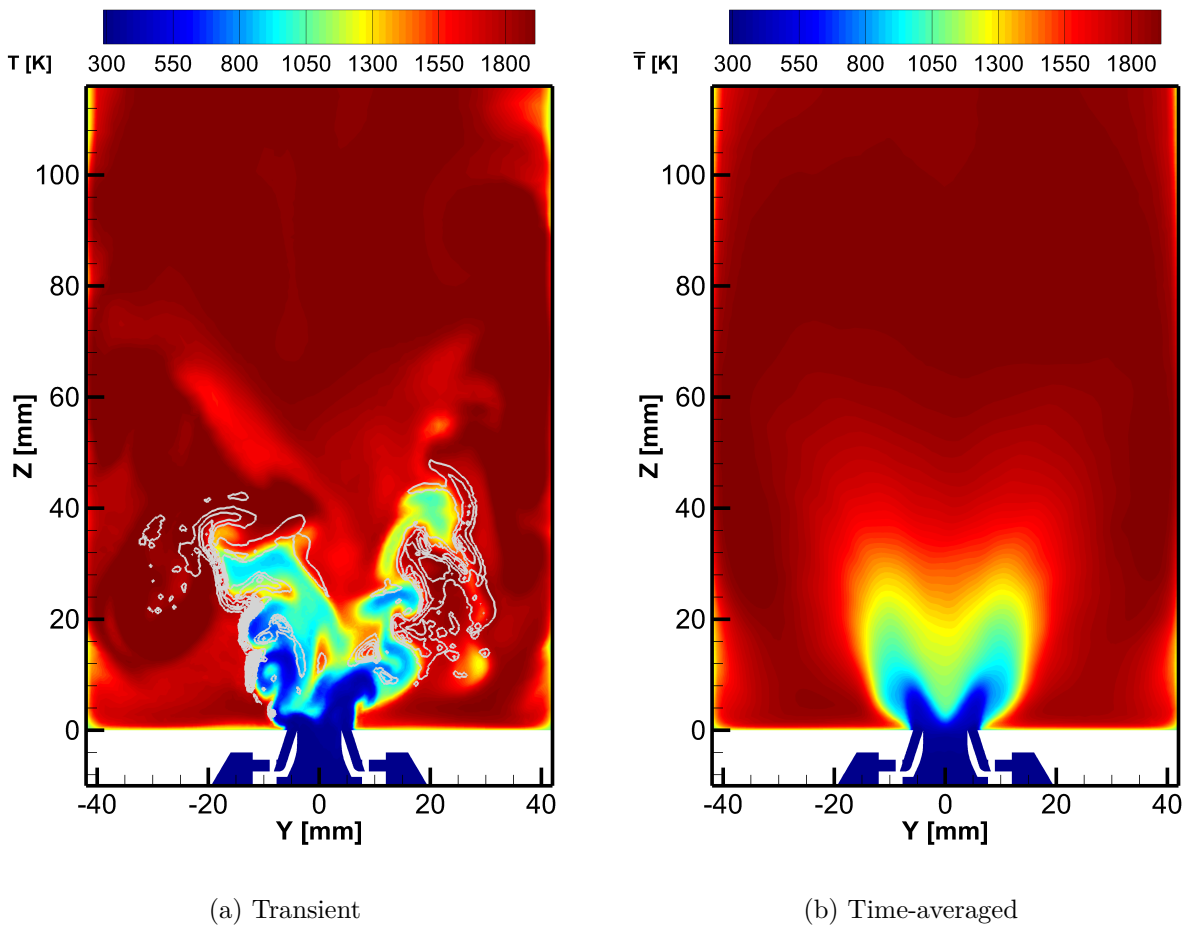
(b) Time-averaged

Figure 5.10.: Simulation results for gas phase temperature of the reacting flow field. Gray lines indicate heat release.

Further insight into the structure of the reaction zone is given by means of time-averaged images of the CH* chemiluminescence from the experiments. Due to the applied measurement technique, these images show the line-of-sight integrated signal along the optical axis of the camera (y-axis). For an adequate comparison with the experimental data, the spatial distribution of OH* in an observation box that resides in the reaction zone is integrated along the y-axis. This results in a corresponding line-of-sight signal (LOS)[1]. Results from simulation and experiment are given in Fig. 5.11. Note that in all images from this series, the signal is normalized to its respective maximum for a better comparison.

Figure 5.11 (a) provides a transient snapshot of the OH* LOS from the simulation. A highly wrinkled structure is visible, mostly ranging from $x = -20$ mm $x = 20$ mm, with an axial extent up to $z = 50$ mm. Time-averaging of this signal results in the distribution shown in Fig. 5.11 (b). A slightly lifted-off and V-shaped flame is observed with two spots of high intensity around $x = \pm 20$ mm. Under the assumption of rotational symmetry around the z-axis, these spots stem from a toroidal zone of maximum reactivity between $z = 20$ mm and $z = 30$ mm, i.e. the main reaction zone. The equivalent experimental result is given in Fig. 5.11 (c). A broader radial extent of the reaction zone is noticeable as well as a slight tilt around the y-axis, in contrast to the strong symmetry in the simulation data. In the work of Grohmann [89] this was traced back to radial asymmetries in the spray distribution (see also Fig. 5.17).

---

[1]Further details are shown in Fig. F.2 in Appendix F.
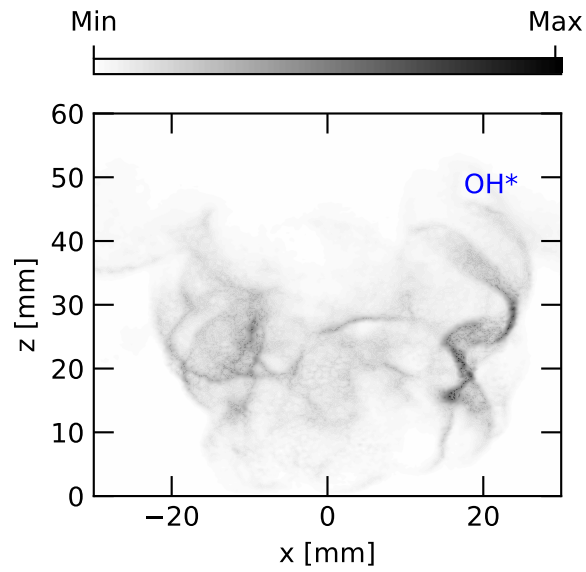
(a) Simulation - transient
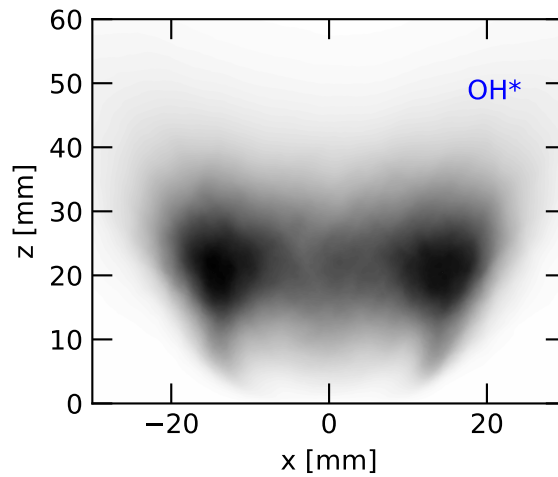
(b) Simulation - time averaged
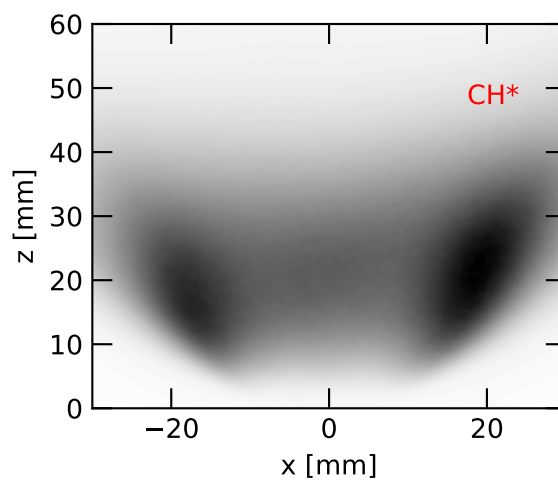
(c) Experiment - time averaged

Figure 5.11.: Line of sight integrated OH^* distribution (simulation) and line of sight integrated CH^* chemiluminescence signal (experiment).
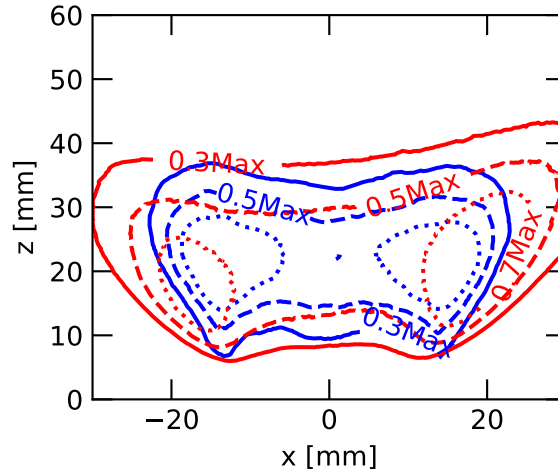
Figure 5.12.: Comparison of line-of-sight integrated OH* distribution from the simulation (—) and CH* chemiluminescence from the experiment (—). Contours show relative levels of 0.3 (solid), 0.5 (dashed) and 0.7 (dotted) maximum intensity.

Figure 5.12 presents a more quantitative comparison of the chemiluminescence LOS. Three contour levels referring to 30%, 50% and 70% of the corresponding maximum intensity of the time-averaged signal are drawn. Regarding the axial extent, the simulation agrees well with the experiment for all three levels. However, as aforementioned, the opening angle of the V-shaped flame is somewhat lower in the simulation. This tendency was also reported by Eckel et al. [51]. They mentioned that despite the fact that OH* and CH* chemiluminescence are generally located very close to each other in the reaction zone [116], studies from one-dimensional flame configurations [193] have shown that the peak of the OH* profile slightly shifts towards the lean side, whereas the CH* peak appears towards the fuel rich side [51]. In the present configuration, this would correspond to a shift of the OH* peak towards the centerline.

In the experiment, local temperature data was collected along radial and axial profiles in the $y - z$ plane. CARS measurement positions are included in Fig. 5.6 as red squares. A comparison of this data with the present simulation is shown in Fig. 5.13 (a) - (e).

At the first two axial positions (Fig. 5.13 (a) - (b)), simulation and experiment agree very well in the colder inner region ($y < \pm15$ mm) and the slope of the following temperature gradient is accurately reproduced. This gradient relates to the region of maximum reactivity (see Fig. 5.12). However, peak temperatures at these positions are overestimated by at least 100 K. In the vicinity of the walls, the isothermal boundary condition forces a steep temperature gradient.

At the further downstream position ($z = 35$ mm, Fig. 5.13 (c)) temperatures from the simulation are higher than the experimental measurements at all positions, although the general tendency in the experimental data is replicated in the simulation.

The fact that the simulation is able to predict the inner region around the z-axis with high precision is also reflected in the axial profile along the center line from Fig. 5.13 (d). Up to
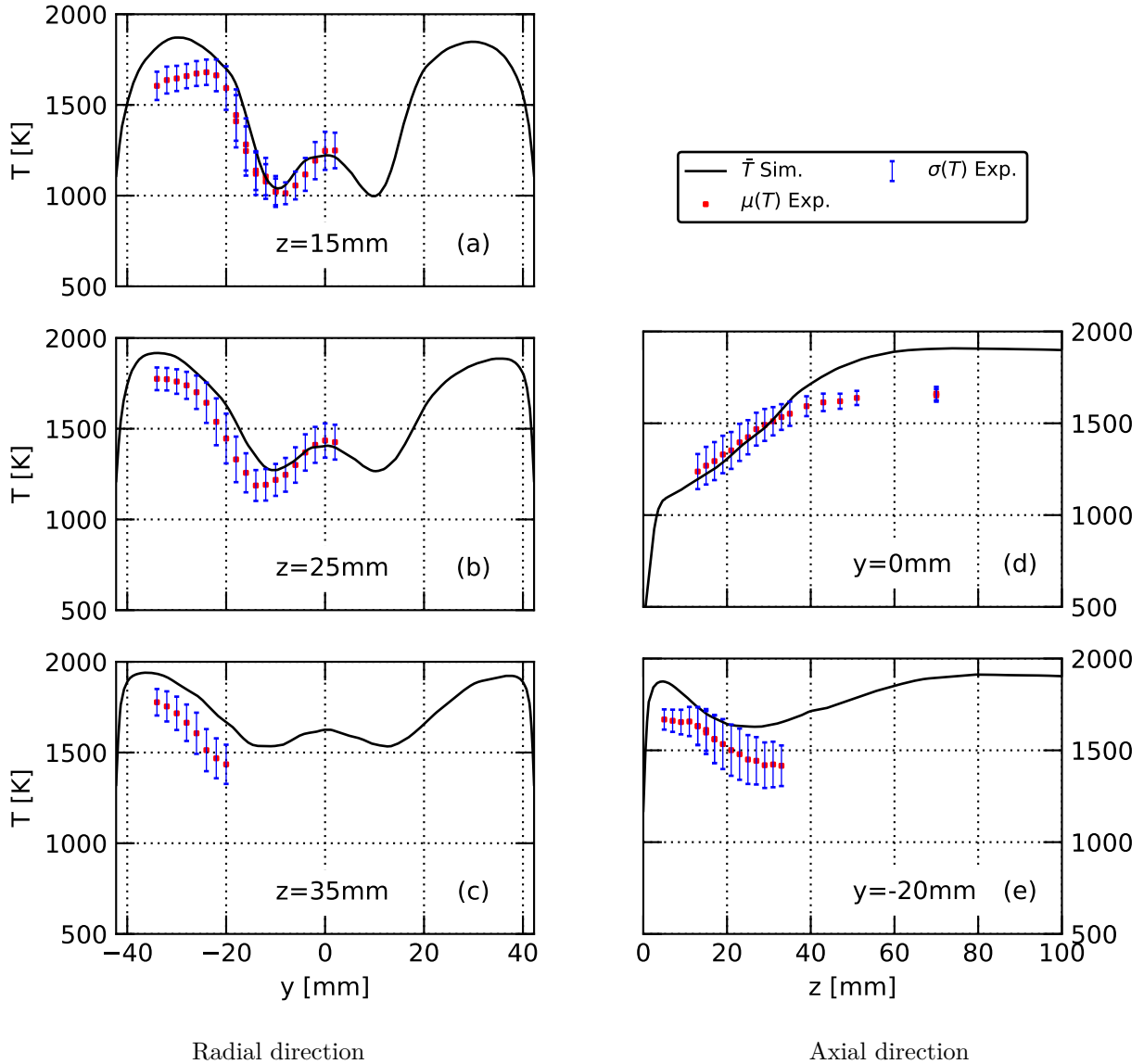
Figure 5.13.: Time-averaged temperature profiles from simulation and experiment. Mean (■) and standard deviation (−) from CARS data.

$z = 35$ mm the simulation matches the experimental data, demonstrating an almost linear rise of temperature in this region. Downstream from $z = 40$ mm, temperature stagnates in the experiment whereas the simulation predicts a further increase up to $z = 60$ mm. Due to this fact, the mean temperature close to the outlet is presumably $150 - 200$ K higher than in the experiment. Since this tendency is also found in the axial profile at $y = -20$ mm, this could be caused by too low thermal losses in the simulation of the combustion chamber.

Since the experimental data in the axial profile at $y = -20$ mm (Fig. 5.13 (e)) corresponds to the outer recirculation zone, the overestimation of temperature in the simulation could be a result of a too low cooling effect of the isothermal walls at the ORZ. Nonetheless, the axial slope of the temperature at $z < 30$ mm is reflected in the simulation.

(a) Droplet temperature   (b) Relative liquid mass flow rate
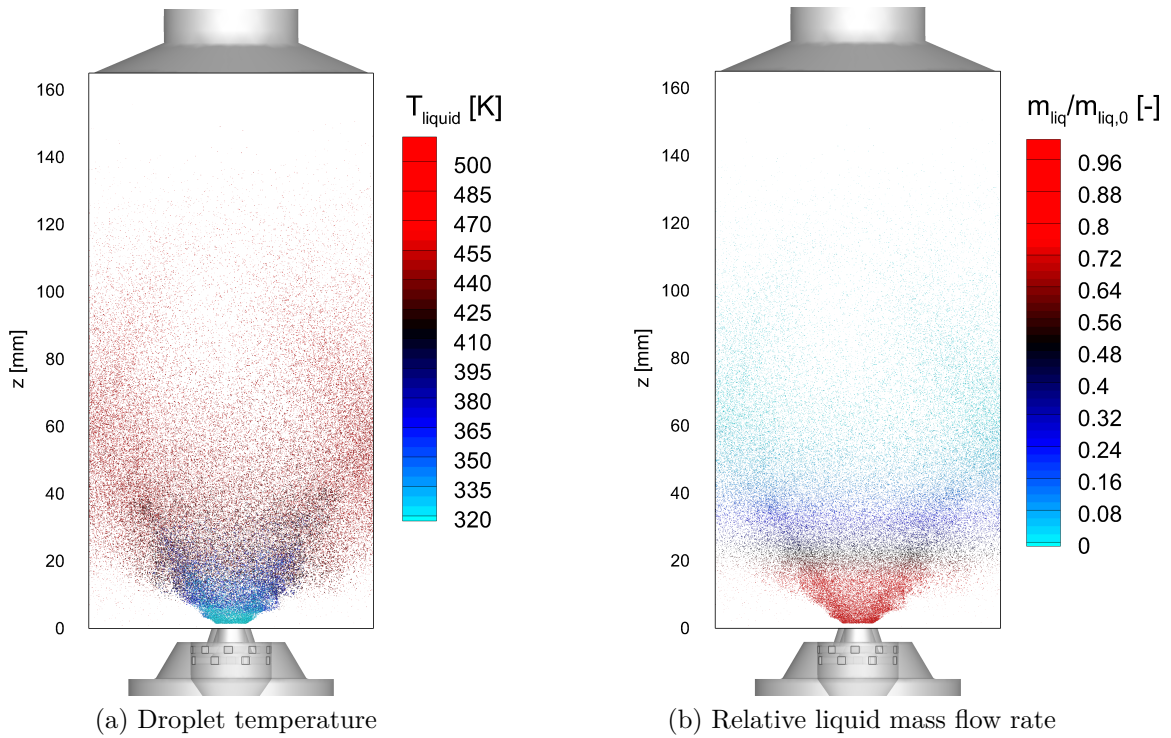
Figure 5.14.: Instantaneous snapshots of the spray distribution inside the combustion chamber.

5.3.3. Reacting flow: Dispersed phase results

Figure 5.14 provides an impression of the spray dispersion inside the combustion chamber by an instantaneous snapshot of the liquid droplets. The spray emerges from the injection plane of the boundary condition above the atomizer in a conical shape. As evident from Fig. 5.14 (a), the droplets are subject to a fast heat up within the first 20 mm, i.e. the main reaction zone. Afterwards, some droplets impinge the windows and distribute further downstream as liquid impingement is treated as fully elastic collisions within the dispersed phase solver. However, this spatial distribution of droplets must be interpreted with respect to the relative mass flow in the dispersed phase. This is shown in Fig. 5.14 (b), where $\dot{m}_{liq}/\dot{m}_{liq,0}$ indicates the ratio of local liquid mass flow $\dot{m}_{liq}$ to the initial liquid mass flow $\dot{m}_{liq,0}$ at the spray boundary condition. It is observable that within the first 20 mm above the atomizer, 50 % of the liquid fuel evaporates and downstream of $z = 40$ mm less than 10 % of the initial mass is kept in the dispersed phase. Therefore, only a small amount of droplets impinge the walls and reach an axial position greater than 50 mm above the atomizer.

Figure 5.15 reflects the process of multicomponent evaporation of the Jet A-1 droplets inside the combustion chamber. For this purpose, instantaneous liquid properties of 10^5 particles from a single simulation timestep are analyzed. Liquid mass fractions of the three CTM fuel families are plotted against the droplet temperature. Furthermore, scatter points are colorized with respect to their axial position. Clearly, droplets with a starting temperature of 320 K heat up to approximately 400 K before the evaporation process starts. At first, cycloalkanes evaporate, followed by the monoaromatics and alkanes. This is caused by the difference in vapor pressure and latent heat of vaporization among the three fuel families [50, 202]. The
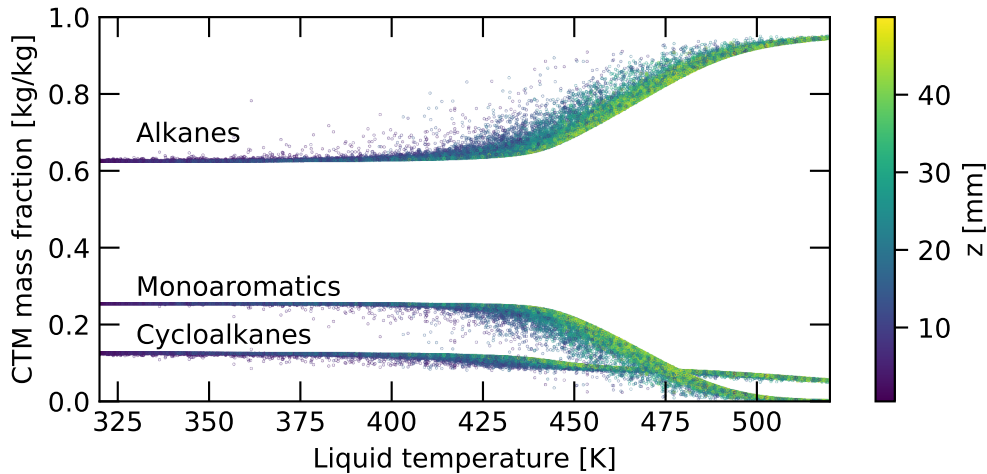
Figure 5.15.: Multicomponent droplet evaporation in the swirl-stabilized spray burner. Scatters represent transient properties of liquid particles.

superimposed axial position confirms that the initial heat up of the droplets mostly takes place at $z < 10$ mm.

In order to validate the spray boundary condition, statistics of the dispersed phase are collected and time-averaged in two registration planes at $z = 15$ mm and $z = 25$ mm which are parallel to the $x - y$ plane. Figure 5.16 provides a comparison between simulation and PDA data (experiment) for the components of droplet velocity. The three components are defined with respect to the global coordinate system. Thus, axial, radial and tangential velocity are derived from the global z, y and x velocity, respectively. Obviously, the droplets experience a swirling motion in the mathematical positive direction with respect to the z-axis, as they couple to the gas flow (see Fig. 5.7-5.9). Droplet data from the simulation is subdivided into three distinct diameters $(10, 30, 50$ µm) to display the droplet dispersion. A ± 10 % margin is added for a better statistical convergence. Therefore, the three size classes are defined as 10 µm $< d < 11$ µm (*small*), 27 µm $< d < 33$ µm (*medium*) and 45 µm $< d < 55$ µm (*large*). In contrast, from the PDA measurements only averaged data regarding the droplet diameter is available.

In general, magnitude and profiles of the velocity components are well reproduced by the simulation. Concerning axial and radial velocity, best agreement is found regarding the large droplets. Medium droplets demonstrate the best match for the tangential component. Similar tendencies are found at $z = 25$ mm. Corresponding results are given in Fig. 5.16 in Appendix F.
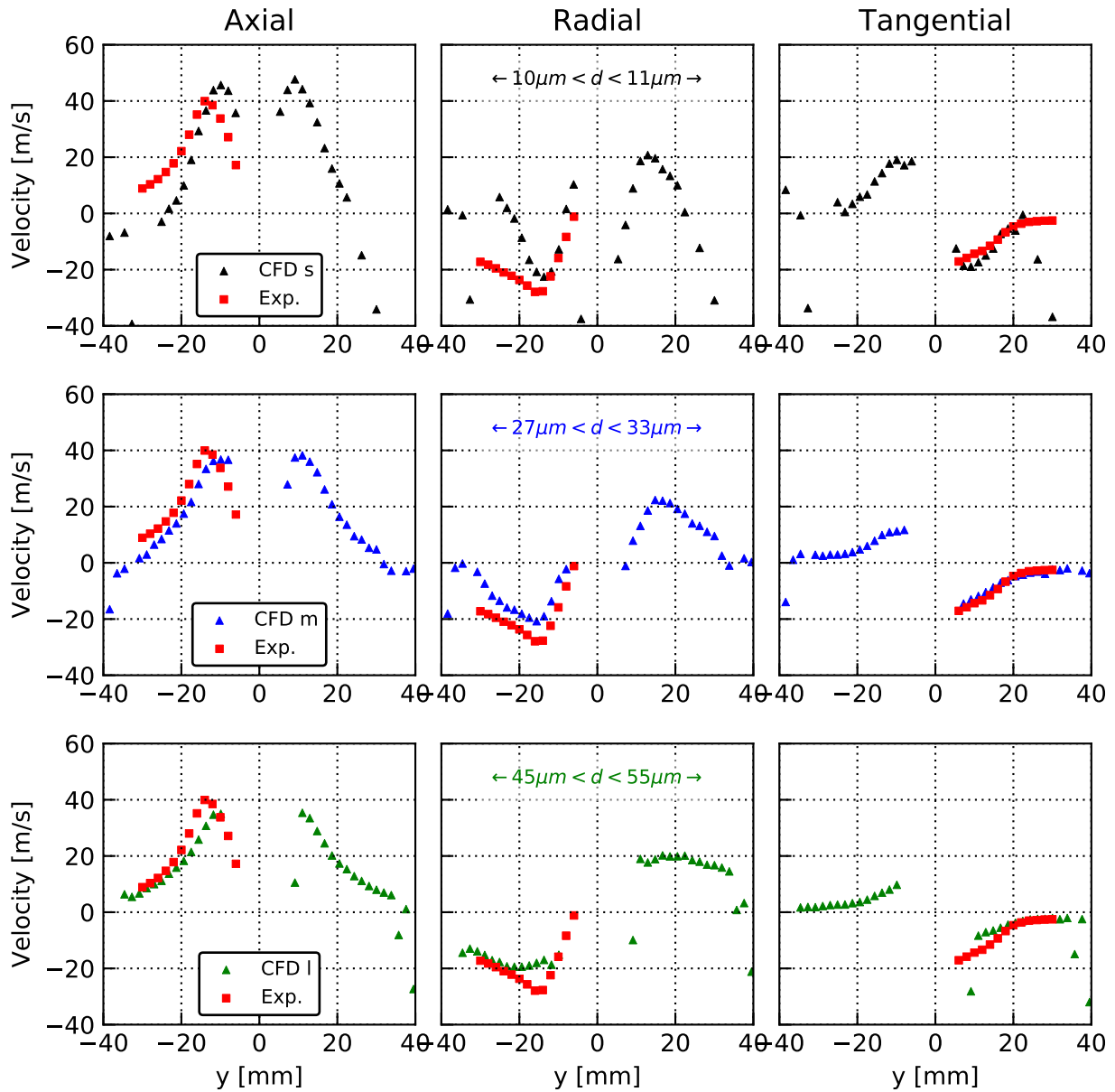
Figure 5.16.: Time averaged profiles of droplet velocity components at $z = 15$ mm. Simulation data is split into small (▲), medium (▲), and large droplets (▲). Experimental data (■) is averaged over all diameters.
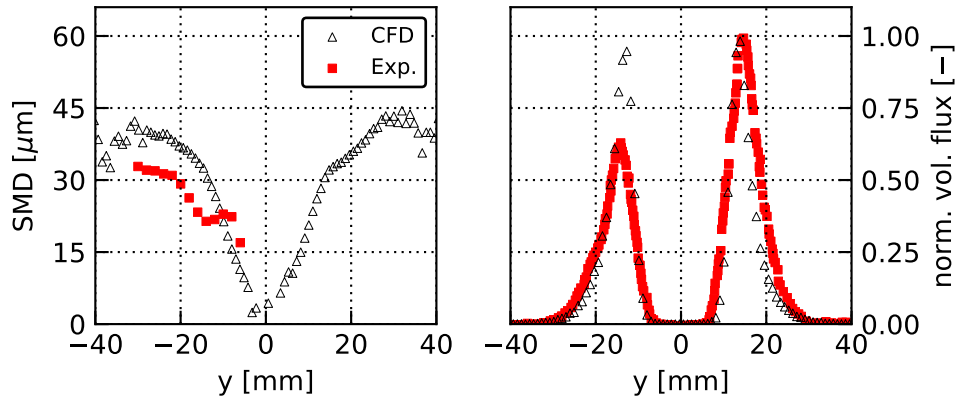
Figure 5.17.: Time averaged profiles of Sauter Mean Diameter (SMD) and normalized liquid volume flux at $z = 15$ mm.

Further spray characteristics are compared in Fig. 5.17 by radial profiles of Sauter Mean Diameter (SMD) and normalized liquid volume flux at $z = 15$ mm. Although experimental data for the SMD ranges between 17µm and 32µm, the simulation predicts a maximum SMD of 40µm and a minimum of 15µm. However, the SMD profiles must be interpreted with respect to the volume flux data for which simulation and experiment are in good agreement. Close to the z-axis ($y = 0$ mm), the SMD in the simulation reaches its minimum while the volume flux drops to almost zero. Therefore, these droplets relate to a very low volume flux. In contrast, at the positions of maximum volume flux ($y \pm 17.5$ mm), the deviation between experiment and simulation is in the magnitude of 5 µm. As already pointed out in the previous section, the experimental data indicates a strong asymmetry in the spray distribution of the prefilming atomizer. This is also evident from the distribution of normalized volume flux. According to Grohmann et al. [90], the asymmetry could have been caused by a non-uniform spray cone created by the primary pressure-swirl atomizer as a result of manufacturing inaccuracies.

5.4. Probabilistic modeling and uncertainty quantification

The previous section demonstrated that by inclusion of all available experimental information concerning initial and boundary conditions, the used simulation models are able to reproduce all aspects of spray combustion in the SSB with high accuracy. However, for a *predictive* simulation, the required *a priori* knowledge about the system under consideration should be reduced to a minimum in order to obtain an unbiased result. This refers to a model prediction which is as independent as possible from prior knowledge regarding the simulation results obtained from the experiment. The reduction in prior knowledge can then be compensated through probabilistic modeling and uncertainty quantification methods to portray the best possible prediction given the current knowledge about the system under consideration. For this purpose, the workflow for uncertainty quantification is applied to the SSB case as detailed in Fig. 5.18. Relevant sources of uncertainties are identified and characterized, followed by a MOAT screening to identify potentials for a reduction of the parameter space of uncertain inputs. Polynomial Chaos expansion is utilized for the propagation of the input uncertainties through the simulation model. Gas phase temperature, flame position and liquid droplet distribution are assessed as quantities of interest.

Regarding the deterministic reference simulation of the SSB, extensive prior knowledge was required to calibrate the spray boundary condition against the available experimental data. To overcome this dependency, in this section, the reconstructed spray boundary condition is replaced by data from an algebraic primary breakup model. In this model, characteristics of the dispersed phase after primary atomization are calculated from geometric quantities of the atomizer as well as properties of the gas flow. Hence, the dependency of the spray boundary condition from the experimental data is notably reduced.
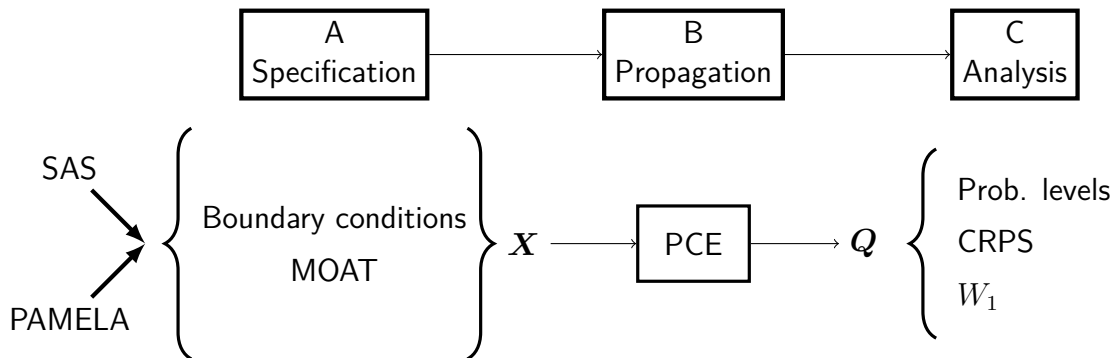
Figure 5.18.: Application of the workflow for uncertainty quantification to the SSB case. X: Uncertain input parameters, Q: Quantity of Interest.

5.4.1. Spray boundary conditions from the PAMELA model

The PAMELA primary breakup model as detailed in Sec. 2.4.3 is used for the definition of the spray boundary condition. As in the reference simulation, droplets start from an annulus with $r_i = 3.5$ mm and $r_o = 4.5$ mm, placed at an axial offset $\Delta z = 1.5$ mm with respect to the atomizer edge (see also Fig. 5.4). The PAMELA model provides an SMD D_{32} and a
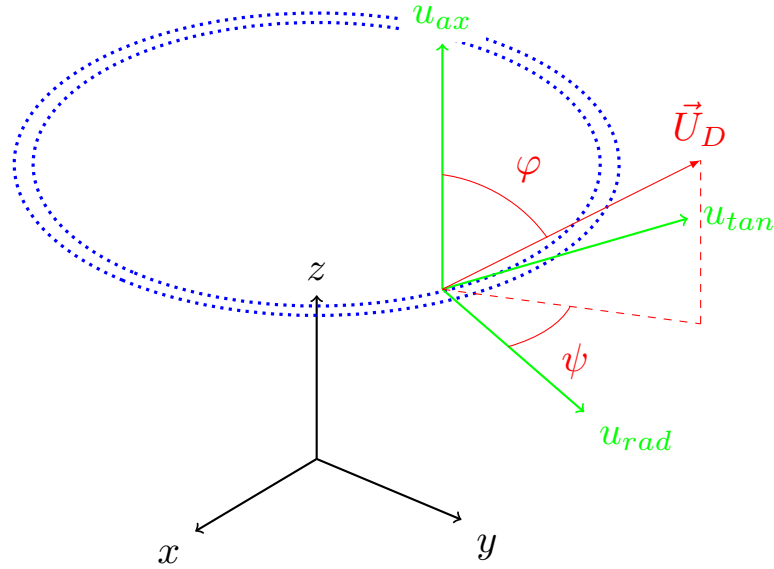
Figure 5.19.: Definition of the velocity vector $\vec{U}_D$ at the spray boundary condition. Black system: Global coordinate system. Green system: Local coordinate system. Blue dots: Droplet starting annulus.

spread factor q for a Rosin-Rammler distribution. Inputs to the model are the atomizer edge thickness h_a, the length of the liquid film L_f along the prefilmer and the mean gas velocity U_G parallel to the liquid film.

For the SSB, the atomizer edge thickness is reported as $h_{a,SSB} = 0.1$ mm [89]. Based on the geometry of the prefilmer (see Fig. 5.1) and the nominal opening angle of the primary pressure-swirl atomizer ($\theta = 60°$), the location where droplets from the primary atomizer impinge the prefilmer surface can be reconstructed and hence the liquid film length is estimated as $L_{f,SSB} = 3.8$ mm. Mean gas velocity $U_{G,SSB}$ alongside the liquid film is extracted from the mean gas field and ranges between 70 and 85 m s^{-1} as the air flow is accelerated within the inner air nozzle.

The PAMELA model does not provide data for the velocity components of the droplets after primary atomization. Therefore, it is assumed that the droplets rapidly couple to the local gas flow at the starting annulus. This is supported by findings from the reference simulation. Close to the starting annulus, most droplets had a Stokes number below 10. Therefore, the velocity vector $\vec{U}_D$ of a droplet starting at the boundary condition is derived from the local vector of the gas velocity. The definition of $\vec{U}_D$ is depicted in Fig. 5.19: In the local polar coordinate system of the droplet, $\vec{U}_D$ is determined by the axial angle φ_D, the swirl angle ψ_D and the velocity magnitude U_D. Respective transformations are detailed in Appendix D.

5.4.2. Step A: Identification and characterization of the uncertainties

Possible uncertainties are identified by analyzing the simulation model for the SSB with respect to the three main categories (numerical uncertainties, model form uncertainties, input uncertainties) from Sec. 3.3.1. This demonstrates the identification and characterization of uncertainties for a complex simulation case.

Numerical uncertainties

The used SAS turbulence model relies on a dynamic adjustment of the $k - \omega$ SST model to an LES like formulation in high turbulence regions. However, this adjustment depends on the ability of the grid to locally resolve turbulent structures, i.e. the local grid resolution. Therefore, SAS simulations are always grid dependent which prohibits a systematic grid convergence study based on Richardson exptrapolation as in the DSHC case. Systematic evaluation of the numerical uncertainties in SAS simulations has been recently reported by Pereira et al. [182] for elementary test cases. An extension of this method to a complex test case like the SSB is out of the scope of the work at hand and for the current study, numerical uncertainties are not further investigated.

Model form uncertainties

Since the problem under consideration constitutes a semi-technical combustion chamber, the difference between the application domain of the used models (*subsystem case*) and their validation domain (mostly *unit problems* or *benchmark cases*) is significant. Thus, the overall simulation model for the SSB might amplify model form uncertainties. However, in the previous section, encouraging results from the deterministic reference simulation have been shown which demonstrated the capability of the used simulation model.

In addition to the amplification of existing model form uncertainties in the submodels, model form uncertainties could arise from an incomplete formulation of the overall simulation model. For example, radiation of the gas phase species as well as spray-wall interaction is neglected in the used simulation model.

Dedicated treatment of model form uncertainties through extrapolation of the model form error from the validation domain to the application domain [177] remains a complex issue and is out of the scope of the work at hand. Major emphasis is put on quantifying the input uncertainties, specifically in the spray boundary condition.

Input uncertainties

Geometry   All geometric dimensions and quantities of the SSB are documented in the work of Grohmann [89]. Furthermore, the reduced complexity of the geometry in comparison to a full-scale aero-engine enables the resolution of all geometric features in the computational grid.

The atomizer edge thickness h_a serves as an input to the primary atomization model. As already mentioned, this parameter is known for the SSB. Uncertainties within the reported manufacturing tolerance have shown to have no significant effect on the droplet size distribution calculated by the PAMELA model.

Modeling constants   The simulation case under consideration involves a number of sub-models and thus numerous modeling constants which might affect the simulation results. For

example, the choice of the Smagorinsky constant C_s in the SAS turbulence model influences the turbulent damping in the LES regions [105].

In the present study, all modeling constants are set to their respective reference values for which they were validated. Impact of uncertainties in these parameters are not further investigated.

Initial and boundary conditions of the gas phase Regarding the boundary condition for the gaseous phase, a simplification applies to the inlet at the plenum, at which the turbulence intensity was not measured in the experiments. Therefore, a uniform inlet velocity rather than synthetic turbulence [121] is imposed. In view of the fact that most of the turbulence is generated in the swirler stages, this uncertainty should not affect the flow inside the combustion chamber. Measurement uncertainties below 1.2 % have been reported for the mass flow rate of the air [89].

Mercier et al. [159] demonstrated that uncertainties in wall temperatures and associated heat losses can have a significant impact on local and global temperature distribution. In the present study, temperature profiles from thermometry measurements are utilized. For this data, Grohmann [89] estimated an error of ± 2 %.

Initial and boundary conditions of the dispersed phase Since the velocity vector of the droplets at the dispersed phase boundary condition is derived from the gas field trajectories, uncertainties are introduced from the variation of the trajectory angle ψ and φ over the starting annulus. In the flow field, ψ ranges between 55° and 63° while φ varies between 26° and 29°. Furthermore, by applying the absolute velocity $U \approx 60 \text{ m s}^{-1}$ of the gas phase at the starting annulus to the dispersed phase, droplets start with a significantly too high momentum and mostly impinge at the combustion chamber walls. Therefore, the droplets' absolute velocity U_D is assumed to be between 25 and 30 m s^{-1}. This is inferred from similar atomizer configurations [110, 235].

Finally, uncertainties exist regarding the temperature of the liquid droplets at the boundary condition. In the experiments, the temperature of the fuel in the supply system was measured at a location close to the primary pressure-swirl atomizer ($T_{liq,exp} = 303$ K). However, the fuel might undergo additional heating during pre-filming atomization due to the surrounding air flow ($T_{air} = 323$ K) as well as radiative heat transfer from the reaction zone. Accordingly, the droplets' temperature is estimated to range between $T_{liq,exp} = 303$ K and $T_{air} = 323$ K.

5.4.3. Step A: Probabilistic simulation model

From the possible uncertainties identified in the previous analysis, only the uncertainties in the spray boundary condition will be analyzed in detail. In the DSHC case, these uncertainties have demonstrated to have a significant effect on the flame position and temperature distribution over the reaction zone. Thus, the input parameters to the PAMELA model are seen as uncertain inputs to the simulation model.

Table 5.2.: Parameter space Ω_{SSB} of the uncertain inputs.

	Description	PDF	Unit	Source
φ_D	axial angle	$\mathcal{U}(26, 29)$	[°]	CFD flow field
ψ_D	swirl angle	$\mathcal{U}(55, 63)$	[°]	CFD flow field
U_D	absolute velocity	$\mathcal{U}(25, 30)$	$[\mathrm{m\,s^{-1}}]$	estimated
U_G	mean gas velocity	$\mathcal{U}(70, 85)$	$[\mathrm{m\,s^{-1}}]$	CFD flow field
T_{liq}	liquid temperature	$\mathcal{U}(303, 320)$	[K]	Grohmann [89]

For simplicity, they are all interpreted as uncorrelated uncertainties and characterized by a uniform distribution function with the respective minimum and maximum from the previous analysis[2]. Note that this assumption differs from the strict application of Probability Bounds Analysis in the DSHC case, but enables insight into the probabilistic structure of the output uncertainties. Hence, precise probability theory instead of strict PBA is applied, resulting in a probabilistic simulation model of the SSB. Table 5.2 provides a summary of the uncertain input parameters which form the input space $\Omega_{\mathrm{SSB}} = [\varphi_D \times \psi_D \times U_D \times U_G \times T_{liq}]$. Note that the uncertainty in the mean gas velocity U_G results in SMDs $D_{32} = 29 - 35$ µm and MMDs $D_{50} = 35 - 41$ µm calculated by the PAMELA model.

5.4.4. Step A: MOAT screening

MOAT sensitivity analysis is utilized to identify potentials for parameter reduction in Ω_{SSB}. Solely for this analysis, the simulation model is simplified by replacing the detailed reaction mechanism with a global, single-step formulation for the three fuel species [271]. Chemical source terms are then calculated through the EDC model. This results in a reduction in computing time by a factor of 25. A comparison for the profiles of mean gas phase temperature from the deterministic reference simulation (FRC) and the simplified simulation model (EDC) using the same boundary conditions is given in Fig. F.5 in Appendix F. The general course of the profiles is well replicated by the simplified model although the magnitude of the temperature is systematically overestimated by $50 - 100$ K at the most positions. This is a known issue when using global reaction mechanisms [180] due to the fact that the formation and consumption of chemical radicals is not accounted for. Nonetheless, since the MOAT analysis aims at qualitatively identifying tendencies in the output quantities of interest over a large variation in the inputs, the reduced simulation model is expected to reproduce these tendencies.

Preferably, the sensitivity of the combustion process to the variation in the input quantities is appraised by representative global quantities. For the SSB case, average position and length of the reaction zone is taken as such a measure, since most other quantities (e.g. temperature profiles) are assumed to depend on the location of the reaction zone. On the basis of the

---

[2]The choice of uniform distribution functions for minimum/maximum data is motivated by the principle of maximum entropy [114, 253].
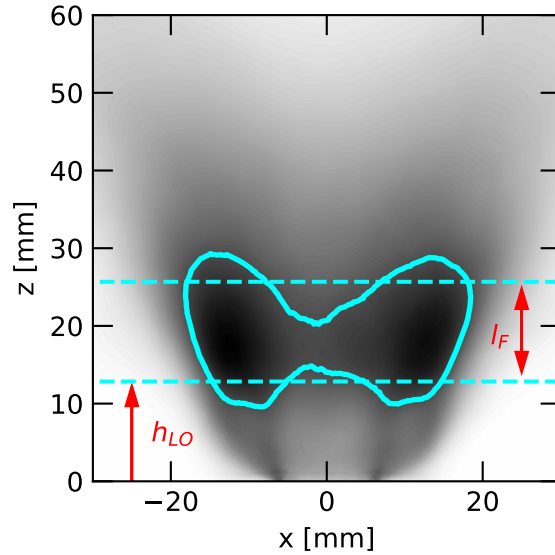
Figure 5.20.: Definition of flame lift-off height h_{LO} and flame length l_F for a threshold value $\upsilon = 70$ %.

averaged, line-of-sight integrated heat release signal hr_{LOS}[3], the flame lift-off height h_{lo} and the flame length l_{F} are derived. For this purpose, h_{lo} is defined as the mean axial distance between the contour $\upsilon \cdot \max(hr_{LOS})$ and the exit plane of the air nozzle, while l_{F} is defined as the difference between the mean extent of this contour minus h_{lo}. In this definition, υ is a threshold value which is set to 50 and 70 %. Consequently, the four parameters $h_{lo,50}$, $h_{lo,70}$, $l_{F,50}$ and $l_{F,70}$ are taken as output quantities of interest for the MOAT screening. A depiction of the parameters' definition is available from Fig. 5.20.

Sixty simulations within Ω_{SSB} are run, resulting in 10 elementary effects for each of the 5 input parameters. Standard deviations σ against modified means μ^* in MOAT plots for h_{LO} and l_F are given in Fig. 5.21 (a) and (b), respectively. Sensitivity of the MOAT results on the threshold value υ can be judged from the comparison of the first and second row.

Although the results are not as clear as in the DSHC case, slight tendencies are observable: The relative positioning of φ, ψ and U_D in the MOAT plot is comparable between h_{LO} and l_F as well as between $\upsilon = 50$ % and $\upsilon = 70$ %. This might be attributed to the fact that these parameters constitute the velocity vector of the droplets at the boundary condition and hence are somewhat coupled at the boundary condition. However, a definitive assessment of their potential interaction cannot be deduced from the MOAT results. The influence of U_G and $T_{liq.}$ on both h_{LO} and l_F changes significantly between $\upsilon = 50$ % and $\upsilon = 70$ % which could be due to the fact that the choice of υ extracts significantly different regions of the reaction zone, as indicated by the red contours in the subplots of the heat release signal in Fig. 5.21 (a). Therefore, the sensitivity of the two regions on the input parameters might differ.

In conclusion, the results from the MOAT analysis remain ambiguous and prohibit a clear distinction between influential and minor input parameters. A reason for this could be the

---

[3]Since OH^* is not available from the global reaction mechanism (EDC) the analysis is based on the local heat release. Especially under atmospheric conditions, the OH^* radical closely follows the local heat release rate [175].

(a) Lift-off height h_{LO}

(b) Flame length l_F

Figure 5.21.: Standard deviation σ of elementary effects plotted against their modified mean μ^* from MOAT screening. Upper row: $\upsilon = 50$ %, lower row: $\upsilon = 70$ %.

stronger coupling of the effects (e.g. evaporation, mixing and flame stabilization) in a confined combustion chamber in comparison to an open flame as in the DSHC case. Consequently, the uncertain parameters might show a tendency of increased interaction, too. Furthermore, the number of considered main effects coul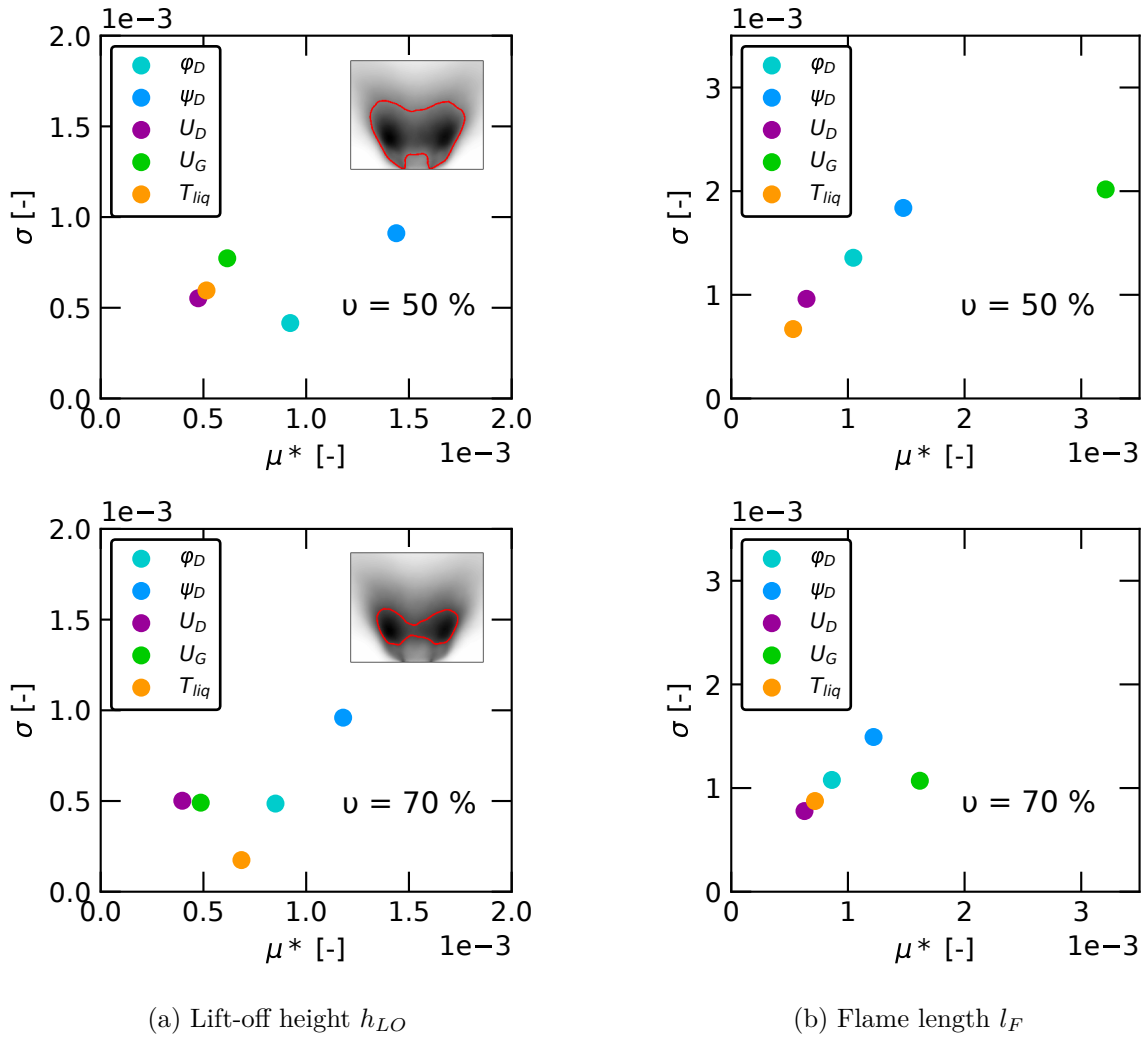d be too low to provide stable means and standard deviations. This could be improved by increasing the sample size and thus the number of simulations in the MOAT analysis. For a parameter space reduction, T_{liq} and U_D could be potentially set to their respective reference value. However, for the following study, Ω_{SSB} remains unchanged.

5.4.5. Step B: Polynomial chaos expansion based propagation of uncertainties

Output uncertainties in the probabilistic simulation model are quantified through Polynomial Chaos expansion. Again, the present study focuses on gas phase temperature since its accurate prediction plays a crucial role in combustor design. However, additional quantities of interest from the gas phase as well as the dispersed phase are considered in order to get insight into the phase-coupling dynamics under the given uncertainties. Formally, the truncated PC expansion of a Quantity of Interest Q from the probabilistic simulation model reads:

$$Q = \sum_{k=0}^{P} \alpha_k \mathbf{\Psi}_k \left(\boldsymbol{\xi} \right) = \sum_{k=0}^{P} \alpha_k \mathbf{\Psi}_k \left(\xi_{\varphi_D}, \xi_{\psi_D}, \xi_{U_D}, \xi_{U_G}, \xi_{T_{liq}} \right). \tag{5.3}$$

Since all uncertainties in Tab. 5.2 follow a uniform distribution function, Legendre polynomials form the basis $\mathbf{\Psi}_k$. As in the DSHC case, multidimensional integration on a Smolyak sparse grid is utilized for the computation of series coefficients α_k. A Level-2 expansion is considered, requiring 71 evaluations of the simulation model. Note that in contrast to the MOAT analysis, the detailed combustion model from the reference simulation is again used.

The fact that precise distribution functions are assigned to all input uncertainties allows for a computation of probability distribution functions for the Quantities of Interest from space filling sampling of Ω_{SSB}. For this purpose, 10^5 samples are drawn from the respective PC expansion.

5.4.6. Step C: Results and discussion

Gas phase

Resulting temperature profiles from the PCE over Ω_{SSB} are shown in Fig. 5.22 (a) - (e). The probability structure of the uncertain simulation results is characterized by probability levels: light gray areas indicate regions with $5\% < \text{Pr}(T) < 95\%$, whereas dark gray areas represent $25\% < \text{Pr}(T) < 75\%$. The median realization is given by cyan lines. In addition, results from the deterministic reference simulation from Sec. 5.3.2 are included as dashed black lines. Most notably, the probability levels clearly reveal a non-uniform distribution of output uncertainties, despite the fact that all input uncertainties were defined as uniformly
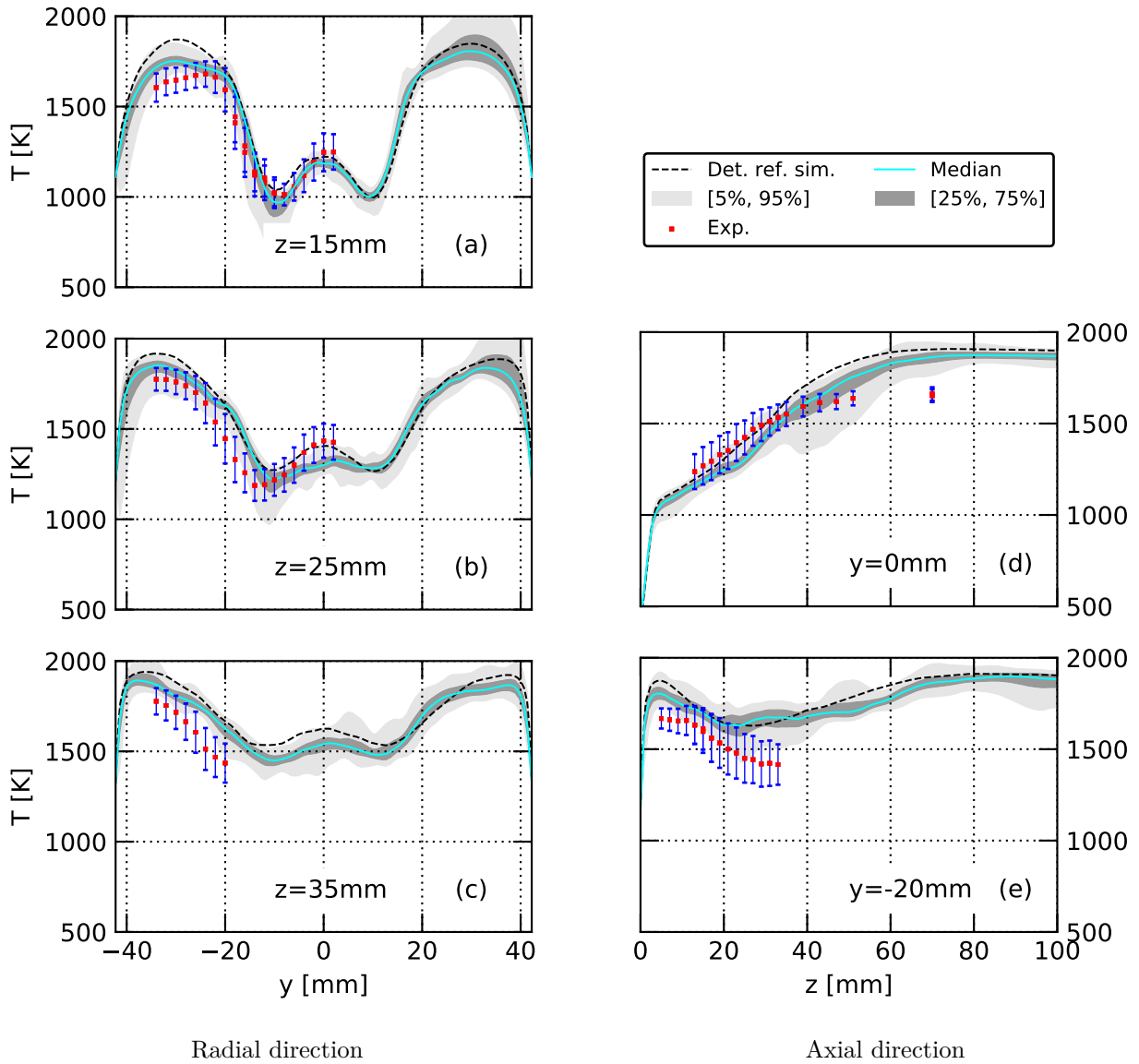
Figure 5.22.: Non-deterministic simulation results for time-averaged profiles of gas phase temperature. Error bars (–) indicate standard deviation of the experimental measurements.

distributed. This highlights the non-linear propagation of uncertainties through the simulation model.

Over all positions, moderate uncertainties in the order of $100-200$ K regarding the $[5\%; 95\%]$ level are visible. In the $z-$profiles, highest uncertainties are located at the high temperature regions ($y \approx \pm 30$ mm) where most of the combustion reactions take place. These processes are closely connected to the supply of fuel components through spray evaporation, which is ultimately linked to the input uncertainties at the spray boundary conditions. At the first two axial positions, the non-deterministic simulation is able to bracket almost all experimental data. However, at $z = 35$ mm (Fig. 5.22 (c)) the temperature profile is still overestimated in the simulation results.

Although the spray boundary condition is symmetric with respect to the $z-$axis, the uncertain simulation results in the $z-$profiles appear slightly asymmetric, especially regarding the $[5\%; 95\%]$ level. This could be caused by noisy data for the construction of the PCE due to incomplete time-averaging in the numerical simulation, insufficient PCE accuracy or a too small sample size for the precise computation of the local PDF. Since the influence of time-averaging was investigated in detail for the reference simulation, the asymmetry is most likely due to local PCE accuracy. For the DSHC case it was demonstrated that the quality of the PC expansion can vary along a profile of QoIs.

Along the axial profile at $y = 0$ mm (Fig. 5.22 (d)), all measurement data except for the last one are included in the uncertainty region. However, the fact that the axial gradient in the experimental data is almost zero over the last few measurement positions whereas the temperature in the simulation still rises up to 1800 K confirms that the temperature in the upper half of the combustor is systematically overestimated in the simulation. As already mentioned in Sec. 5.3.2, this could be caused by too low thermal losses. Furthermore, as the present study confirms that this tendency is not related to uncertainties in the spray boundary condition, it could stem from a general modeling error.

A significant increase in local uncertainty in the $y = 0$ mm profile (Fig. 5.22 (d)) is found between $z = 40$ and $z = 80$ mm. This coincides with the axial position of possible spray-wall impingement (see Sec. 5.3.3) after which the droplets are reflected back towards the centerline region. Presumably, this impingement depends on the droplets' starting velocity U_D and their axial angle φ_D. Hence, uncertainties in these quantities might influence the spray impingement location and finally the temperature profiles downstream of the respective location.

The tendency in the $z-$profiles that highest uncertainties are found in the high temperature regions is also reflected in the $y = -20$ mm profile (Fig. 5.22 (e)). Here, the mean of the experimental data is within or below the 5 % quantile at all positions.

Results for the axial component of gas phase velocity in Fig. 5.23 (a) - (e) demonstrate that uncertainties in the temperature distribution couple with uncertainties in the gas phase velocity. As in the temperature profiles, highest uncertainties in the $z-$profiles are found around the reaction zone. Moreover, the range of the $[5 \%, 95\%]$ level increases with increasing axial distance. This tendency is also present in the axial profiles ($y = 0$ mm, $y = -20$ mm;
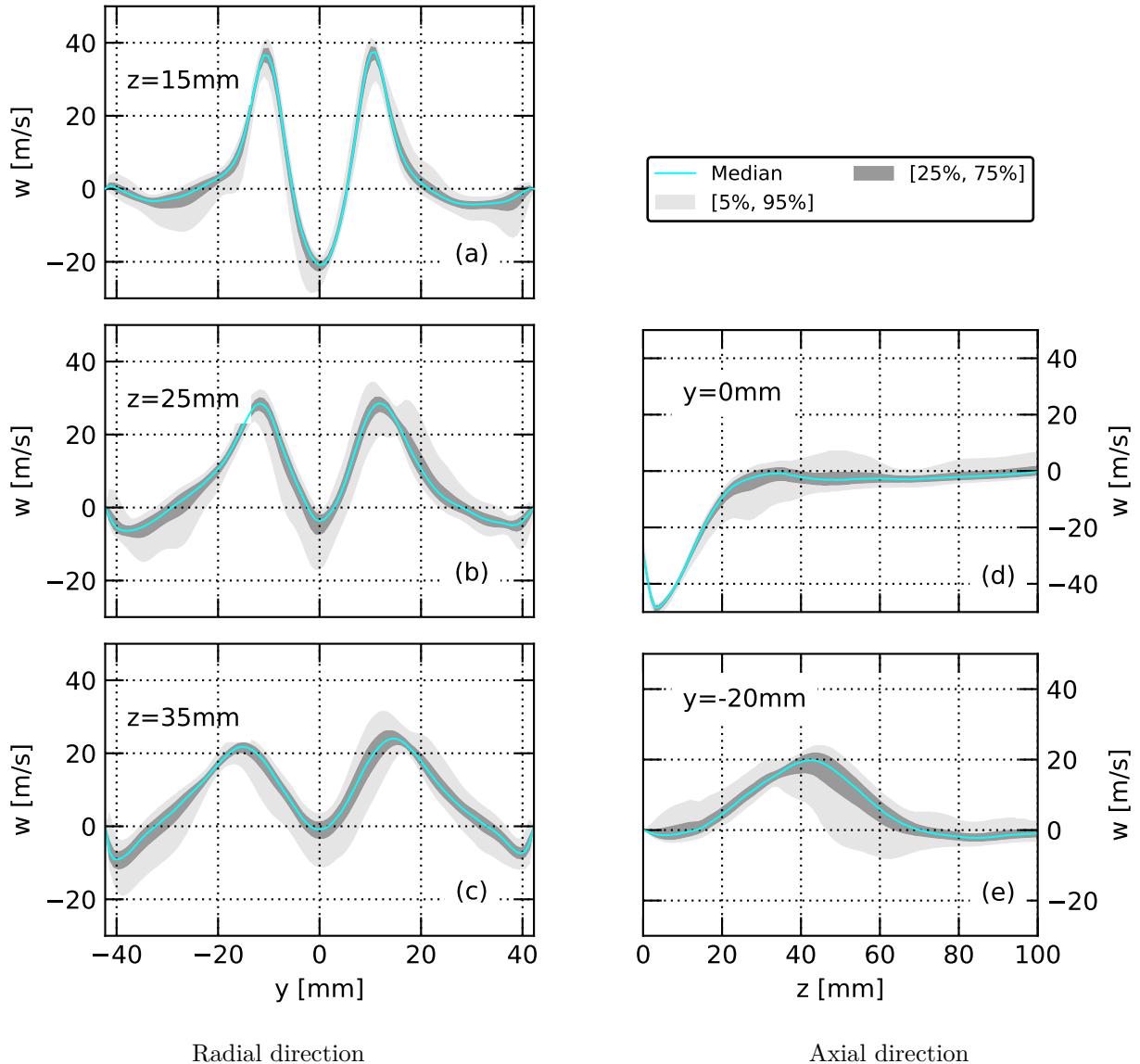
Figure 5.23.: Non-deterministic simulation results for time-averaged profiles of axial velocity in the gas phase.

Fig. 5.23 (d) - (e)) and might be an indicator that the backflow of hot combustion products is also affected by the input uncertainties.

Dispersed phase

Non-deterministic results from the dispersed phase at $z = 15$ mm are shown in Fig. 5.24. The droplet size spectrum is split into the same three size classes as for Fig. 5.16 in the deterministic reference simulation: $10\,\mu m < d < 11\,\mu m$ (*small*), $27\,\mu m < d < 33\,\mu m$ (*medium*) and $45\,\mu m < d < 55\,\mu m$ (*large*). Note that non-deterministic simulation results are only shown for locations at which sufficient time-averaged droplet data is available from all 71 simulations. Otherwise, the PC expansion would be prone to high approximation errors.

Despite the fact that all input uncertainties from Tab. 5.2 are directly linked to the dispersed phase, output uncertainties in the components of droplet velocity are low, especially for the
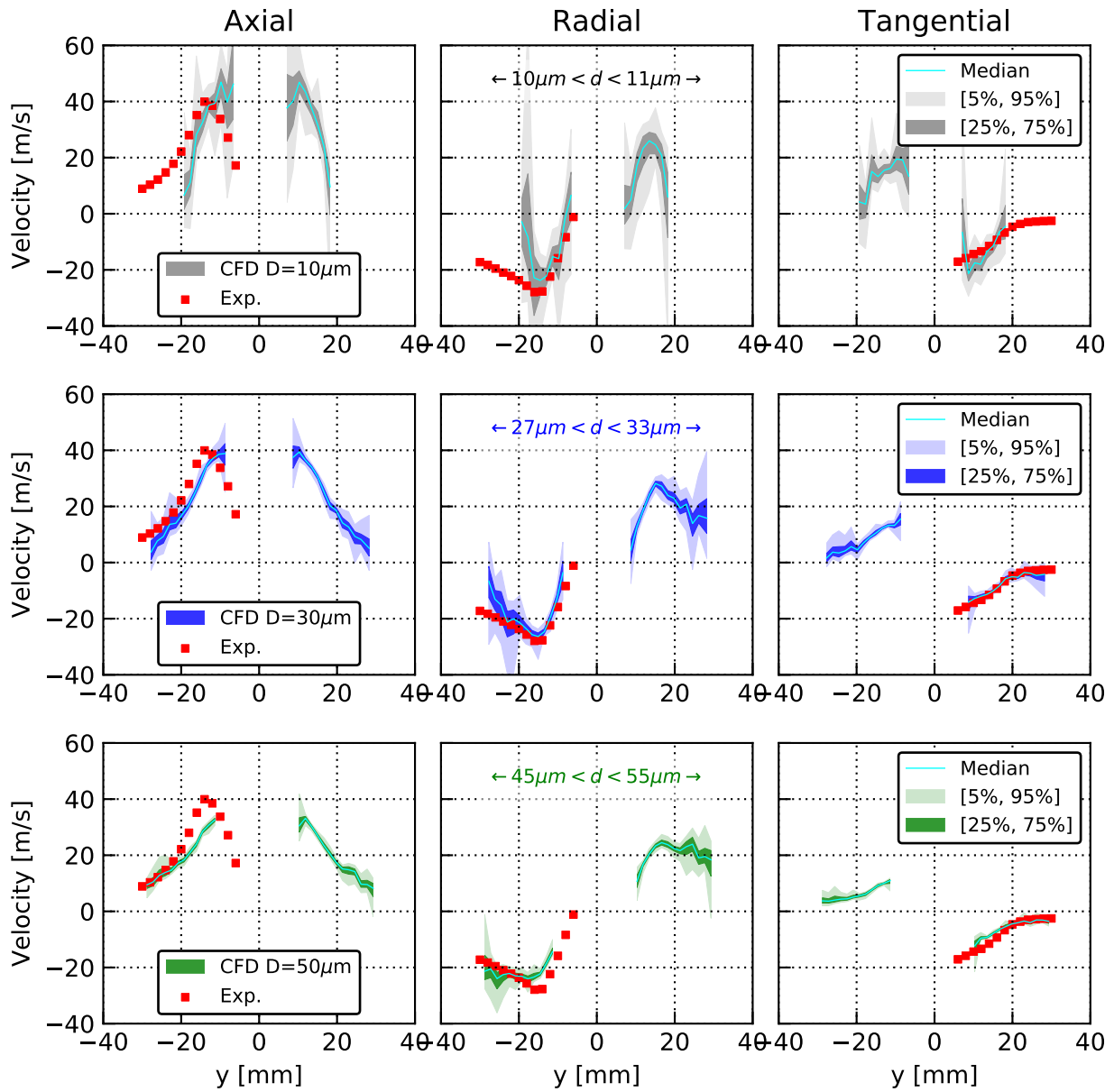
Figure 5.24.: Non-deterministic simulation results for time averaged profiles of droplet velocity components at $z = 15$ mm. Simulation data is split into small (■), medium (■), and large droplets (■) as defined in Sec. 5.3.3. Experimental data (■) is averaged over all diameters.
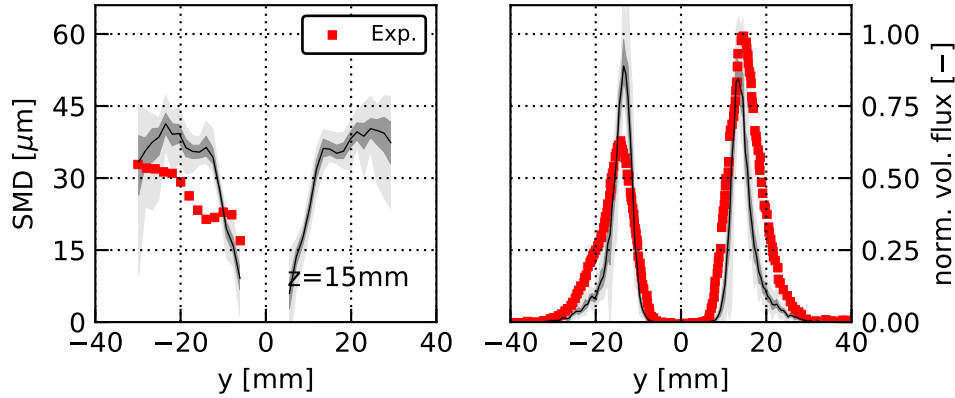
Figure 5.25.: Non-deterministic simulation results for time averaged profiles of Sauter Mean Diameter (SMD) and normalized liquid volume flux at $z = 15$ mm.

medium (blue) and large (green) droplets. The fact that the magnitude of uncertainty increases towards lower droplet diameters can be explained by their low Stokes number and thus higher tendencies to couple to the local gas velocity. As aforementioned, output uncertainties are also present in the velocity components of the gas field. Hence, these uncertainties might be passed on to the small droplets. In contrast, uncertainties in the velocity components of the large droplets simply reflect the input uncertainty in the absolute velocity U_D of 5 m s^{-1}.

At all radial locations for which uncertain results are available, the simulation results agree with the experimental data in at least one size class. This verifies the assumption made in the construction of the spray boundary condition that the droplet starting trajectories can be derived from the local gas velocities. Through this approach, a similar accuracy of the simulation regarding the experimental data is achieved, compared to the deterministic reference simulation in which the droplet velocities were calibrated against experimental data.

Figure 5.25 provides results for Sauter Mean Diameter and normalized volume flux at $z = 15$ mm. The radial distribution of the SMD is similar as in the deterministic reference simulation and shows the same tendency in overestimating the diameter. At the radial position of maximum volume flux ($y \approx \pm 17.5$ mm) the uncertainty level with respect to the [5 %; 95 %] interval is in the magnitude of 5 µm which is the range of SMDs provided by the PAMELA model under the given uncertainty for U_G.

The radial position of maximum volume flux appears almost unaffected by the input uncertainties, confirming that the distribution of droplets is dominated by the gas field in the SSB case.

For brevity, additional plots for droplet velocities and mean diameter at $z = 25$ mm are given in Appendix F. Similar phenomena and tendencies as discussed for $z = 15$ mm can be identified.

(a) Lift-off height   (b) Flame length
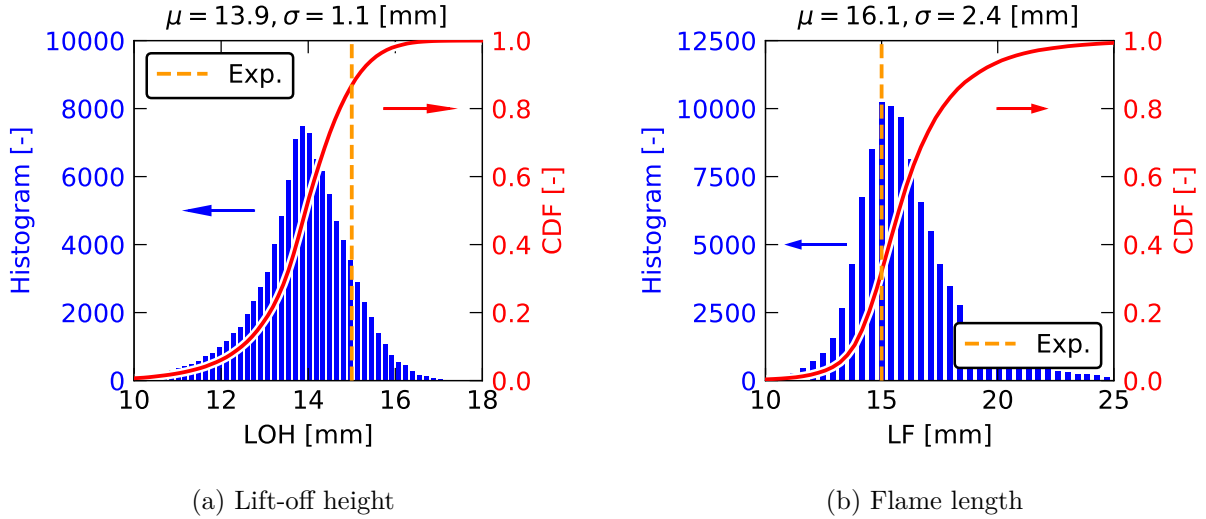
Figure 5.26.: Non-deterministic simulation results for flame lift-off height and flame length with respect to a threshold value $\upsilon = 50\ \%$.

Reaction zone

Insight into the probability structure of a scalar quantity of interest under the given uncertainties is provided by the example of mean flame lift-off height h_{LO} and mean flame length L_{F}. Both quantities are derived from the OH^* field as described in Sec. 5.4.4 and 5.3.2, using a threshold of $\upsilon = 50\ \%$.

Figure 5.26 summarizes results from space filling sampling of the PCE over Ω_{SSB} through histograms and the corresponding empirical CDFs $\hat{\mathcal{C}}_{L_{\mathrm{F}}}$ and $\hat{\mathcal{C}}_{h_{\mathrm{LO}}}$. As evident from the histograms, both QoIs follow a distribution function that resembles a normal distribution, despite the fact that all input uncertainties are uniformly distributed. As already discussed for the temperature profiles, this points out that the flame stabilization in the SSB follows a highly non-linear mechanism regarding the injection of liquid fuel droplets.

Experimental results are indicated by orange dashed lines. In case of L_{F} (Fig. 5.26 (b)), the experimental value coincides with the *mode* of $\hat{\mathcal{P}}_{L_{\mathrm{F}}}$, i.e. the most probable realization from the simulation. This should not be confused with the *mean* realization $\mu_{L_{\mathrm{F}}} = 16$ mm, which is greater than the experimental value. Regarding h_{LO} most realizations underestimate the true lift-off height from the experiment (Fig. 5.26 (a)). From $\hat{\mathcal{C}}_{h_{\mathrm{LO}}}$ it can be inferred that 80 % of the realizations are below the experimental value.

Remarks on parameter space reduction

The MOAT analysis in Sec. 5.4.4 did not show a distinct importance ranking of the uncertain inputs and thus, the uncertain parameter space Ω_{SSB} remained unchanged for the propagation of uncertainties. However, it was speculated that T_{liq} and U_D could be set to their respective reference values due to the MOAT results. Consequently, the five-dimensional input parameter space Ω_{SSB} would be reduced to a three-dimensional input parameter space $\Omega_{\mathrm{SSB,red.}}$.
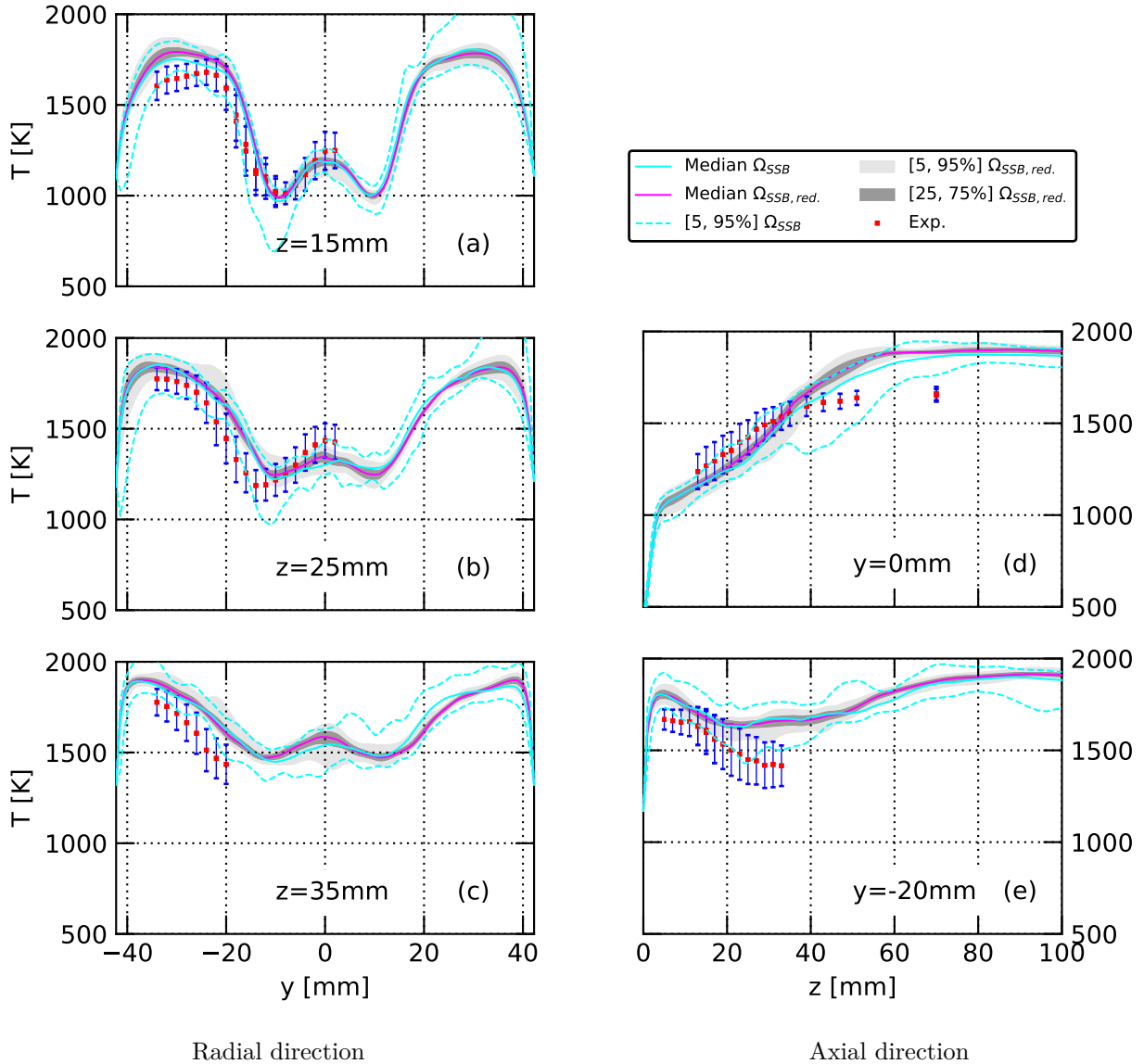
Figure 5.27.: Non-deterministic simulation results for time-averaged profiles of gas phase temperature. Probability levels are given with respect to $\Omega_{\text{SSB,red.}}$.

In order to shed light on the potential for parameter reduction in the SSB case, results for the temperature profiles from the propagation of uncertainties in Ω_{SSB} and $\Omega_{\text{SSB,red.}}$ are compared from a *posterior* perspective, i.e. after the uncertainty quantification. For this purpose, an L2 PCE of the reduced parameter space $\Omega_{\text{SSB,red.}} = [\varphi_D \times \psi_D \times U_G]$ is constructed using the same approach as described in Sec. 5.4.5. This requires 31 evaluations of the high-fidelity simulation model in which T_{liq} is set to 320 K and U_D is set to 27.5 m s^{-1}. A summary of $\Omega_{\text{SSB,red.}}$ is given in Tab. F.1 in Appendix F.

Figure 5.27 shows non-deterministic results with respect to $\Omega_{\text{SSB,red.}}$ for the temperature profiles. For comparison, the bounds of the [5 %; 95 %] probability interval from the full parameter space Ω_{SSB} are indicated with dashed cyan lines. Only minor differences between the median realizations from $\Omega_{\text{SSB,red.}}$ and Ω_{SSB} are visible. However, when comparing the [5 %; 95 %] probability interval it can be observed that this interval widens distinctly when considering Ω_{SSB} instead of $\Omega_{\text{SSB,red.}}$. Thus, the additional uncertainties in Ω_{SSB} seem to have
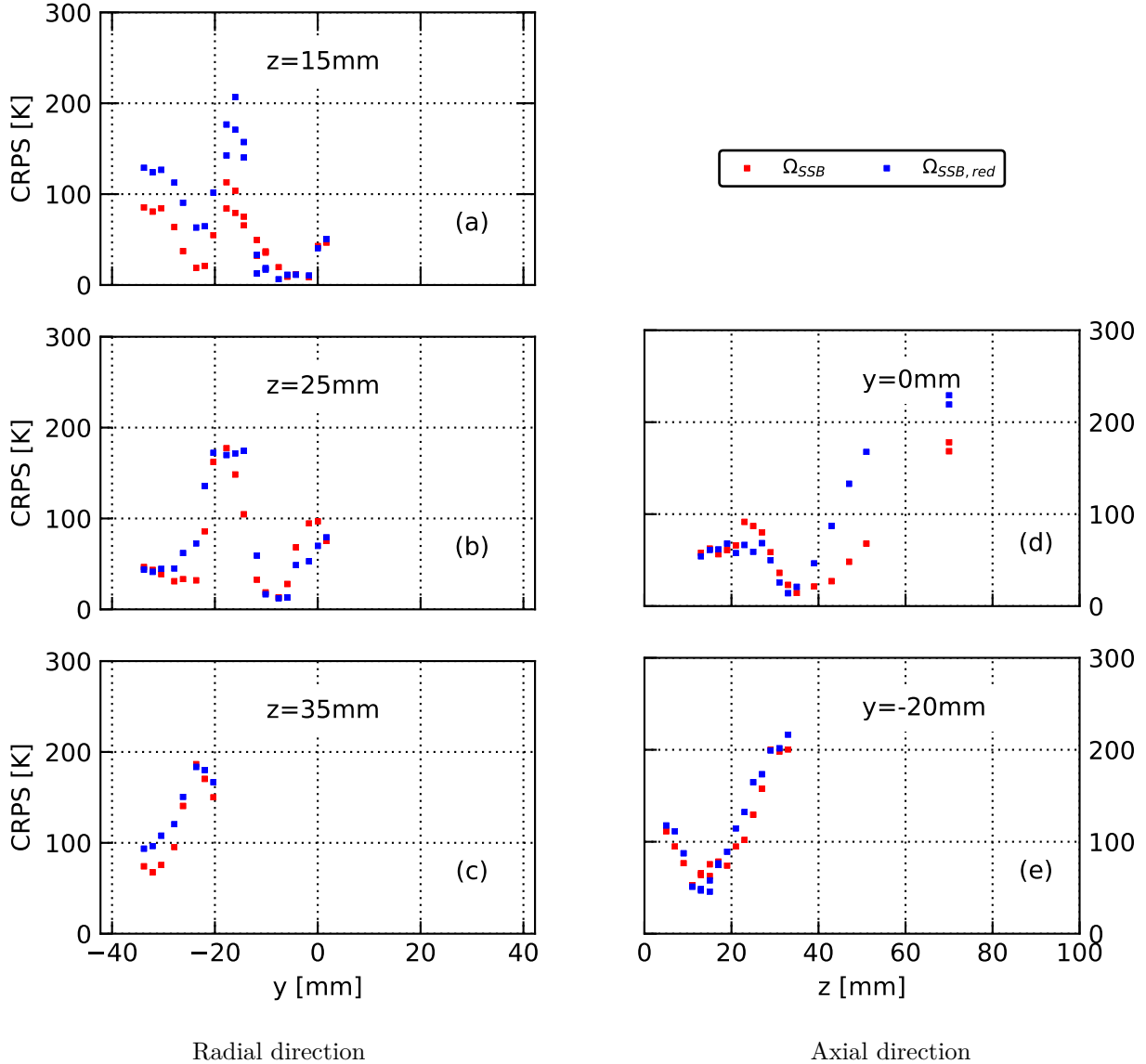
Figure 5.28.: Continuous Ranked Probability Score for the probabilistic temperature predictions. Full input parameter space ($\blacksquare$), reduced input parameter space ($\blacksquare$).

an effect especially in the low probability regions. Although not shown here for brevity, the difference in the [25 %; 75 %] between $\Omega_{\text{SSB,red.}}$ and Ω_{SSB} is smaller than the one identified for the [5 %; 95 %] probability interval.

For a quantitative comparison of the two non-deterministic simulations, the accuracy metrics *Continous Rankend Probabilty Score* (CRPS) from Eq. (3.10) in Sec. 3.3.3 and *Wasserstein-1* (W_1) from Eq. (3.11) in Sec. 3.3.3 are calculated for both simulation results.

In the calculation of the CRPS, the mean of the experimental data μ_{exp} at each location is interpreted as a *certain* observation. The CRPS yields a generalized mean absolute error in case of uncertain predictions and certain experimental observation. Thus, the measurement error from the experiment is not taken into account and the CRPS is calculated from the local cumulative distribution function of the temperature from the non-deterministic simulation and the mean temperature from the experiment. The local CRPS for the temperature predictions
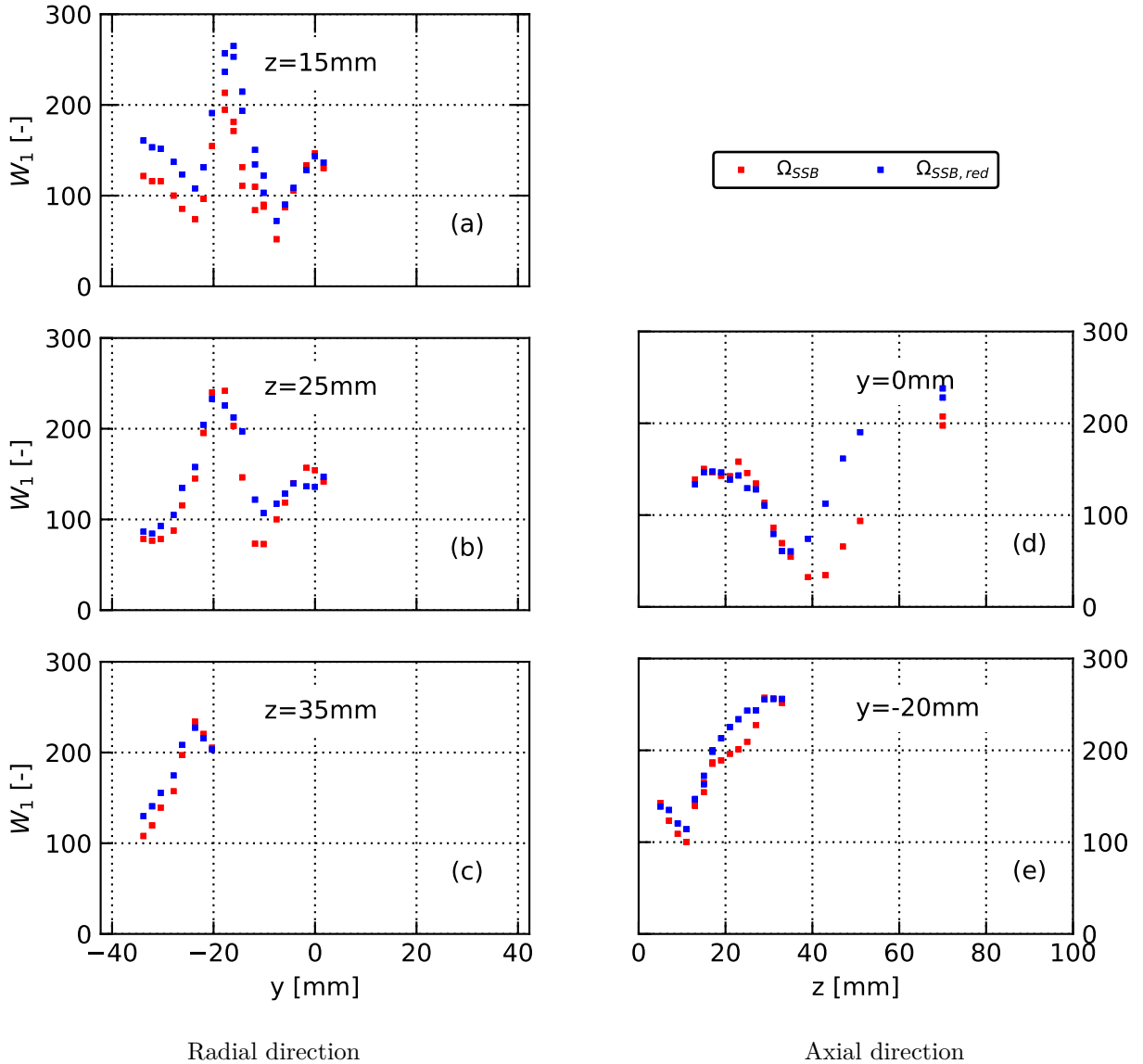
Figure 5.29.: Wasserstein metric W_1 for the probabilistic temperature predictions. Full input parameter space (■), reduced input parameter space (■).

from the non-deterministic simulation is given in Fig. 5.28 (a) - (e). For the red squares, the CRPS is calculated from the simulation results taken into account the full input parameter space Ω_{SSB} whereas for the blue squares, the CRPS is calculated from the simulation results based on the reduced input parameter space $\Omega_{\mathrm{SSB,red.}}$. Note that the CRPS is only calculated at radial and axial positions for which experimental data is available.

Deviations between the CRPS for Ω_{SSB} and $\Omega_{\mathrm{SSB,red.}}$ are below $10 - 20$ K over the most positions except for the profiles at $z = 15$ mm (Fig. 5.28 (a)) and $y = 0$ mm (Fig. 5.28 (d)). Here, the CRPS mostly reduces when taking into account the full parameter space Ω_{SSB}. This means that at these positions, it is more likely to observe the experimental data in the non-deterministic simulation results from Ω_{SSB} than in results from $\Omega_{\mathrm{SSB,red.}}$.

In order to compare the probability structure of the non-deterministic simulation results and the experimental data including measurement errors, the Wasserstein-1 metric for the temperature results is calculated at the same positions as the CRPS. For this purpose, the

measurement uncertainty and hence the uncertain observation is assumed to follow a normal distribution $\mathcal{N}(\mu_{exp}, \sigma_{exp})$. The standard deviation σ_{exp} is available from the experimental database [22].

Results for W_1 are given in Fig. 5.29 (a) - (e). The same tendency as for the CRPS is evident from the profiles of the W_1 metric. Again, differences are mainly found in the profiles at $z = 15$ mm (Fig. 5.29 (a)) and $y = 0$ mm (Fig. 5.29 (d)). In terms of W_1 this can be interpreted that even though the input uncertainty as well as the output uncertainty increases between $\Omega_{\text{SSB,red.}}$ and Ω_{SSB} (see Fig. 5.27), the probability structure of the prediction from Ω_{SSB} closer resembles the experimental data at these positions.

In summary, the two metrics confirm that the non-deterministic simulations from Ω_{SSB} and $\Omega_{\text{SSB,red.}}$ are both able to predict the experimental data with similar accuracy at the most positions, although larger probability intervals for the [5 %; 95 %] range were identified in Fig. 5.27.

Role of the experimental data for the spray boundary condition

For the probabilistic simulation model, the calibrated spray boundary condition was replaced by an algebraic primary breakup model. Thus, the required prior knowledge was reduced and the resulting lack in information was characterized as input uncertainties. Results from the propagation of uncertainties confirm that the probabilistic simulation model is still able to reproduce all aspects of multiphase combustion in the SSB with high accuracy.

Furthermore, the clear portrayal of output uncertainties and probability levels enhances the interpretation of the simulation results and helps identify quantities for which the prediction is highly uncertain (flame lift-off height) or potentially wrong (temperature at $z > 60$ mm). This enables model updating and confident application of the model in cases where only limited data regarding the spray phase is available from the experiment.

6. Summary and conclusions

The work at hand aimed at applying state of the art UQ methods to simulation problems involving turbulent spray combustion. In such simulations the formulation of boundary conditions for the spray after primary atomization introduces a major source of uncertainties. Therefore, special emphasis was placed on the quantification of uncertainties in the simulation results due to incomplete knowledge in the construction of the spray boundary conditions.

Since non-intrusive uncertainty quantification mostly relies on spaces filling sampling of the uncertain parameter space, this direct approach was found to be unfeasible for complex simulations. To overcome this limitation, a workflow for uncertainty quantification utilizing surrogate models in lieu of the computational expensive simulation was proposed. The present study successfully demonstrated the application of this workflow for the forward propagation of uncertainties in two test cases with different complexity.

The *Delft Spray in Hot Coflow* (DSHC) flame involved an unconfined spray flame burning liquid ethanol. Uncertainties in key parameters of the spray boundary condition were treated as epistemic uncertainties with the respective bounds derived from an analysis of existing simulations in the literature. Uncertainties in the used RANS simulation and the surrogate models were evaluated by means of solution extrapolation and holdout validation, respectively. Based on the findings of an a priori MOAT sensitivity analysis, the stochastic dimension of the input was reduced to the four most influential parameters. Probabilistic bounds of the Quantities of Interest were then obtained from space filling sampling of the surrogate models. Both PCE and Gaussian Process Regression resulted in comparable probability bounds. An extensive uncertainty region around the deterministic reference simulation was revealed. Regions were identified where the UQ-based simulation is unable to bracket the experimental data. This was attributed to a general modeling error in the RANS model regarding the mixing of fuel and oxidizer in the inner flame region. From an a posteriori sensitivity analysis, the majority of the uncertainty in the temperature profiles was connected to the spray cone angle of the atomizer which controls the position of the droplets and transport of gaseous fuel to the reaction zone. The aggregation of all analyzed sources of uncertainties confirmed that the total predictive uncertainty in this case is primarily due to the input uncertainties.

The DLR *Standard Spray Burner* (SSB) constituted a simulation problem which reflects characteristics typically found in modern aeroengine combustors. In order to resolve the complex three-dimensional and unsteady flow structure, hybrid URANS/LES was utilized. By inclusion of all available experimental information concerning the spray boundary conditions, the used simulation setup was able to reproduce all aspects of spray combustion in the SSB with high accuracy. To overcome the dependency from the experimental data for the spray

phase - i.e. the need for calibration against existing data -, an algebraic primary breakup model was incorporated. The resulting reduction in prior knowledge was compensated through probabilistic modeling and uncertainty quantification methods. The breakup model provided data for the mean diameter in the spray, but no information regarding the droplet velocities. The velocity vector of the droplets at the boundary condition was estimated from the local gas field and treated as uniformly distributed uncertainties. Further uncertainties regarding the spray boundary condition resulted in a six-dimensional parameter space of uncertain inputs. Due to their importance in the design process, temperature distribution and flame position were considered as the main quantities of interest. Results from the MOAT analysis remained ambiguous and prohibited a clear distinction between influential and minor input parameters. Output uncertainties in the simulation were then quantified through Polynomial Chaos Expansion. Moderate uncertainties were found in the results for the gas phase temperature as well as the droplet velocities. Finally, the potential for a parameter space reduction was further examined by comparing the uncertain predictions from the full and the reduced parameter space. For this purpose, accuracy metrics regarding the prediction of the temperature profiles were calculated.

6.1. Conclusions and outlook

On the basis of these results the following conclusions are drawn:

Role of uncertainties with increasing system complexity   Although the SSB case involved a higher level of complexity compared to the DSHC case, lower uncertainties in the temperature profiles were identified compared to the latter. Therefore, an increase in system complexity does not necessarily result in higher output uncertainties. The highly non-linear interplay between the different sub-phenomena can diminish the effect of input uncertainties which were found to be important in a simpler test case. Specifically in the SSB, the combustor walls prevented a shifting of the flame as in the DSHC case. On the other hand, this led to a potentially stronger coupling of sub-effects which prohibited a definitive verdict in the MOAT analysis. Finally, it should be kept in mind that uncertainties in the output must always be interpreted with respect to the uncertainties in the output. This makes a general statement regarding the role of uncertainties at different levels of system complexity challenging.

Propagation of uncertainties through coupling effects   The present work focused on input uncertainties in the spray boundary conditions. Hence, input uncertainties were primarily introduced to the dispersed phase of the reacting multiphase system. However, both test cases revealed that these uncertainties affect quantities of interest in the dispersed and the continuous phase (e.g. gas phase temperature and velocity or flame position). This highlighted the propagation of input uncertainties through coupling effects throughout the thermo-chemical process (see Fig. 1.2). In view of this fact it is important to note that other input uncertainties which were not considered in the present study need to be studied. For

example, uncertainties in the chemical reaction rates would alter the temperature field and thus influence the local evaporation of droplets.

Results from Probability Bounds Analysis (PBA) as opposed to precise probability theory For the DSHC, case strict PBA was applied and interval valued epistemic uncertainties were assumed resulting in large intervals of *possible* realizations for the temperature profiles. In contrast, uniformly distributed uncertainties were presumed in the SSB case which enabled the calculation of probability levels for the uncertain simulation results. The latter approach represented a slight deviation from strict PBA but was in agreement with the precise probability theory. This yielded a *best estimated prediction* of the quantities of interest under the given uncertainties. However, it should be pointed out that this best estimate purely relied on the assumption of uniform input uncertainties. In contrast, probability bounds from PBA are known to be larger [177] but always reflect the state of knowledge without further assumptions. Therefore, the impact of the application of different UQ frameworks needs to be further studied.

Potential of UQ in the simulation of spray combustion Apart from the clear portrayal of uncertainties, it was shown that UQ studies can provide guidelines for the improvement of validation experiments. In the DSHC case, a precise experimental measurement of the spray mean trajectory angle $\bar{\varphi}$ would significantly decrease the uncertainties in the simulation and thus provide a reliable basis for validation studies. However, systematic uncertainty quantification requires the identification and adequate characterization of all sources of uncertainties. Therefore, a precise definition of input uncertainties by means of PDFs should be included in the design of validation experiments. Since these information are often not available in early stages of a design process, structured approaches such as *expert elicitation* [9] should be utilized to avoid biased opinions or subjective estimates regarding possible uncertainties.

Finally, the SSB case clearly demonstrated the added value of uncertainty quantification when only limited data regarding the spray boundary conditions is available. With the additional information concerning the uncertainties in the simulation results, risks can be identified from the comparison with the requirements and performance targets as suggested in Fig. 1.1 in the introduction. Thereby, decision-making in the design and development process can be supported and advanced towards risk-informed decision-making.

A. Definitions and concepts for verification, validation and uncertainty quantification

Definitions from the NASA Standard STD-7009A

Credibility. The quality to elicit belief or trust in modeling and simulation results. [250]

Data Pedigree. A record of traceability from the data's source through all aspects of its transmission, storage, and processing to its final form used in the development of an M&S.

Input Pedigree. A record of the traceability from the input data's source through all aspects of its transmission, storage, and processing to its final form when using an M&S.

Uncertainty. A broad general term used to describe an imperfect state of knowledge or a variability resulting from a variety of factors, including but not limited to, lack of knowledge, applicability of information, physical variation, randomness or stochastic behavior, indeterminacy, judgment, and approximation.

Verification. The process of dermining the extent to which a model or simulation is compliant with its requirements and specifications as detailed in its conceptual models, mathematical models, or other constructs. [250]

Validation. The process of determining the degree to which a model or a simulation is an accurate representation of the real world from the perspective of the intended uses of the model or simulation. [250]

Validation Hierarchy

The construction of suitable validation experiments still poses major challenges due to the complexity of most modern engineering problems. Therefore, the validation process is generally broken down into a *complexity* or *validation hierarchy* [34, 147] consisting of multiple, progressively simpler tiers. Within this approach, the accuracy of the modeling results are compared with experimental data at different degrees of physics coupling and geometric complexity. A schematic of a validation hierarchy including examples for the simulation of spray combustion in an aeroengine is given in Fig. A.1.

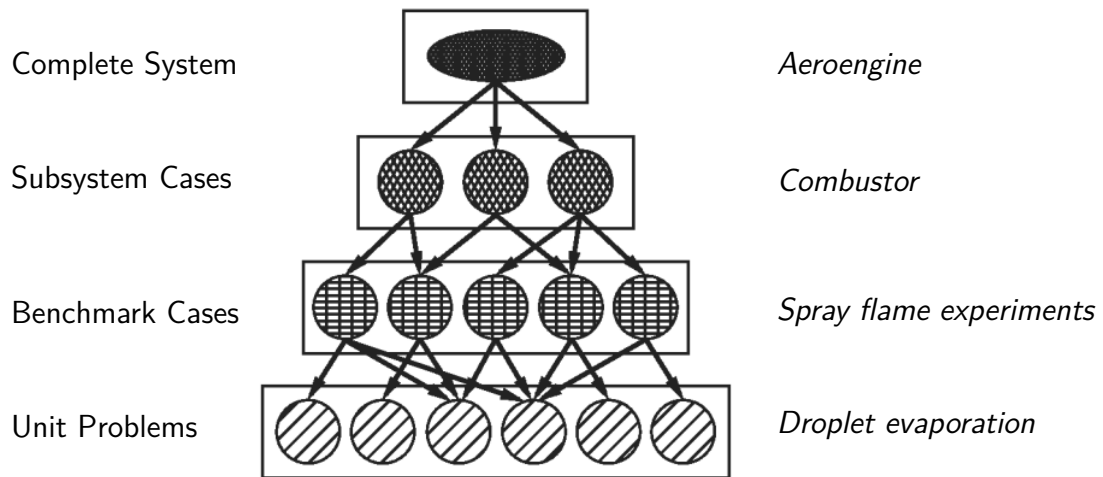Complete System ... Aeroengine

Subsystem Cases ... *Combustor*

Benchmark Cases ... *Spray flame experiments*

Unit Problems ... *Droplet evaporation*

Figure A.1.: Validation tiers of a system hierarchy according to the AIAA validation guide [4].

B. Fundamental definitions from probability theory

Random variables A random variable X is defined as a function on a sample space Ω, i.e. a set of *possible* outcomes:

$$X : \Omega \mapsto \mathbb{R}. \tag{B.1}$$

Hence, $X(\omega)$ is an actual outcome with a real value. Informally, a random variable can be seen as a variable whose values depend on outcomes of a random phenomenon [47]. The probability that X results the set S is defined as

$$\mathrm{Pr}(X \in S) = \mathrm{Pr}(\{\omega \in \Omega | X(\omega) \in S\}). \tag{B.2}$$

Distribution functions The cumulative distribution function (CDF) $\mathcal{C}_X$ of a random variable X is

$$\mathcal{C}_X(x) = \mathrm{Pr}(X \leq x). \tag{B.3}$$

In case of a continuous random variable a probability density function (PDF) $\mathcal{P}_X$ is defined as

$$\mathrm{Pr}(a < X < b) = \int_a^b \mathcal{P}_X(x)\mathrm{d}x \quad \text{with} \quad \int_{-\infty}^{\infty} \mathcal{P}_X(x)\mathrm{d}x = 1. \tag{B.4}$$

Note that CDF and PDF are interdependent:

$$\mathcal{C}_X(x) = \mathrm{Pr}(X \leq x) = \int_{-\infty}^{x} \mathcal{P}_X(\tilde{x})\mathrm{d}\tilde{x}. \tag{B.5}$$

Expectation and variance If X has a PDF $\mathcal{P}_X$ then the expectation $\mathbb{E}(X)$ (or first moment μ) is given as

$$\mathbb{E}(X) = \int_{-\infty}^{\infty} \mathcal{P}_X(x)\mathrm{d}x = \mu. \tag{B.6}$$

The variance of X is

$$\mathbb{V}(X) = \mathbb{E}((X - \mathbb{E}(X))^2) = \sigma^2, \tag{B.7}$$

also characterized by the standard deviation $\sigma = \sqrt{\mathbb{V}(X)}$.

Covariance and correlation As a measure of the joint variability of two random variables X and Y, the covariance $\mathrm{Cov}(X,Y)$ is introduced as

$$\mathrm{Cov}(X,Y) = \mathbb{E}((X - \mathbb{E}(X))(Y - \mathbb{E}(Y))) = \mathbb{E}(XY) - \mathbb{E}(X)\mathbb{E}(Y). \tag{B.8}$$

A positive covariance is one way to quantify that X and Y tend to increase together. A negative value quantifies a tendency for increases in one to accompany decreases in the other [179].

The covariance between two standardized variables, i.e. they have mean 0 and variance 1, is their correlation:

$$\text{Corr}(X,Y) = \text{Cov}\left(\frac{X - \mathbb{E}(X)}{\sqrt{\mathbb{V}(X)}}, \frac{Y - \mathbb{E}(Y)}{\sqrt{\mathbb{V}(Y)}}\right). \tag{B.9}$$

C. Stochastic inlet forcing approach for DSHC H$_{\text{II}}$

Time-coherent, stochastic forcing at the boundary condition of the secondary burner is realized with a first order Langevin equation [192] given as

$$\Phi(t + \Delta t) = \Phi(t) - \frac{\Phi(t)\Delta t}{\tau_t} + \sqrt{\frac{2\sigma^2 \Delta t}{\tau_t}}\xi_{\mathcal{N}}(t). \qquad (C.1)$$

Here, $\Phi \in [T, U_{cf}]$ and τ_t defines the integral turbulent time-scale upstream of the boundary condition. τ_t is predefined by measurements [213]. σ is the standard deviation of the process and $\xi_{\mathcal{N}}(t)$ is a random forcing with Gaussian distribution which is independent of Φ and fulfills the properties

$$\langle \xi(t) \rangle = 0, \quad \langle \xi(t)^2 \rangle = 1 \qquad (C.2)$$

$$\langle \xi(t)\xi(t') \rangle = 0, \quad t \neq t'. \qquad (C.3)$$

Equation C.1 therefore realizes an ergodic, statistically stationary Ornstein-Uhlenbeck process. A resulting forcing signal for the temperature fluctuations is shown in Fig. C.1.
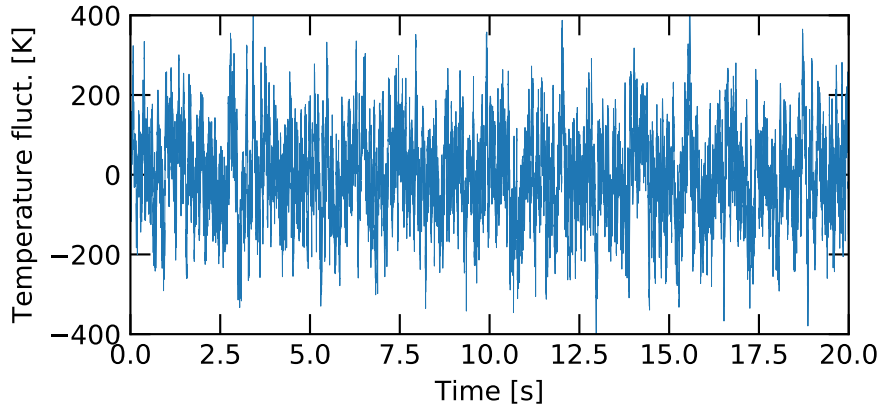
Figure C.1.: Exemplary upstream forcing signal for the temperature fluctuations from Eq. C.1. $\Phi = T, \Delta t = 10^{-5}$ s, $\sigma = 100$ K, $\tau_t = 0.025$ s.

D. Definition of the droplet starting velocity in the SSB

For the simulations with spray boundary conditions from the PAMELA model, the vector of the droplet starting velocity is defined by the axial angle φ_D, the swirl angle ψ_D and the velocity magnitude U_D. These quantities are given with respect to the local coordinate system of the droplet at the boundary condition (see Fig. 5.19). The connection with the axial, radial and tangential velocity components u_{ax}, u_{rad} and u_{tan} in the local coordinate system is given by the following transformations.

Calculation of the trajectory angles from the velocity components

$$\varphi_D = \arctan\left(\frac{u_{ax}}{u_{rad}}\right) \tag{D.1}$$

$$\psi_D = \arctan\left(\frac{u_{tan}}{u_{rad}}\right) \tag{D.2}$$

$$U_D = \sqrt{u_{ax}^2 + u_{rad}^2 + u_{tan}^2} \tag{D.3}$$

Calculation of the velocity components from the trajectory angles

$$u_{tan} = \sqrt{\frac{\tan\left(\psi_D\right)^2 \tan\left(\varphi_D\right)^2 U_D^2}{1 + \tan\left(\psi_D\right)^2 \tan\left(\varphi_D\right)^2 + \tan\left(\varphi_D\right)^2}} \tag{D.4}$$

$$u_{rad} = \frac{u_{tan}}{\tan\left(\psi_D\right)} \tag{D.5}$$

$$u_{ax} = \sqrt{U_D^2 - u_{rad}^2 - u_{tan}^2} \tag{D.6}$$

E. Additional plots for DSHC
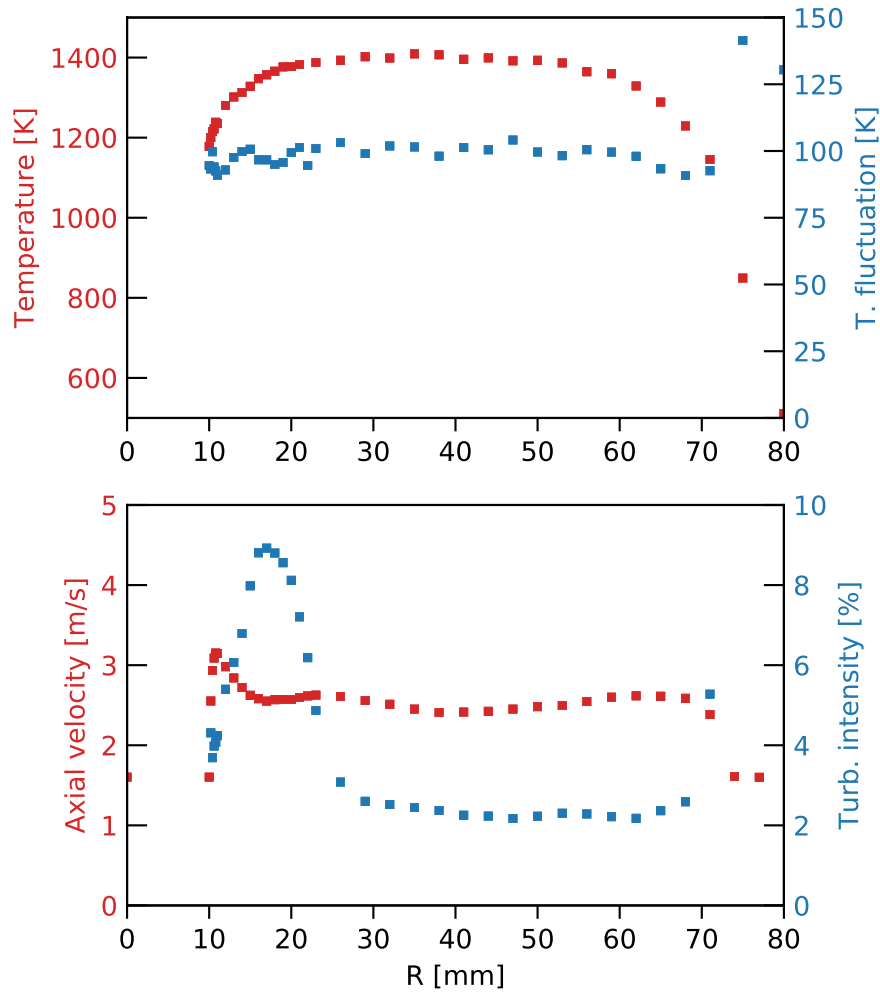
Figure E.1.: Radial profiles of temperature and velocity at the coflow outlet. Data from the experimental characterization of the DSHC burner by Rodriues et al. [32].

F. Additional plots for the SSB
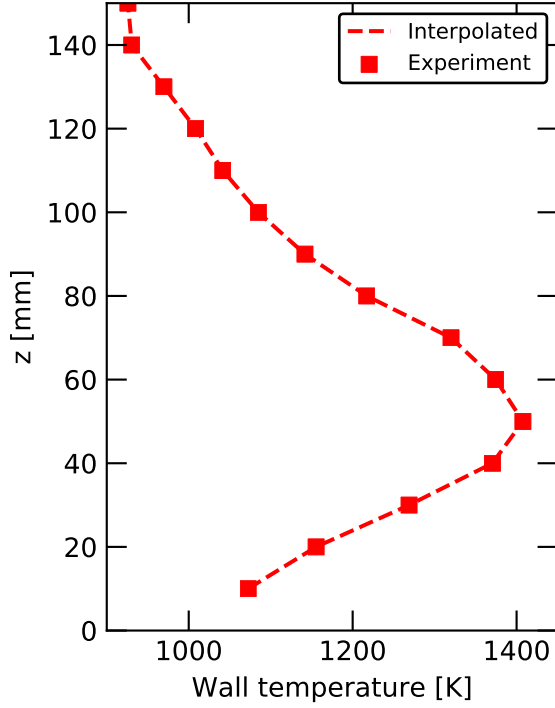
(a) Combustion chamber walls
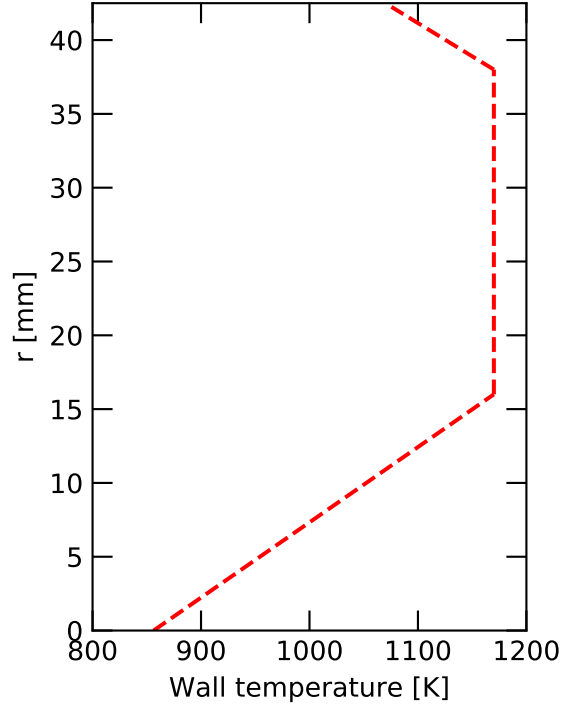
(b) Combustion chamber baseplate

Figure F.1.: Temperature profiles for the isothermal boundary condition in the combustion chamber.

Table F.1.: Parameter space $\Omega_{SSB,red}$ of the uncertain inputs.

	Description	PDF	Constant	Unit
φ_D	axial angle	$\mathcal{U}(26,29)$	-	[°]
$_D$	swirl angle	$\mathcal{U}(55,63)$	-	[°]
U_D	absolute velocity	-	27.5	$[\mathrm{m\,s^{-1}}]$
U_G	gas velocity	$\mathcal{U}(70,85)$	-	$[\mathrm{m\,s^{-1}}]$
T_{liq}	liquid temperature	-	320.25	[K]
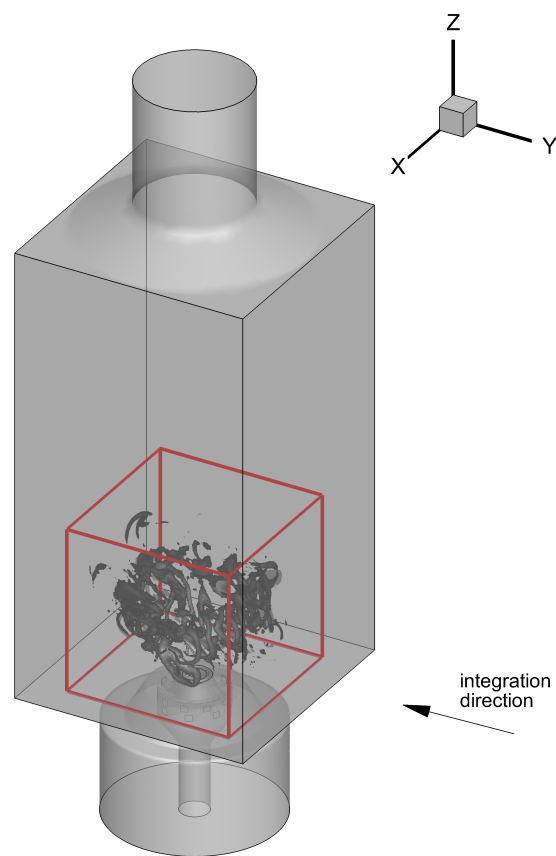
Figure F.2.: Depiction of the line-of-sight integration of the OH* signal in the reaction zone. Observation box (—) and integration direction along the *y*-axis
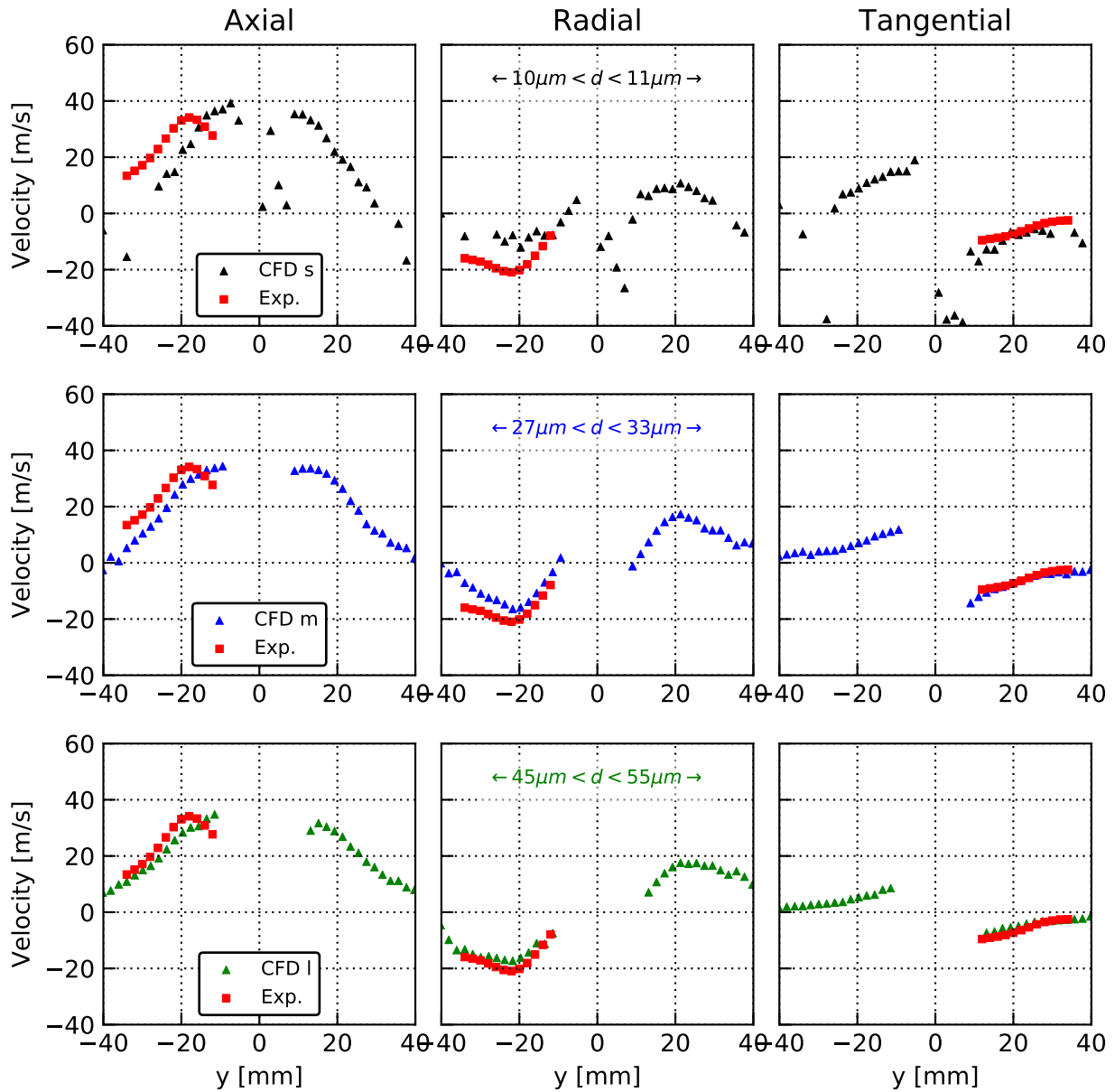
Figure F.3.: Time averaged profiles of droplet velocity components at $z = 25$ mm. Simulation data is split into small (▲), medium (▲), and large droplets (▲). Experimental data (■) is averaged over all diameters.
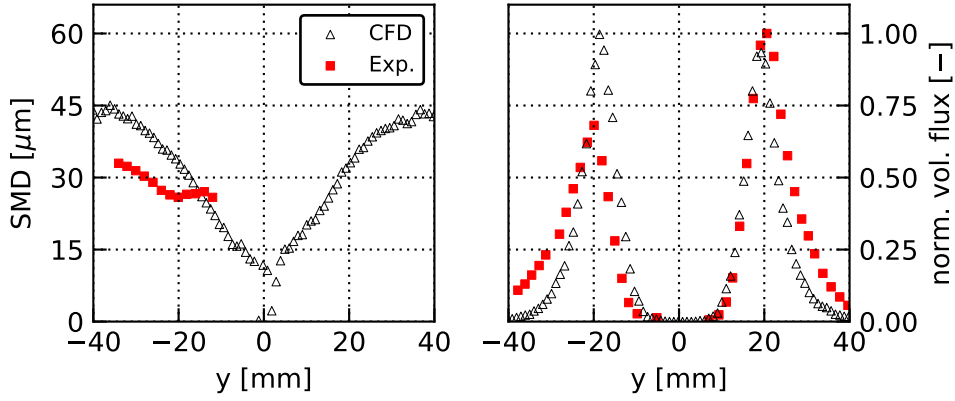
Figure F.4.: Time averaged profiles of Sauter Mean Diameter (SMD) and normalized liquid volume flux at $z = 25$ mm.

(a) Radial direction

(b) Axial direction
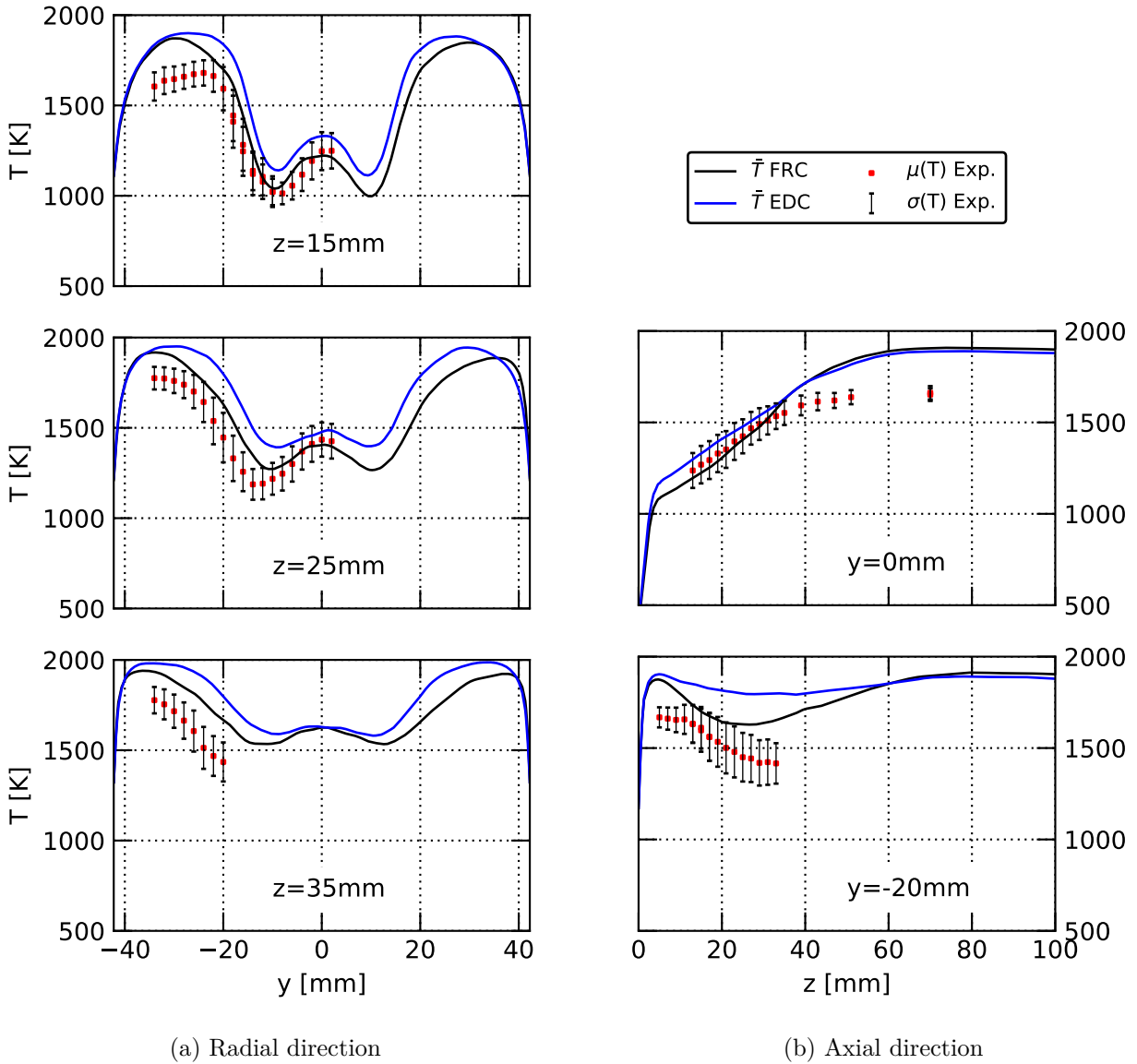
Figure F.5.: Time-averaged temperature profiles from simulations with the EDC and FRC combustion model for the reference case. Mean (■) and standard deviation (─) from CARS data.
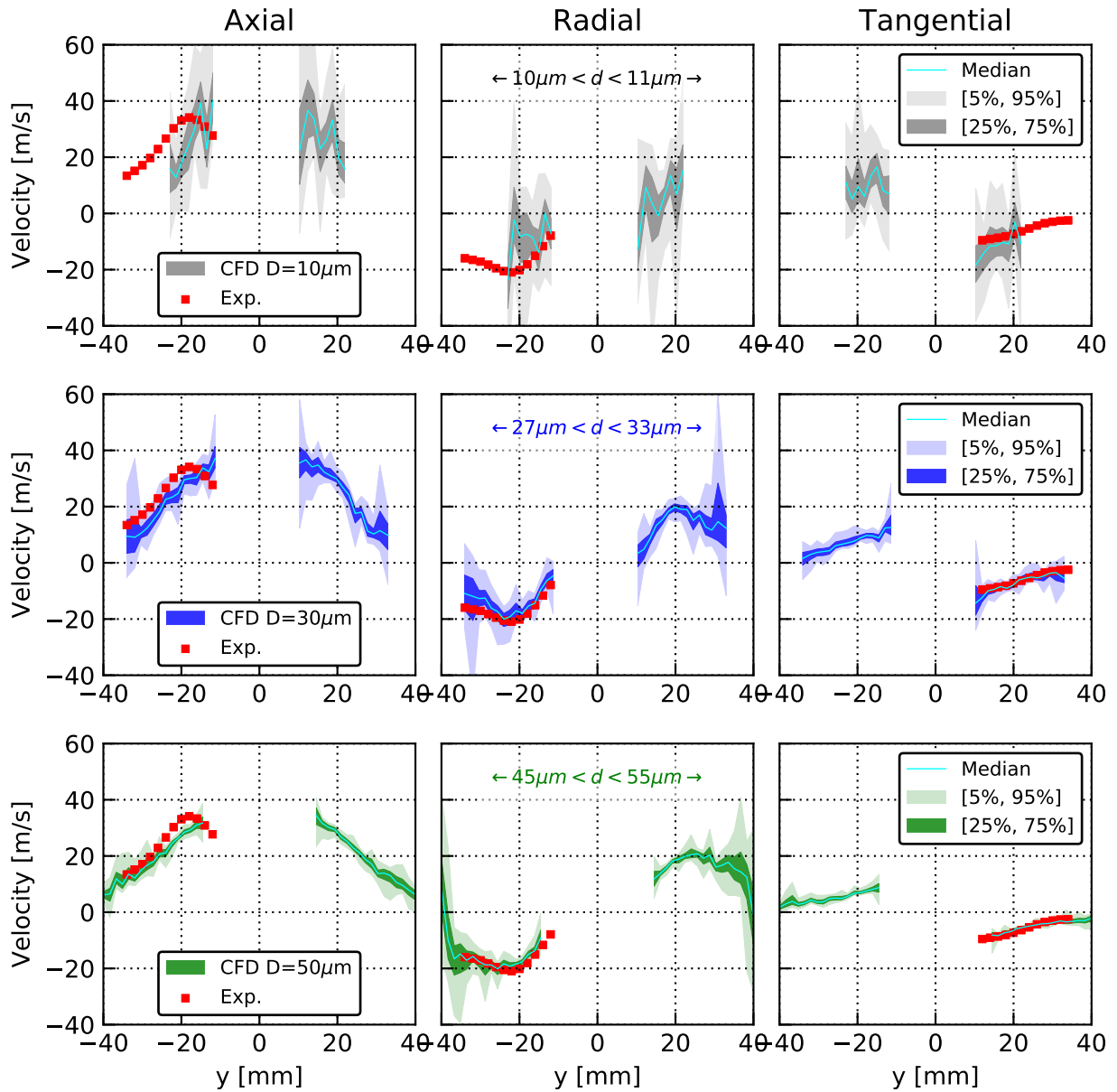
Figure F.6.: Time averaged profiles of droplet velocity components at $z = 25$ mm. Simulation data is split into small (▲), medium (▲), and large droplets (▲). Experimental data (■) is averaged over all diameters.
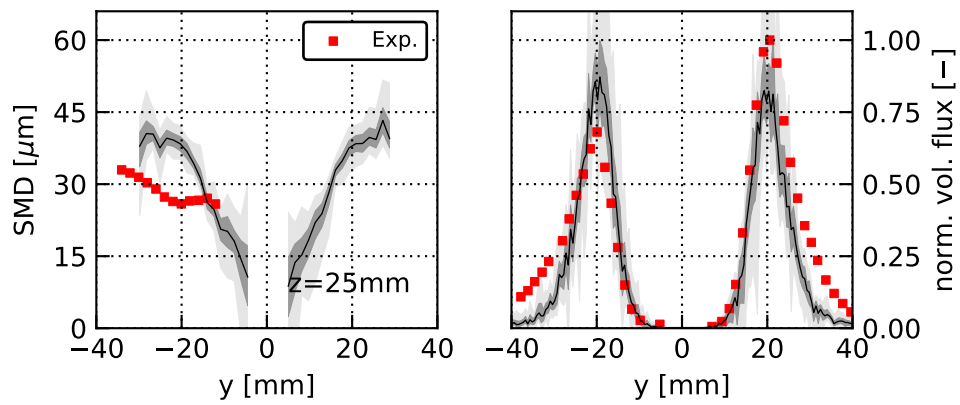
Figure F.7.: Time averaged profiles of Sauter Mean Diameter (SMD) and normalized liquid volume flux at $z = 25$ mm.

Bibliography

[1]   Abani, N. and Ghoniem, A. F. "Large eddy simulations of coal gasification in an entrained flow gasifier". In: *Fuel* 104 (2013), pp. 664–680.

[2]   Abramzon, B. and Sirignano, W. "Droplet vaporization model for spray combustion calculations". In: *International Journal of Heat and Mass Transfer* 32.9 (1989), pp. 1605–1618.

[3]   Adams, B., Bauman, L., et al. "Dakota, A Multilevel Parallel Object-Oriented Framework for Design Optimization, Parameter Estimation, Uncertainty Quantification, and Sensitivity Analysis: Version 6.4 User's Manual". In: *Sandia Technical Report SAND2014-4633* (2016).

[4]   AIAA. *Guide for the Verification and Validation of Computational Fluid Dynamics Simulations (AIAA G-077-1998 (2002)).* 1998.

[5]   Askey, R. and Wilson, J. A. *Some basic hypergeometric orthogonal polynomials that generalize Jacobi polynomials.* Vol. 319. American Mathematical Soc., 1985.

[6]   Aughenbaugh, J. M. and Paredis, C. J. "The value of using imprecise probabilities in engineering design". In: *Journal of Mechanical Design* 128.4 (2006), pp. 969–979.

[7]   Avdonin, A., Jaensch, S., et al. "Uncertainty quantification and sensitivity analysis of thermoacoustic stability with non-intrusive polynomial chaos expansion". In: *Combustion and Flame* 189 (2018), pp. 300–310.

[8]   Avramova, M. N. and Ivanov, K. N. "Verification, validation and uncertainty quantification in multi-physics modeling for nuclear reactor design and safety analysis". In: *Progress in Nuclear Energy* 52.7 (2010), pp. 601–614.

[9]   Ayyub, B. M. *Elicitation of expert opinions for uncertainty and risks.* CRC press, 2001.

[10]   Babushok, V. and Dakdancha, A. "Global kinetic parameters for high-temperature gas-phase reactions". In: *Combustion, Explosion and Shock Waves* 29.4 (1993), pp. 464–489.

[11]   Bauerheim, M., Ndiaye, A., et al. "Surrogates for Combustion Instabilities in Annular Combustors". In: *Uncertainty Management for Robust Industrial Design in Aeronautics.* Springer, 2019, pp. 247–263.

[12]   Beale, J. C. and Reitz, R. D. "Modeling spray atomization with the Kelvin-Helmholtz/Rayleigh-Taylor hybrid model". In: *Atomization and sprays* 9.6 (1999), pp. 623–650.

[13]   Begoli, E., Bhattacharya, T., et al. "The need for uncertainty quantification in machine-assisted medical decision making". In: *Nature Machine Intelligence* 1.1 (2019), pp. 20–23.

[14]   Bengtsson, T., Bickel, P., et al. "Curse-of-dimensionality revisited: Collapse of the particle filter in very large scale systems". In: *Probability and statistics: Essays in honor of David A. Freedman*. Institute of Mathematical Statistics, 2008, pp. 316–334.

[15]   Bini, M. and Jones, W. "Large-eddy simulation of particle-laden turbulent flows". In: *Journal of Fluid Mechanics* 614 (2008), pp. 207–252.

[16]   Blacha, T., Di Domenico, M., et al. "Modeling of soot and NOx in a full scale turbine engine combustor with detailed chemistry". In: *Proceedings of ASME 2011 Turbo Expo*. American Society of Mechanical Engineers. 2011, pp. 33–42.

[17]   Bobkov, S. and Ledoux, M. "One-dimensional empirical measures, order statistics and Kantorovich transport distances". In: *preprint* (2014).

[18]   Booker, A. J., Dennis, J. E., et al. "A rigorous framework for optimization of expensive functions by surrogates". In: *Structural optimization* 17.1 (1999), pp. 1–13.

[19]   Borghesi, G., Mastorakos, E., et al. "Complex chemistry DNS of n-heptane spray autoignition at high pressure and intermediate temperature conditions". In: *Combustion and Flame* 160.7 (2013), pp. 1254–1275.

[20]   Boudier, G., Gicquel, L., et al. "Comparison of LES, RANS and experiments in an aeronautical gas turbine combustion chamber". In: *Proceedings of the Combustion Institute* 31.2 (2007), pp. 3075–3082.

[21]   Campolongo, F., Cariboni, J., et al. "An effective screening design for sensitivity analysis of large models". In: *Environmental Modelling & Software* 22.10 (2007), pp. 1509–1518.

[22]   Cantu, L. M., Grohmann, J., et al. "Temperature measurements in confined swirling spray flames by vibrational coherent anti-stokes Raman spectroscopy". In: *Experimental Thermal and Fluid Science* 95 (2018), pp. 52–59.

[23]   Casella, G. and Berger, R. L. *Statistical inference*. Vol. 2. Duxbury Pacific Grove, CA, 2002.

[24]   Cavaliere, A. and Joannon, M. de. "Mild Combustion". In: *Progress in Energy and Combustion Science* 30.4 (2004), pp. 329–366.

[25]   Celikyilmaz, A. and Turksen, I. B. "Modeling uncertainty with fuzzy logic". In: *Studies in Fuzziness and Soft Computing* 240 (2009), pp. 149–215.

[26]   Chaussonnet, G., Vermorel, O., et al. "A new phenomenological model to predict drop size distribution in Large-Eddy Simulations of airblast atomizers". In: *International Journal of Multiphase Flow* 80 (2016), pp. 29–42.

[27] Chaussonnet, G. "Modeling of liquid film and breakup phenomena in Large-Eddy Simulations of aeroengines fueled by airblast atomizers". PhD thesis. Institut National Polytechnique de Toulouse (INP Toulouse), 2014.

[28] Chiu, H.-H. "Advances and challenges in droplet and spray combustion. I. Toward a unified theory of droplet aerothermochemistry". In: *Progress in Energy and Combustion Science* 26.4-6 (2000), pp. 381–416.

[29] Choi, S.-K., Grandhi, R. V., et al. "Polynomial chaos expansion with latin hypercube sampling for estimating response variability". In: *AIAA journal* 42.6 (2004), pp. 1191–1198.

[30] Choudhary, A., Voyles, I. T., et al. "Probability Bounds Analysis Applied to the Sandia Verification and Validation Challenge Problem". In: *Journal of Verification, Validation and Uncertainty Quantification* 1.1 (2016), pp. 1–13.

[31] Clift, R., Grace, J. R., et al. *Bubbles, drops, and particles.* Courier Corporation, 2005.

[32] Correia Rodrigues, H. "Spray combustion in moderate and intense low-oxygen conditions: An experimental study". PhD thesis. TU Delft, Delft University of Technology, 2015.

[33] Corson, D., Jaiman, R., et al. "Industrial application of RANS modelling: capabilities and needs". In: *International Journal of Computational Fluid Dynamics* 23.4 (2009), pp. 337–347.

[34] Cosner, R. "CFD validation requirements for technology transition". In: *Fluid Dynamics Conference.* 1995, p. 2227.

[35] Cotterman, R. L., Bender, R., et al. "Phase equilibria for mixtures containing very many components. Development and application of continuous thermodynamics for chemical process design". In: *Industrial & Engineering Chemistry Process Design and Development* 24.1 (1985), pp. 194–203.

[36] Cristianini, N., Shawe-Taylor, J., et al. *An introduction to support vector machines and other kernel-based learning methods.* Cambridge university press, 2000.

[37] Dagaut, P. and Cathonnet, M. "The ignition, oxidation, and combustion of kerosene: A review of experimental and kinetic modeling". In: *Progress in Energy and Combustion Science* 32.1 (2006), pp. 48–92.

[38] Davidson, L. "Large eddy simulations: how to evaluate resolution". In: *International Journal of Heat and Fluid Flow* 30.5 (2009), pp. 1016–1025.

[39] Davis, P. J. and Rabinowitz, P. *Methods of numerical integration.* Courier Corporation, 2007.

[40] Deardorff, J. "On the magnitude of the subgrid scale eddy coefficient". In: *Journal of Computational Physics* 7.1 (1971), pp. 120–133.

[41]   Denaro, F. M. "What does Finite Volume-based implicit filtering really resolve in Large-Eddy Simulations?" In: *Journal of Computational Physics* 230.10 (2011), pp. 3849–3883.

[42]   Di Domenico, M., Gerlinger, P., et al. "Numerical simulations of confined, turbulent, lean, premixed flames using a detailed chemistry combustion model". In: *Proceedings of ASME 2011 Turbo Expo*. American Society of Mechanical Engineers. 2011, pp. 519–530.

[43]   Domenico, M. D. "Numerical simulations of soot formation in turbulent flows". eng. PhD thesis. Universität Stuttgart, 2008.

[44]   Domingo, P., Vervisch, L., et al. "DNS analysis of partially premixed combustion in spray and gaseous turbulent flame-bases stabilized in hot air". In: *Combustion and Flame* 140.3 (2005), pp. 172–195.

[45]   Doué, N., Le Clercq, P., et al. "Validation of a multicomponent-fuel droplet evaporation model based on continuous thermodynamics". In: *Proceeding of ICLASS 2006* (2006).

[46]   Dryer, F. L. "Chemical kinetic and combustion characteristics of transportation fuels". In: *Proceedings of the Combustion Institute* 35.1 (2015), pp. 117–144.

[47]   Durrett, R. *Probability: theory and examples*. Vol. 49. Cambridge University Press, 2019.

[48]   Eberle, C., Gerlinger, P. M., et al. "Large eddy simulations of a sooting lifted turbulent jet-flame". In: *55th AIAA Aerospace Sciences Meeting*. 2017, p. 1785.

[49]   Eckel, G., Rachner, M., et al. "Assessment of two particle dispersion models for Large Eddy Simulations of confined swirling flows". In: *10th International Conference on Multiphase Flow - ICMF*. 2019.

[50]   Eckel, G. "Large Eddy Simulation of Turbulent Reacting Multi-Phase Flows". PhD thesis. Universität Stuttgart, 2018.

[51]   Eckel, G., Grohmann, J., et al. "LES of a swirl-stabilized kerosene spray flame with a multi-component vaporization model and detailed chemistry". In: *Combustion and Flame* 207 (2019), pp. 134–152.

[52]   Eckel, G., Le Clercq, P., et al. "Entrained flow gasification. Part 3: Insight into the injector near-field by Large Eddy Simulation with detailed chemistry". In: *Fuel* 223 (2018), pp. 164–178.

[53]   Eckel, G., Rachner, M., et al. "Semi-Empiricalmpirical Model for the unsteady Shear Breakup of liquid Jets in Cross-Flow". In: *Atomization and Sprays* 26.7 (2016).

[54]   Edwards, T., Moses, C., et al. "Evaluation of combustion performance of alternative aviation fuels". In: *46th AIAA/ASME/SAE/ASEE Joint Propulsion Conference & Exhibit*. 2010, p. 7155.

[55]   Enderle, B., Eckel, G., et al. "Large Eddy Simulation of Turbulent Ethanol Spray Flames under MILD conditions using a Finite Rate Chemistry Combustion Model". In: *Proceedings of ICLASS 2018, 14th Triennial International Conference on Liquid Atomization and Spray Systems*. 2018.

[56]   Enderle, B., Grimm, F., et al. "Derivation and Numerical study of spray boundary conditions for a pressure swirl atomizer issuing into co-flowing air". In: *Proceedings of GPPS Forum 18*. 2018.

[57]   Enderle, B., Grimm, F., et al. "Numerical Simulation of a model spray flame under MILD conditions using stochastic upstream flow and temperature forcing". In: *Proceedings of GPPS Forum 18*. 2018.

[58]   Enderle, B., Rauch, B., et al. "Non-intrusive uncertainty quantification in the simulation of turbulent spray combustion using Polynomial Chaos Expansion: A case study". In: *Combustion and Flame* 213 (2020), pp. 26–38.

[59]   Enderle, B., Rauch, B., et al. "Towards affordable Uncertainty Quantification in the Simulation of Turbulent Spray Combustion via Surrogate Modeling". In: *AIAA Scitech 2019 Forum*. 2019, p. 1727.

[60]   Esclapez, L., Ma, P. C., et al. "Fuel effects on lean blow-out in a realistic gas turbine combustor". In: *Combustion and Flame* 181 (2017), pp. 82–99.

[61]   Faeth, G. "Evaporation and combustion of sprays". In: *Progress in Energy and Combustion Science* 9.1-2 (1983), pp. 1–76.

[62]   Felden, A., Esclapez, L., et al. "Including real fuel chemistry in LES of turbulent spray combustion". In: *Combustion and Flame* 193 (2018), pp. 397–416.

[63]   Ferson, S. and Ginzburg, L. R. "Different methods are needed to propagate ignorance and variability". In: *Reliability Engineering & System Safety* 54.2-3 (1996), pp. 133–144.

[64]   Ferson, S. and Hajagos, J. G. "Arithmetic with uncertain numbers: rigorous and (often) best possible answers". In: *Reliability Engineering & System Safety* 85.1-3 (2004), pp. 135–152.

[65]   Fiolitakis, A. "Numerische Berechnung von Stickoxiden in turbulenten Flammen mit Transportgleichungs-PDF-Verfahren". PhD thesis. Universität Stuttgart, 2014.

[66]   Fishman, G. *Monte Carlo: concepts, algorithms, and applications*. Springer Science & Business Media, 2013.

[67]   Forrester, A. I., Sóbester, A., et al. "Multi-fidelity optimization via surrogate modelling". In: *Proceedings of the Royal Society A: Mathematical, Physical and Engineering Sciences* 463.2088 (2007), pp. 3251–3269.

[68]   Forrester, A., Keane, A., et al. *Engineering design via surrogate modelling: a practical guide*. John Wiley & Sons, 2008.

[69]   Friedman, J. H. "Multivariate adaptive regression splines". In: *The Annals of Statistics* (1991), pp. 1–67.

[70] Friedman, J. H. "Stochastic gradient boosting". In: *Computational Statistics & Data Analysis* 38.4 (2002), pp. 367–378.

[71] Friedman, J., Hastie, T., et al. *The elements of statistical learning.* Vol. 1. 10. Springer Series in Statistics New York, USA: 2001.

[72] Fröhlich, J. *Large eddy simulation turbulenter Strömungen.* Vol. 1. Springer, 2006.

[73] Gallot-Lavallée, S., Jones, W., et al. "Large Eddy Simulation of an ethanol spray flame under MILD combustion with the stochastic fields method". In: *Proceedings of the Combustion Institute* 36.2 (2016), pp. 2577–2584.

[74] Gautschi, W. *Orthogonal polynomials.* Oxford university press Oxford, 2004.

[75] Gavrilov, A., Sentyabov, A., et al. "Vortical structures and pressure pulsations in draft tube of a Francis-99 turbine at part load: RANS and hybrid RANS/LES analysis". In: *International Journal of Heat and Fluid Flow* 63 (2017), pp. 158–171.

[76] Gelman, A., Carlin, J. B., et al. *Bayesian data analysis.* Chapman and Hall/CRC, 2013.

[77] Gepperth, S., Guildenbecher, D., et al. "Pre-filming primary atomization: Experiments and modeling". In: *23rd European Conference on Liquid Atomization and Spray Systems (ILASS-Europe 2010).* 2010, pp. 6–8.

[78] Gerlinger, P., Stoll, P., et al. "An implicit multigrid method for the simulation of chemically reacting flows". In: *Journal of Computational Physics* 146.1 (1998), pp. 322–345.

[79] Gerlinger, P. *Numerische Verbrennungssimulation: Effiziente numerische Simulation turbulenter Verbrennung.* Springer-Verlag, 2005.

[80] Ghanem, R. and Ghiocel, D. "Stochastic seismic soil-structure interaction using the homogeneous chaos expansion". In: *Proc. 12th ASCE Engineering Mechanics Division Conference, La Jolla, California, USA.* 1998.

[81] Gicquel, L. Y., Staffelbach, G., et al. "Large eddy simulations of gaseous flames in gas turbine combustion chambers". In: *Progress in Energy and Combustion Science* 38.6 (2012), pp. 782–817.

[82] Giunta, A., Swiler, L., et al. "The surfpack software library for surrogate modeling of sparse irregularly spaced multidimensional data". In: *11th AIAA/ISSMO Multidisciplinary Analysis and Optimization Conference.* 2006, p. 7049.

[83] Gneiting, T. and Raftery, A. E. "Strictly proper scoring rules, prediction, and estimation". In: *Journal of the American statistical Association* 102.477 (2007), pp. 359–378.

[84] Goodwin, N. et al. "Bridging the gap between deterministic and probabilistic uncertainty quantification using advanced proxy based methods". In: *SPE Reservoir Simulation Symposium.* Society of Petroleum Engineers. 2015.

[85] Gorissen, D., Couckuyt, I., et al. "A surrogate modeling and adaptive sampling toolbox for computer based design". In: *Journal of Machine Learning Research* 11.Jul (2010), pp. 2051–2055.

[86] Gorokhovski, M. and Herrmann, M. "Modeling primary atomization". In: *Annual Reviews in Fluid Mechanics* 40 (2008), pp. 343–366.

[87] Gosman, A. and Loannides, E. "Aspects of computer simulation of liquid-fueled combustors". In: *Journal of Energy* 7.6 (1983), pp. 482–490.

[88] Grohmann, J., Rauch, B., et al. "Influence of Single-Component Fuels on Gas-Turbine Model Combustor Lean Blowout". In: *Journal of Propulsion and Power* 34.1 (2017), pp. 97–107.

[89] Grohmann, J. "Experimentelle Untersuchungen zum Einfluss von Kohlenwasserstoffen auf das Verbrennungsverhalten drallstabilisierter Sprayflammen". PhD thesis. Universität Stuttgart, 2019.

[90] Grohmann, J., O'Loughlin, W., et al. "Comparison of the Combustion Characteristics of Liquid Single-Component Fuels in a Gas Turbine Model Combustor". In: *Proceedings of ASME Turbo Expo 2016*. American Society of Mechanical Engineers. 2016, GT2016–56177.

[91] Grohmann, J., Rauch, B., et al. "Investigation of differences in lean blowout of liquid single-component fuels in a gas turbine model combustor". In: *52nd AIAA/SAE/ASEE Joint Propulsion Conference*. 2016, p. 4647.

[92] Group, T. *THETA Theory Manual*. Tech. rep. German Aerospace Center (DLR), 2012.

[93] Guan, J. W. and Bell, D. A. *Evidence theory and its applications*. Elsevier Science Inc., 1992.

[94] Hallett, W. L. "A simple model for the vaporization of droplets with large numbers of components". In: *Combustion and Flame* 121.1-2 (2000), pp. 334–344.

[95] Hammersley, J. *Monte carlo methods*. Springer Science & Business Media, 2013.

[96] Helton, J., Johnson, J., et al. "An exploration of alternative approaches to the representation of uncertainty in model predictions". In: *Reliability Engineering & System Safety* 85.1 (2004), pp. 39–71.

[97] Hertz, J. A. *Introduction to the theory of neural computation*. CRC Press, 2018.

[98] Hinze, J. O. *Turbulence*. McGraw-Hill, 1972.

[99] Hochgreb, S. "Mind the gap: Turbulent combustion model validation and future needs". In: *Proceedings of the Combustion Institute* 37.2 (2019), pp. 2091–2107.

[100] Homma, T. and Saltelli, A. "Importance measures in global sensitivity analysis of nonlinear models". In: *Reliability Engineering & System Safety* 52.1 (1996), pp. 1–17.

[101] Hu, X., Chen, X., et al. "Review of improved Monte Carlo methods in uncertainty-based design optimization for aerospace vehicles". In: *Progress in Aerospace Sciences* 86 (2016), pp. 20–27.

[102] Hubbard, G., Denny, V., et al. "Droplet evaporation: effects of transients and variable properties". In: *International Journal of Heat and Mass Transfer* 18.9 (1975), pp. 1003–1008.

[103] Huh, K. "A phenomenological model of diesel spray atomization". In: *Proceedings of The International Conference on Multiphase Flows' 91*. 1991.

[104] Iaccarino, G. "Introduction to Uncertainty Quantification in Computational Science". In: *Lecture Notes for ME470, Stanford University*. 2009.

[105] Ivanova, E. "Numerical simulations of turbulent mixing in complex flows". eng. PhD thesis. Universität Stuttgart, 2012.

[106] Jamali, S. H. "Computational Modeling of Turbulent Ethanol Spray Flames in a Hot Diluted Coflow". PhD thesis. TU Delft, Delft University of Technology, 2014.

[107] Jenny, P., Roekaerts, D., et al. "Modeling of turbulent dilute spray combustion". In: *Progress in Energy and Combustion Science* 38.6 (2012), pp. 846–887.

[108] Johnson, R., Wu, H., et al. "A general probabilistic approach for the quantitative assessment of LES combustion models". In: *Combustion and Flame* 183 (2017), pp. 88–101.

[109] Jones, D. R., Schonlau, M., et al. "Efficient global optimization of expensive black-box functions". In: *Journal of Global optimization* 13.4 (1998), pp. 455–492.

[110] Jones, W., Marquis, A., et al. "Large-eddy simulation of spray combustion in a gas turbine combustor". In: *Combustion and Flame* 161.1 (2014), pp. 222–239.

[111] Jones, W. and Launder, B. E. "The prediction of laminarization with a two-equation model of turbulence". In: *International Journal of Heat and Mass Transfer* 15.2 (1972), pp. 301–314.

[112] Joos, F. *Technische Verbrennung*. Springer, 2006.

[113] Kang, Z., Wang, Z.-g., et al. "Review on pressure swirl injector in liquid rocket engine". In: *Acta Astronautica* 145 (2018), pp. 174–198.

[114] Kapur, J. N. and Kesavan, H. K. "Entropy Optimization Principles and their Applications". In: *Entropy and energy dissipation in water resources*. Springer, 1992, pp. 3–20.

[115] Kathrotia, T. "Reaction kinetics modeling of OH*, CH*, and C2* chemiluminescence". PhD thesis. Universität Heidelberg, 2011.

[116] Kathrotia, T., Riedel, U., et al. "Experimental and numerical study of chemiluminescent species in low-pressure flames". In: *Applied Physics B* 107.3 (2012), pp. 571–584.

[117] Kearfott, R. B. and Kreinovich, V. *Applications of interval computations*. Vol. 3. Springer Science & Business Media, 2013.

[118] Keese, A. "Numerical solution of systems with stochastic uncertainties: a general purpose framework for stochastic finite elements". PhD thesis. TU Braunschweig, 2004.

[119] Khalil, M., Lacaze, G., et al. "Uncertainty quantification in LES of a turbulent bluff-body stabilized flame". In: *Proceedings of the Combustion Institute* 35.2 (2015), pp. 1147–1156.

[120] Kim, S. H. and Boukouvala, F. "Machine learning-based surrogate modeling for data-driven optimization: a comparison of subset selection for regression techniques". In: *Optimization Letters* (2019), pp. 1–22.

[121] Klein, M., Sadiki, A., et al. "A digital filter based generation of inflow data for spatially developing direct numerical or large eddy simulations". In: *Journal of Computational Physics* 186.2 (2003), pp. 652–665.

[122] Kolmogorov, A. N. "Dissipation of energy in locally isotropic turbulence". In: *Akademiia Nauk SSSR Doklady*. Vol. 32. 1941, p. 16.

[123] Kuo, K. K.-y. and Acharya, R. *Applications of turbulent and multiphase combustion*. John Wiley & Sons, 2012.

[124] Kuo, K. K.-y. and Acharya, R. *Fundamentals of Turbulent and Multi-Phase Combustion*. John Wiley & Sons, 2012.

[125] Launder, B. E. and Sharma, B. "Application of the energy-dissipation model of turbulence to the calculation of flow near a spinning disc". In: *Letters in Heat and Mass Transfer* 1.2 (1974), pp. 131–137.

[126] Le Clercq, P., Doué, N., et al. "Validation of a multicomponent-fuel model for spray computations". In: *AIAA Aerospace Science Meeting, Orlando*. 2009, pp. 5–8.

[127] Le Maître, O. and Knio, O. M. "Stochastic Spectral Methods for Uncertainty Quantification". In: *Proceedings of the 38th Conference of Dutch-Flemish NA Communities, Woudschoten*. 2017.

[128] Le Maître, O. and Knio, O. M. *Spectral methods for uncertainty quantification: with applications to computational fluid dynamics*. Springer Science & Business Media, 2010.

[129] Lefebvre, A. *Atomization and sprays*. Vol. 1040. 2756. CRC press, 1988.

[130] Lefebvre, A. H. "Airblast atomization". In: *Progress in Energy and Combustion Science* 6.3 (1980), pp. 233–261.

[131] Lefebvre, A. H. *Gas turbine combustion*. CRC Press, 2010.

[132] Leonard, A. "Energy cascade in large-eddy simulations of turbulent fluid flows". In: *Advances in Geophysics*. Vol. 18. Elsevier, 1975, pp. 237–248.

[133] Lieuwen, T. C. and Yang, V. *Gas turbine emissions*. Vol. 38. Cambridge university press, 2013.

[134] Loeppky, J. L., Sacks, J., et al. "Choosing the sample size of a computer experiment: A practical guide". In: *Technometrics* 51.4 (2009), pp. 366–376.

[135] Loeven, G., Witteveen, J., et al. "Probabilistic collocation: an efficient non-intrusive approach for arbitrarily distributed parametric uncertainties". In: *45th AIAA Aerospace Sciences Meeting and Exhibit.* 2007, p. 317.

[136] Lourier, J.-M., Stöhr, M., et al. "Scale Adaptive Simulation of a thermoacoustic instability in a partially premixed lean swirl combustor". In: *Combustion and Flame* 183 (2017), pp. 343–357. ISSN: 0010-2180.

[137] Lucca-Negro, O. and O'Doherty, T. "Vortex breakdown: a review". In: *Progress in Energy and Combustion Science* 27.4 (2001), pp. 431–481. ISSN: 0360-1285.

[138] Ma, L., Zhu, S., et al. "Numerical investigation of ethanol spray-in-hot-coflow flame using steady flamelet model". In: *Proceedings of the Eighth Mediterranean Combustion Symposium.* 2013, pp. 1–12.

[139] Ma, L. "Computational Modeling of Turbulent Spray Combustion". PhD thesis. TU Delft, 2016.

[140] Ma, L. and Roekaerts, D. "Modeling of spray jet flame under MILD condition with non-adiabatic FGM and a new conditional droplet injection model". In: *Combustion and Flame* 165 (2016), pp. 402–423.

[141] Ma, L. and Roekaerts, D. "Numerical study of the multi-flame structure in spray combustion". In: *Proceedings of the Combustion Institute* 36.2 (2017), pp. 2603–2613.

[142] Ma, L. and Roekaerts, D. "Structure of spray in hot-diluted coflow flames under different coflow conditions: A numerical study". In: *Combustion and Flame* 172 (2016), pp. 20–37.

[143] Magnussen, B. F. and Hjertager, B. H. "On mathematical modeling of turbulent combustion with special emphasis on soot formation and combustion". In: *Symposium (international) on Combustion.* Vol. 16. 1. Elsevier. 1977, pp. 719–729.

[144] Malik, M. R. and Bushnell, D. M. "Role of computational fluid dynamics and wind tunnels in aeronautics R and D". In: *NASA/TP–2012-217602* (2012).

[145] Marrel, A., Saint-Geours, N., et al. "Sensitivity analysis of spatial and/or temporal phenomena". In: *Springer Handbook on Uncertainty Quantification, Springer* (2017), pp. 1327–1357.

[146] Marrel, A., Saint-Geours, N., et al. "Sensitivity analysis of spatial and/or temporal phenomena". In: *Handbook of Uncertainty Quantification* (2016), pp. 1–31.

[147] Marvin, J. G. "Perspective on computational fluid dynamics validation". In: *AIAA Journal* 33.10 (1995), pp. 1778–1787.

[148] Masquelet, M., Yan, J., et al. "Uncertainty quantification in large eddy simulations of a rich-dome aviation gas turbine". In: *Proceedings of ASME Turbo Expo 2017.* American Society of Mechanical Engineers. 2017, GT2017–64835.

[149] Matheron, G. "Principles of geostatistics". In: *Economic Geology* 58.8 (1963), pp. 1246–1266.

[150] McKay, M. D., Beckman, R. J., et al. "Comparison of three methods for selecting values of input variables in the analysis of output from a computer code". In: *Technometrics* 21.2 (1979), pp. 239–245.

[151] Meier, W., Barlow, R., et al. "Raman/Rayleigh/LIF measurements in a turbulent CH4/H2/N2 jet diffusion flame: experimental techniques and turbulence–chemistry interaction". In: *Combustion and Flame* 123.3 (2000), pp. 326–343. ISSN: 0010-2180.

[152] Ménard, T., Tanguy, S., et al. "Coupling level set/VOF/ghost fluid methods: Validation and application to 3D simulation of the primary break-up of a liquid jet". In: *International Journal of Multiphase Flow* 33.5 (2007), pp. 510–524.

[153] Menter, F. R. "Best practice: scale-resolving simulations in ANSYS CFD". In: *ANSYS Germany GmbH* 1 (2012).

[154] Menter, F. R. "Two-equation eddy-viscosity turbulence models for engineering applications". In: *AIAA Journal* 32.8 (1994), pp. 1598–1605.

[155] Menter, F. R., Kuntz, M., et al. "Ten years of industrial experience with the SST turbulence model". In: *Turbulence, heat and mass transfer* 4.1 (2003), pp. 625–632.

[156] Menter, F. and Egorov, Y. "A scale adaptive simulation model using two-equation models". In: *43rd AIAA Aerospace Sciences Meeting and Exhibit*. 2005, p. 1095.

[157] Menter, F., Kuntz, M., et al. "A scale-adaptive simulation model for turbulent flow predictions". In: *41st Aerospace Sciences Meeting and Exhibit*. 2003, p. 767.

[158] Menter, F. and Egorov, Y. "The scale-adaptive simulation method for unsteady turbulent flow predictions. Part 1: theory and model description". In: *Flow, Turbulence and Combustion* 85.1 (2010), pp. 113–138.

[159] Mercier, R., Schmitt, T., et al. "The influence of combustion SGS submodels on the resolved flame propagation. Application to the LES of the Cambridge stratified flames". In: *Proceedings of the Combustion Institute* 35.2 (2015), pp. 1259–1267.

[160] Methling, T. "Entwicklung des linearen Transformationsmodells für die Analyse und Optimierung chemisch-kinetischer Prozesse". PhD thesis. Universität Stuttgart, 2017.

[161] Miller, R., Harstad, K., et al. "Evaluation of equilibrium and non-equilibrium evaporation models for many-droplet gas-liquid flow simulations". In: *International Journal of Multiphase Flow* 24.6 (1998), pp. 1025–1055.

[162] Moin, P. and Mahesh, K. "Direct numerical simulation: a tool in turbulence research". In: *Annual review of fluid mechanics* 30.1 (1998), pp. 539–578.

[163] Montgomery, D. C. *Design and analysis of experiments*. John wiley & sons, 2017.

[164] Montomoli, F., Carnevale, M., et al. *Uncertainty quantification in computational fluid dynamics and aircraft engines*. Springer, 2015.

[165] Moore, R. E. *Methods and applications of interval analysis*. SIAM, 1979.

[166] Morris, M. D. "Factorial sampling plans for preliminary computational experiments". In: *Technometrics* 33.2 (1991), pp. 161–174.

[167] Mueller, M. E., Iaccarino, G., et al. "Chemical kinetic uncertainty quantification for large eddy simulation of turbulent nonpremixed combustion". In: *Proceedings of the Combustion Institute* 34.1 (2013), pp. 1299–1306.

[168] Mueller, M. E. and Raman, V. "Effects of turbulent combustion modeling errors on soot evolution in a turbulent nonpremixed jet flame". In: *Combustion and Flame* 161.7 (2014), pp. 1842–1848.

[169] Mueller, M. E. and Raman, V. "Model form uncertainty quantification in turbulent combustion simulations: Peer models". In: *Combustion and Flame* 187 (2018), pp. 137–146.

[170] Müller, A., Meier, R., et al. "The influence of unsteady flow conditions on liquid sheet atomisation". In: *Atomization and Spray Processes* (2004), pp. 134–138.

[171] Myers, R. H., Montgomery, D. C., et al. "Response surface methodology: a retrospective and literature survey". In: *Journal of quality technology* 36.1 (2004), pp. 53–77.

[172] Najm, H. N. "Uncertainty quantification and polynomial chaos techniques in computational fluid dynamics". In: *Annual review of fluid mechanics* 41 (2009), pp. 35–52.

[173] Nicoud, F. and Ducros, F. "Subgrid-scale stress modelling based on the square of the velocity gradient tensor". In: *Flow, turbulence and Combustion* 62.3 (1999), pp. 183–200.

[174] Niederreiter, H. *Random number generation and quasi-Monte Carlo methods*. Vol. 63. Siam, 1992.

[175] Nori, V. N. "Modeling and analysis of chemiluminescence sensing for syngas, methane and Jet-A combustion". PhD thesis. Georgia Institute of Technology, 2008.

[176] Oberkampf, W. L. "Uncertainty quantification using evidence theory". In: *Proceedings from the Advanced Simulation & Computing Workshop*. 2005.

[177] Oberkampf, W. L. and Roy, C. J. *Verification and validation in scientific computing*. Cambridge University Press, 2010.

[178] Oberkampf, W. L., Trucano, T. G., et al. "Verification, validation, and predictive capability in computational engineering and physics". In: *Applied Mechanics Reviews* 57.5 (2004), pp. 345–384.

[179] Owen, A. B. *Course Stat 200: Introduction to Statistical Inference*. Stanford University, 2018.

[180] Parente, A., Galletti, C., et al. "Effect of the combustion model and kinetic mechanism on the MILD combustion in an industrial burner fed with hydrogen enriched fuels". In: *International Journal of Hydrogen Energy* 33.24 (2008), pp. 7553–7564.

[181] Pei, Y., Davis, M. J., et al. "Engine Combustion Network (ECN): Global sensitivity analysis of Spray A for different combustion vessels". In: *Combustion and Flame* 162.6 (2015), pp. 2337–2347.

[182] Pereira, F. "The Importance of Verification and Validation for Scale-Resolving Simulations of Turbulence". In: *Proceedings of the AMSE Verification and Validation Symposium - VVS2020-8843*. 2020.

[183] Peters, N. *Turbulent combustion*. 2001.

[184] Phillips, T. S. and Roy, C. J. "Richardson extrapolation-based discretization uncertainty estimation for computational fluid dynamics". In: *Journal of Fluids Engineering* 136.12 (2014), p. 121401.

[185] Pitsch, H. "Large-eddy simulation of turbulent combustion". In: *Annual Reviews of Fluid Mechanics* 38 (2006), pp. 453–482.

[186] Poinsot, T. and Veynante, D. *Theoretical and numerical combustion*. RT Edwards, Inc., 2005.

[187] Pollard, A., Castillo, L., et al. *Whither Turbulence and Big Data in the 21st Century?* Springer, 2016.

[188] Pollard, D. *A user's guide to measure theoretic probability*. Vol. 8. Cambridge University Press, 2002.

[189] Pope, S. "PDF methods for turbulent reactive flows". In: *Progress in Energy and Combustion Science* 11.2 (1985), pp. 119–192. ISSN: 0360-1285.

[190] Pope, S. "The probability approach to the modelling of turbulent reacting flows". In: *Combustion and Flame* 27 (1976), pp. 299–312. ISSN: 0010-2180.

[191] Pope, S. B. "Ten questions concerning the large-eddy simulation of turbulent flows". In: *New Journal of Physics* 6.1 (2004), p. 35.

[192] Pope, S. B. *Turbulent flows*. 2001.

[193] Prabasena, B., Röder, M., et al. "Strain rate and fuel composition dependence of chemiluminescent species profiles in non-premixed counterflow flames: comparison with model results". In: *Applied Physics B* 107.3 (2012), pp. 561–569.

[194] Prager, J., Najm, H. N., et al. "Uncertainty quantification of reaction mechanisms accounting for correlations introduced by rate rules and fitted Arrhenius parameters". In: *Combustion and Flame* 160.9 (2013), pp. 1583–1593.

[195] Qin, C. and Loth, E. "Numerical description of a pressure-swirl nozzle spray". In: *Chemical Engineering and Processing: Process Intensification* 107 (2016), pp. 68–79.

[196] Rachner, M., Brandt, M., et al. "A numerical and experimental study of fuel evaporation and mixing for lean premixed combustion at high pressure". In: *Symposium (International) on Combustion*. Vol. 26. 2. Elsevier. 1996, pp. 2741–2748.

[197] Rachner, M. *Die Stoffeigenschaften von Kerosin Jet A-1*. DLR Mitteilung 98-01. Deutsches Zentrum für Luft- und Raumfahrt (DLR), 1998.

[198] Rachner, M., Becker, J., et al. "Modelling of the atomization of a plain liquid fuel jet in crossflow at gas turbine conditions". In: *Aerospace Science and Technology* 6.7 (2002), pp. 495–506.

[199] Rachner, M. and Doué, N. *SPRAYSIM documentation - CTM handbook*. Tech. rep. German Aerospace Center (DLR), 2009.

[200] Raman, V. and Hassanaly, M. "Emerging trends in numerical simulations of combustion systems". In: *Proceedings of the Combustion Institute* 37.2 (2019), pp. 2073–2089.

[201] Rasmussen, C. E. "Gaussian processes in machine learning". In: *Summer School on Machine Learning*. Springer. 2003, pp. 63–71.

[202] Rauch, B. "Systematic Accuracy Assessment for Alternative Aviation Fuel Evaporation Models". PhD thesis. Stuttgart University, 2018.

[203] Rauch, B., Le Clercq, P., et al. "Application of uncertainty quantification for the validation of spray evaporation models". In: *Proceedings of ILASS – Europe 2016, 27th Annual Conference on Liquid Atomization and Spray Systems*. 2016.

[204] Reagan, M. T., Najm, H. N., et al. "Uncertainty quantification in reacting-flow simulations through non-intrusive spectral projection". In: *Combustion and Flame* 132.3 (2003), pp. 545–555.

[205] Reagan, M., Najm, H., et al. "Spectral stochastic uncertainty quantification in chemical systems". In: *Combustion Theory and Modelling* 8.3 (2004), pp. 607–632.

[206] Red-Horse, J. and Benjamin, A. S. "A probabilistic approach to uncertainty quantification with limited information". In: *Reliability Engineering & System Safety* 85.1-3 (2004), pp. 183–190.

[207] Reichling, G. "Development of Numerical Methods for the Calculation of Thermo-Acoustic Interactions in Gas Turbine Combustion Chambers". PhD thesis. Universität Stuttgart, 2014.

[208] Rey, S. J. "Mathematical Models in Geography". In: *International Encyclopedia of the Social & Behavioral Sciences (Second Edition)*. Ed. by J. D. Wright. Second Edition. Oxford: Elsevier, 2015, pp. 785–790.

[209] Rittler, A., Proch, F., et al. "LES of the Sydney piloted spray flame series with the PFGM/ATF approach and different sub-filter models". In: *Combustion and Flame* 162.4 (2015), pp. 1575–1598.

[210] Roache, P. J. *Fundamentals of verification and validation*. hermosa publ., 2009.

[211] Roache, P. J. "Perspective: a method for uniform reporting of grid refinement studies". In: *Journal of Fluids Engineering* 116.3 (1994), pp. 405–413.

[212]   Rodrigues, H. C., Tummers, M., et al. "Effects of coflow temperature and composition on ethanol spray flames in hot-diluted coflow". In: *International Journal of Heat and Fluid Flow* 51 (2015), pp. 309–323.

[213]   Rodrigues, H. C., Tummers, M. J., et al. "Spray flame structure in conventional and hot-diluted combustion regime". In: *Combustion and Flame* 162.3 (2015), pp. 759–773.

[214]   Röhl, O. and Peters, N. "A reduced mechanism for ethanol oxidation". In: *4th European Combustion Meeting (ECM 2009), Vienna, Austria, April.* 2009, pp. 14–17.

[215]   Rosin, P. "Laws governing the fineness of powdered coal". In: *Journal of Institute of Fuel* 7 (1933), pp. 29–36.

[216]   Roy, C. J. and Oberkampf, W. L. "A comprehensive framework for verification, validation, and uncertainty quantification in scientific computing". In: *Computer Methods in Applied Mechanics and Engineering* 200.25 (2011), pp. 2131–2144.

[217]   Ruoff, S. J., Rauch, B., et al. "Assessment of the comparability of droplet evaporation fuel sensitivities between a unit test case and an aviation gas turbine combustor". In: *AIAA Scitech 2019 Forum.* 2019, p. 0727.

[218]   Sacks, J., Welch, W. J., et al. "Design and analysis of computer experiments". In: *Statistical Science* (1989), pp. 409–423.

[219]   Sagaut, P. and Grohens, R. "Discrete filters for large eddy simulation". In: *International Journal for Numerical Methods in Fluids* 31.8 (1999), pp. 1195–1220.

[220]   Sagaut, P. *Large eddy simulation for incompressible flows: an introduction.* Springer Science & Business Media, 2006.

[221]   Sagaut, P. *Multiscale and multiresolution approaches in turbulence: LES, DES and hybrid RANS/LES methods: applications and guidelines.* World Scientific, 2013.

[222]   Saggese, C., Singh, A. V., et al. "The distillation curve and sooting propensity of a typical jet fuel". In: *Fuel* 235 (2019), pp. 350–362.

[223]   Saltelli, A., Ratto, M., et al. *Global sensitivity analysis: the primer.* John Wiley & Sons, 2008.

[224]   Saltelli, A., Tarantola, S., et al. *Sensitivity analysis in practice: a guide to assessing scientific models.* John Wiley & Sons, 2004.

[225]   Sankararaman, S. and Goebel, K. "Uncertainty quantification in remaining useful life of aerospace components using state space models and inverse form". In: *54th AIAA/ASME/ASCE/AHS/ASC Structures, Structural Dynamics, and Materials Conference.* 2013, p. 1537.

[226]   Santner, T. J., Williams, B. J., et al. *The design and analysis of computer experiments.* Springer Science & Business Media, 2013.

[227]   Santolaya, J., Aisa, L., et al. "Experimental study of near-field flow structure in hollow cone pressure swirl sprays". In: *Journal of Propulsion and Power* 23.2 (2007), pp. 382–389.

[228] Sazhin, S. S. "Advanced models of fuel droplet heating and evaporation". In: *Progress in Energy and Combustion Science* 32.2 (2006), pp. 162–214.

[229] Schlichting, H. and Gersten, K. *Boundary-layer theory.* Springer, 2016.

[230] Schmehl, R. "Tropfendeformation und Nachzerfall bei der technischen Gemischaufbereitung". PhD thesis. Universität Karlsruhe, 2004.

[231] Schmidt, D. P., Nouar, I., et al. *Pressure-swirl atomization in the near field.* Tech. rep. SAE Technical Paper, 1999.

[232] Schulz, E., Speekenbrink, M., et al. "A tutorial on Gaussian process regression: Modelling, exploring, and exploiting functions". In: *Journal of Mathematical Psychology* 85 (2018), pp. 1–16.

[233] Schwarzkopf, J. D., Sommerfeld, M., et al. *Multiphase flows with droplets and particles.* CRC press, 2011.

[234] Senecal, P., Schmidt, D. P., et al. "Modeling high-speed viscous liquid sheet atomization". In: *International Journal of Multiphase Flow* 25.6 (1999), pp. 1073–1097.

[235] Setzwein, F., Ess, P., et al. "Large-Eddy Simulation of Spray Flames in the DLR Generic Single Sector Combustor". In: *AIAA Propulsion and Energy 2019 Forum.* 2019, p. 3865.

[236] Shafer, G. *A mathematical theory of evidence.* Vol. 42. Princeton university press, 1976.

[237] Sheen, D. A. and Wang, H. "The method of uncertainty quantification and minimization using polynomial chaos expansions". In: *Combustion and Flame* 158.12 (2011), pp. 2358–2374.

[238] Shinjo, J. and Umemura, A. "Simulation of liquid jet primary breakup: Dynamics of ligament and droplet formation". In: *International Journal of Multiphase Flow* 36.7 (2010), pp. 513–532.

[239] Sirignano, W. A. *Fluid dynamics and transport of droplets and sprays.* Cambridge university press, 2010.

[240] Slavinskaya, N. "Skeletal mechanism for kerosene combustion with PAH production". In: *Proceedings of 46th AIAA Aerospace Sciences Meeting and Exhibit, Reno (USA), Paper.* 0992. 2008.

[241] Sloan, J., Sun, Y., et al. "Uncertainty quantification for discrimination of nuclear events as violations of the comprehensive nuclear-test-ban treaty". In: *Journal of Environmental Radioactivity* 155 (2016), pp. 130–139.

[242] Smolyak, S. A. "Quadrature and interpolation formulas for tensor products of certain classes of functions". In: *Doklady Akademii Nauk.* Vol. 148. 5. Russian Academy of Sciences. 1963, pp. 1042–1045.

[243] Sobol, I. M. "Sensitivity estimates for nonlinear mathematical models". In: *Mathematical Modelling and Computational Experiments* 1.4 (1993), pp. 407–414.

[244] Sobol, I. M., Asotsky, D., et al. "Construction and Comparison of High-Dimensional Sobol'Generators". In: *Wilmott* 2011.56 (2011), pp. 64–79.

[245] Sommerfeld, M. "Analysis of isothermal and evaporating turbulent sprays by phase-Doppler anemometry and numerical calculations". In: *International Journal of Heat and Fluid Flow* 19.2 (1998), pp. 173–186.

[246] Spalart, P. R. "Detached-eddy simulation". In: *Annual review of fluid mechanics* 41 (2009), pp. 181–202.

[247] Spalart, P. R., Deck, S., et al. "A new version of detached-eddy simulation, resistant to ambiguous grid densities". In: *Theoretical and Computational Fluid Dynamics* 20.3 (2006), p. 181.

[248] Spalding, D. "Mixing and chemical reaction in steady confined turbulent flames". In: *Symposium (International) on Combustion*. Vol. 13. 1. Elsevier. 1971, pp. 649–657.

[249] Speziale, C. "Turbulence modeling for time-dependent RANS and VLES: a review". In: *AIAA journal* 36.2 (1998), pp. 173–184.

[250] *Standard for Models and Simulations STD-7009A*. National Aeronautics and Space Administration (NASA), 2016.

[251] Stern, F., Wilson, R. V., et al. "Comprehensive approach to verification and validation of CFD simulations—part 1: methodology and procedures". In: *Journal of Fluids Engineering* 123.4 (2001), pp. 793–802.

[252] Sudret, B. "Global sensitivity analysis using polynomial chaos expansions". In: *Reliability Engineering & System Safety* 93.7 (2008), pp. 964–979.

[253] Sudret, B. "Uncertainty propagation and sensitivity analysis in mechanical models–Contributions to structural reliability and stochastic spectral methods". In: *Habilitation a diriger des recherches, Université Blaise Pascal, Clermont-Ferrand, France* (2007), p. 18.

[254] Sudret, B., Marelli, S., et al. "Surrogate models for uncertainty quantification: An overview". In: *2017 11th European Conference on Antennas and Propagation (EUCAP)*. IEEE. 2017, pp. 793–797.

[255] Syred, N. "A review of oscillation mechanisms and the role of the precessing vortex core (PVC) in swirl combustion systems". In: *Progress in Energy and Combustion Science* 32.2 (2006), pp. 93–161.

[256] Tamim, J. and Hallett, W. L. "A continuous thermodynamics model for multicomponent droplet vaporization". In: *Chemical Engineering Science* 50.18 (1995), pp. 2933–2942.

[257] Tang, Y., Hassanaly, M., et al. "A comprehensive modeling procedure for estimating statistical properties of forced ignition". In: *Combustion and Flame* 206 (2019), pp. 158–176.

[258] Tanner, F. X. *A cascade atomization and drop breakup model for the simulation of high-pressure liquid jets*. Tech. rep. SAE Technical Paper, 2003.

[259]   Tropea, C. "Optical particle characterization in flows". In: *Annual Review of Fluid Mechanics* 43 (2011), pp. 399–426.

[260]   Trucano, T. G., Swiler, L. P., et al. "Calibration, validation, and sensitivity analysis: What's what". In: *Reliability Engineering & System Safety* 91.10 (2006), pp. 1331–1357.

[261]   Tucker, W. T. and Ferson, S. "Probability bounds analysis in environmental risk assessment". In: *Applied Biomathematics, Setauket, New York* (2003).

[262]   Turner, M., Sazhin, S., et al. "A breakup model for transient Diesel fuel sprays". In: *Fuel* 97 (2012), pp. 288–305.

[263]   Turnquist, B. and Owkes, M. "multiUQ: An intrusive uncertainty quantification tool for gas-liquid multiphase flows". In: *Journal of Computational Physics* 399 (2019), p. 108951.

[264]   Tzvieli, A. "Possibility theory: An approach to computerized processing of uncertainty". In: *Journal of the American Society for Information Science* 41.2 (1990), pp. 153–154.

[265]   Van Dam, N. and Rutland, C. "Uncertainty Quantification of Large-Eddy Spray Simulations". In: *Journal of Verification, Validation and Uncertainty Quantification* 1.2 (2016), p. 021006.

[266]   Vasu, S. S., Davidson, D. F., et al. "Jet fuel ignition delay times: Shock tube experiments over wide conditions and surrogate model predictions". In: *Combustion and Flame* 152.1 (2008), pp. 125–143.

[267]   Versteeg, H. K. and Malalasekera, W. *An introduction to computational fluid dynamics: the finite volume method*. Pearson Education, 2007.

[268]   Wand, M. P. and Jones, M. C. *Kernel smoothing*. Chapman and Hall/CRC, 1994.

[269]   Warnatz, J., Maas, U., et al. *Combustion*. 4th ed. Springer, 2006.

[270]   Welch, W. J., Buck, R. J., et al. "Screening, predicting, and computer experiments". In: *Technometrics* 34.1 (1992), pp. 15–25.

[271]   Westbrook, C. K. and Dryer, F. L. "Simplified reaction mechanisms for the oxidation of hydrocarbon fuels in flames". In: *Combustion Science and Technology* 27.1-2 (1981), pp. 31–43.

[272]   Whitson, C. H. et al. "Characterizing hydrocarbon plus fractions". In: *Society of Petroleum Engineers Journal* 23.04 (1983), pp. 683–694.

[273]   Wiener, N. "The homogeneous chaos". In: *American Journal of Mathematics* 60.4 (1938), pp. 897–936.

[274]   Wilcox, D. C. et al. *Turbulence modeling for CFD*. Vol. 2. DCW industries La Canada, CA, 1998.

[275]   Williams, C. K. and Rasmussen, C. E. *Gaussian processes for machine learning*. Vol. 2. 3. MIT press Cambridge, MA, 2006.

[276] Wolf, P., Balakrishnan, R., et al. "Using LES to study reacting flows and instabilities in annular combustion chambers". In: *Flow, Turbulence and Combustion* 88.1-2 (2012), pp. 191–206.

[277] Wünning, J. and Wünning, J. "Flameless oxidation to reduce thermal no-formation". In: *Progress in Energy and Combustion Science* 23.1 (1997), pp. 81–94. ISSN: 0360-1285. DOI: `http://dx.doi.org/10.1016/S0360-1285(97)00006-3`.

[278] Xing, F., Kumar, A., et al. "Flameless combustion with liquid fuel: A review focusing on fundamentals and gas turbine application". In: *Applied Energy* 193 (2017), pp. 28–51.

[279] Xiu, D. and Karniadakis, G. E. "The Wiener–Askey polynomial chaos for stochastic differential equations". In: *SIAM journal on scientific computing* 24.2 (2002), pp. 619–644.

[280] Yao, W., Chen, X., et al. "Review of uncertainty-based multidisciplinary design optimization methods for aerospace vehicles". In: *Progress in Aerospace Sciences* 47.6 (2011), pp. 450–479.

[281] Yondo, R., Andrés, E., et al. "A review on design of experiments and surrogate models in aircraft real-time and many-query aerodynamic analyses". In: *Progress in aerospace sciences* 96 (2018), pp. 23–61.

[282] Yuen, M. and Chen, L. "On drag of evaporating liquid droplets". In: *Combustion science and technology* 179.1-2 (1976), pp. 319–342.

[283] Zang, T. A. *Needs and opportunities for uncertainty-based multidisciplinary design methods for aerospace vehicles*. National Aeronautics and Space Administration, Langley Research Center, 2002.

Lebenslauf

Persönliche Daten

Name	Benedict Enderle
Geburtstag	01.11.1988
Geburtsort	Berlin
Nationalität	Deutsch

Schulausbildung

1999 − 2008	Otto-Hahn-Gymnasium Karlsruhe

Zivildienst

08/2008 − 05/2009	Diakonie-Klinikum Stuttgart

Studium

04/2013 − 07/2015	M.Sc. Luft- und Raumfahrttechnik, Universität Stuttgart
10/2014 − 04/2015	Masterarbeit, University of California, Davis - USA
10/2009 − 03/2013	B.Sc. Luft- und Raumfahrttechnik, Universität Stuttgart

Berufliche Tätigkeit

seit 2015	Wissenschaftlicher Mitarbeiter, Deutsches Zentrum für Luft- und Raumfahrt e.V. Institut für Verbrennungstechnik, Stuttgart